On the Preliminary Design of Aerospace-grade Compact Heat Exchangers

From Ram Air Cooling Ducts to Energy Harvesting Systems

Fabio Beltrame

On the Preliminary Design of Aerospace-Grade Compact Heat Exchangers

From ram-air cooling ducts to energy harvesting systems

On the Preliminary Design of Aerospace-Grade Compact Heat Exchangers

From ram-air cooling ducts to energy harvesting systems

Dissertation

for the purpose of obtaining the degree of doctor
at Delft University of Technology,
by the authority of the Rector Magnificus Prof.dr.ir. H. Bijl,
chair of the Board for Doctorates,
to be defended publicly on
Friday the 16th of January 2026 at 10:00 o'clock

by

Fabio Beltrame

This dissertation has been approved by the promotors.

Composition of the doctoral committee:

Rector Magnificus,	Chairperson
Prof. dr. ir. P. Colonna di Paliano,	Delft University of Technology, *promotor*
Dr. C.M. De Servi,	Delft University of Technology, *copromotor*
Independent members:	
Prof. dr. M. Kotsonis	Delft University of Technology
Prof. dr. ir. S. Lecompte	Ghent University, Belgium
Prof. dr. K. Kyprianidis	Mälardalen University, Sweden
Dr. S. Evans	Pratt & Whitney, USA
Prof. dr. ir. L.L.M. Veldhuis	Delft University of Technology, *reserve member*

The research presented in this dissertation has been performed at the Flight Performance and Propulsion Section, Department of Flow Physics and Technology, Faculty of Aerospace Engineering. This work is part of the research project "Airborne Thermal Energy Harvesting for Aircraft" (ARENA), funded by the Applied and Engineering Sciences Division of the Dutch Organization for Scientific Research (NWO), Open Technology Program of the Ministry of Economic Affairs, Grant No. 17906.

Cover design: Anna Tsarkova

Copyright © 2025 by F. Beltrame

ISBN 978-94-6518-215-5

An electronic version of this dissertation is available at
http://repository.tudelft.nl/.

An expert
is someone who has made all the mistakes
which can be made
in a narrow field.

Niels Bohr

CONTENTS

SUMMARY

The improvement of the efficiency of aircraft propulsion systems and the reduction of fuel consumption are key objectives in the development of next-generation propulsion systems. The feasibility and performance of promising concepts such as combined-cycle engines, hybrid-electric propulsion, and hydrogen-fueled systems often depend on complex thermal management or cooling systems, where compact heat exchangers (HXs) are critical components. More in detail, the integration of HXs in airborne systems is limited by strict space and volume constraints as well as by the impact of pressure losses and mass on the performance of the propulsion system. Therefore, sub-optimal HX designs can offset or even negate potential performance gains.

This dissertation documents research work performed as part of the ARENA project, which aims to develop methodologies for assessing the fuel-saving potential of airborne organic Rankine cycle thermal energy harvesting systems serving as bottoming units to gas turbine engines, leveraging unconventional propulsion system configurations. The first objective of the present research is to advance the state-of-the-art regarding methodologies for the optimal design and integration of aerospace-grade compact HXs into novel propulsion systems. The second objective is to investigate the potential of the Meredith effect, whereby the drag introduced by an air-cooled HX is offset by the acceleration of the heated airflow through a nozzle, for airborne ORC units, and to develop methods for the optimal design of the ram air cooling system.

To this end, an HX model for single- and multi-pass configurations, applicable for sizing and rating problems of components operating with sub- and supercritical working fluids, was implemented in the in-house software *HeXacode* and validated with experimental data. Preliminary design tools based on this HX model have been embedded within the system design framework for integrated system-and-component optimization of aero engines featuring an ORC bottoming unit. The system design framework was used to optimize the design of combined-cycle auxiliary power unit (CC-APU), turboshaft (CC-TS), and turbofan (CC-TF) configurations. The results demonstrate that achieving optimal performance requires balancing HX thermal effectiveness, pressure loss, and mass. However, this integrated optimization approach is computationally time-consuming. Therefore, a data-driven surrogate modeling methodology has been developed to predict the performance of optimized HXs under variable operating conditions and design specifications. This method reduces the computational cost associated with system optimization studies by more than half.

Results of optimal combined cycle engine configurations demonstrated that the thermal energy rejected by the condenser to the ram air stream can increase propulsive efficiency and specific thrust. This thrust gain is primarily influenced by the total pressure losses in the duct, ram-air temperature increase, and total to static nozzle pressure ratio. Therefore, the thrust that can be generated by the ram air cooling duct is much larger in the case of the CC-TF, whereby the condenser is positioned aft of the fan and outlet

guide vane within the bypass duct, compared to the CC-TS configuration.

Due to the significant influence of the ram air cooling duct on the aerodynamic performance of the propulsion system, an accurate duct model is required for preliminary design studies. Therefore, a CFD model of the ram air duct has been developed, whereby the HX is modeled as a porous zone while a steady state RANS solver is used for the airflow within the duct. The CFD model has been used to develop a lumped parameter model of the ram air duct. The accuracy of the developed lumped parameter model is comparable to that of the CFD model, and enables fast evaluation of the duct performance at both design and off-design conditions. The lumped parameter model is also used to quantify the influence of HX and duct geometric design, heat rejection, and total pressure losses on drag recovery through the Meredith effect, providing new guidelines for ram air cooling systems for airborne applications.

The methodologies developed in this research work are directly applicable to waste heat recovery systems, fuel-cell-based electric propulsion or turbo-electric propulsion systems, and support early-stage preliminary design assessments. These results contribute to reducing the uncertainty in adopting combined-cycle and other novel propulsion systems, and to guiding future development of lightweight, high-performance HXs for low-emission aviation.

SAMENVATTING

Het verbeteren van de efficiëntie van vliegtuigvoortstuwingssystemen en het verminderen van het brandstofverbruik zijn belangrijke doelstellingen bij de ontwikkeling van volgende generatie voortstuwingssystemen. De haalbaarheid en prestaties van veelbelovende concepten zoals gecombineerde-cyclusmotoren, hybride-elektrische voortstuwing en waterstofsystemen zijn vaak afhankelijk van complexe thermische beheer- of koelsystemen, waarbij compacte warmtewisselaars (HX's) cruciale componenten zijn. Meer in detail: de integratie van HX's in luchtgedragen systemen wordt beperkt door strikte ruimte- en volumebeperkingen, evenals door de impact van drukverliezen en massa op de prestaties van het voortstuwingssysteem. Suboptimale HX-ontwerpen kunnen daarom potentiële prestatieverbeteringen tenietdoen of zelfs tenietdoen.

Dit proefschrift documenteert onderzoekswerk dat is uitgevoerd in het kader van het ARENA-project, dat tot doel heeft methodologieën te ontwikkelen voor het beoordelen van het brandstofbesparende potentieel van luchtgedragen organische Rankine-cyclus thermische energieopwekkingssystemen die dienen als bottoming units voor gasturbinemotoren, waarbij gebruik wordt gemaakt van onconventionele voortstuwingsconfiguraties.

Hiertoe werd een HX-model voor single- en multi-pass configuraties, toepasbaar op dimensionerings- en beoordelingsproblemen van componenten die werken met sub- en superkritische werkvloeistoffen, geïmplementeerd in de eigen software *HeXacode* en gevalideerd met experimentele data. Voorlopige ontwerptools gebaseerd op dit HX-model zijn ingebed in het systeemontwerpkader voor geïntegreerde systeem- en componentoptimalisatie van vliegtuigmotoren met een ORC-bodemeenheid. Het systeemontwerpkader werd gebruikt om het ontwerp van gecombineerde cyclushulpaggregaten (CC-APU), turboshaft (CC-TS) en turbofan (CC-TF) configuraties te optimaliseren. De resultaten tonen aan dat het bereiken van optimale prestaties een evenwicht vereist tussen de thermische effectiviteit, het drukverlies en de massa van HX. Deze geïntegreerde optimalisatiebenadering is echter rekenintensief. Daarom is een datagestuurde surrogaatmodelleringsmethodologie ontwikkeld om de prestaties van geoptimaliseerde HX'en onder variabele bedrijfsomstandigheden en ontwerpspecificaties te voorspellen. Deze methode verlaagt de rekenkosten die gepaard gaan met systeemoptimalisatiestudies met meer dan de helft.

Resultaten van optimale gecombineerde cyclus motorconfiguraties toonden aan dat de thermische energie die door de condensor naar de ram-airstroom wordt afgevoerd, het voortstuwingsrendement en de specifieke stuwkracht kan verhogen. Deze stuwkrachtwinst wordt voornamelijk beïnvloed door de totale drukverliezen in het kanaal, de temperatuurstijging van de ram-air en de verhouding tussen de totale en de statische druk in de nozzle. Daarom is de stuwkracht die door het ram-air koelkanaal kan worden gegenereerd veel groter in het geval van de CC-TF, waarbij de condensor achter de ventilator en de uitlaatgeleider in het bypasskanaal is geplaatst, vergeleken met de

CC-TS-configuratie.

Vanwege de aanzienlijke invloed van het ram-air-koelkanaal op de aerodynamische prestaties van het voortstuwingssysteem, is een nauwkeurig kanaalmodel vereist voor voorlopige ontwerpstudies. Daarom is een CFD-model van het ram-air-kanaal ontwikkeld, waarbij de HX is gemodelleerd als een poreuze zone, terwijl een steady-state RANS-solver is gebruikt voor de luchtstroom in het kanaal. Het CFD-model is gebruikt om een gecombineerd parametermodel van het ram-air-kanaal te ontwikkelen. De nauwkeurigheid van het ontwikkelde gecombineerde parametermodel is vergelijkbaar met die van het CFD-model en maakt een snelle evaluatie van de kanaalprestaties mogelijk, zowel onder ontwerp- als off-design-omstandigheden. Het gecombineerde parametermodel wordt ook gebruikt om de invloed van HX en het geometrische ontwerp van het kanaal, warmteafvoer en totale drukverliezen op de luchtweerstandsherstel door middel van het Meredith-effect te kwantificeren, wat nieuwe richtlijnen oplevert voor ram-air-koelsystemen voor toepassingen in de lucht.

De in dit onderzoek ontwikkelde methodologieën zijn direct toepasbaar op systemen voor warmteterugwinning, elektrische voortstuwingssystemen op basis van brandstofcellen of turbo-elektrische voortstuwingssystemen, en ondersteunen voorlopige ontwerpbeoordelingen in een vroeg stadium. Deze resultaten dragen bij aan het verminderen van de onzekerheid bij de invoering van gecombineerde-cyclus- en andere nieuwe voortstuwingssystemen, en aan het sturen van de toekomstige ontwikkeling van lichtgewicht, krachtige HX's voor emissiearme luchtvaart.

1

INTRODUCTION

The history of mankind
is the history of ideas.

Luigi Pirandello

1

1.1. CONTEXT

In the absence of immediate and coordinated intervention, the ongoing climate crisis is expected to trigger profound and potentially irreversible transformations in natural ecosystems, with cascading consequences for human society [1] [2]. Mitigating these outcomes requires implementing multi-layered strategies encompassing societal behavioral shifts, coherent international and national policy frameworks, and the accelerated development and deployment of innovative technological solutions [3]. The aviation sector is under increasing pressure due to environmental regulations aimed at reducing the environmental footprint of air transportation, primarily in terms of carbon dioxide CO_2 and nitrogen oxide NO_x emissions [4].

At the time of writing, the aviation sector accounts for ≈ 2.5% of all human-induced CO_2 emissions, and ≈ 13% of total transportation emissions, yearly [5]. Carbon dioxide emissions, along with nitrogen oxide emissions, the formation of condensation trails, and the release of soot and sulfate aerosols, alter the chemical composition of the upper atmosphere. The radiative balance in this region is also affected by nitrogen oxides, which impact the quantities of ozone (O_3) and stratospheric water vapor, thereby influencing the climate [6]. These non-CO_2 emissions contribute to an additional net warming effect, resulting in aviation's overall contribution to human-induced global warming being approximately 4% today [7]. However, this share is projected to rise significantly in the coming decades as demand for air travel continues to grow [8] [9].

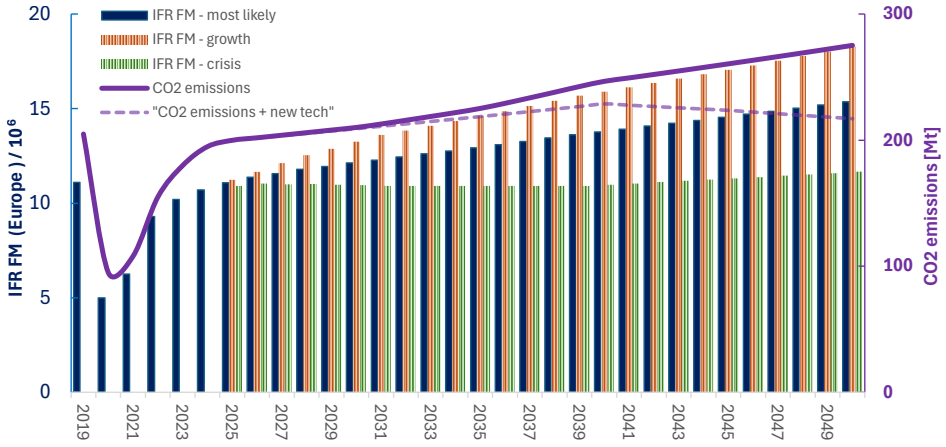

Figure 1.1: Historical evolution and projection of the civil aviation flight movements (IFR FM) in Europe for the most likely scenario (|), in case of continued economic growth (||) and of economic crisis and fuel price surge (||). The CO_2 emissions are reported on the right-hand y-axis for the most likely scenario (–) and in case new-gen engines gradually replace the older generation engines (- -). Data collected from [10] [11] [12].

Figure 1.1 reports the total number of take-offs and landings in Europe, obtained from data related to *instrument flight rules* or IFR, therefore those that must comply with regulations about aircraft operation in civil aviation. The graph shows the extrapolation to the near future for (i) the most likely scenario (baseline), (ii) a scenario of economic growth, and (iii) a scenario of economic crisis accompanied by a sharp rise in fuel prices.

The CO_2 emission projections associated with EU commercial aviation are proportional to the number of flights unless part of the older generation of aero engines is retired and new generation engines are deployed starting from 2040. Note that the chart only reports carbon dioxide emissions, although other greenhouse gas emissions, such as NO_x and water vapor that form contrails, are also important metrics that new generation engines and policies are accounting for.

Over the past decades, continuous advancements in turbofan engines, enabled by improved aerodynamics and materials, have led to a significant decrease in thrust-specific fuel consumption (TSFC), with modern engines achieving values around 13 mg/Ns compared to approximately 19 mg/Ns of 1980s turbofans [13] [14]. Such traditional technological improvements include increasing the pressure ratio, turbine inlet temperature, and bypass ratio to achieve gains in propulsive and thermal efficiency. However, the rate of improvement has progressively diminished in the last decades, as contemporary engine design optimizations approach the practical, structural, and material limits [15].

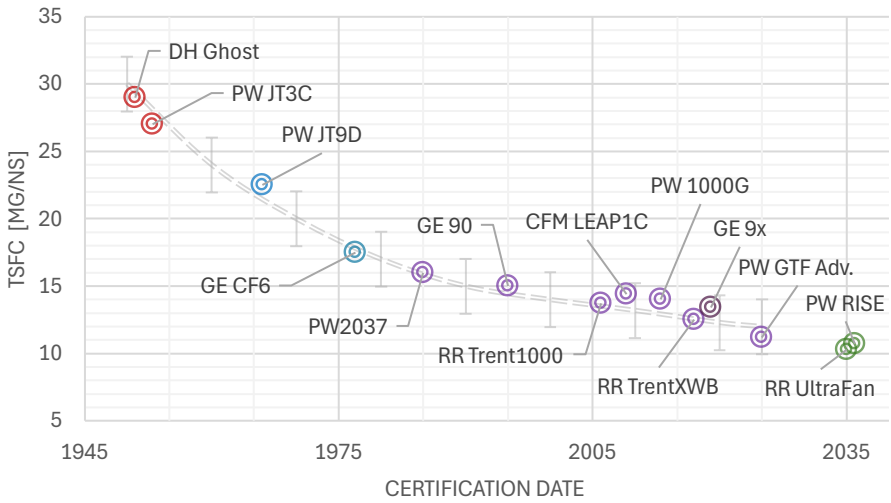

Figure 1.2: Cruise thrust-specific fuel consumption (TSFC) of representative engines over the approximated certification date. Red markers correspond to turbojet engines, blue markers to turbofan engines with bypass ratios below 6, purple markers are modern high-bypass ratio turbofans, while the green markers are new-generation engines expected to enter service around 2035. Data collected from [16], [17], [18], [14]

This trend is clear in Figure 1.2, which shows the TSFC during cruise conditions of representative engines. At the same time, the aviation sector continues to expand, leading to a net increase in global fuel consumption and emissions despite improvements in engine performance. To address this challenge, the Advisory Council for Aviation Research and Innovation in Europe (ACARE) has set ambitious goals within the Flightpath 2050 framework [19], targeting (i) a 75% reduction in CO_2 emissions and a 90% reduction in NO_x emissions per passenger-kilometer, and (ii) a 65% reduction in noise emission during flight. All improvements are compared to the year 2000 levels. Similarly, inter-

national regulatory bodies such as the International Civil Aviation Organization (ICAO) and national programs such as NASA's Sustainable Flight National Partnership have established ambitious long-term targets to drastically reduce greenhouse gas emissions, aiming at net-zero carbon emissions from aviation by 2050 [20] [21]. Meeting such objectives requires a paradigm shift from conventional propulsion system configurations toward novel system architectures leveraging new materials and manufacturing technologies, alternative fuels, novel propulsion concepts combining multiple cycles, new power generation systems, waste heat recovery solutions, and electrification.

1.2. NOVEL PROPULSION SYSTEM CONCEPTS FOR COMMERCIAL AVIATION

Engine manufacturers are investing considerable resources in research programs aimed at reducing fuel consumption and emissions by improving the propulsive and thermal efficiency of propulsion systems and their integration into the airframe. Current research on propulsion systems is concentrating on (i) the improvement of existing aero engine configurations by component optimization and the use of advanced manufacturing techniques and materials, (ii) the electrification and hybridization of propulsion systems, and (iii) the adoption of unconventional thermodynamic cycle configurations.

1.2.1. IMPROVED CONVENTIONAL CONFIGURATIONS

A notable development in advanced turbofan architecture is the GTF® Advantage engine by Pratt & Whitney [22], which targets fuel efficiency improvements beyond 20%, reduced noise footprint, and 4% more takeoff thrust at sea level over current engines [23]. The 100% SAF-compatible engine features enhancements to the engine core, such as advanced airfoil design with improved coatings of the high-pressure turbine and optimized cooling, which increase engine durability, extending engine maintenance interval by up to 40% [24]. The engine has been certified in early 2025 by the Federal Aviation Administration (FAA) and will power the A320neo aircraft [24].

Another notable research program is the one related to the development of the UltraFan® engine concept, led by Rolls-Royce with support from the Clean Aviation framework. The UltraFan is currently the largest aero engine demonstrator ever built, featuring a fan diameter of 3.55 m. The objectives of the program include a 25% reduction in fuel consumption and CO_2 emissions compared to first-generation Trent engines, a 40% reduction in NO_x, and a 30% reduction in noise levels thanks to a redesign of the engine configuration, a carbon-titanium fan system, and a lightweight composite casing [25]. Central to the UltraFan concept is a new gearbox that transfers over 50 MW of power, allowing the fan and low-pressure turbine to operate at their optimal speeds. In parallel, advanced manufacturing techniques such as additive layer manufacturing and the use of ceramic matrix composites support higher operating temperatures and reduced component mass. The UltraFan demonstrator is scheduled to be tested using 100% SAF and is expected to enter the market in the 2030s.

A relevant example of a research program aimed at a large increase in propulsive efficiency is the Revolutionary Innovation for Sustainable Engines (RISE) program, a collaborative initiative led by CFM International, a partnership between Safran and Gen-

eral Electric. Launched in 2021, the RISE program aims to develop a next-generation open rotor propulsion system targeting a > 20% reduction of fuel consumption and CO_2 emissions compared to modern aero engines. The engine prototype incorporates a single-stage open rotor followed by variable-pitch stator vanes, enabling efficient flow management, compliance with future noise regulations, and eliminating the need for a thrust reverser [26]. The open fan configuration is engineered to operate at speeds up to Mach 0.8, aligning with current single-aisle aircraft requirements. Moreover, the engine is being designed for compatibility with sustainable aviation fuels and hydrogen.

1.2.2. MORE ELECTRIC PROPULSION

In recent years, extensive research into electrified propulsion systems has been conducted. Electrification pathways are generally categorized into three types: turboelectric, fully electric, and hybrid-electric [27].

- In the turboelectric configurations, the mechanical powertrain is replaced by an electrically driven propulsion system powered by one or more gas turbines. The NASA N3-X [28] is an example of a fully turboelectric aircraft with a hybrid wing-body airframe.[1] The benefits of such architecture include enhanced propulsive efficiency and better airframe-propulsion integration if combined with distributed propulsion (DP) and boundary layer ingestion (BLI). However, it is estimated that turboelectric propulsion systems would be approximately 10% less efficient compared to mechanically-driven engines, primarily due to the many losses and weight addition inherent to electrical energy conversion, like those due to electric motors, cables, power electronics, etc. [29]. Their implementation in large aircraft is currently constrained by the availability of high-specific-power electrical generators, motors, and superconducting components suitable for aviation.

- Fully electric propulsion systems rely exclusively on battery packs for onboard energy storage. The primary advantages of this configuration include the elimination of in-flight emissions and a significant reduction in acoustic noise. However, the low specific energy of contemporary batteries remains a critical limitation, with values that are 20 to 50 times lower than those of jet fuel [27]. As a result, fully electric aircraft have long been considered suitable only for short-range missions with limited payload capacity. Recent studies, however, have challenged the correctness of this limitation. For instance, Wolleswinkel et al. [30] demonstrated by means of calculations that fully electric aircraft adopting a narrow fuselage layout, high energy mass fraction, and high lift-to-drag ratio can achieve ranges approaching 1000 km, even in the case of a medium-size aircraft. This performance is attainable under realistic assumptions about future battery technologies, specifically a pack-level energy density of approximately 300 Wh/kg. De Vries et al. [31] performed the conceptual design of a 76-ton electric aircraft for a mission range of 800 km. With the assumption of a battery pack energy density of 360 Wh/kg, the estimated energy consumption was 167 Wh per passenger-kilometer, which is

[1] The N3-X concept is a turboelectric aircraft concept with a hybrid wing-body airframe, boundary layer ingestion, distributed propulsion, and superconducting materials to minimize transmission losses

significantly lower than what is estimated in the case where kerosene and SAF are used to store energy.

- Hybrid-electric propulsion (HEP) systems integrate a power generation system, such as a gas turbine, whose function is either to charge electric batteries and/or to drive propellers, and an electric power train driving propellers. Two primary configurations are considered, namely the parallel and series layouts. In parallel configurations, the gas turbine and electric motor operate concurrently to provide thrust across various flight phases. In series configurations, the gas turbine operates near its optimal point to accumulate electrical energy, which is used to drive the electric propulsion system, functionally resembling a turboelectric architecture with energy buffering. Hybrid-electric architectures enable greater operational flexibility compared to purely turboelectric systems and introduce redundancy in power generation and delivery [32]. Additionally, such configurations allow for supplementing the power-intensive phases of flight, i.e., takeoff and climb, with electrical power. As a result, the core gas turbine can be downsized and designed for maximum cruise efficiency, thereby reducing mission fuel consumption [27].

The implementation of electric propulsion systems (EPS) is associated with considerable technological challenges. These include increased system complexity, weight penalties due to batteries and power electronics, power distribution losses, airframe integration issues, and complex thermal management systems (TMS) that must operate under highly variable conditions [33]. Among these challenges, the design of the TMS is particularly critical even at the early conceptual stage, as it directly influences the overall aircraft mass, aerodynamic drag, and propulsion system efficiency [34]. Typical TMS configurations employ liquid cooling via cold plates for powertrain components and utilize ram air as the heat sink [35]. These systems incorporate one or more compact air-to-liquid heat exchangers (HXs) to reject thermal energy to the ambient. These components are usually placed inside ram air ducts and introduce a significant drag penalty, primarily due to the total pressure losses across the HX core. Additionally, HXs account for over 50% of the total TMS mass, which is approximately 1.27 kg $\pm$ 14.5% per kilowatt of rejected thermal power [34], excluding redundancy requirements. The weight of the TMS is thus an important metric for the evaluation of electric aircraft configurations. For instance, the TMS of an electric aircraft that must continuously reject 350-400 kW of thermal power to the environment would weigh over 500 kg and introduce a significant drag penalty. However, the design of the TMS is often neglected and, as a consequence, the effect of the TMS weight and drag on the aircraft performance is often roughly approximated [31], [34]. More electric propulsion systems remain a promising solution for sustainable aviation, particularly in combination with novel aircraft configurations [30], [31]. The feasibility of large-scale adoption will ultimately depend on the rate of progress in battery chemistry, electric motor efficiency, as well as integrated system and component design optimization techniques [33].

The number of research projects on hybrid electric aircraft propulsion architectures is increasing in response to technological advancements in hydrogen storage and fuel cell technology. One of the primary advantages of liquid hydrogen (LH2) lies in its high

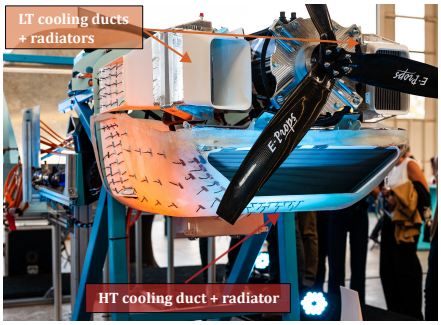

(a) Photograph of the nose of the demonstrator developed within the Phoenix project at TU Delft [36] during wind tunnel tests. The low-temperature (LT) cooling ducts for the power electronics are positioned on the left and right-hand side of the electric motor and propeller. The high-temperature (HT) cooling duct rejects thermal power to maintain the FC stack within the operating temperature limits.

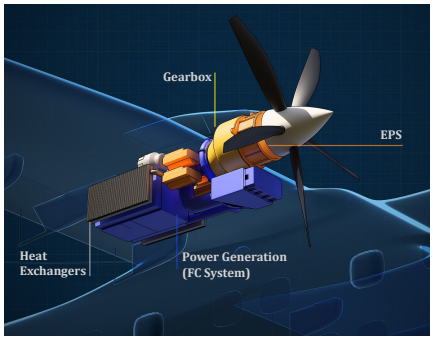

(b) Simplified CAD representation of the Zeroavia ZA600 hydrogen-electric engine concept. The nacelle and ram air ducts are omitted. Image adapted from the illustration reported in Ref. [37].

Figure 1.3: Fuel cell-based hydrogen-electric propulsion system (EPS) demonstrators.

gravimetric energy density (≈ 120 MJ/kg), which is nearly three times greater than that of conventional jet fuel [38]. The use of hydrogen as fuel for gas turbines is not a new concept. In addition to eliminating in-flight CO_2 emissions, hydrogen combustion has been shown to reduce energy-specific fuel consumption by about 1.6% compared to kerosene [39]. However, hydrogen combustion does not eliminate NO_x emissions. Moreover, the increased water vapor emissions necessitate careful consideration to limit contrail formation and the associated climate impact. In contrast, fuel cells (FC) convert hydrogen directly into electricity via electrochemical reactions, eliminating NO_x emissions. Recent advancements in FC technology, particularly for high-temperature proton-exchange membrane (LT/HT-PEMFC) variants, suggest that mass-specific power values of approximately 3 kW/kg could be achieved by 2035, alongside overall conversion efficiency in the range of 50–70%. These improvements open the possibility for fuel cell-powered hybrid-electric aircraft capable of missions of up to 800 nautical miles with a payload of 75 passengers [39]. Furthermore, the cryogenic temperatures of hydrogen fuel lines can be exploited to enable low-resistance electrical power transmission using superconducting materials [38]. Despite these advantages, the integration of LH2 into aircraft propulsion systems poses significant challenges. Storage of LH2 at cryogenic temperatures (−253° C) requires (i) lightweight composite tanks targeting 70% gravimetric efficiency [2] by 2035, (ii) effective multi-layer insulation (MLI) or foam-based solutions to minimize boil-off, and (iii) robust LH2 delivery infrastructure and safety systems capable of handling large-scale cryogenic spillage scenarios [39]. Moreover, LH2 tanks occupy 2–4 times the volume of kerosene tanks due to the much lower volumetric energy density of LH2. The larger tanks require fuselage redesign for optimal placement and structural integrity, and they affect payload and passenger capacity [38]. Thermal man-

[2] The mass of hydrogen stored relative to the total mass of the fuel storage system.

agement is another critical hurdle for fuel cell systems, which generate large amounts of heat that must be transferred to the environment to keep the FC system within operational temperature limits. Compact HXs are used to precondition cryogenic hydrogen while simultaneously cooling down power electronic systems and/or the FC stack. However, the cooling capability of LH2 alone is often insufficient, and ram air cooling is also investigated. Due to the relatively low operating temperatures of fuel cells, especially if compared to internal combustion engines, the mean temperature difference in the radiator is quite small. This results in complex cooling systems with large HXs and air ducts, which add weight and drag. Figure 1.3a highlights the large size of the cooling ducts required for a small hydrogen-powered 1-seater Sling-4 aircraft demonstrator being developed by Aerodelft. [3] The ducts are positioned in the nose of the aircraft, around the electric-powered propeller. Figure 1.3b shows the Zeroavia [4] hydrogen-electric engine concept, which requires two large heat exchangers positioned on the left and right sides of the fuel cell stack [37].

Despite these obstacles, ongoing research into advanced tank materials, high-temperature fuel cells, and cryogenic electrical systems aims to make hydrogen-powered hybrid electric aircraft a viable option for regional aircraft and eventually commercial aviation in general.

1.2.3. UNCONVENTIONAL CYCLE CONFIGURATIONS

Modern gas turbine engines discharge to the environment nearly half of the net calorific value of the fuel as thermal energy in the exhaust stream, as indicated in Figure 1.4. Recovering this residual heat allows for an increase in the thermodynamic efficiency of the engine. Relevant thermodynamic cycle improvements include recuperation, intercooling, and combined cycle (CC) configurations. A power plant configuration in which the exhaust of the gas turbine is the energy source of a Rankine power plant is the most common configuration in large-capacity stationary power generation. Such a configuration is termed "combined cycle". The application of this concept to aviation propulsion is under investigation, whereby the main problem is the demanding constraint on weight and volume.

Recuperation in gas turbines for ground applications is an established solution to improve thermodynamic cycle performance [40]. However, the use of recuperation in aero engines remains limited by the challenges associated with the design of the recuperator, which transfers thermal energy from the turbine exhaust to the high-pressure air entering the combustor, thereby increasing cycle efficiency. Extensive research on compact recuperator designs capable of operating at high temperatures and with high-speed flows has been documented in the literature [41]–[44]. An intercooled engine configuration is characterized by a heat exchanger, i.e., the intercooler, placed between the high-pressure (HPC) and low-pressure (LPC) compressors. The intercooler reduces the temperature of the air before entering the second compression stage, thereby decreasing the required compression work and increasing thermal efficiency. Intercooled engine

[3] Aerodelft is a student team of TU Delft working on the development of a hydrogen-powered electric aircraft demonstrator called Project Phoenix. More info at https://aerodelft.nl/.

[4] Zeroavia is a company working on hydrogen-electric and electric propulsion systems. More info at https://zeroavia.com/.

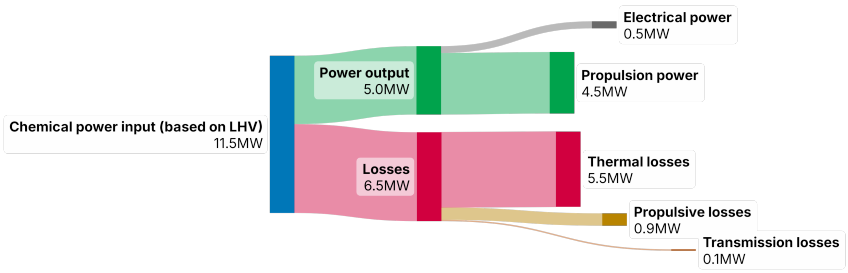

Figure 1.4: Sankey diagram of a modern turbofan engine operating in cruise conditions, with performance similar to that of the CFM LEAP 1A engine, showing the approximate breakdown of the input chemical energy, based on the lower heating value (LHV) of jet fuel.

configurations alone lead to minimal fuel burn reductions (up to 3.4% [45]) compared to conventional TF architectures, and can be effective only for high engine overall pressure ratios (OPR≥ 50) [46] at the cost of increased NO_x emissions.

The combined application of intercooling and recuperation enables a higher thermodynamic cycle efficiency improvement and may reduce TSFC at lower OPR and turbine inlet temperatures (TIT) compared to optimum values of conventional turbofan engines [47]. An additional benefit of adopting engines featuring a lower TIT and OPR is the reduction of NO_x emissions [48]. A notable example of such configuration is the Intercooled Recuperated Aero engine (IRA) concept [49], pioneered by MTU aero engines and investigated within the framework of several past European research programs such as CLEAN/FP5, NEWAC/FP6, LEMCOTEC/FP7, and NEWAC [46], [48]. The baseline IRA configuration features a conventional recuperation layout, whereby a single recuperator, positioned downstream of the LPT, recovers thermal energy from the hot exhaust gases of the gas turbine and transfers it to the HPC discharge air before it enters the combustor [50]. This configuration may lead to an increase in engine thermal efficiency at moderate OPR. The key enabler of this technical solution is the compact recuperator topology developed by MTU. The recuperator geometry consists of two bent banks of staggered elliptical tube bundles positioned at an angle with respect to the exhaust flow [51]. The pressure drop introduced by the recuperator positioned in the exhaust duct, however, significantly affects the system performance [51]. Since mass and pressure drop are proportional to the HX size, lower heat exchanger effectiveness should be prioritized [47]. Nonetheless, lower effectiveness also reduces the thermodynamic benefit of recuperation. In addition, the conventional recuperation configuration (CR) is subject to highly unsteady flow conditions at the recuperator inlet, which can degrade performance [50]. To overcome this limitation, the Alternative Recuperation (AR) configuration [50] involves placing the recuperator between the high-pressure and low-pressure turbines of the aero engine. This arrangement increases the average temperature difference between the hot and cold streams, thereby lowering the required HX effectiveness at comparable heat duties and potentially improving cycle performance at high OPR. However, there are some limitations to this approach: (i) the AR configuration only outperforms CR at high pressure ratios, (ii) the limited inter-turbine space restricts the feasibility of this approach in aero engines, and (iii) the effect of the HX pressure loss on the system is

much larger as it determines the degree of expansion in the power turbine. The Staged Heat Recovery (SHR) configuration is an attempt to integrate the benefits of both AR and CR configurations by incorporating two recuperators: a primary HX placed between the turbines and a secondary one downstream of the LPT [50]. The staged heat recovery configuration may allow for marginally higher performance than the CR configuration under specific combinations of heat exchanger effectiveness and pressure loss, provided that the heat exchangers are designed to meet strict geometric and aerodynamic constraints [46]. In summary, the efficiency and feasibility of intercooled recuperated aero engines depend on (i) the thermohydraulic performance and weight of the heat exchangers, and (ii) their integration and positioning within the engine architecture.

While intercooled recuperated engines improve thermal efficiency by recovering thermal energy within the same thermodynamic cycle, combined cycle engine concepts couple the main gas turbine cycle with a secondary cycle to enhance thermal efficiency and specific thrust. The Water-Enhanced Turbofan (WET) is a CC engine configuration proposed by an industrial consortium led by MTU Aero Engines within the framework of the Clean Aviation joint undertaking [52]. The WET engine is conceived to enhance thermal efficiency and reduce emissions by partially recovering thermal energy from the exhaust stream and reintroducing it into the cycle in the form of superheated steam. In contrast to conventional recuperative cycles, the proposed configuration implements the Cheng thermodynamic cycle [53], i.e., a parallel integration of a Joule-Brayton gas turbine and a Clausius-Rankine steam cycle, which introduces a dedicated quasi-closed water circuit onboard the engine [54] to harvest thermal energy downstream of the low-pressure turbine (LPT). Water vapor present in the combustion products is first condensed and collected in a separator, then pressurized in the liquid state by a pump. The pressurized water is subsequently evaporated using heat extracted from the core exhaust flow. The superheated steam is first expanded in a dedicated steam turbine, providing power to the low-pressure spool driving the fan, and then injected into the airstream exiting the high-pressure compressor (HPC). Steam injection enables (i) a reduction of peak flame temperature leading to a decrease of NO_x emissions, and (ii) an increase in the specific heat capacity of the combustion gases, thereby enhancing specific work, increasing overall cycle efficiency, and reducing fuel consumption. The homogenization of the temperature distribution across the flame reduces NO_x emissions by up to 90% if compared to current turbofan engines [55]. The combination of lower combustion temperature and higher heat capacity enables the turbine to extract more specific work from the core flow, allowing for a much more compact engine design and reduced core turbomachinery weight [56]. The WET concept is conceived to be compatible with a range of fuel types, including SAF and hydrogen. The use of hydrogen offers several advantages. First, for a given energy content, its combustion yields approximately 2.8 times more water than kerosene, thereby enhancing the water recovery potential of the system. Second, its cryogenic storage temperature enables its use as a low-temperature heat sink in the condenser, reducing both the size and weight of this component. However, the integration and optimal design of heat exchangers are the main problems affecting the development of the WET engine. Two key components in the system are the vaporizer, which is located downstream of the LPT, and the condenser, which is integrated within the bypass duct of the TF engine. The condenser, in particular, plays a pivotal role as

it must ensure sufficient condensation to sustain the water loop while minimizing the drag penalty associated with ram air cooling [56]. An additional benefit of condensing water vapor from the exhaust stream is the reduction of water vapor content in the engine wake and, consequently, the likelihood of persistent contrail formation. Reductions in contrail formation of up to 50% have been estimated [55], resulting in a substantial mitigation of non-CO_2 climate impact. If both CO_2 and non-CO_2 effects are considered, the total environmental impact of the WET engine is projected to be approximately 40% lower than that of a reference geared turbofan engine. However, recent developments in the WET engine project showed that weight and size were unfavorable compared to the benefits the technology could theoretically offer [57]. Therefore, MTU aero engines redirected research efforts toward the Sustainable Water-Injecting Turbofan Comprising Hybrid-Electrics (SWITCH) project, partnering up with Pratt & Whitney and the sister company Collins Aerospace [58]. This project builds upon the foundational principles of the WET concept, aiming to retain its core environmental benefits while enhancing propulsion system efficiency through the integration of a hybrid-electric geared turbofan system. In addition to improving overall cycle performance, the SWITCH system is being designed for full compatibility with sustainable aviation fuels (SAF) and is under evaluation for future application with hydrogen propulsion systems [58].

Another notable combined-cycle engine concept is the Hydrogen Steam Injected Intercooled Turbine Engine (HySIITE), led by Pratt & Whitney and supported by ARPA-E for the research on novel HX designs [59]. The HySIITE concept combines steam injection with intercooling to improve thermodynamic efficiency and reduce pollutant emissions. The reverse-mounted engine core burns hydrogen to generate power and water vapor [60]. The hot air and steam exhaust pass through a condenser, which uses ram air and liquid hydrogen as a heat sink. This heat exchanger cools down the exhaust gases, allowing water to be extracted via a separator while simultaneously vaporizing liquid hydrogen before injection into the combustor [61]. A portion of the collected water mass flow is diverted to the evaporator, which harvests thermal energy from the engine core exhaust. The resulting steam is injected into the combustor. The remaining mass flow of liquid water is injected into the compressor for evaporative intercooling. Steam injection increases specific work output, thermal efficiency, and suppresses NO_x formation, while intercooling between compressor stages reduces the compression work and mitigates thermal gradients, offering additional performance gains and benefits for component durability [60]. Despite its potential, the realization of the HySIITE engine poses several engineering challenges. The high-temperature heat exchangers required for hydrogen preconditioning and steam generation are a critical aspect of system integration. These components must comply with severe space and weight constraints and must also endure large thermal transients and temperature gradients [60].

1.2.4. COMBINED CYCLE CONFIGURATIONS WITH ORC WASTE HEAT RECOVERY SYSTEM

The organic Rankine cycle (ORC) concept has been successfully implemented in waste heat recovery (WHR) systems, including stationary power plants and truck powertrains [62]. Its potential for future aero engines has been recently considered [63], [64]. A key advantage of the ORC concept is its flexibility, primarily due to the wide selection of

working fluids (WF). This flexibility allows for designing the optimal cycle and components depending on the heat source and sink temperatures and the power capacity by selecting a suitable working fluid [62]. As a result, ORC systems are well suited for the conversion of medium-grade thermal energy sources such as the exhaust gases of gas turbines, where temperatures typically reach ≈ 550° C [3]. Conversely, a standard steam Rankine cycle would not be feasible for such applications due to the complexity and size of the components for such applications. Figure 1.5 shows the process flow diagram of a non-recuperated subcritical ORC system and the corresponding thermodynamic cycle in the temperature-specific entropy diagram of an exemplary working fluid, namely R1233zd(e).[5] ORC systems producing net power ranging from tens to hundreds of kW employ working fluids made of molecules with high molecular mass and complexity. The low sound speed of such fluids, combined with the need for a high expansion ratio, implies that the turbine, usually a single-stage radial turbine, is highly supersonic [65]. In addition, the working fluid in the stator is in non-ideal thermodynamic states; therefore, property variations cannot be modeled with the ideal gas law, and complex equations of state models must be employed. The branch of fluid mechanics that treats these flows is called non-ideal compressible fluid dynamics (NICFD) [66]. NICFD effects must be correctly accounted for in the design of the expander [65].

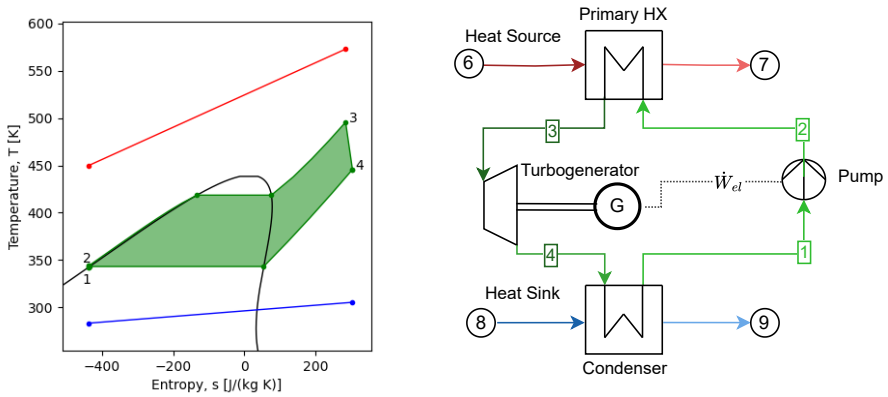

Figure 1.5: T-s diagram (left) and process flow diagram (right) of an exemplary non-recuperated ORC system. The working fluid is R1233zd(e), the heat source is a 1.5 kg/s stream of hot air, and the cold sink is 1 kg/s of a 50/50 water-glycol mix. The cycle generates 21 kW of net power, assuming turbine and pump isentropic efficiencies of 0.8 and 0.7, respectively. The pump requires $\dot{W}_{\mathrm{el}} = 1.5$ kW of power, which is ≈ 7% of the turbine gross power. The T-s diagram was generated using the tool documented in [67].

While the concept of ORC-based WHR systems for aero engines is promising [63], [64], the actual fuel-saving capabilities are still highly uncertain. As is the case for the other engine cycle configurations, the demanding constraints on mass, volume, and efficiency are the main technical challenges. An initial study by Zarati et al. [68] examined a non-recuperated, air-cooled ORC system powered by a 2 MW-class turboprop engine. Both the evaporator and condenser were modeled as plate-fin heat exchangers

[5] R1233zd(e) is a hydrofluoroolefin refrigerant.

with offset-strip fins. Heat exchanger sizing and zero-dimensional ram-air duct modeling for the cooling system were performed, and the main result is that it is estimated that a 1.7% reduction in fuel consumption is achievable over a 550 km mission compared to the benchmark engine. According to this simplified analysis, the mass of the ORC turbogenerator and of the condenser are the largest among those of the components of the ORC system, resulting in a mass-specific power of approximately 0.33 kW/kg [68], which would be too low for further consideration. The results also indicate that the thermal energy discharged by the condenser into the ram air may be exploited to offset the aerodynamic drag penalty; however, the detailed design of the cooling system was not performed. Two independent and contemporary simulation studies [69], [70] recently examined recuperated supercritical CO_2 cycle systems integrated into high-bypass turbofans to recover thermal energy from the exhaust. These studies reported rather different estimates of the fuel-saving potential due to differences in the assumed exhaust gas temperatures and in the calculated heat exchanger masses. Moreover, De Servi et al. [69] estimated a significant performance degradation of the CC engine as a function of pressure losses in the heat exchangers. Conversely to the results reported in Ref. [68], the authors in Ref. [69] estimate a negative impact of the cooler in the bypass duct on system performance; however, drag recovery via thermal energy discharge into ram air was not considered. This underscores the necessity for high-fidelity modeling and design optimization of the primary components, particularly the heat exchangers, to correctly assess the potential of combined cycle solutions.

In 2020, the Propulsion & Power group of TU Delft, with the advice and support of Airbus, Safran, MTU, NASA, and tier-n suppliers, engaged in a research project on airborne combined cycle gas turbine engines, namely the ARENA project.[6] The project aimed at studying the fuel-saving potential of novel combined cycle aero engine concepts featuring thermal energy harvesting via high-temperature ORC systems. The main objective is pursued by developing and verifying the necessary methods and modeling tools for system and component-level design optimization. Research efforts focused on (i) the modeling and performance assessment of the combined cycle engine and the integration of the propulsion system within the aircraft [71], (ii) the design optimization and optimal integration of compact heat exchangers (i.e., the evaporator and condenser) within the engine, and (iii) the development and validation of high-temperature radial inflow turbine (hiTORC-RIT) models and design methods [65].

Part of the research carried out within the ARENA project considered different propulsion system solutions to reduce the fuel consumption of the ONERA Dragon aircraft concept [72]. More in detail, two propulsion system configurations featuring a supercritical non-recuperated ORC bottoming unit were simulated and the results analyzed. In both case studies, the ORC system uses cyclopentane as the working fluid. The first configuration is documented in Ref. [73] and investigates a combined cycle turboshaft engine (CC-TS) providing electrical power to an under-the-wing distributed propulsion (DP) system. The process flow diagram of this engine configuration is reported in Fig. 3.6. The ORC unit features two condensers positioned inside planar ram air ducts at an angle of 70° to reduce the frontal area of the engine nacelle. The primary HX is placed within the exhaust stream of the free power turbine (FPT), which is mechanically cou-

[6] AiRborne thermal ENergy harvesting for Aircraft. https://kcorc.org/arena/.

pled to two generators. The thermal efficiency of the optimized ORC unit at cruise is 17.2%. It generates a net electric power output of 335 kW and weighs approximately 260 kg, of which the heat exchangers account for nearly half of the weight. The twin CC-TS engine configuration results in an estimated 1.5% reduction in total mission fuel consumption relative to the baseline configuration. The fuel-saving potential of this propulsion system configuration is primarily limited by the integration and performance of the heat exchangers, which negatively affect the gas turbine efficiency and the propulsive efficiency. The results of the optimization study also showed that condensers with low effectiveness ($\approx 50\%$) and high condensation temperature (125° C) allow for the exploitation of the Meredith effect, i.e., the phenomenon whereby the drag caused by a cooling system can be offset by the thrust that can be produced by the heated air expansion after passing through the HX. This thrust is directly influenced by the ram air total temperature increase across the HX and the total pressure of the air before entering the HX core [74]. Therefore, in a subsequent study reported in Ref. [71], an alternative CC engine configuration is proposed for improved propulsive efficiency: the combined-cycle turbofan (CC-TF). The process flow diagram of this configuration is reported in Fig. 3.8. In this configuration, the engine, besides providing power to the DP system, also drives a fan, thus providing thrust. An additional degree of freedom is therefore introduced in the design optimization framework to determine the optimal thrust distribution between the DP and the CC-TF. In contrast to the CC-TS configuration, the low-pressure turbine in the CC-TF is directly coupled to the electric generators. The heat duty of the ORC unit condenser is split between eight smaller, equally sized, inclined condensers arranged according to an octagonal pattern to fit inside the bypass duct of the engine. The condensers are exposed to a pressurized airflow, which increases the potential of the Meredith effect. The optimized CC-TF engine features a 546 kg ORC unit characterized by a thermal efficiency of 17.7%, providing 571 kW of electric power during cruise. This configuration yields an estimated total mission fuel mass reduction of approximately 4% relative to the baseline propulsion system of the aircraft, primarily due to a 13% increase in the engine bypass propulsive efficiency and 30% increase in specific thrust.

In summary, the performance of both combined-cycle engine configurations is strongly dependent on the integration and design of the heat exchangers into the engine and of the engine into the aircraft. The function of the primary HX, or evaporator, is to transfer thermal energy from the exhaust gases to the working fluid while minimizing pressure losses to avoid degrading the performance of the gas turbine. Although reducing gas-side velocity can theoretically reduce frictional losses, it increases the back pressure of the turbine, resulting in a net performance penalty equivalent to a larger pressure drop across the heat exchanger. Consequently, the evaporator must be designed to limit pressure losses at high velocities and maintain its structural integrity and fouling resistance. Typical design choices for exhaust-mounted evaporators include (i) prioritizing primary surface geometries over extended surfaces to ensure robustness and fouling resistance, (ii) minimizing the free-flow to frontal area ratio to reduce local flow acceleration, and (iii) leveraging unconventional shapes and placements to optimize space utilization [75]. The condenser is housed within a ram air duct that relies on either the motion of the aircraft or a dedicated fan for the supply of cooling air from the environment. Due to volume limitations, compact extended-surface heat exchangers are typically selected in

current feasibility studies [35], [74], [76]. The ram air duct architecture directly affects system-level performance by influencing the overall propulsive efficiency of the engine [74]. Its design must minimize total pressure loss and added mass while maximizing heat rejection. Furthermore, increasing the ram air temperature rise across the condenser can improve drag recovery via the Meredith effect, but reduces ORC system efficiency and increases the system mass.

1.3. HEAT EXCHANGERS FOR AIRBORNE SYSTEMS

A heat exchanger (HX) is a device that enables the transfer of thermal energy between fluids, between a solid surface and a fluid, or between solid particulates and a fluid, at different temperatures and in thermal contact without external work or heat interactions [77]. Heat exchangers are key components in modern aircraft systems: they are employed for thermal control of propulsion system components, avionics, as well as for the cooling of the cabin and cockpit environments. The increasing interest in advanced thermal management systems and waste heat recovery is driven by the ongoing development of novel propulsion architectures and the progressive electrification of aircraft. These trends have intensified the need for compact, lightweight, high-performance heat exchangers. The open literature documents two principal research directions in the field of compact HX design for aerospace applications: (i) the optimization of conventional core geometries using preliminary design methods and parameterized geometry layouts, and (ii) the application of high-fidelity numerical methods for the shape optimization of unconventional HX cores. Heat exchanger topologies commonly employed in airborne systems include flat-tube cores with louvered fins [78], bare micro-tube bundle cores [75], finned elliptical tube bundles [50], and plate-fin HXs with offset-strip fins [68]. The preliminary design of these components within a system design framework often relies on the ϵ-NTU method [77] due to its simplicity and computational speed. When coupled with appropriate thermohydraulic correlations, this methodology supports parametric optimization of HX geometry and performance [79], [80], provided that the validity of the employed correlations is preserved across the explored design space.

Advancements in computational resources, including GPU-based parallelization [81], have facilitated the application of computational fluid dynamics (CFD)-based design optimization methods to compact HX core geometries. These methodologies aim to enhance thermohydraulic performance by modifying either the shape or the topology of the HX core [82]. In shape optimization, the geometry is altered within predefined boundaries using parametrization techniques, without changing the topological configuration of the core. Conversely, topology optimization is a method that directly modifies the distribution of the material at the interface between two fluid sides, optimizing its shape and layout within a defined domain [83]. Shape and topology optimization methodologies enable the design of unconventional geometries that can lead to designs outperforming conventional designs in specific applications [84]. For instance, Pai Raikar et al. [85] performed the shape optimization of a tubular HX core using an adjoint-based method combined with Reynolds-Averaged Navier–Stokes (RANS) CFD simulations. Results indicate a 25% reduction in pressure drop without affecting the heat transfer rate. The authors of Ref. [86] employed a genetic algorithm to perform topology optimization of rectangular fin structures, maximizing a fitness function based on both

heat transfer and pressure loss. The performance associated with the resulting geometries is up to 89% better in terms of heat transfer-to-pressure drop ratio compared to the baseline. However, the application of topology optimization to aerospace-grade heat exchangers remains limited due to several challenges. These include the complexity of manufacturing the resulting geometries, difficulties related to leakage and powder removal, and the strict requirements for fouling resistance and maintainability of airborne components [87]. Recent advancements in Additive Manufacturing (AM) techniques [7] are progressively addressing these challenges by enabling the fabrication of complex geometries generated by topology and shape optimization procedures. Furthermore, ongoing studies on AM-induced surface roughness suggest that an optimal surface finish may exist, offering a favorable trade-off between frictional losses and heat transfer performance [88].

1.4. MOTIVATION

The propulsion system architectures discussed in Section 1.2 might lead to performance improvements compared to the state of the art, provided several technical challenges are overcome and at the cost of additional complexity. Challenges are related to excessive mass and volume, aerodynamic drag, reliable off-design operation, compliance with geometric constraints, manufacturing, and maintainability. Compact heat exchangers are key components of these systems, as their design directly impacts thermodynamic performance, weight, volume, and aircraft drag, thereby affecting the overall feasibility of innovative propulsion systems [42], [74], [89]. For this reason, their optimal design and integration within the propulsion system can arguably only be achieved through an integrated design optimization approach, in which the design of the system and its main components is carried out simultaneously. The selection of HX topology, geometry, flow configuration, and layout for airborne applications must account for stringent constraints related to available space and mass. These aspects, however, are often overlooked: HX type and layout are typically selected based on engineering judgment and prior experience, while the system is designed according to a sequential approach. In this sequential approach, the system configuration and thermodynamic cycle are performed first, while the detailed component design is subsequently addressed without proper coupling between the two [90]. The result of this approach is the attainment of a sub-optimal design [78].

For instance, in [91], the authors conduct an exploratory study on the integration of a bottoming supercritical CO_2 waste heat recovery (WHR) unit to reduce aero engine fuel consumption. The study first addresses the optimization of the WHR unit thermodynamic cycle targeting maximum net power output, and subsequently details the design of the primary heat exchanger positioned in the core flow of a modern turbofan and the cooler positioned in the bypass duct. The topology and geometries of the HXs were selected a priori based on a literature survey and were not optimized. Similarly, the authors in [92] document the optimization of the thermal management system configuration of a hybrid-electric hydrogen-powered aircraft. Results indicate that the heat transfer area

[7] Among the most common AM technologies for aerospace applications Direct Energy Deposition (DED), Powder Bed Fusion (PBF), Binder Jetting (BJT) and Sheet Lamination (SL) methods [83] stand out.

of the heat exchanger that rejects thermal energy to the ambient air has the largest influence on the drag of the system. However, the study employs simplified pinch-point analysis-based heat exchanger models with constant heat transfer coefficients and does not address HX weight or size. Conversely, the research work documented in [93] details the multi-objective optimization of an offset-strip-fin heat exchanger that recovers waste heat released by the batteries and power electronics of an electric vehicle and transfers it to the heat pump, thereby enhancing the system efficiency. The optimization process targets geometries that minimize pressure loss and maximize the heat transfer rate that satisfy imposed size constraints. The methodology does not include the model of the waste heat recovery system and solely focuses on the heat exchanger performance at given operating conditions. More recently, an integrated system design optimization method has been developed in which the thermodynamic cycle, component sizing, and working fluid are taken into account simultaneously [94]. The methodology has been applied to perform a multi-objective optimization of an electrically-driven vapor compression cycle (VCC) for the environmental control system (ECS) of a rotorcraft [94] for maximum system efficiency and minimum weight. The integrated system design framework has also been used to perform the multipoint and multi-objective design optimization of a bleed-less air cycle machine (ACM) and an electrically driven VCC system for a single-aisle, short-haul aircraft [78].

Improvements in the computational speed of CFD simulations, particularly driven by GPU parallelization [95], have enabled the application of CFD-based optimization methods to enhance the performance of compact heat exchangers by exploiting unconventional core geometries. Nonetheless, despite their potential, detailed CFD simulations of compact HX cores remain computationally expensive [96], rendering such methods impractical for iterative use in integrated system-level optimization frameworks or during early-stage design exploration studies. In this context, the selection of HX topology, flow configuration, and core geometry plays a pivotal role in determining the trade-off between component mass and thermohydraulic performance, which is subject to the operating conditions and spatial constraints. There is consequently a clear need for accurate and computationally efficient preliminary design tools and compact HX design selection guidelines to support early-stage design decisions.

Moreover, the aforementioned research studies on novel aircraft propulsion systems underscore the potential of utilizing ram air as a heat sink (See Refs. [32], [34], [35], [56], [74], [97]). This highlights the necessity of accurately designing the cooling system. One of the benefits of using ram air lies in the possibility of converting part of the thermal energy absorbed by the airflow into kinetic energy, thereby mitigating or even offsetting the drag penalty of the cooling system [74]. This phenomenon, historically exploited in aircraft oil cooling radiator and duct design [98], is referred to as the Meredith effect and should not be overlooked, as it may offer valuable synergies between the thermal management system or waste heat recovery unit design and the aircraft propulsive efficiency. Despite its relevance, simplified models based solely on momentum and energy balance are often employed to model ducted heat exchangers within system-level studies [68], [74], [97]. These models typically neglect the effect of the HX installation on the flow within the duct, which may lead to sub-optimal designs and overly optimistic performance estimates. To address this limitation, CFD simulations can be used to predict

the flow inside ram air ducts housing compact HXs. However, the detailed simulation of the flow through a compact HX core is still considered computationally expensive [76]. To reduce the computational cost associated with the simulation of the HX, various strategies have been proposed, including the removal of extended surfaces from the core geometry [89], the use of an external 0-D model employing empirical correlations [76], or the use of a porous media model (PMM), to simulate the presence of the HX within the CFD simulation framework [96], [99]–[101]. The use of PMM for compact heat exchangers in airborne applications has been successfully applied in research studies documented in the literature [102], [103] and is considered an established methodology capable of capturing the bulk flow behavior through ducted HXs with significantly reduced computational resources [101]. However, limited research is currently available regarding the accuracy of lumped parameter models for ram air ducts design and their consistency with CFD-based simulation frameworks employing PMMs [76]. Further investigation is needed to assess the predictive capabilities of these simplified models and their suitability for conceptual and preliminary design studies.

In light of the evaluated literature, the motivations driving this research can be summarized as follows:

- *the lack of guidelines or methodologies for the preliminary design of aerospace-grade compact heat exchangers,* especially in relation to the demanding requirements of novel concepts for propulsion systems. Conventional performance evaluation criteria and standard design practices may lead to sub-optimal system configurations and, as a result, misleading system performance assessment [104], [105];

- *The need for accurate, modular, and robust models for the parametric design optimization of heat exchangers for complex airborne thermal systems.* In addition, a method for the integration of the optimal heat exchanger performance assessment into the system preliminary design *requires the derivation of surrogate models trained on detailed models.*

- Given that the performance of heat exchangers rejecting thermal energy is critical, given the strong penalty due to drag increase, *The necessity of assessing the accuracy of state-of-the-art ram air duct modeling capabilities,* and, based on the results, *the demand for design guidelines for ram air duct cooling systems.*

1.5. ORIGINAL CONTRIBUTIONS

The contributions documented in this dissertation can be outlined as follows:

- A methodology for the preliminary design optimization of single and multi-pass HXs with different flow arrangements and topologies has been developed, implemented, and validated against experimental data available in the scientific literature. The method can be used to perform the sizing and rating of recuperators, condensers, or evaporators operating with any working fluid in sub-critical and supercritical thermodynamic states. The method has been implemented in a computer program named *HeXacode*, which was employed within the integrated

system-and-component design optimization framework for aero engines incorporating an ORC bottoming unit, i.e., the *ARENA* framework [71]. Optimal geometric design trends for compact HX topologies have been identified using a sensitivity study and a multi-objective optimization routine, which can also be used to compare the sets of Pareto optimal solutions of different HX topologies for a chosen application. *HeXacode* is, therefore, an in-house software suite coded in Python for the preliminary design, optimization, and rating of compact (and especially aerospace-grade) heat exchangers and cooling ducts.

- A data-driven surrogate modeling approach has been developed to predict the performance of optimized compact heat exchangers as a function of varying thermodynamic conditions. This method enables system-level preliminary design studies without the need to explicitly perform detailed component design or geometry optimization within the system optimization framework. The dataset used to train the model has been generated using the HX sizing tool implemented in *HeXacode* coupled with an evolutionary multi-objective optimization algorithm. The computational time associated with the integrated system and HX design is reduced to less than half of the original value.

- The developed HX sizing and rating models of *HeXacode* have been integrated into a ram air duct model coded in Python for on and off-design system calculations. In parallel, a higher-fidelity model based on two-dimensional Reynolds-Averaged Navier–Stokes (RANS) simulations has been developed, whereby the heat exchanger is modeled as an anisotropic porous medium. This CFD simulation framework allows to obtain a significant reduction in the computational cost associated with detailed flow simulations of ducted heat exchangers while preserving relevant flow features, making it suitable for duct shape optimization and parametric studies. The calibration of the porous media heat transfer and pressure drop characteristics is carried out using tools available within *HeXacode*. The predictive capabilities of the ram air duct lumped parameter model show good agreement with the CFD model, supporting its suitability for preliminary design studies.

1.6. OUTLINE

This dissertation is structured in six chapters and contains research work published in international conference proceedings and peer-reviewed journals. The content of the five chapters following this introduction is summarized as follows.

Chapter 2 presents a classification of compact heat exchangers and introduces the main criteria used for performance evaluation in conventional design practice. The limitations of standard HX selection procedures for airborne thermal systems are discussed, along with the specific challenges associated with the integration of compact heat exchangers within the airframe or engine.

Chapter 3 details a novel methodology for the design and rating of compact HXs, implemented into the in-house *HeXacode* software, developed as part of this research. The

chapter also documents the results of integrating this method within an integrated design optimization framework for combined cycle engine configurations[71]. Moreover, a geometry optimization method is applied to prescribed compact HX topologies to identify optimal design trends and evaluate trade-offs between mass and pressure losses under prescribed spatial constraints.

Chapter 4 describes a data-driven surrogate modeling method developed to reduce computational cost and improve convergence robustness of the numerical solver in the integrated design optimization of complex systems, such as gas turbines coupled with a bottoming ORC unit. The method involves replacing the HX model implemented in *HeXacode* in the integrated design framework with a surrogate model capable of predicting the performance of optimized heat exchanger configurations under prescribed operating conditions. The effectiveness of the proposed methodology is demonstrated through the multi-objective optimization of the ORC waste heat recovery unit in two case studies, both with and without the use of the surrogate model.

Chapter 5 documents the development of a lumped parameter model to address the design and the off-design performance estimation of ram air cooling ducts housing heat exchangers. The model is verified against a higher fidelity simulation framework, which leverages RANS simulations to solve the flow field inside the ram air duct and a porous zone to simulate the presence of the HX inside the duct. The lumped parameter model is used to derive new design guidelines for ram air cooling ducts, with emphasis on the impact of space constraints, thermal energy discharge, and pressure losses on the net drag of the duct.

Chapter 6 includes a summary of the main conclusions of this research, the limitations of the proposed methodology, and recommendations for future research in the field of compact heat exchangers for aircraft propulsion systems.

BIBLIOGRAPHY

[1] T. Park, H. Hashimoto, W. Wang, *et al.*, "What does global land climate look like at 2°c warming?", *Earth's Future*, vol. 11, no. 5, 2023. DOI: https://doi.org/10.1029/2022EF003330.

[2] W. J. Ripple, C. Wolf, T. M. Newsome, *et al.*, "World scientists' warning to humanity: A second notice", *BioScience*, vol. 67, no. 12, pp. 1026–1028, Nov. 2017, ISSN: 0006-3568. DOI: 10.1093/biosci/bix125.

[3] M. Astolfi, M. Baresi, J. van Buijtenen, *et al.*, "Thermal Energy Harvesting - The Path to Tapping into a Large CO2-free European Power Source", Knowledge Center on Organic Rankine Cycle technology – KCORC, Tech. Rep., 2022.

[4] "Reducing emissions from aviation", European Commission: Climate action, Tech. Rep. [Online]. Available: https://climate.ec.europa.eu/eu-action/transport/reducing-emissions-aviation_en.

[5] L. Rupcic, E. Pierrat, K. Saavedra-Rubio, N. Thonemann, C. Ogugua, and A. Laurent, "Environmental impacts in the civil aviation sector: Current state and guidance", *Transportation Research Part D: Transport and Environment*, vol. 119, p. 103 717, 2023, ISSN: 1361-9209. DOI: https://doi.org/10.1016/j.trd.2023.103717.

[6] L. Megill, K. Deck, and V. Grewe, "Alternative climate metrics to the global warming potential are more suitable for assessing aviation non-co_2 effects", *Commun Earth Environ*, vol. 5, no. 249, 2024. DOI: 10.1038/s43247-024-01423-6.

[7] M. Klower, M. R. Allen, D. S. Lee, S. R. Proud, L. Gallagher, and A. Skowron, "Quantifying aviation's contribution to global warming", *Environmental Research Letters*, vol. 16, no. 10, Nov. 2021. DOI: 10.1088/1748-9326/ac286e.

[8] T. Planes, S. Delbecq, V. Pommier-Budinger, and E. Benard, "Simulation and evaluation of sustainable climate trajectories for aviation", *Journal of Environmental Management*, vol. 295, 2021, ISSN: 0301-4797. DOI: https://doi.org/10.1016/j.jenvman.2021.113079.

[9] S. Gössling and A. Humpe, "The global scale, distribution and growth of aviation: Implications for climate change", *Global Environmental Change*, vol. 65, p. 102 194, 2020, ISSN: 0959-3780. DOI: https://doi.org/10.1016/j.gloenvcha.2020.102194.

[10] R. Medina, "Eurocontrol aviation long term outlook: Flights and co2 emissions forecast 2024-2050", Eurocontrol, Tech. Rep., 2024.

[11] Eurocontrol. "Eurocontrol forecast 2025-2031". (2025), [Online]. Available: https://www.eurocontrol.int/publication/eurocontrol-forecast-2025-2031.

[12] R. S. Gregg Flemingm Ivan de Lepinay, "Environmental trends in aviation to 2050", ICAO, Tech. Rep., 2024.

[13] A. Bensel, "Characteristics of the specific fuel consumption for jet engines", *Aircraft Design and Systems Group (AERO)*, 2018. DOI: https://doi.org/10.15488/4316.

[14] B. L. Koff, "Gas turbine technology evolution: A designers perspective", *Journal of Propulsion and Power*, vol. 20, no. 4, pp. 577–595, 2004. DOI: 10.2514/1.4361. [Online]. Available: ttps://doi.org/10.2514/1.4361.

[15] S. Gossling and C. Lyle, "Transition policies for climatically sustainable aviation", *Transport Reviews*, vol. 41, no. 5, pp. 643–658, 2021. DOI: 10.1080/01441647.2021.1938284.

[16] X. Zheng and D. Rutherford, "Fuel burn of new commercial jet aircraft: 1960 to 2019", The international council on clean transportation (ICCT), Tech. Rep., 2020.

[17] ICAO. "Icao aircraft engine emissions databank". (2024), [Online]. Available: https://www.easa.europa.eu/en/domains/environment/icao-aircraft-engine-emissions-databank.

[18] A. Celikel and F. Jelinek, "Fuel burn of new commercial jet aircraft: 1960 to 2014", FORECASTING CIVIL AVIATION FUEL BURN and EMISSIONS IN EUROPE, Tech. Rep., 2001.

[19] Flightpath2050. "Flightpath 2050 – europe's vision for aviation – maintaining global leadership and serving society's needs", European Commission. (2011), [Online]. Available: https://op.europa.eu/en/publication-detail/-/publication/296a9bd7-fef9-4ae8-82c4-a21ff48be673.

[20] "Sustainable flight national partnership", NASA. (2022), [Online]. Available: https://op.europa.eu/en/publication-detail/-/publication/296a9bd7-fef9-4ae8-82c4-a21ff48be673.

[21] "Long term global aspirational goal (ltag) for international aviation", ICAO. (2022), [Online]. Available: https://www.icao.int/environmental-protection/Pages/LTAG.aspx.

[22] "Gtf advantage engine", Pratt & Whitney. (2025), [Online]. Available: https://www.prattwhitney.com/en/products/commercial-engines/gtf/advantage.

[23] "GTF Advantage: The most efficient engine for the A320neo family", Pratt & Whitney. (2025), [Online]. Available: https://www.prattwhitney.com/en/landing-pages-pw/gtf-advantage---the-most-efficient-engine-for-the-a320neo.

[24] "Making a more durable GTF engine", RTX. (2025), [Online]. Available: https://www.rtx.com/news/2025/06/06/making-a-more-durable-gtf-engineo.

[25] "Ultrafan project", Rolls Royce. (2021), [Online]. Available: https://www.rolls-royce.com/innovation/ultrafan.aspx.

[26] "Revolutionary Innovation for Sustainable Engineering program whitepaper", CFM International, Tech. Rep., 2021. [Online]. Available: https://www.cfmaeroengines.com/wp-content/uploads/2021/07/CFM_RISE_Whitepaper_Media.pdf.

[27] B. A. Adu-Gyamfi and C. Good, "Electric aviation: A review of concepts and enabling technologies", *Transportation Engineering*, vol. 9, p. 100 134, 2022, ISSN: 2666-691X. DOI: https://doi.org/10.1016/j.treng.2022.100134.

[28] L. Meng-Sing, K. Hyoungjin, and L. May-Fun, "Challenges and progress in aerodynamic design of hybrid wingbody aircraft with embedded engines", NASA, Tech. Rep., 2016. [Online]. Available: https://ntrs.nasa.gov/citations/20160007898.

[29] S. Samuelsson and T. Grönstedt, "Performance analysis of turbo-electric propulsion system with fuselage boundary layer ingestion", *Aerospace Science and Technology*, vol. 109, p. 106 412, 2021, ISSN: 1270-9638. DOI: https://doi.org/10.1016/j.ast.2020.106412. [Online]. Available: https://www.sciencedirect.com/science/article/pii/S1270963820310944.

[30] R. E. Wolleswinkel, R. de Vries, M. Hoogreef, and R. Vos, "A new perspective on battery-electric aviation, part i: Reassessment of achievable range", in *AIAA SCITECH 2024 Forum*. 2024. DOI: 10.2514/6.2024-1489. [Online]. Available: https://arc.aiaa.org/doi/abs/10.2514/6.2024-1489.

[31] R. de Vries, R. E. Wolleswinkel, M. Hoogreef, and R. Vos, "A new perspective on battery-electric aviation, part ii: Conceptual design of a 90-seater", in *AIAA SCITECH 2024 Forum*. 2024. DOI: 10.2514/6.2024-1490. eprint: https://arc.aiaa.org/doi/pdf/10.2514/6.2024-1490. [Online]. Available: https://arc.aiaa.org/doi/abs/10.2514/6.2024-1490.

[32] M. Asli, P. König, D. Sharma, *et al.*, "Thermal management challenges in hybrid-electric propulsion aircraft", *Progress in Aerospace Sciences*, vol. 144, p. 100 967, 2024, ISSN: 0376-0421. DOI: https://doi.org/10.1016/j.paerosci.2023.100967. [Online]. Available: https://www.sciencedirect.com/science/article/pii/S0376042123000830.

[33] B. J. Brelje and J. R. Martins, "Electric, hybrid, and turboelectric fixed-wing aircraft: A review of concepts, models, and design approaches", *Progress in Aerospace Sciences*, vol. 104, pp. 1–19, 2019, ISSN: 0376-0421. DOI: https://doi.org/10.1016/j.paerosci.2018.06.004.

[34] V. G. Gkoutzamanis, S. E. Tsentis, O. S. Valsamis Mylonas, *et al.*, "Thermal management system considerations for a hybrid-electric commuter aircraft", *Journal of Thermophysics and Heat Transfer*, vol. 36, no. 3, pp. 650–666, 2022. DOI: 10.2514/1.T6433.

[35] M. Coutinho, D. Bento, A. Souza, *et al.*, "A review on the recent developments in thermal management systems for hybrid-electric aircraft", *Applied Thermal Engineering*, vol. 227, p. 120 427, 2023, ISSN: 1359-4311. DOI: https://doi.org/10.1016/j.applthermaleng.2023.120427.

[36] "Project phoenix", AeroDelft. (2025), [Online]. Available: https://aerodelft.nl/project-phoenix/.

[37] "Scaling hydrogen electric propulsion for large aircraft", ZeroAvia. (2025), [Online]. Available: https://zeroavia.com/download-scaling-h2-whitepaper/#download-h2scaling.

[38] M. Soleymani, V. Mostafavi, M. Hebert, S. Kelouwani, and L. Boulon, "Hydrogen propulsion systems for aircraft, a review on recent advances and ongoing challenges", *International Journal of Hydrogen Energy*, vol. 91, pp. 137–171, 2024, ISSN: 0360-3199. DOI: https://doi.org/10.1016/j.ijhydene.2024.10.131.

[39] S. Tiwari, M. J. Pekris, and J. J. Doherty, "A review of liquid hydrogen aircraft and propulsion technologies", *International Journal of Hydrogen Energy*, vol. 57, pp. 1174–1196, 2024, ISSN: 0360-3199. DOI: https://doi.org/10.1016/j.ijhydene.2023.12.263. [Online]. Available: https://www.sciencedirect.com/science/article/pii/S0360319923065631.

[40] R. Cai and L. Jiang, "Analysis of the recuperative gas turbine cycle with a recuperator located between turbines", *Applied Thermal Engineering*, vol. 26, no. 1, pp. 89–96, 2006, ISSN: 1359-4311. DOI: https://doi.org/10.1016/j.applthermaleng.2005.04.016.

[41] K. Yakinthos, D. Missirlis, A. Palikaras, P. Storm, B. Simon, and A. Goulas, "Optimization of the design of recuperative heat exchangers in the exhaust nozzle of an aero engine", *Applied Mathematical Modelling*, vol. 31, no. 11, pp. 2524–2541, 2007, ISSN: 0307-904X. DOI: https://doi.org/10.1016/j.apm.2006.10.008.

[42] C. Albanakis, K. Yakinthos, K. Kritikos, D. Missirlis, A. Goulas, and P. Storm, "The effect of heat transfer on the pressure drop through a heat exchanger for aero engine applications", *Applied Thermal Engineering*, vol. 29, no. 4, pp. 634–644, 2009, ISSN: 1359-4311. DOI: https://doi.org/10.1016/j.applthermaleng.2008.03.034.

[43] J. M. Lee, P. W. Kwan, C. M. Son, and M. Y. Ha, "Characterizations of aerothermal performance of novel cross-corrugated plate heat exchangers for advanced cycle aero-engines", *International Journal of Heat and Mass Transfer*, vol. 85, pp. 166–180, 2015, ISSN: 0017-9310. DOI: https://doi.org/10.1016/j.ijheatmasstransfer.2015.01.127.

[44] N. Tran and C.-C. Wang, "Effects of tube shapes on the performance of recuperative and regenerative heat exchangers", *Energy*, vol. 169, pp. 1–17, 2019, ISSN: 0360-5442. DOI: https://doi.org/10.1016/j.energy.2018.11.127.

[45] L. Xu and T. Grönstedt, "Design and analysis of an intercooled turbofan engine", *Journal of Engineering for Gas Turbines and Power*, vol. 132, no. 11, p. 114 503, Aug. 2010, ISSN: 0742-4795. DOI: 10.1115/1.4000857.

[46] A. Goulas, S. Donnerhack, M. Flouros, D. Misirlis, Z. Vlahostergios, and K. Yakinthos, "Thermodynamics cycle analysis, pressure loss, and heat transfer assessment of a recuperative system for aero-engines", *Journal of Engineering for Gas Turbines and Power*, vol. 137, no. 4, p. 041 205, Nov. 2014, ISSN: 0742-4795. DOI: 10.1115/1.4028584.

[47] G. Hao and W. Zhan-xue, "Effects of intercooling and recuperation on turbofan engine performance", in *Proceedings of 2011 International Conference on Electronic & Mechanical Engineering and Information Technology*, vol. 5, 2011, pp. 2482–2485. DOI: 10.1109/EMEIT.2011.6023545.

[48] K. G. Kyprianidis, T. Grönstedt, S. O. T. Ogaji, P. Pilidis, and R. Singh, "Assessment of future aero-engine designs with intercooled and intercooled recuperated cores", *Journal of Engineering for Gas Turbines and Power*, vol. 133, no. 1, p. 011 701, Sep. 2010, ISSN: 0742-4795. DOI: 10.1115/1.4001982.

[49] S. Boggia and K. Rüd, "Intercooled recuperated gas turbine engine concept", in *41st AIAA/ASME/SAE/ASEE Joint Propulsion Conference & Exhibit*. AIAA, 2005. DOI: 10.2514/6.2005-4192.

[50] C. Salpingidou, Z. Vlahostergios, D. Misirlis, *et al.*, "Thermodynamic analysis of recuperative gas turbines and aero engines", *Applied Thermal Engineering*, vol. 124, pp. 250–260, 2017, ISSN: 1359-4311. DOI: https://doi.org/10.1016/j.applthermaleng.2017.05.169. [Online]. Available: https://www.sciencedirect.com/science/article/pii/S1359431116342946.

[51] H. Schoenenborn, E. Ebert, B. Simon, and P. Storm, "Thermomechanical design of a heat exchanger for a recuperative aeroengine", *Journal of Engineering for Gas Turbines and Power*, vol. 128, no. 4, pp. 736–744, Sep. 2006, ISSN: 0742-4795. DOI: 10.1115/1.1850510.

[52] O. Schmitz, S. Kaiser, H. Klingels, *et al.*, "Aero engine concepts beyond 2030: Part 3—experimental demonstration of technological feasibility", *Journal of Engineering for Gas Turbines and Power*, vol. 143, no. 2, p. 021 003, Jan. 2021, ISSN: 0742-4795. DOI: 10.1115/1.4048994. [Online]. Available: https://doi.org/10.1115/1.4048994.

[53] D. Y. Cheng, "Advanced cheng combined cycle", US6644011B2, 2001.

[54] O. Schmitz, H. Klingels, and P. Kufner, "Aero engine concepts beyond 2030: Part 1—the steam injecting and recovering aero engine", *Journal of Engineering for Gas Turbines and Power*, vol. 143, no. 2, p. 021 001, Jan. 2021, ISSN: 0742-4795. DOI: 10.1115/1.4048985. [Online]. Available: https://doi.org/10.1115/1.4048985.

[55] S. Kaiser, O. Schmitz, P. Ziegler, and H. Klingels, "The water-enhanced turbofan as enabler for climate-neutral aviation", *Applied Sciences*, vol. 12, no. 23, 2022, doi: 10.3390/app122312431.

[56] *Water Enhanced Turbofan: Improved Thermodynamic Cycle Using Hydrogen as Fuel*, vol. Volume 1: Aircraft Engine, Turbo Expo, Jun. 2023, V001T01A006. DOI: 10.1115/GT2023-100807. [Online]. Available: https://doi.org/10.1115/GT2023-100807.

[57] "Mtu stops development of water enhanced turbofan – focus on other technologies", Aviation Direct. (2025), [Online]. Available: https://aviation.direct/en/mtu-stellt-entwicklung-des-water-enhanced-turbofan-ein-fokus-auf-andere-technologien.

[58] "Clean aviation switch project to advance hybrid-electric and water-enhanced turbofan technologies", MTU Press Release. (2025), [Online]. Available: https://www.mtu.de/newsroom/press/latest-press-releases/press-release-detail/clean-aviation-switch-project-to-advance-hybrid-electric-and-water-enhanced-turbofan-technologies/.

[59] "Hydrogen steam injected intercooled turbine engine", ARPA-E. (2021), [Online]. Available: https://arpa-e.energy.gov/programs-and-initiatives/search-all-projects/hydrogen-steam-and-inter-cooled-turbine-engine-hysite.

[60] "Poised for a future of hydrogen-powered planes", RTX. (2025), [Online]. Available: https://www.rtx.com/news/2025/03/15/paving-the-way-for-planes-powered-by-hydrogen.

[61] "Pratt outlines hydrogen steam-injection engine concept", AIN magazine. (Jan. 2025), [Online]. Available: https://www.ainonline.com/aviation-news/futureflight/2025-01-28/pratt-whitney-hydrogen-engine-projects-shows-promise-steam.

[62] P. Colonna, E. Casati, C. Trapp, *et al.*, "Organic rankine cycle power systems: From the concept to current technology, applications, and an outlook to the future", *Journal of Engineering for Gas Turbines and Power*, vol. 137, no. 10, p. 100 801, Oct. 2015, ISSN: 0742-4795. DOI: 10.1115/1.4029884.

[63] G. Pateropoulos, T. Efstathiadis, and A. Kalfas, "Organic Rankine cycle for turboprop engine application", *The Aeronautical Journal*, vol. 125, no. 1291, pp. 1666–1686, 2021. DOI: 10.1017/aer.2021.32.

[64] C. Zhang, G. Ling, L. Li, and X. Guo, "Fluid selection and parametric analysis of organic Rankine cycle applicable to the turboshaft engine with a recuperator", *Energy*, vol. 308, p. 132 816, 2024, ISSN: 0360-5442. DOI: https://doi.org/10.1016/j.energy.2024.132816.

[65] M. Majer and M. Pini, "Design guidelines for high-pressure ratio supersonic radial-inflow turbines of organic rankine cycle systems", *Journal of the Global Power and Propulsion Society*, vol. 9, pp. 19–46, 2025. DOI: 10.33737/jgpps/195437.

[66] A. Guardone, P. Colonna, M. Pini, and A. Spinelli, "Nonideal compressible fluid dynamics of dense vapors and supercritical fluids", *Annual Review of Fluid Mechanics*, vol. 56, no. Volume 56, 2024, pp. 241–269, 2024, ISSN: 1545-4479. DOI: https://doi.org/10.1146/annurev-fluid-120720-033342.

[67] M. T. White, "pocketORC: A browser-based calculator for teaching organic rankine cycle power systems", Seville, Spain: 7th International Seminar on ORC Power Systems, 2023. DOI: 10.12795/9788447227457_9.

[68] K. Zarati, S. Maalouf, and A. Isikveren, "Potential of the bottom organic Rankine cycle to recover energy on turboprop engine architecture", in *ISABE 2017*, 2017.

[69] C. De Servi, L. Azzini, M. Pini, G. Rao, and P. Colonna, "Exploratory assessment of a combined-cycle engine concept for aircraft propulsion", in *1st Global Power and Propulsion Forum*, 2017.

[70] F. Jacob, A. M. Rolt, J. M. Sebastiampillai, V. Sethi, M. Belmonte, and P. Cobas, "Performance of a supercritical co2 bottoming cycle for aero applications", *Applied Sciences*, vol. 7, no. 3, 2017, ISSN: 2076-3417. DOI: 10.3390/app7030255. [Online]. Available: https://www.mdpi.com/2076-3417/7/3/255.

[71] D. Krempus, C. M. D. Servi, R. Vos, and P. Colonna, "Organic rankine cycle waste heat recovery systems for aircraft engines", Ph.D. dissertation, Delft University of Technology, 2025.

[72] P. Schmollgruber, D. Donjat, M. Ridel, *et al.*, "Multidisciplinary design and performance of the ONERA hybrid electric distributed propulsion concept (Dragon)", in *AIAA SciTech Forum*, doi: 10.2514/6.2020-0501, 2020.

[73] D. Krempus, F. Beltrame, M. Majer, C. M. De Servi, and R. Vos, "Orc waste heat recovery system for the turboshaft engines of turboelectric aircraft: Correction", in *TU Delft Flight Performance and Propulsion*, vol. 10^{th} EUCASS, 2023. [Online]. Available: https://resolver.tudelft.nl/uuid:3eca4e81-1449-4cce-8e6c-cf8d2929d6ea.

[74] A. C. Frey, J. Stonham, D. Bosak, C. M. Sangan, and O. J. Pountney, "Radiators in fuel cell powered aircraft: The effect of heat rejection on drag", *Applied Thermal Engineering*, vol. 274, p. 126 697, 2025, ISSN: 1359-4311. DOI: https://doi.org/10.1016/j.applthermaleng.2025.126697.

[75] C.-P. Bury, L. Vesely, J. Kapat, M. Shi, and M. Stoia, "Design and integration of a microtube precooler into an aircraft engine waste heat recovery and fuel systems", in *ASME Turbo Expo*, vol. Volume 11: Supercritical CO2, 2024. DOI: 10.1115/GT2024-129421.

[76] E. J. Adler, A. H. R. Lamkin, and J. R. R. A. Martins, "Aircraft ducted heat exchanger aerodynamic shape and thermal optimization", *ASME Journal of Heat and Mass Transfer*, vol. 147, no. 1, p. 011 902, Sep. 2024, ISSN: 2832-8450. DOI: 10.1115/1.4066438. [Online]. Available: https://doi.org/10.1115/1.4066438.

[77] D. Shah R. Sekulic, *Fundamentals of heat exchanger design*. John Wiley and Sons, 2003.

[78] A. Giuffre', F. Ascione, P. Colonna, and C. De Servi, "Integrated design optimization of environmental control systems for next-generation aircraft", *Journal of Aircraft*, pp. 1–18, 2025. DOI: 10.2514/1.C038093.

[79] M. Yousefi, R. Enayatifar, A. N. Darus, and A. H. Abdullah, "Optimization of plate-fin heat exchangers by an improved harmony search algorithm", *Applied Thermal Engineering*, vol. 50, no. 1, pp. 877–885, 2013, ISSN: 1359-4311. DOI: https://doi.org/10.1016/j.applthermaleng.2012.05.038. [Online]. Available: https://www.sciencedirect.com/science/article/pii/S1359431112004164.

[80] T. A. Khan and W. Li, "Optimal design of plate-fin heat exchanger by combining multi-objective algorithms", *International Journal of Heat and Mass Transfer*, vol. 108, pp. 1560–1572, 2017, ISSN: 0017-9310. DOI: https://doi.org/10.1016/j.ijheatmasstransfer.2017.01.031.

[81] X. Zhang, X. Guo, Y. Weng, X. Zhang, Y. Lu, and Z. Zhao, "Hybrid mpi and cuda parallel finite volume unstructured cfd simulations on a multi-gpu system", *Future Generation Computer Systems*, vol. 139, pp. 1–16, 2023, ISSN: 0167-739X. DOI: https://doi.org/10.1016/j.future.2022.09.005.

[82] A. Fawaz, Y. Hua, S. Le Corre, Y. Fan, and L. Luo, "Topology optimization of heat exchangers: A review", *Energy*, vol. 252, p. 124 053, 2022, ISSN: 0360-5442. DOI: https://doi.org/10.1016/j.energy.2022.124053. [Online]. Available: https://www.sciencedirect.com/science/article/pii/S0360544222009562.

[83] F. Careri, R. H. Khan, C. Todd, and M. M. Attallah, "Additive manufacturing of heat exchangers in aerospace applications: A review", *Applied Thermal Engineering*, vol. 235, p. 121 387, 2023, ISSN: 1359-4311. DOI: https://doi.org/10.1016/j.applthermaleng.2023.121387.

[84] D. Bacellar, V. Aute, Z. Huang, and R. R. and, "Design optimization and validation of high-performance heat exchangers using approximation assisted optimization and additive manufacturing", *Science and Technology for the Built Environment*, vol. 23, no. 6, pp. 896–911, 2017. DOI: 10.1080/23744731.2017.1333877.

[85] P. Pai Raikar, N. Anand, M. Pini, and C. De Servi, "Concurrent optimization of multiple heat transfer surfaces using adjoint-based optimization with a cad-based parametrization", *International Journal of Heat and Mass Transfer*, vol. 236, p. 126 230, 2025, ISSN: 0017-9310. DOI: https://doi.org/10.1016/j.ijheatmasstransfer.2024.126230. [Online]. Available: https://www.sciencedirect.com/science/article/pii/S0017931024010603.

[86] B. S. Mekki, J. Langer, and S. Lynch, "Genetic algorithm based topology optimization of heat exchanger fins used in aerospace applications", *International Journal of Heat and Mass Transfer*, vol. 170, p. 121 002, 2021, ISSN: 0017-9310. DOI: https://doi.org/10.1016/j.ijheatmasstransfer.2021.121002.

[87] S. Sun, B. Rankouhi, D. J. Thoma, *et al.*, "Topology optimization, additive manufacturing and thermo-hydraulic testing of heat sinks", *International Journal of Heat and Mass Transfer*, vol. 224, p. 125 281, 2024, ISSN: 0017-9310. DOI: https://doi.org/10.1016/j.ijheatmasstransfer.2024.125281.

[88] P. Gradld, "Directed energy deposition: An additive manufacturing technology for large high-temperature compact heat exchangers: Process characterization and fluid dynamic performance", Ph.D. dissertation, Delft University of Technology, 2025.

[89] A. C. Patrao, I. Jonsson, C. Xisto, A. Lundbladh, and T. Gronstedt, "Compact heat exchangers for hydrogen-fueled aero engine intercooling and recuperation", *Applied Thermal Engineering*, vol. 243, p. 122 538, 2024, ISSN: 1359-4311. DOI: https://doi.org/10.1016/j.applthermaleng.2024.122538.

[90] C.-P. Bury, M. Stoia, L. Vesely, and J. Kapat, "Optimized design of primary heat exchanger for jet engine waste heat recovery system", in *AIAA SCITECH 2024 Forum*. AIAA, 2024. DOI: 10.2514/6.2024-2758.

[91] L. Vesely, J. Kapat, C. Bringhenti, G. B. Ribeiro, and J. T. Tomita, "Innovative design of waste heat recovery heat exchangers", in *AIAA SCITECH 2024 Forum*. AIAA, 2024. DOI: 10.2514/6.2024-2757.

[92] J. Wen, C. Wan, G. Xu, L. Zhuang, B. Dong, and J. Chen, "Optimization of thermal management system architecture in hydrogen engine employing improved genetic algorithm", *Energy*, vol. 297, p. 131 279, 2024, ISSN: 0360-5442. DOI: https://doi.org/10.1016/j.energy.2024.131279.

[93] Y. Park, J. Kim, J. Oh, U. Han, and H. Lee, "Multi-objective optimization of an offset strip fin heat exchanger for waste heat recovery in electric vehicles", *Applied Thermal Engineering*, vol. 228, p. 120 533, 2023, ISSN: 1359-4311. DOI: https://doi.org/10.1016/j.applthermaleng.2023.120533.

[94] F. Ascione, P. Colonna, and C. De Servi, "Integrated design optimization method for novel vapour-compression-cycle-based environmental control systems", *Applied Thermal Engineering*, vol. 236, p. 121 261, 2024, ISSN: 1359-4311. DOI: https://doi.org/10.1016/j.applthermaleng.2023.121261.

[95] Y. Zhang, W. Ren, H. Yu, and H. Li, "Development of gpu-based parallel cfd solver for unstructured meshes", in *2023 7th International Conference on Electrical, Mechanical and Computer Engineering (ICEMCE)*, 2023, pp. 469–473. DOI: 10.1109/ICEMCE60359.2023.10490481.

[96] Q. Zhu, M. Pishahang, M. Caccia, *et al.*, "Validation of the Porous Medium Approximation for Hydrodynamics Analysis in Compact Heat Exchangers", *Journal of Fluids Engineering*, vol. 144, no. 8, p. 081 403, 2022, ISSN: 0098-2202. DOI: 10.1115/1.4053898.

[97] J. W. Chapman, S. L. Schnulo, and M. P. Nitzsche, "Development of a thermal management system for electrified aircraft", in *AIAA Scitech 2020 Forum*. ARC, 2020. DOI: 10.2514/6.2020-0545.

[98] F. W. Meredith, "Cooling of aircraft engines with special reference to ethylene glycol radiators enclosed in ducts", Aeronautical Research Committee Reports and Memoranda, Tech. Rep. No 1683, Aug. 1935. [Online]. Available: https://naca.central.cranfield.ac.uk/handle/1826.2/1425?show=full.

[99] K. Hooman and H. Gurgenci, "Porous medium modeling of air-cooled condensers", *Transport in Porous Media*, vol. 84, pp. 257–273, 2010. DOI: https://doi.org/10.1007/s11242-009-9497-8.

[100] Z.-Z. Li, Y.-D. Ding, Q. Liao, M. Cheng, and X. Zhu, "An approach based on the porous media model for numerical simulation of 3d finned-tubes heat exchanger", *International Journal of Heat and Mass Transfer*, vol. 173, p. 121 226, 2021, ISSN: 0017-9310. DOI: https://doi.org/10.1016/j.ijheatmasstransfer.2021.121226.

[101] Y. Wu, R. Xu, C. Wang, and P. Jiang, "Novel three-equation porous media model for prediction of compact heat exchanger and its case study for microtube bundle precooler", *International Journal of Heat and Mass Transfer*, vol. 248, p. 127 177, 2025, ISSN: 0017-9310. DOI: https://doi.org/10.1016/j.ijheatmasstransfer.2025.127177.

[102] D. Missirlis, S. Donnerhack, O. Seite, *et al.*, "Numerical development of a heat transfer and pressure drop porosity model for a heat exchanger for aero engine applications", *Applied Thermal Engineering*, vol. 30, no. 11, pp. 1341–1350, 2010, ISSN: 1359-4311. DOI: https://doi.org/10.1016/j.applthermaleng.2010.02.021.

[103] M. Musto, N. Bianco, G. Rotondo, F. Toscano, and G. Pezzella, "A simplified methodology to simulate a heat exchanger in an aircraft's oil cooler by means of a porous media model", *Applied Thermal Engineering*, vol. 94, pp. 836–845, 2016, ISSN: 1359-4311. DOI: https://doi.org/10.1016/j.applthermaleng.2015.10.147.

[104] F. Beltrame, D. Krempus, P. Colonna, and C. M. D. Servi, "Reduced order modelling of optimized heat exchangers for maximum mass-specific performance of airborne orc waste heat recovery units", in *Proceedings of the* 7^{th} *International Seminar on ORC Power Systems*. Seville, Spain: University of Seville, 2023. DOI: 10.12795/9788447227457_93.

[105] P. Miltén, I. Johnsson, A. Lundbladh, and C. Xisto, "Generalized Method for the Conceptual Design of Compact Heat Exchangers", *Journal of Engineering for Gas Turbines and Power*, vol. 146, no. 11, p. 111 018, Aug. 2024, ISSN: 0742-4795. DOI: 10.1115/1.4065922. [Online]. Available: https://doi.org/10.1115/1.4065922.

2

Compact Heat Exchanger Preliminary Design: Challenges and Limitations

Unforeseen surprises are the rule in science,
not the exception.

Leonard Susskind

2.1. INTRODUCTION

A key step in the preliminary design of airborne thermal management systems is the selection of the most appropriate heat exchanger(HX) topologies and layout for the intended application. A suboptimal choice can negatively impact system efficiency, weight, and cost. In the case of feasibility studies of novel thermal system concepts, this may even lead to the premature dismissal of otherwise promising solutions. To facilitate informed decision-making in the selection of HX topologies, a variety of Performance Evaluation Criteria (PEC) have been proposed in the literature. These criteria can be used to compare and rank the thermohydraulic performance of different heat transfer surface geometries. However, due to the complexity and multidimensional nature of HX performance assessment and preliminary design, these general criteria may lead to inconclusive or even misleading results if applied to the design of airborne thermal systems. In such systems, volume and weight are as important as thermohydraulic performance in determining the suitability of a specific HX configuration.

This chapter is structured as follows. Section 2.2 describes the general characteristics of the main classes of HXs, with emphasis on the compact heat exchanger (CHX) configurations investigated in this dissertation. Section 2.3 provides an overview of the current literature on performance evaluation criteria (PEC) methodologies used to compare HX geometries and, in principle, to guide the designer in the choice of the best topologies for the application of interest. These performance metrics combine information about the thermohydraulic characteristics of a given HX topology with key geometrical parameters of the heat transfer surface, such as area compactness. The shortcomings of these methods for airborne applications are also discussed. Subsequently, Section 2.4 details the decision-making process that leads to the identification of the flow configuration and candidate topologies best suited for the target application. Finally, Section 2.5 introduces the methodology adopted in this study for comparing and ranking heat exchanger topologies. The novelty of this approach lies in the comparison of only the best-performing designs, thereby eliminating the need for an initial selection of candidate geometries for each topology. The design of a balanced air-to-air plate-fin heat exchanger is chosen as an illustrative case study. The results obtained are then used to derive general design guidelines for this type of HX in the context of airborne applications.

2.2. CLASSIFICATION OF HEAT EXCHANGERS

Heat exchangers are generally classified according to the characteristics listed below [1]–[3].

- **Number of fluids.** Most heat exchangers transfer thermal energy between two fluids, which may be in gaseous, liquid, supercritical, or two-phase states. The fluids are typically separated by a heat transfer surface, which can be classified as either primary or extended. In the case of primary surfaces, all heat transfer occurs across the wall that directly separates the two media. In contrast, extended surface designs incorporate additional elements, such as fins, that do not separate the fluids but significantly increase the available heat transfer area.

- **Predominant heat transfer mechanism.** The majority of aerospace-grade HXs rely on forced convection to transfer thermal energy between fluids. Heat conduction through the HX core material along the flow direction is generally very low compared to the total heat duty, and thus its impact on performance is negligible, except in HXs characterized by very high effectiveness (≥ 0.9). Heat transfer devices relying on conduction and radiation are uncommon in airborne applications, though they may find use in space systems.

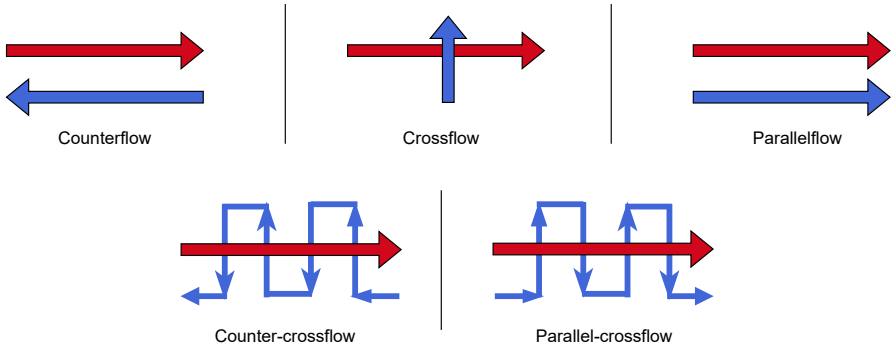

Figure 2.1: Visual representation of standard flow arrangements

- **Flow arrangement.** The flow arrangement refers to the orientation and direction of the hot and cold streams within the heat exchanger core. Although there are theoretically countless configurations for a two-fluid heat exchanger, most devices utilize the standard flow arrangements illustrated in Figure 2.1. In a parallel flow arrangement, both fluids enter the HX from the same side and flow in the same direction. Heat exchangers with such a flow configuration typically exhibit low effectiveness. Conversely, in a counterflow arrangement, the two fluids exit the HX core on opposite sides and thus flow in opposite directions. This arrangement yields the highest theoretical effectiveness for a given number of transfer units (NTU) of the HX. In cross-flow configurations, the fluids flow in a direction perpendicular to each other, although crossflow arrangements with angles different from 90°are also possible. Each stream in a crossflow configuration can be classified as either mixed or unmixed. In a mixed flow, fluid mixing occurs in the transverse direction (normal to the main flow direction), whereas in an unmixed flow configuration, the fluid is channeled through separate passages that prevent mixing. Flow mixing negatively affects HX effectiveness. Thus, the performance of a mixed–unmixed cross-flow HX tends to be lower than that of an unmixed–unmixed cross-flow device for the same heat transfer characteristics and area. For HXs with multiple passes, in which one or more streams change flow direction, the overall flow arrangement can be defined based on both the macroscopic flow direction and the local flow arrangement. For instance, an evaporator in which the evaporating fluid flows through multiple passes but enters the HX from the side opposite to that of the hot stream has a macroscopic counterflow arrangement regardless of the num-

ber of passes. Since the flow direction in each pass is perpendicular to that of the hot stream, the local flow arrangement is of the crossflow type. In this case, the overall flow configuration of the evaporator is termed counter-crossflow.

- **Construction features.** The vast majority of two-fluid heat exchangers can be classified based on four primary construction features or elements that define the geometry of these devices: tubular, plate-type, extended surface, and regenerative designs [1]. *Tubular HXs* consist of arrays of tubes which may have various shapes and cross-sections: elliptical, rectangular, flat, or twisted. One fluid, typically the one with the higher heat capacity rate, flows inside the tube, while the other flows externally, generally in a plane perpendicular to the tube main axis, with different incidence angles in case of a multi-pass configuration. The heat transfer surface in this category of HXs is typically only of the primary type, though it is not uncommon to enhance the heat transfer by adopting tubes with external fins, or with micro-fins or turbulators on the inner surface. Common topologies in this category include shell-and-tube, double pipe, spiral tube, and tube bundle HXs. *Plate-type HXs* (PHEs) are usually constructed from thin metal plates that are stacked in layers or wound to fit within a cylindrical casing. These plates can feature a smooth surface or various forms of corrugation and shapes to enhance heat transfer [2]. Several manufacturing techniques are used to assemble the plates, resulting in different PHE topologies. Gasketed, welded, and vacuum brazed plate HXs are the most common. Additional topologies in this HX category include spiral plate, lamella, and printed circuit HXs, each offering unique advantages in terms of compactness, performance, and mechanical strength. Typical advantages of PHEs are (i) an almost ideal counterflow arrangement, which facilitates designs with high thermal effectiveness, (ii) high heat transfer coefficients, (iii) good flow uniformity and absence of flow-induced vibrations and noise, and (iv) ease of maintenance in the case of gasketed assemblies. However, PHEs also present the following limitations. They are generally unsuitable for high-pressure and temperature applications, or those involving large pressure or temperature differences. Their geometric layout results in low and nearly equal free-flow to frontal area ratios on both fluid sides, making them less effective in case of streams having significantly different densities and flow rates, or for phase-change applications due to the large variation in volumetric flow that occurs during the phase-change process. Finally, PHXs can usually accommodate only up to about 300 m^2 of heat transfer area per cubic meter of volume [2]. For this reason, they are often not regarded as compact heat exchangers. *Extended surface heat exchangers*, conversely, can reach high values of heat transfer area compactness. In these types of HXs, the primary heat transfer surface, i.e., the construction element that separates the hot and cold streams, is extended by adding fins on one or both fluid sides. Compared to equivalent designs without fins, extended surface HXs feature up to 12 times more heat transfer area per unit volume. Moreover, certain fin geometries, such as offset-strip fins or louvered fins, may enhance the heat transfer coefficient up to 400% relative to smooth, straight channels, by repeatedly breaking the thermal boundary layer through periodic flow disruptions [1]. However, this thermal performance enhancement comes at the cost of higher pressure drops across the HX

core. Additionally, the heat transfer area effectiveness is reduced due to the lower average temperature of the extended surface compared to the primary surface. As a consequence, the effective temperature difference driving the heat transfer is lower than in an equivalent HX without fins. The rationale for employing extended surfaces lies in balancing the thermal resistances on the two sides of an HX. For instance, in gas-to-liquid HXs, the heat transfer coefficient on the gas side is typically an order of magnitude lower than that of the liquid side [2]. This disparity creates a barrier to heat transfer that offsets the benefit of high heat transfer coefficients on the liquid side. Incorporating fins on the gas side mitigates such an imbalance by increasing the surface area available for heat transfer, thereby reducing the volume required to exchange a given thermal load. This strategy is particularly advantageous in applications in which reducing the equivalent hydraulic diameter of the flow channels is constrained by limitations related to manufacturability or pressure drop. The most common extended surface topologies are those of plate-fin and tube-fin HXs. The geometric variety of such topologies is extensive due to the wide range of possible combinations of fin shapes, channel geometries, and tube profiles. *Regenerative heat exchangers* transfer thermal energy between fluids via a heat storage matrix. The flow across the matrix is periodically reversed so that thermal energy is stored and released cyclically [3]. Due to their complexity and operating principle, regenerative HXs are typically employed only in large power plants or the process industry, and therefore are not considered in the present work.

- **Heat transfer area compactness.** Heat exchanger compactness is commonly characterized in the literature using two distinct metrics: specific compactness β_s and overall HX compactness β. Specific compactness, or heat transfer surface density, is defined as the heat transfer area on one side of the HX per unit volume of that fluid side. Conversely, the overall compactness is defined as the ratio of the heat transfer area on the side with the higher thermal resistance to the total volume of the HX core. Unlike specific compactness, this metric depends on the geometry of both fluid sides. Figure 2.2 illustrates the typical range of compactness values for the most common HX types. Conventionally, an HX is considered compact if it exhibits a heat transfer surface density exceeding 700 m^2/m^3 or, in case of at least one fluid in a gaseous state, a hydraulic diameter $d_h \leq 6$mm. For liquid or multiphase flows, the threshold is generally lower, at around 400 m^2/m^3 [1]. Compact heat exchangers offer several benefits, including reduced structural support elements, lower fluid inventory, smaller footprints, and easier integration into space-constrained systems. These advantages translate into cost savings and improved operational efficiency [1] and make CHXs an attractive solution for modern aerospace thermal systems, for which space and weight are critical aspects.

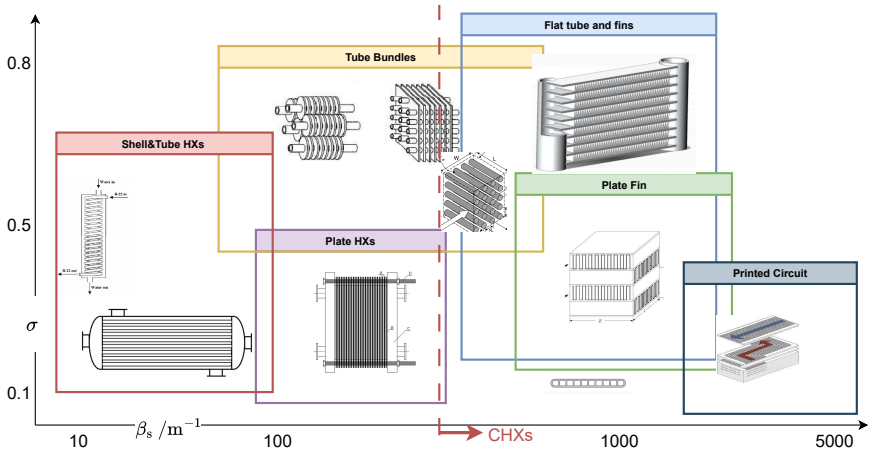

Figure 2.2: Representative range of heat transfer surface density and free-flow to frontal area ratio σ for common types of HXs.

2.3. PERFORMANCE EVALUATION CRITERIA FOR RANKING HX TOPOLOGIES

As discussed in Section 1.4, the optimal HX geometry for any given application should be identified through an integrated optimization of the preliminary design of the HX and that of the intended system. In theory, this process must be repeated for each candidate HX topology. However, such an approach is computationally expensive and, depending on the system complexity and constraints, may lead to numerical convergence issues, particularly if sub-optimal HX topologies and designs are considered. An alternative strategy consists of selecting promising topologies in the first stages of the design process and restricting the range of the design variable defining the HX geometry based on system requirements. However this strategy often relies on manufacturers' expertise, empirical knowledge and extensive field experience [4]. The so-called Performance Evaluation Criteria (PEC) are metrics that have been proposed in the literature to rank and compare the thermohydraulic performance of different HX geometries and topologies. The objective of these metrics is to facilitate the assessment of candidate HX geometries for industrial applications [5].

A variety of PEC formulations have been developed, particularly for extended surface HXs [6]. Given the complexity and multidimensional nature of HX performance assessment, the use of a single PEC is often insufficient for a comprehensive assessment [7]. Thorough reviews of the most common PEC adopted in the literature can be found in Refs. [6], [8], [9]. The suitability of each criterion depends on both the HX topology and the intended application. Moreover, the outcome of a PEC-based comparison is influenced by the assumptions of the methodology and the choice of design specifications held constant in the analysis, such as mass flow rates or effectiveness [10]. Specifically for aerospace applications, the suitability of these PEC is debatable. Weight and volume

are critical factors in topology selection and often have a greater impact on system performance compared to pressure drop. Furthermore, the operating conditions are such that even small changes in the HX geometry can significantly affect system performance. Consequently, selecting candidate geometries a priori may bias the comparative assessment of different topologies. These issues are discussed further in the following.

One of the earliest and most intuitive approaches for ranking the performance of heat transfer surfaces or topologies consists of comparing their Colburn factor $j = \mathrm{St}\,\mathrm{Pr}^{2/3}$ and Fanning friction coefficient f as a function of the Reynolds number. The Reynolds number is generally defined using the hydraulic diameter d_h of the flow passages characteristic of the geometry of interest [11]. Both the Colburn and Fanning friction factors are essential quantities for the modeling of the thermohydraulic performance of a heat transfer surface or topology. The Colburn factor is used to determine the heat transfer coefficient of the surface (h) as

$$h = j\,\mathrm{Re}\,\mathrm{Pr}^{1/3}\frac{k}{d_h}, \tag{2.1}$$

where k is the fluid conductivity, while the friction factor correlates with the pressure drop per unit length L of a heat transfer surface as

$$\frac{\Delta P}{L} = \frac{2\dot{m}^2 f}{\rho A_0^2 d_h}, \tag{2.2}$$

where A_0 is the free flow area. This geometric parameter can be expressed, according to the definition of the hydraulic diameter, as a function of the heat transfer surface area (A) as

$$A_0 = \frac{d_h A}{4L}. \tag{2.3}$$

Figure 2.3 illustrates in two distinct charts the variation of the Colburn (lower curve) and Fanning friction factor (upper curve) with Reynolds number for specific plain fin and a wavy fin geometries. The comparison of the two charts suggests the better performance of the wavy fin geometry at higher Reynolds numbers. This is primarily attributed to the periodic disruption of the thermal boundary layer caused by the wavy profile of the flow channels. Conversely, plain fin surfaces exhibit a rather rapid decline in the Colburn factor, and thus in the heat transfer coefficient for given fluid properties, as the Reynolds number increases [12]. Similarly, Figure 2.4 shows the j and f trends for two different fin geometries, whose topologies are among the most commonly adopted in compact HXs, namely louvered fins and offset-strip fins. A comparison of the trends for these two fins may lead engineers to conclude that the louvered fin surface outperforms the offset-strip-fin geometry at high airflow velocities in terms of pressure drop, due to the lower friction factor at higher Reynolds numbers. However, this conclusion is not always valid, as the Colburn factor of the offset-strip fins is slightly larger. Moreover, the pressure drop of the HX is also dependent on the HX size, surface efficiency, and flow acceleration through the HX core. Therefore, j and f curves alone are insufficient to characterize the thermohydraulic performance of extended surface topologies [5]. For instance, optimally designed HX cores with offset strip fins tend to outperform louvered fin-based

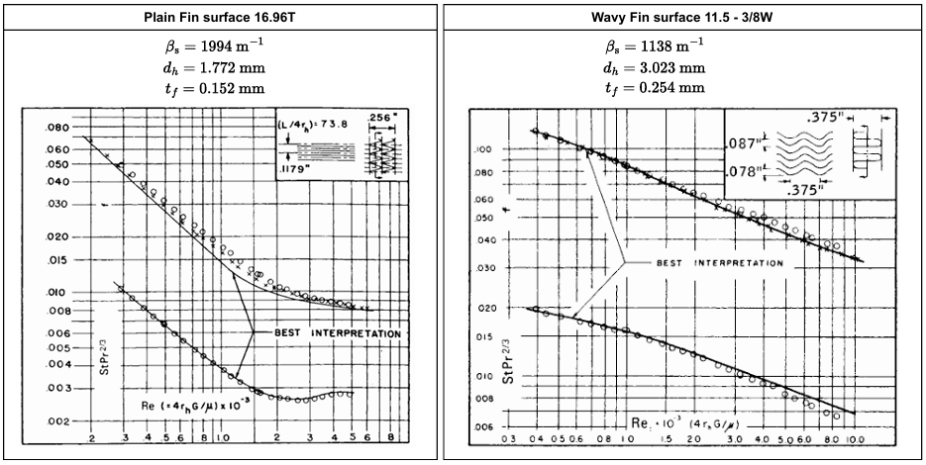

Figure 2.3: Colburn and Fanning friction factors for a plain fin (left) and a wavy fin (right) heat transfer surface as a function of Reynolds number. Data adapted from [11]

designs in terms of pressure drop at high Reynolds numbers, especially if heavier HX designs are acceptable, as demonstrated in [13]. This example highlights a key limitation of evaluating fin topologies based on performance charts such as those in Figure 2.3 and 2.4: the curves represent the performance of a specific fin geometry and do not generalize to all design options within the same fin category. Fins of the same topology but differing in geometric configuration can exhibit significantly different thermohydraulic characteristics. As such, the adjustment of the fin geometrical parameters is essential to optimize compact HX designs. Additionally, typical performance charts do not account for other critical factors relevant to aerospace applications, such as weight and size.

The area goodness factor (AGF), defined as the ratio of the Colburn and friction factor, is a performance metric introduced to compare the required free flow area (A_0) of specific heat transfer surfaces, for given operating conditions, i.e., mass flow rate, temperature difference, and pressure drop [11]. The free-flow area is directly related to the geometrical frontal area via the free-flow to frontal area ratio (σ), which, in turn, can be expressed as a function of the heat transfer area density (β_s) and the hydraulic diameter of the surface as

$$4\,\sigma = d_h\,\beta_s. \tag{2.4}$$

Combining Eqs. 2.3 and 2.4 yields the following expression for the heat transfer surface density

$$\beta_s = \frac{4\,\sigma\,A}{A_0\,L}. \tag{2.5}$$

The required heat transfer area (A) can be determined from the definition of the fluid-specific number of transfer units

$$\mathrm{ntu} = \frac{\eta_0\ j\ \mathrm{Re}\ \mathrm{Pr}^{1/3}\ k}{d_h(\dot{m}c_p)}A\,, \tag{2.6}$$

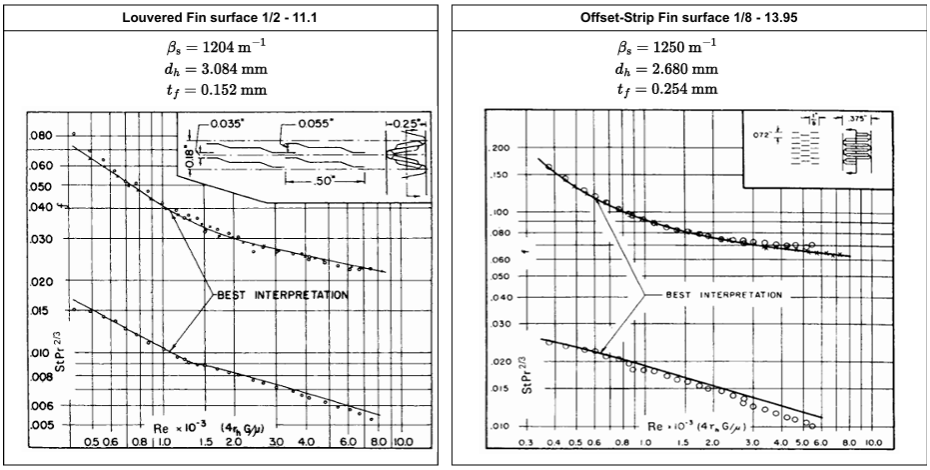

Figure 2.4: Colburn and friction factors for a louvered fin (left) and an offset-strip fin (right) heat transfer surface as a function of Reynolds number. Data adapted from [11]

provided that an estimate of the heat transfer surface efficiency η_0 is known. The heat transfer surface efficiency η_0 can be determined based on the extended surface over total heat transfer area ratio A_e/A and the fin efficiency η_f as

$$\eta_0 = 1 - \frac{A_e}{A}\left(1 - \eta_f\right). \tag{2.7}$$

Combining Eqs. 2.2 and 2.6, the AGF can be then expressed as

$$\mathrm{AGF} = \frac{j}{f} = \frac{1}{\eta_0 A_0^2}\left(\frac{\dot{m}^2 \mathrm{ntu}}{2\rho\Delta P}\right). \tag{2.8}$$

Therefore, the AGF metric can be used to rank the candidate heat transfer surface geometries provided that j and f charts are available. Its interpretation depends on the design specifications, as outlined below.

- For prescribed values of ntu and pressure drop in the design, higher AGF values indicate smaller free-flow areas A_0 required to achieve the target heat duty.
- If ntu and A_0 are instead fixed, higher AGF values correspond to lower pressure drops.
- for given A_0 and ΔP, a higher AGF implies a smaller required heat transfer area.

The parameters enclosed in the parentheses of Equation 2.8 are dependent on the design specifications of the considered fluid side of the HX at hand and are only marginally influenced by the thermohydraulic performance of the selected HX topology [14]. In addition, the AGF shows very limited variation across different CHX geometries. It follows that this metric alone is insufficient to establish a conclusive ranking of the heat transfer

geometries explored in the preliminary design phase of a HX [5].

A dimensionless parameter used to assess the thermal performance of a topology relative to the projected volume of the HX, while accounting for the effects of operating conditions, is the volume goodness factor (VGF) [6], which is defined as

$$\mathrm{VGF} = \frac{\dot{Q}}{V\,\Delta T} = \eta_0\, h\, \beta_\mathrm{s} = \frac{\eta_0\, j\, Re\, Pr^{1/3}\, k\, \beta_\mathrm{s}}{d_\mathrm{h}}. \tag{2.9}$$

More in detail, the VGF quantifies the heat transfer rate achieved per unit volume V of the considered HX side and per unit of temperature difference between the corresponding fluid and the wall separating the hot and cold streams $\Delta T = (T_\mathrm{w} - T_\mathrm{m})$ [1].

The thermohydraulic performance of extended surfaces with different hydraulic diameters can be compared by plotting the VGF, as defined in Equation 2.9, against the pumping power per unit volume

$$E\,\beta_\mathrm{s} = \frac{\dot{m}\,\Delta P}{\rho\, V} = \frac{\dot{m}\,\Delta P\,\beta_\mathrm{s}}{\rho\, A} = \frac{Re\,\mu\,\Delta P\,\beta_\mathrm{s}}{4\rho} = \frac{2\sigma\,\mu^3\, f\, Re^3}{\rho^2\, d_\mathrm{h}^4}, \tag{2.10}$$

given the mean fluid properties on the HX side being considered (i.e., density ρ and dynamic viscosity μ). Thus, for a fixed heat duty, mass flow rate, and temperature difference, surfaces characterized by higher values of VGF for a prescribed $E\beta_\mathrm{s}$ yield designs that occupy less volume to exchange the targeted heat duty for the same pressure drop on the considered HX side. The drawback of this approach lies in its limited generality, as it requires full specification of the geometry of the heat transfer surface and involves an iterative procedure to guess the best operating Reynolds numbers for the comparison of the different heat transfer surfaces [1].

In an attempt to increase the general applicability of PEC, La Haye et al. [15] analyzed the j and f data collected experimentally by Kays and London [11] for a wide variety of extended surface topologies. Two dimensionless performance parameters were defined: the heat transfer performance factor, $J = j\ Re$, and the pumping power factor, $F = f\ Re^3$. These metrics were plotted against the dimensionless boundary layer disturbance length, l/d_h, where l denotes the average streamwise distance over which the extended surface periodically disrupts the boundary layer or generates a repeating characteristic flow structure. The authors found that, regardless of the topology, both J and F correlate consistently with l/d_h, although only in the fully turbulent flow regime, indicating that this parameter provides a useful basis for a direct comparison of the thermohydraulic performance of different heat transfer geometries. However, a limitation of this approach is that different extended surface topologies may have similar J and F values for a given l/d_h ratio, yet result in significantly different HX designs in terms of size, shape, and weight. Consequently, this method serves primarily as a general guide for selecting a set of promising geometries for the application of interest [15].

The PEC proposed by La Haye et al. was adapted by Soland et al. [16] to enable the comparison of any surface type under specified operating conditions. As a first step,

the heat transfer and the friction factor for each extended surface topology tested by Kays & London were recalculated, taking the bare area of the extended geometry as the reference. Analogously, the Reynolds number was recomputed based on the hydraulic diameter and flow area corresponding to the channel cross-section as if the fins were not present. The transformed – or "nominal" according to the terminology adopted by Soland et al. – quantities were then used to estimate for each surface topology of interest the pumping power per unit volume

$$\frac{P_{\text{diss}}}{V} \propto \frac{f_{\text{n}}\, Re_{\text{n}}^3}{D_{\text{n}}^4} \tag{2.11}$$

and the heat transfer rate per unit volume, and the heat capacity rate of the fluid

$$\frac{\text{ntu}}{V} = \frac{A\, h_{\text{n}}}{V\, \dot{m}\, c_p} \propto \frac{j_{\text{n}}\, Re_{\text{n}}}{D_{\text{n}}^2}. \tag{2.12}$$

Note that Equation 2.11 and 2.12 represent special cases of Equation 2.10 and 2.9, respectively, if the heat transfer surfaces are of the primary type and they operate under the same inlet flow conditions. Heat transfer topologies having the same nominal diameters are compared based on the trend of P/V vs ntu/V. However, this PEC method is still affected by important limitations. First, surfaces exhibiting greater compactness tend to rank more favorably, but may yield designs that are either too heavy or with unacceptably large frontal areas and short flow lengths. Second, the method accounts for neither the surface efficiency nor the entrance and exit contributions to pressure drop. Third, the comparison is based on the assumption that the thermal resistance on the other side of the heat transfer topologies being evaluated is negligible [16].

Sahiti et al. [17] proposed a ranking approach based on modified volume goodness factor metrics derived from those introduced by Soland et al. [16]. The authors evaluated the method by using it to compare the performance of an experimentally tested pin fin heat exchanger with that of an equivalent smooth pipe heat exchanger. The authors recommend comparing different heat transfer topologies by plotting the heat transfer rate per unit volume against the required pumping power per unit volume, for given mass flow rates, inlet temperatures of the hot and cold streams, and HX flow length. The heat transfer rate per unit volume of the HX is estimated via the ϵ-NTU method. This enables a more reliable evaluation of the heat transfer performance achievable with the candidate topologies, compared to other methods that assume a constant heat transfer driving temperature difference or a linear relationship between heat transfer rate and NTU [17]. However, the assumption of a constant flow length in the comparison of the different heat transfer surfaces limits the applicability of the method. Moreover, the projected weight of the HX is not considered in the ranking process[7].

Fugmann et al. [7] introduced a method that extends the PEC-based approaches using volume goodness factor metrics to assess the performance of extended heat transfer surfaces with different characteristic lengths. The performance of the candidate surfaces is characterized and compared according to metrics related to the volume, mass, and power required to pump the fluid through the heat transfer surface. Table 2.1 reports

the definition and mathematical expression of these three metrics, referred to as energy, volume, and mass efficiencies. Note that the energy efficiency is essentially a modified form of the area goodness factor, with the difference that it takes into account the fin efficiency and the free flow to frontal area ratio ($\sigma = A_0/A_{\text{fr}}$) specific to the fluid side under consideration. The mass efficiency is equivalent to the volume efficiency multiplied by a factor proportional to the inverse of the material density and the complement of the structure porosity $1-\phi_{\text{st}}$. As a result, two identical geometries made of different materials are characterized by distinct mass efficiency values.

Description	Key Figure	Definition	Expression	Alternate expression
Energy efficiency	ϵ_E^*	$\frac{\dot{Q}}{P_{\text{diss}}}\frac{\mu u^2}{k}$	$\frac{Nu}{2f}\frac{\eta_0 d_{\text{h}}\beta_{\text{s}}}{Re}$	$\frac{\text{AGF}}{2}Pr^{1/3}4\sigma\eta_0$
Volume efficiency	ϵ_V^*	$\frac{\dot{Q}}{V_{\text{st}}}\frac{\nu^2}{u^2 k}$	$\frac{Nu}{Re^2}\eta_0 d_{\text{h}}\beta_{\text{s}}$	$\frac{j\,Pr^{1/3}}{Re}4\sigma\eta_0$
Mass efficiency	ϵ_M^*	$\frac{\dot{Q}}{M_{\text{st}}}\frac{\rho\nu^2}{u^2 k}$	$\frac{Nu}{Re^2}\frac{\eta_0 d_h\beta_{\text{s}}\rho}{\rho_{\text{st}}(1-\phi_{\text{st}})}$	$\epsilon_V^*\frac{\rho_f}{\rho_{\text{st}}}\frac{1}{1-\phi_{\text{st}}}$

Table 2.1: Non-dimensional performance metrics. Adapted from [7].

The comparison of the heat transfer surfaces is carried out based on the metrics of Table 2.1 for a given fluid mass flow rate and average pressure, heat duty, mean temperature difference, and free flow area. Moreover, to ensure a fair comparison of the heat transfer surfaces, the thermal resistance on the opposite fluid side has to be small and constant. The performance metrics take into account not only the surface efficiency and differences in characteristic lengths, but also the projected weight of the portion of the HX core under consideration. The best extended surface can then be identified from the set of candidate geometries by assigning an application-dependent weighting factor to each of the three metrics. However, evaluating heat transfer topologies on the basis of a combination of volume and mass efficiencies as defined in Table 2.1 can lead to misleading conclusions, especially for airborne or mobile applications. In most cases in which extended surfaces are needed, namely in HXs operating with at least one fluid in a gaseous state, the optimal HX design is typically the one that utilizes all the available space on the fluid side with the highest thermal resistance [13]. If both the cold and hot stream sides are characterized by high thermal resistance, the optimal HX geometry tends to occupy the full available space. In such a case, the optimal designs are those that minimize the pressure drop on one or both fluid sides (depending on the application), while also minimizing the core weight. This highlights the sensitivity of this PEC to the weighting factors applied to the individual performance metrics.

While all previous PEC methods are applied after selecting a set of candidate heat transfer topologies and, for each topology, a set of candidate geometries, Milten et al. [10] introduced a generalized approach to evaluate the performance of HXs without the need to specify the heat transfer surface geometry. More in detail, in their method, the core geometry is modeled using geometric parameters, such as the surface area density, structure porosity, and solid volume fraction, whose definitions are topology-

independent. These parameters can be estimated for any geometry and are used, in combination with the dimensionless flow length l/d_h, and the Reynolds number, to model the aerothermal performance of a generic HX. This is achieved through *ad-hoc* correlations derived by the authors by fitting a subset of the experimental data of Kays & London [11], expressed in terms of the same performance metrics J and F proposed by La Haye et al. [15], as a function of the dimensionless flow length. Moreover, the authors of Ref. [10] argue that defining a universal performance metric to identify the best HX topology that is valid for any arbitrary application is impractical. For this reason, the optimal values of the geometric parameters modeling the HX performance are obtained by solving an optimization problem, with the objective function definition tailored to the specific requirements of the application under consideration. Although the resulting optimal values do not identify a specific HX geometry or size, they reduce the HX design space and guide the designer in the selection of appropriate topologies. The authors demonstrated their generalized methodology through a case study involving the design of an air-to-air single pass crossflow intercooler of a turbofan engine. A limitation of this method is the large uncertainty associated with the generalized correlations derived by the authors. Furthermore, these correlations were not developed using optimized geometries; as a result, the performance of a given topology may be underestimated if the training dataset includes configurations that yield suboptimal HX designs in terms of pressure loss and mass.

In summary, while existing PEC methods are valuable tools for characterizing the thermohydraulic performance of heat transfer surface topologies [7], their applicability to HX design, especially for aerospace systems such as those discussed in Sec. 1.2, remains limited due to several critical shortcomings. Most notably, these methods typically compare a small number of predefined heat transfer geometries, without first identifying the best designs for each candidate topology. As a result, the outcome of a ranking process based on a PEC is highly dependent on the assumed geometry, which may not reflect the potential of the candidate topologies. Furthermore, in the context of aerospace applications, key performance metrics alongside pressure drop which affects drag, are

1. volume, which has to be minimized to enable seamless integration of HXs into the intended system aboard the aircraft,

2. weight, which directly impacts aircraft drag or reduces maximum payload, and

3. resilience to flow-induced vibrations and fouling.

These metrics are either only indirectly taken into account or entirely neglected, despite being primary design drivers.

Many PEC also rely on simplifying assumptions, such as fixed flow length, free flow area, or hydraulic diameter, which limit their generality and applicability across different operating conditions and applications. Another major limitation is the inability of these methods to verify whether a given candidate geometry could yield a design complying with the spatial constraints imposed by the integration environment – a check that requires a dedicated preliminary design model. Moreover, the use of more comprehensive

metrics, such as the VGF or the dimensionless metrics in Table 2.1, relies on iterative procedures that are time-consuming and application-specific. Although the PEC proposed in Ref. [10] leverages topology-independent geometric parameters, it relies on generalized thermohydraulic performance correlations derived from empirical datasets for non-optimized geometries and requires integration with an optimization routine. This increases both the uncertainty in the performance comparison and the computational complexity, without guaranteeing the identification of the optimal HX configuration.

2.4. PRELIMINARY STEPS FOR THE SELECTION OF SUITABLE HX DESIGNS

The first step in HX design is the definition of the process specifications that have to be met in both design and off-design conditions, along with the identification of the problem constraints. Then, the HX construction features and material are selected based on (i) the characteristics of the hot and cold streams, (ii) the operating pressures and temperatures, (iii) space and weight constraints, and (iv) considerations related to fouling, leakage risk, manufacturing technology, and cost [1]. The choice of the flow arrangement is, instead, made taking into account the required HX effectiveness and system integration constraints, such as duct layout, orientation, and space limitations.

Once these preliminary activities have been completed, the designer has to identify the optimal HX topology and geometry among several options. The variability in geometric characteristics and thermohydraulic performance of the different classes of HX topologies is extremely wide, as shown before. Each class and specific type of HX topology operates optimally within a defined range of operating conditions. As a consequence, depending on the design specifications, some HX topologies may yield infeasible designs while others may lead to solutions that differ significantly in terms of HX size, weight, and pressure drop performance.

The first step in identifying the most suitable HX topologies consists of narrowing down the possible design options based on the characteristics of the involved process or application. Before illustrating how this task can be accomplished, consider the HX types analyzed in the present dissertation, namely

1. evaporators or supercritical heaters that transfer thermal energy from a gas to a working fluid in a liquid, vapor, supercritical, or two-phase state;

2. condensers, coolers, or desuperheaters that transfer thermal energy from a working fluid in a liquid, vapor, or two-phase state to a gas;

3. single-phase heat exchangers that transfer thermal energy between two single-phase fluids, either in a vapor or liquid state.

These types of HXs generally operate with streams characterized by different heat capacity rates and thus are defined as imbalanced. The degree of imbalance is quantified by the heat capacity rate ratio, which reads

$$C^* = \frac{C_{min}}{C_{max}} = \frac{\min(C_h, C_c)}{\max(C_h, C_c)} \in [0,1] \,, \tag{2.13}$$

where C_h and C_c are the heat capacity rates of the hot and cold streams. The heat capacity rate of a flow is defined as the product of the mass flow rate and the derivative of the fluid specific enthalpy as a function of temperature

$$C_{h,c} = \dot{m}_{h,c} \frac{\partial h_{h,c}}{\partial T_{h,c}} . \tag{2.14}$$

This ratio represents the amount of thermal energy transferred to or from the fluid at hand per unit temperature difference. Condensers and evaporators are the HX types with the highest degree of imbalance since C^* is close to zero. Conversely, balanced HXs are characterized by C^* close to one. The thermal energy in these HXs is typically transferred between two fluids in the same thermodynamic phase, and the heat transfer topologies on the cold and hot sides are usually similar.

The degree of imbalance influences the selection of heat transfer topologies. In **condensers** and **evaporators**, the gas side is characterized by a much lower heat transfer coefficient despite a much larger volumetric flow rate. As a result, this side governs the overall resistance to heat transfer. Therefore, optimal designs feature larger free-flow to frontal area ratios on the gas side to limit pressure drop, along with extended heat transfer surfaces comprised of fins or other heat transfer enhancement devices, such as rib turbulators, to reduce the thermal resistance. Note that the adoption of fins is not always beneficial. Specifically, the presence of fins (i) increases the pressure gradient within the HX core compared to an equivalent design without fins, (ii) reduces the heat transfer area effectiveness, and (iii) increases susceptibility to performance degradation during operation due to fouling. Additionally, in applications involving extreme temperatures or corrosive streams, the use of fins may be infeasible. In such cases, primary surface topologies, such as mini or micro-tube bundles, can be an effective alternative to finned topologies, as they allow for similar values of heat transfer area compactness.

Regarding the working fluid side, i.e., the side with the lesser contribution to the overall thermal resistance, the heat transfer area is often of the primary type and consists of small channels or tubes of various cross-sectional shapes. The internal surface of the channels may be smooth or equipped with heat transfer enhancement features such as small corrugations and turbulators. The best-suited common topologies for CHXs operating with a high degree of imbalance are

- flat tube HXs, with or without microchannels on the working fluid side, featuring fins characterized by a high extended surface to primary surface area ratio on the gas side, such as louvered or offset strip fins;
- bundles of mini or micro tubes with circular or elliptical cross-sectional profiles, arranged in staggered or inline configurations, and possibly equipped with external fins. The tube bundle flow arrangement can be of the crossflow, counterflow, or multi-pass counter-crossflow type, with the gas stream potentially impinging the tubes at various angles. Common external fin topologies include pin, circular helical, annular, slotted, and serrated fins.

For applications characterized by a low degree of imbalance, such as **gas-to-air coolers**, **air-to-air intercoolers**, or **vapor-to-vapor recuperators**, plate fin heat exchangers

(PFHXs) are typically the most suitable design option. These heat exchangers incorporate extended surfaces for both the hot and cold streams, although the topology and geometric configuration may differ between the two HX sides. Common fin topologies adopted in PFHXs include offset-strip, louvered, wavy, and pin fins, each offering a specific trade-off between heat transfer performance and pressure drop. Since the fluids on both sides of PFHXs generally do not undergo a phase change and their thermophysical properties vary quasi-linearly with temperature, sizing or rating models based on the ϵ-NTU method and a few control volumes are sufficiently accurate for preliminary performance assessment. In the case of design problems involving stringent spatial or pressure drop constraints, selecting the optimal heat transfer surfaces for PFHXs can be even more challenging than for HXs with a high degree of imbalance. The reason is that, in PFHXs, both fluid sides contribute significantly and often comparably to the overall thermal resistance. Consequently, the surface geometry must be carefully tailored on each side of the HX to meet the design requirements.

The preliminary assessment of the degree of imbalance of the heat exchanger targeted in the design is, however, not sufficient to select suitable candidate HX topologies, though the number of possible options is significantly reduced. At the same time, each selected topology admits multiple flow arrangements and geometric configurations. In this regard, the selection of the most appropriate flow arrangement is primarily driven by three factors:

- **Targeted HX effectiveness**. The effectiveness is a dimensionless parameter that expresses how much thermal power is transferred compared to that achievable in a hypothetical HX with infinite heat transfer surface, given the same stream inlet temperatures and design specifications. Crossflow arrangements are common in aerospace applications due to their construction simplicity and ease of integration; however, crossflow HXs are characterized by lower effectiveness compared to designs with a counterflow arrangement [2], since the average temperature difference between the hot and cold streams is smaller if the streams flow perpendicularly rather than in opposite directions. A solution to increase the average temperature difference is to adopt a crossflow arrangement with multiple streamwise passes, provided that other requirements allow it. In a counter-crossflow arrangement, the temperature difference between the two streams is increased with respect to a pure crossflow configuration, resulting in a greater overall HX effectiveness.

- **Integration constraints**. Limitations related to available space and routing of the piping or ducting within the system may render some flow arrangements practically unfeasible.

- **Range of admissible flow velocities**. The free flow area on each fluid side should ensure that flow velocities within the HX core remain within the validity range of the empirical correlations used for heat transfer and pressure drop calculations. At the same time, the resulting pressure losses must remain within the acceptable bounds for the specific application. For instance, for some crossflow condenser configurations, the working fluid is routed through multiple fluid passes, each with

a distinct free-flow area to accommodate the large density variations associated with condensing flows. These passes are typically arranged vertically in a transverse direction with respect to the cooling gas stream. Unlike counter-crossflow arrangements, transverse multi-pass arrangements do not increase heat-exchanger effectiveness. However, they remain suitable for phase-change heat exchangers, such as condensers and evaporators, because their effectiveness is largely insensitive to flow arrangement when $C^* \approx 0$. This configuration enables adjustment of the working-fluid velocity while maximizing the frontal area on the opposite side of the heat exchanger, where the stream with the highest volumetric flow rate passes.

2.5. PROPOSED METHOD FOR SELECTION OF HEAT EXCHANGER TOPOLOGY

In view of the limitations of the PEC-based methods highlighted in Sec. 2.3, this work introduces an alternative approach to compare and rank different HX topologies. The proposed method integrates an HX preliminary design model with a multi-objective optimization framework to enable a systematic comparison of the optimal geometries of the various candidate topologies under realistic space, weight, and pressure constraints. The ranking of the HX geometry is subsequently driven by the performance metrics most relevant to the intended application, making this approach particularly suitable for aerospace applications.

More in detail, once the most suitable candidate HX topologies and flow configurations have been selected based on the considerations outlined in Sec. 2.4, an optimization problem is solved for each HX topology to obtain the sets of Pareto-optimal solutions that minimize mass and pressure drop on both fluid streams, while satisfying specific spatial constraints. The HX design specifications are defined to reflect the expected system design characteristics. If the design space of the application is too broad to identify a single representative system solution, the optimization is repeated for different design specifications of the HX. The Pareto sets are subsequently compared to identify the most promising topologies and the pressure drop and weight ranges in which they are optimal. Note that for HXs with a high degree of imbalance, the pressure drop on the side with the highest thermal resistance typically has the greatest impact on system performance. Thus, a bi-objective optimization targeting the minimization of mass and pressure drop on the critical side is often sufficient for an effective comparative ranking of the considered heat transfer topologies. The main advantage of this performance evaluation method is that it enables the comparison of only the best geometries of each topology. Core geometries that are suboptimal with respect to the specified objective functions or that do not satisfy the design constraints are automatically excluded from consideration. However, the drawback of this method is that it requires coupling a sufficiently accurate HX sizing model with a robust optimization algorithm and the solution of several optimization problems. In the case of complex flow arrangements and/or HXs featuring multiple fluid phases, simplified rating models based on the ϵ-NTU or mean logarithmic temperature difference methods and a single control volume for the whole HX geometry are typically inadequate for a reliable performance assessment. In such

cases, HX models based on a finite volume approach (see Sec. 3.2) are required, thus increasing the computational cost of the optimizations.

2.5.1. EXEMPLARY APPLICATION

To demonstrate the proposed methodology for comparing and ranking HX topologies, a balanced air-to-air crossflow PFHX is selected as a case study. This design problem is chosen since selecting the optimal heat transfer surfaces for PFHXs is generally more complicated than for other types of HXs, given that both the hot and cold sides are characterized by comparable thermal resistance. Table 2.2 reports the design specifications for this PFHX. The figures of merit considered to discriminate among the various fin topologies are the weight of the corresponding optimal HX design and the pressure drops on both fluid sides.

Table 2.2: Design specifications of the air-to-air PFHX considered in the case study.

	$\dot{m}$ / kg s^{-1}	T_{in} /K	P_{in} /bar	L_{max} /m	$\dot{Q}$ / kW
Hot Side	2.1	900	2	0.5	1080
Cold Side	2	200	2	0.5	

The sizing of the PFHX is performed using an in-house tool developed in Python. The sizing routine leverages the ϵ-NTU method for predicting the required overall thermal conductance (UA) and iteratively solves for the heat transfer area necessary to satisfy the targeted heat duty. The fluid properties are adjusted at every iteration based on the calculated pressure drops. The relation between ϵ and NTU for HXs with a crossflow arrangement is dependent on (i) whether the flows are mixed or unmixed and (ii) which stream has the lower heat capacity rate[1]. In the case of a crossflow HX in which both fluids are unmixed, the relation between effectiveness and NTU is approximated by the following semi-empirical equation

$$\epsilon = 1 - \exp\left\{\frac{\mathrm{NTU}^{0.22}}{C^*}\left[\exp(-C^*\mathrm{NTU}^{0.78}) - 1\right]\right\}. \tag{2.15}$$

The accuracy of Equation 2.15 depends on (i) the actual flow paths within the HX core and (ii) the effectiveness of the HX [1]. Several fin topologies result in flow patterns that cannot be classified as entirely unmixed or fully mixed. Under these conditions, Equation 2.15 may overestimate the HX performance [18]. The error becomes particularly significant at high HX effectiveness values ($\epsilon > 0.9$), although this issue does not arise in the present case study. The accuracy of the sizing routine has been verified by comparing the estimated pressure drops and HX core size with data of test cases available in the open literature [19], [20]. The deviation in the estimated overall core size with respect to the literature references is within 2%, while the relative error in the pressure drop calculations remains below 6%.

The sizing routine is coupled with an NSGA-III optimization algorithm [21] to identify the optimal HX geometry for each of the candidate fin topologies, under the assumption that the same fin type is adopted on both HX sides. This choice is justified by the fact that $C^* = 1$, which simplifies the design process as the number of design options for

the analyzed test case is reduced. Three fin topologies have been considered: offset-strip fins (osf), louvered fins (lf), and triangular wavy fins (twf). The heat transfer and pressure drop correlations used for each topology are detailed in Appendix A. The optimization algorithm targets solutions that minimize the HX core mass and the pressure drop on both fluid sides, while simultaneously satisfying constraints on the HX size. Thus, the constrained multi-objective optimization problem is formulated as

$$\begin{aligned} \text{minimize} \quad & \frac{M_{\text{HX}}}{\dot{Q}} \, ; \, \frac{\Delta P_{\text{c}}}{P_{\text{c,in}}} \, ; \, \frac{\Delta P_{\text{h}}}{P_{\text{h,in}}}, \\ \text{subject to} \quad & X \leq L_{\text{h,max}} \\ & Y = Y_{\text{max}}, \\ & Z \leq L_{\text{c,max}}, \\ & x_{\text{D}}^{\text{L}} \leq x_{\text{D}} \leq x_{\text{D}}^{\text{U}} \, , \end{aligned} \tag{2.16}$$

where X_{D} is the set of topology-specific optimization variables, and X, Y, and Z represent the length of the HX core along the axial, transverse, and vertical directions, respectively. The upper and lower bounds of the design vector x_{D} are defined according to the validity range of the heat transfer and pressure drop correlations. The no-flow length Y_{max} is fixed to 1 m, while the hot and cold side maximum dimensions are set to 0.75 m based on similar case studies reported in Ref. [19] and [22]. The initial population comprises 20 individuals for each optimization variable. The NSGA-III algorithm employed in this study leverages the structured reference point generation method by Das and Dennis [23] with 12 partitions, i.e., the number of gaps between two consecutive points along an objective axis.

Figure 2.5 presents the outcome of the three multi-objective optimizations. The x and y axes of each chart represent the relative pressure drops on the hot and cold side, respectively, while the color scale indicates the thermal power that each HX geometry can transfer per kilogram of core weight. These results show that offset-strip-fin (osf) cores reach a heat transfer rate per unit mass comparable to that of cores with louvered fins (lf) for the same level of pressure drop in the hot and cold streams. However, osf-based designs tend to be more favorable if low-pressure drops are targeted, while the adoption of a louvered fin topology allows for lighter HXs. Heat exchanger cores featuring wavy fins (twf) tend to be significantly heavier than those obtained with the other fin topologies. Since the heat transfer surface compactness of this topology is comparable to that of the other two topologies, PFHX designs with wavy fins are, on average, larger than those featuring offset-strip fins or louvered fins. At the same time, many of these heavier designs exhibit very low-pressure drops. The key conclusions from the application of the proposed methodology for comparing and ranking HX topologies to the PFHX design test case are summarized below.

- Offset strip fin PFHX cores are the best option if both mass and pressure drops are critical factors for the application of interest. This topology of PFHX is therefore recommended for the design of heat exchangers that transfer thermal energy from a hot gas to ambient air.

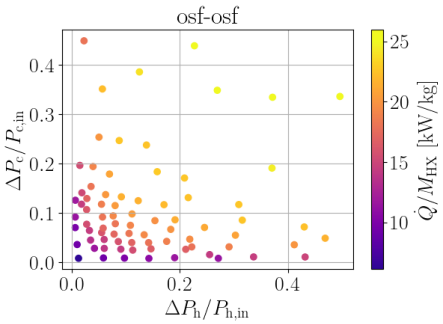

(a) Offset-strip fins

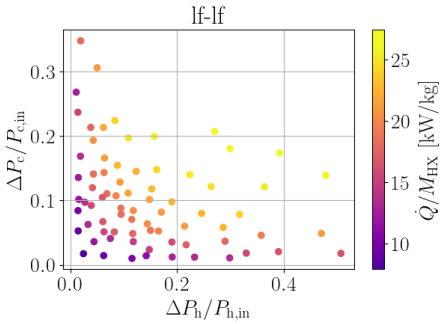

(b) louvered fins

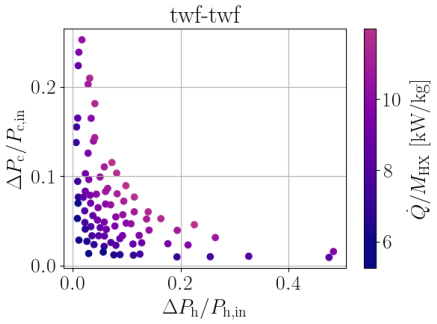

(c) Wavy fins

Figure 2.5: Sets of Pareto optimal solutions for three topologies of PFHXs obtained for the design specifications of Table 2.2.

- Louvered fin cores are more suitable if the primary design objective is to maximize compactness and the thermal duty per unit mass of HX core. Thanks to the large number of geometric parameters that can be adjusted, louvered fins offer the broadest design space among the investigated topologies, resulting in HX designs that span a wide range of pressure drops, free flow to frontal area ratios, and core weights.

- Wavy fin cores allow for designs that satisfy the imposed space constraints with significantly lower pressure drops. At comparable pressure drops, wavy fin designs are only 5 to 20% heavier than the solutions obtained with the other two extended surface topologies. Therefore, the use of wavy fins is recommended for applications where weight is not a critical metric.

NOMENCLATURE

Roman symbols

A	Surface area [m^2]
A_0	Free flow area [m^2]
C^*	Heat capacity ratio [-]
C	Heat capacity [$W K^{-1}$]
c_p	Isobaric specific heat capacity [$kg m^2 s^{-2} K^{-1}$]
d_h	Hydraulic diameter [m]
D_n	Nominal diameter [m]
E	P_{diss} per unit surface area [Wm^{-2}]
Eu	Euler number [-]
F_h	Fin height [m]
F_p	Fin pitch [m]
f	Friction factor [-]
$F = f\,Re^3$	Pumping power factor [-]
G	Mass flux [$kg m^{-2} s^{-1}$]
g	Gravitational acceleration [m/s^2]
h	Heat transfer coefficient [$W m^{-2} K^{-1}$]
	Specific enthalpy [$J kg^{-1}$]
j	Colburn factor [-]
$J = j\,Re$	Heat transfer performance factor [-]
k	Thermal conductivity [$W m^{-1} K^{-1}$]
L	Flow length [m]
L_p	Louver pitch [m]
L_l	Louver length [m]
L_α	Louver angle [°]
L_s	Length of fin strip [m]
l_f	Fin length along heat conduction [m]
M	Mass [kg]
$\dot{m}$	Mass flow rate [$kg s^{-1}$]
ntu	Fluid-side number of transfer units[-]
NTU	Number of transfer units[-]
Nu	Nusselt number [-]
P	Pressure [Pa]
	Pumping power [W]
Pr	Prandtl number [-]
$\dot{Q}$	Heat duty / thermal power [W]
Re	Reynolds number [-]
T	Temperature [K]
t	Thickness [m]
T_p	Transversal flat tube pitch [m]
U	Overall transfer coefficient [$W m^{-2} K^{-1}$]
u	Velocity [$m s^{-1}$]
V	Volume [m^3]
X	Width [m]
x_D	Design variables array [-]
Y	Height [m]
Z	Depth [m]

Greek symbols

α	Fin pitch over height ratio [-]
β	Heat transfer area compactness [m^{-1}]
β_s	Fluid side-specific area compactness [m^{-1}]
γ	Fin thickness over pitch ratio [-]
δ	Fin thickness over fin depth ratio [-]
ϵ	Effectiveness [-]
η	Efficiency [-]
μ	Dynamic viscosity [$kgs^{-1}m^{-1}$]
ρ	Density [$kg m^{-3}$]
σ	Free flow to frontal area ratio [-]

Subscripts

0	Overall heat transfer surface
c	Cold side
diss	Dissipated
e	Secondary(extended) heat transfer area
f	Fin
HX	Heat Exchanger
i	Relative to a specific fluid side
in	HX inlet conditions
lm	Logarithmic mean
max	Maximum allowed value
n	reference to nominal diameter
ref	Reference
st	Core structure
x,f	Cross-sectional area of fin

Superscripts

L	Lower bound
U	Upper bound

Abbreviations

AGF	Area goodness factor
APU	Auxiliary power unit
CC	Combined cycle
CHX	Compact heat exchanger
FV	Finite-volume
HX	Heat exchanger
lf	Louvered fin topology
MB	Moving boundary
ORC	Organic Rankine cycle
osf	Offset-strip fin topology
PCHX	Printed circuit heat exchangers
PEC	Performance evaluation criteria
PHE	Plate heat exchangers
PFHX	Plate-fin heat exchangers
STHX	Shell and tube heat exchangers
twf	Triangular wavy fin topology
VGF	Volume goodness factor
WF	Working fluid
WHR	Waste heat recovery

BIBLIOGRAPHY

[1] D. Shah R. Sekulic, *Fundamentals of heat exchanger design*. John Wiley and Sons, 2003.

[2] J. Hesselgreaves, R. Law, and D. Reay, *Compact Heat Exchangers: : Selection, Design, and Operation*. Elsevier Science, 2016, Second edition, ISBN: 978-0-08-100305-3.

[3] S. Kakaç, H. Liu, and A. Pramuanjaroenkij, *Heat Exchangers: Selection, Rating, and Thermal Design, third edition*. CRC Press, 2012. DOI: https://doi.org/10.1201/b11784.

[4] J. E. Hesselgreaves, R. Law, and D. A. Reay, "Chapter 2- industrial compact exchangers", in *Compact Heat Exchangers (Second Edition)*, J. E. Hesselgreaves, R. Law, and D. A. Reay, Eds., Second Edition, Butterworth-Heinemann, 2017, pp. 35–89, ISBN: 978-0-08-100305-3. DOI: https://doi.org/10.1016/B978-0-08-100305-3.00002-1.

[5] J. E. Hesselgreaves, R. Law, and D. A. Reay, "Chapter 4 - surface comparisons, size, shape and weight relationships", in *Compact Heat Exchangers (Second Edition)*, J. E. Hesselgreaves, R. Law, and D. A. Reay, Eds., Second Edition, Butterworth-Heinemann, 2017, pp. 129–155, ISBN: 978-0-08-100305-3. DOI: https://doi.org/10.1016/B978-0-08-100305-3.00004-5.

[6] K. Stone, "Review of literature on heat transfer enhancement in compact heat exchangers", Air Conditioning and Refrigeration Center, Tech. Rep., 1996.

[7] H. Fugmann, E. Laurenz, and L. Schnabel, "Multi-dimensional performance evaluation of heat exchanger surface enhancements", *energies*, 2019.

[8] M. Yilmaz, O. Sara, and S. Karsli, "Performance evaluation criteria for heat exchangers based on second law analysis", *Exergy int. J.*, 2001.

[9] M. Yilmaz, O. Comakli, S. Yapici, and S. O.N., "Performance evaluation criteria for heat exchangers based on first law analysis", *journal of enhanced heat transfer*, 2005.

[10] P. Miltén, I. Johnsson, A. Lundbladh, and C. Xisto, "Generalized Method for the Conceptual Design of Compact Heat Exchangers", *Journal of Engineering for Gas Turbines and Power*, vol. 146, no. 11, p. 111 018, Aug. 2024, ISSN: 0742-4795. DOI: 10.1115/1.4065922. [Online]. Available: https://doi.org/10.1115/1.4065922.

[11] A. Kays W.M. London, *Compact heat exchangers*. Scientific International, 2018.

[12] J. E. Hesselgreaves, R. Law, and D. A. Reay, "Chapter 6 - surface types and correlations", in *Compact Heat Exchangers (Second Edition)*, J. E. Hesselgreaves, R. Law, and D. A. Reay, Eds., Second Edition, Butterworth-Heinemann, 2017, pp. 221–274, ISBN: 978-0-08-100305-3. DOI: https://doi.org/10.1016/B978-0-08-100305-3.00006-9.

[13] F. Beltrame, P. Colonna, and C. M. De Servi, "Optimal design of aircraft thermal systems and their heat exchangers leveraging a data-driven surrogate model", *International Journal of Heat and Mass Transfer*, vol. 253, p. 127 502, 2025, ISSN: 0017-9310. DOI: https://doi.org/10.1016/j.ijheatmasstransfer.2025.127502.

[14] T. Cowell, "Comparison of compact heat transfer surfaces", *Journal of Heat Transfer*, 1990.

[15] P. LaHaye, F. Neugebauer, and R. Sakhuja, "A generalized prediction of heat transfer surfaces", *Journal of Heat Transfer*, 1974.

[16] J. G. Soland, J. Mack W. M., and W. M. Rohsenow, "Performance ranking of plate-fin heat exchanger surfaces", *Journal of Heat Transfer*, vol. 100, no. 3, pp. 514–519, Aug. 1978, ISSN: 0022-1481. DOI: 10.1115/1.3450840.

[17] N. Sahiti, F. Durst, and A. Dewan, "Strategy for selection of elements for heat transfer enhancement", *Int. J. Heat and Mass Transfer*, 2006.

[18] M. A. DIGIOVANNI and R. L. WEBB, "Uncertainty in effectiveness-ntu calculations for crossflow heat exchangers", *Heat Transfer Engineering*, vol. 10, no. 3, pp. 61–70, 1989. DOI: 10.1080/01457638908939709.

[19] M. Yousefi, R. Enayatifar, A. N. Darus, and A. H. Abdullah, "Optimization of plate-fin heat exchangers by an improved harmony search algorithm", *Applied Thermal Engineering*, vol. 50, no. 1, pp. 877–885, 2013, ISSN: 1359-4311. DOI: https://doi.org/10.1016/j.applthermaleng.2012.05.038. [Online]. Available: https://www.sciencedirect.com/science/article/pii/S1359431112004164.

[20] T. A. Khan and W. Li, "Optimal design of plate-fin heat exchanger by combining multi-objective algorithms", *International Journal of Heat and Mass Transfer*, vol. 108, pp. 1560–1572, 2017, ISSN: 0017-9310. DOI: https://doi.org/10.1016/j.ijheatmasstransfer.2017.01.031.

[21] K. Deb and H. Jain, "An evolutionary many-objective optimization algorithm using reference-point-based nondominated sorting approach, part i: Solving problems with box constraints", *IEEE Transactions on Evolutionary Computation*, vol. 18, no. 4, pp. 577–601, 2014. DOI: 10.1109/TEVC.2013.2281535.

[22] G. Xie, B. Sunden, and Q. Wang, "Optimization of compact heat exchangers by a genetic algorithm", *Applied Thermal Engineering*, vol. 28, no. 8, pp. 895–906, 2008, ISSN: 1359-4311. DOI: https://doi.org/10.1016/j.applthermaleng.2007.07.008.

[23] I. Das and J. E. Dennis, "Normal-boundary intersection: A new method for generating the pareto surface in nonlinear multicriteria optimization problems", *SIAM Journal on Optimization*, vol. 8, no. 3, pp. 631–657, 1998. DOI: 10.1137/S1052623496307510. [Online]. Available: https://doi.org/10.1137/S1052623496307510.

3

Compact Heat Exchanger for Airborne Thermal Systems, from Modeling to Design Guidelines

Il mondo è fatto di eventi, non di cose.

Carlo Rovelli

3.1. INTRODUCTION

A variety of methods for the design and performance analysis of heat exchangers have been proposed in the literature, each characterized by specific application domains, governing equations, computational complexity, and level of accuracy. The most detailed models, though also the most computationally demanding, are based on a fine discretization of the HX geometry in cells. These interconnected non-overlapping cells generally encompass portions of the flow paths on either the hot or cold streams, or the wall material separating them. Thanks to the discretization scheme, the differential equations of mass and energy conservation, and thermal energy transport within the heat exchanger can be approximated using numerical techniques, most commonly finite difference methods [1]. In contrast, the momentum conservation equation is commonly replaced by analytical formulations that incorporate empirical coefficients to relate pressure drop to flow velocity. These complex models are rarely used for the preliminary design of HXs, as this task would require the iterative solution of a large nonlinear system of equations.

Preliminary HX sizing is, instead, typically carried out using analytical formulations obtained by integrating the governing differential equations for fluid flow and heat transfer under simplifying assumptions (e.g., constant specific heat, absence of phase change) and for specific flow configurations (e.g., counterflow, parallel flow). For such a reason, these analytical formulations may be referred to as integral methods. Among the most commonly adopted approaches of this type are the mean logarithmic temperature difference (LMTD) approach, the effectiveness-Number of Transfer Units ($\epsilon - NTU$) method, and its $P - NTU$ variant, which was developed specifically for shell-and-tube HXs [2]. These three methods are essentially equivalent, as they are derived from the same governing equations under identical simplifying assumptions, namely: the fluid properties and the overall heat transfer coefficient are assumed constant throughout the entire heat exchanger, or at least within the portion being analyzed, and heat conduction along the flow direction in both the fluids and the exchanger walls is considered negligible. Moreover, as in other modeling approaches, flow maldistribution effects and thermal losses towards the environment are neglected. The primary differences among these methods lie in the required inputs and the choice of the process quantity used as the iteration variable in the solution procedure.

More in detail, the LMTD method requires both the inlet and outlet temperatures of the hot and cold streams as inputs and allows for the explicit calculation of the heat transfer area given the HX heat duty, provided that an estimate of the global heat transfer coefficient U is available. For flow arrangements other than the parallel-flow or counterflow configurations, for which closed-form analytical expressions are available, the LMTD must be corrected by a factor F to account for the different temperature distribution within the HX. The values of F are mapped according to the flow arrangement as a function of NTU and the ratio between the heat capacity rates of the two streams (C^*). The LMTD approach is less suitable for off-design performance simulation, as, in this case, the outlet temperatures are unknowns of the problem. The presence of these variables in the LMTD expression complicates the numerical solution.

The $\epsilon - NTU$ method requires, as input, the inlet temperatures of the hot and cold streams and the target effectiveness of the HX. The NTU value corresponding to the tar-

get effectiveness (ϵ) is determined using specific functional relationships that depend on the flow arrangement and the ratio of the heat capacity rates. Once NTU is known, the required heat transfer area can be calculated based on an estimate of the overall heat transfer coefficient. A major limitation of the $\epsilon - NTU$ approach is that the definition of effectiveness depends on identifying the stream with the minimum heat capacity rate. If the heat capacity rates of the hot and cold streams are similar and their values change during the iterations of the calculation process, such as in off-design simulations, this dependence can lead to a shift in the stream with the minimum heat capacity rate, causing numerical instabilities. Such a limitation is addressed by the $P - NTU$ method, whose correlations between the temperature effectiveness P and the associated NTU are defined with respect to a fixed side of the HX [3].

The assumption of constant fluid properties and heat transfer coefficients does not hold if one of the two streams undergoes a phase change or is in a supercritical state near the critical point. Moreover, the functional relationships between the effectiveness and the number of transfer units are dependent on the flow arrangement and flow mixing conditions; therefore, for unconventional HX flow configurations, these correlations are often not available. These limitations have motivated the development of more sophisticated modeling methods that are independent of the flow arrangement and that account, to a certain extent, for changes in thermophysical properties as well as in flow conditions throughout the HX. The two predominant approaches in this context are the moving-boundary (MB) and finite-volume (FV) methods. In the moving-boundary method, the HX is divided into control volumes of variable size, whose boundaries align with the interfaces between the different phases of the working fluids. Each control volume spans both fluid sides of the HX, thus encompassing a specific combination of thermodynamic phases of the hot and cold streams. Conversely, in finite-volume-based methods, the heat exchanger geometry is often discretized into several fixed-size control volumes or cells along the flow paths, irrespective of the phase boundaries [4]. In both approaches, the flow properties are assumed constant within each control volume.

Moving-boundary models generally require significantly less computational resources than those based on the finite-volume discretization approach, thanks to the use of fewer control volumes [5]. However, FV models may be more accurate for specific applications in which flow properties change significantly within the HX core, such as those involving working fluids in a state close to the critical point. Generally, FV methods are more flexible and less susceptible to convergence issues if compared to MB models, as shown in Ref. [6]. Convergence issues in the simulation of moving-boundary HX models are related to the sensitivity of the method to initial guess values [7] and to changes in the size of control volumes [4].

Bell et al. [7] proposed a generalized MB model capable of handling different combinations of fluid states on either side of an HX. The method leverages an initial pinch point analysis to avoid unfeasible temperature distributions and enhance convergence. However, the proposed MB model has the following limitations: (i) it does not account for the effect of pressure drop on enthalpy and the corresponding temperature variation during phase change, (ii) it is limited to sub-critical fluid states, and (iii) it cannot be used in the case of fluid mixtures. Kim et al. [5] introduced a predefined distribution of enthalpy in each of the control volumes of a standard MB model to account for the tem-

perature glide in the two-phase region of a binary mixture and improve convergence. Although the modified MB model allows for capturing the non-linear temperature distribution, its computational cost is almost three times that of a standard MB model, and its accuracy remains lower than that of finite volume-based models. Chu and Zhang [8] propose a moving boundary and finite volume coupling algorithm to combine the high computational efficiency of MB methods with the accuracy of finite volume methods such as those reported in Ref. [9] and [10]. In particular, in the method reported in Ref. [8], a finite volume discretization scheme is used to estimate the heat duty and flow property variation in each cell of the moving boundary model. The resulting hybrid model can effectively handle large variations in the fluid thermophysical properties, achieving an accuracy comparable to that of traditional finite volume methods while halving computational time for similar mesh sizes adopted with the two modeling approaches. However, the model is more than an order of magnitude slower than standard MB models. Illàn-Gòmez et al. [11] present a computationally efficient finite-volume discretization method for the rating of plate HX evaporators. Similar to the work documented in Ref. [12], each control volume is characterized by an imposed heat duty, ensuring that only one fluid phase is present within each volume. The model accounts also for the effect of pressure drop on the fluid temperature profile, and the solution is obtained by adapting the heat duty so as to match the total heat transfer area.

Based on the reviewed literature sources, it is possible to conclude that finite volume-based methods are the most accurate yet computationally expensive modeling approach, capable of dealing with multi-phase flow, fluid mixtures, and even supercritical fluid states, provided that the spatial discretization of the heat transfer device is sufficiently fine to resolve local property variations. Experimental validations of FV models showed that their accuracy is comparable to the uncertainty of the adopted heat transfer and pressure drop correlations [11]. However, most HX analysis methods (i) neglect the effect of pressure drop along the flow path, (ii) feature numerical solution methodologies tailored to specific HX topologies, and (iii) adopt control volumes of fixed size. These limitations have been partially addressed by recent studies such as those in Ref. [11] and [12]. These methods, however, have been developed for specific HX types, flow regimes, and relatively simple flow configurations.

In this context, the objective of the work documented in this chapter is to develop robust and computationally efficient heat exchanger models that are applicable to any HX type, while providing sufficient accuracy for preliminary design purposes. Moreover, the modeling approach should offer sufficient flexibility to adapt the design problem formulation to the specific requirements of the application of interest, for instance, by allowing for the selection of different combinations of design variables, constraints, and inputs. The chapter is structured as follows. Section 3.2 describes the modeling approach that is used for both the preliminary design and rating of compact HXs. The models leverage a discretization method based on enthalpy drops rather than cells of fixed size, and constitute the basis of the software tool *HeXacode*, as discussed in Section 1.5. The validation assessment of the modeling methodology is reported in Section 3.3, where the numerical predictions obtained using the rating tool implemented in *HeXacode* are compared against experimental data available in the literature. Subsequently, in Section 3.4, HX

preliminary design models are integrated within a system design optimization framework introduced in Ref. [13] for the assessment of combined cycle gas turbine systems for airborne applications. Optimal design guidelines for common compact HX topologies are identified and discussed in Section 3.5. Finally, Section 3.6 presents the application of the methodology discussed in Section 2.5 for the systematic comparison of compact HX topologies to select the most suitable geometry for an air-cooled condenser of an airborne energy harvesting system.

3.2. PRELIMINARY DESIGN METHODOLOGY

All models and methodologies developed for the sizing, rating, and optimization of heat exchangers – whether as standalone components or integrated within ram air ducts – have been implemented in Python language and incorporated into the in-house framework for HX simulation and preliminary design called *HeXacode*. This framework includes: (i) one- and two-dimensional finite-volume-based models for solving HX rating or sizing problems; (ii) single- or multi-objective optimization tools for identifying the optimal geometry or the set of Pareto optimal solutions for the given design specifications and constraints; and (iii) tools for design and off-design analysis of ram air ducts housing heat exchangers. This set of models and tools has been validated against data reported in the literature or predictions from other established software packages for HX design and performance simulation. The suitability of *HeXacode* for the design of HXs of airborne thermal systems has been demonstrated by using it, in combination with the ARENA framework – a multidisciplinary and modular simulation platform developed by the P&P group of Delft University of Technology for the preliminary design optimization of combined-cycle engines, as introduced in Sec. 1.2.4 – to assess the feasibility of ORC-based energy harvesting units aboard aircraft.

3.2.1. HEAT EXCHANGER BASE MODEL

The core structure of the HX models developed in this work is based on a two-dimensional discretization of the geometry into control volumes, or cells, characterized by a specific heat duty. Each control volume encompasses a portion of the hot and cold stream sides as well as the separating wall. Following a procedure similar to that of the FV–MB hybrid model reported in Ref. [8], the method begins by identifying the number of thermodynamic states within the HX. For each combination of fluid phases on either side of the HX, a moving boundary cell is defined, each characterized by a specific heat duty. If no phase change occurs, a single MB zone is defined. In contrast, for a condenser or evaporator, three MB zones are typically considered. These encompass the superheated vapor, two-phase flow, and subcooled liquid regions within the HX.

Each MB zone is discretized into a user-defined number of control volumes (CVs). To each CV is assigned a fraction of the heat duty of the MB zone. As shown in Figure 3.1, a single CV or cell "n" is characterized by two inlet and two outlet nodes for each fluid stream, and a "bulk" node to which the average fluid properties and the average wall temperature are assigned. In each cell, fluid properties vary only in the X and Z directions; therefore, they are assumed to be uniform along the transverse (Y) direction.

Mass, momentum, and energy equations are solved in each CV to determine: (i) the heat transfer area needed to satisfy the imposed local heat duty, and (ii) the pressure drop across the cell for each fluid stream. The solution of the resulting system of equations requires an iterative procedure in which the heat transfer area and fluid properties in each CV are recursively updated using the calculated values from the previous iteration.

The HX model also incorporates several conditional checks to ensure the reliability of the results. In particular, the minimum temperature difference between the two streams is verified in each control volume to prevent non-physical temperature distributions. Bounds are also imposed on flow velocity and pressure drop to ensure that the validity range of the adopted empirical correlations is not exceeded. Moreover, an adaptive relaxation factor is activated when the relative change in heat transfer area or pressure drop exceeds predefined thresholds, enhancing the robustness of the solution procedure and decreasing the required number of iterations. More specifically, the relaxation factor dampens the oscillations in the heat transfer area estimated by the numerical solution procedure for a specified heat duty.

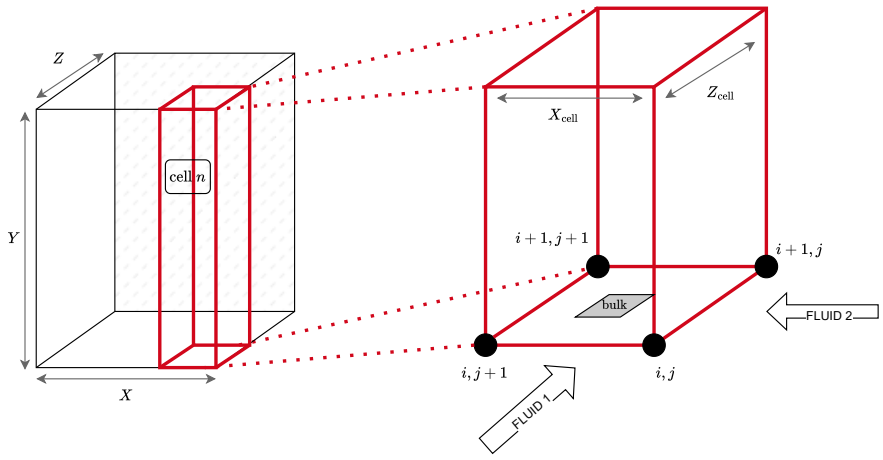

Figure 3.1: Sketch of the discretization approach of the HX core into cells or control volumes with a local cross-flow arrangement. The inlet nodes of fluid stream 1 or 2 are characterized by the indices i or j, respectively. The outlet nodes of fluid stream 1 or 2 are instead denoted by $i+1$ or $j+1$. The average fluid properties and mean wall temperature are associated with the "bulk" node.

This modeling approach can be applied to both sizing and rating problems. In rating or off-design calculations, the heat duty is initially set as a guess. This value is updated in each iteration until the difference between the calculated and the specified heat transfer area of the HX falls below a prescribed threshold. For single-pass HXs, a uniform heat duty distribution is used as a first guess, whereas a logarithmic distribution is used for multi-pass counter-crossflow HXs. This approach ensures a higher discretization resolution only where it is most needed, namely in zones of the model domain with significant variations in thermodynamic properties. Traditional HX modeling methods typically partition the HX geometry using a uniform spatial discretization scheme. Thus,

the change in fluid properties across each CV may differ significantly. For example, consider a single-pass crossflow heater operating with a supercritical fluid. When a uniform spatial discretization scheme is adopted, the mean logarithmic temperature difference in each CV tends to diminish along the flow direction of the hot and cold streams: cells close to the HX inlets exhibit larger temperature differences and, consequently, higher local heat duties, while those in proximity of the outlet sections contribute less to the overall heat transfer. Since the thermophysical properties of supercritical fluids vary strongly with temperature, the calculations in the upstream cells are therefore affected by larger approximation errors than those closer to the HX outlets. By imposing a uniform heat duty across the control volumes, the approximation error associated with the averaging of the thermodynamic properties remains relatively consistent throughout the model domain. The drawback of this approach is that the heat transfer area varies in each CV. In multi-pass counter-crossflow configurations, the logarithmic heat duty distribution provides a more balanced allocation of the heat transfer area across the working fluid passes. Within each pass, the heat duty is then distributed uniformly, as in the case of single-pass HXs.

The fluid properties in each node (i, j) are evaluated using the appropriate thermodynamic equation of state, interfaced with the HX model through either the open-source software Coolprop [14] in the case of pure fluids, or a commercial software in the case of mixtures [15]. The average temperatures and pressures associated with the "bulk" node on each fluid side are instead computed as the arithmetic mean of the corresponding values at the inlet and outlet nodes of the cell. Local heat transfer coefficients and friction factors are computed using empirical correlations selected based on the fluid phase, flow regime, and the topology of the heat transfer area. Each correlation is valid over a specific range of flow and thermodynamic property conditions, typically defined in terms of Reynolds and Prandtl numbers, as well as of geometric parameters. For an overview of the correlations adopted in the studies documented in this thesis, the reader is referred to Appendix A.

The average heat transfer coefficients on the hot and cold sides of each control volume n, namely h_{h}^{n} and h_{c}^{n}, are used to compute the overall heat transfer coefficient, U_{h}^{n}. The definition of this quantity, taking as reference the heat transfer area of the hot side, reads

$$U_{\mathrm{h}}{}^{n} = \left(\frac{\alpha_{\mathrm{R}}}{\eta_{0,\mathrm{c}}^{n}\, h_{\mathrm{c}}^{n}} + \frac{1}{\eta_{0,\mathrm{h}}^{n}\, h_{\mathrm{h}}^{n}} + \hat{R}_{\mathrm{W}}\, \alpha_{\mathrm{h,W}} \right)^{-1}, \tag{3.1}$$

where α_{R} is the ratio between the hot and cold side heat transfer area compactness, $\eta_{0,c}$ and $\eta_{0,h}$ are the cold and hot side surface efficiencies, $\alpha_{\mathrm{h,W}}$ is the ratio of the hot side to wall heat transfer area, and $\hat{R}_{\mathrm{W}}$ is the wall thermal resistance, estimated as shown in Ref. [16]. The surface efficiencies in equation 3.1 are calculated as follows

$$\eta_0 = 1 - \frac{A_{\mathrm{e}}}{A}(1 - \eta_{\mathrm{f}}), \tag{3.2}$$

in which A_{e} is the extended area on the considered HX side, and η_{f} is the fin efficiency. Assuming uniform thickness, an adiabatic tip, and a constant rectangular cross-section

for the heat conduction path, the efficiency of a thin fin can be estimated as

$$\eta_f = \frac{\tanh(m\, l_f)}{m\, l_f} \tag{3.3}$$

with

$$m = \sqrt{\frac{h\, P_{x,f}}{k_{st} A_{x,f}}}\,. \tag{3.4}$$

In the expression above, h is the heat transfer coefficient, k_{st} is the conductivity of the fin material, and l_f is the fin length along the heat conduction path, which is, for instance, equal to half the fin height for fins placed between two primary surfaces [3]. The ratio of the perimeter $P_{x,f}$ over the cross-sectional area $A_{x,f}$ can be expressed as

$$\frac{P_{x,f}}{A_{x,f}} = 2\left(\frac{1}{t_f} + \frac{1}{F_d}\right). \tag{3.5}$$

For thin fins, namely those exhibiting a depth (F_d) much larger than the thickness (t_f), the ratio of the perimeter over the cross-sectional area is approximately equal to two times the inverse of the average fin thickness.

Given the chosen convention for the global heat transfer coefficient, the heat transfer area of each CV can be calculated as

$$A_h^n = \frac{Q^n}{U_h^n\, F^n\, \Delta T_{lm}^n}, \tag{3.6}$$

where Q^n is the heat duty in the CV of interest, $\Delta T_{lm}{}^n$ is the local mean logarithmic temperature difference

$$\Delta T_{ml}^n = \frac{(T_h^i - T_c^{j+1}) - (T_h^{i+1} - T_c^j)}{\ln(T_h^i - T_c^{j+1}) - \ln(T_h^{i+1} - T_c^j)}\,, \tag{3.7}$$

and F^n is its correction factor, which, in turn, is estimated depending on the local effectiveness, flow arrangement, and heat capacity ratio [1]. Note that F^n is lower than unity for any flow arrangement different from pure counterflow. In condensers and evaporators characterized by relatively small pressure drops, the heat capacity ratio is equal to 0, and $F^n \to 1$ regardless of the flow arrangement. Furthermore, estimating F^n is unnecessary if the HX is subdivided into multiple control volumes. As the number of control volumes n increases, the temperature difference between the inlet nodes $(i,\, j)$ and outlet nodes $(i+1,\, j+1)$ on each fluid side decreases. As demonstrated in Appendix C, by decreasing the effectiveness of each control volume, the differences between the logarithmic mean temperature difference and the true mean temperature difference between the two fluid streams are reduced. Consequently, the correction factor approaches unity [3].

Accurate evaluation of the heat transfer and pressure drop coefficients in the CVs may require knowledge of the wall temperature. Assuming no fouling, the wall temperature in each control volume can be estimated as

$$T_{\mathrm{w}}^{n} = \frac{(\eta_0 hA)_{\mathrm{h}}^{n}\, T_{\mathrm{h}}^{n} + (\eta_0 hA)_{\mathrm{c}}^{n}\, T_{\mathrm{c}}^{n}}{(\eta_0 hA)_{\mathrm{h}}^{n} + (\eta_0 hA)_{\mathrm{c}}^{n}}. \tag{3.8}$$

Note that in Equation 3.8, the effect of wall conduction is assumed to be negligible. This assumption is valid for the majority of applications, as R_{W} is usually 2 to 5 orders of magnitude smaller than the thermal resistance on either of the fluid sides [16].

The solution of the preliminary design problem of an HX involves an iterative procedure in which the heat transfer area in each CV is recalculated until the relative difference between two successive iterations falls below a specified threshold, set by default at 1%. Once convergence is achieved, the model returns the overall pressure drops on both fluid sides, the HX size, the mass of the dry HX, and that of the working fluid during operation. This last quantity is computed by adding together the fluid inventory in each CV, namely

$$M_{\mathrm{wf}} = \sum_{n=0}^{N_{\mathrm{cv}}} \left(A_0^{n}\, \Delta x^{n}\, \frac{\rho_{\mathrm{node}}^{n} + \rho_{\mathrm{node}}^{n+1}}{2} \right), \tag{3.9}$$

where Δx^{n} denotes the length of the control volume n along the flow direction of the stream of interest, and N_{cv} is the total number of control volumes.

3.2.2. FROM HEAT TRANSFER AREA TO HEAT EXCHANGER GEOMETRY

The previous section describes the methodology used to determine the heat transfer area that is required to exchange a given heat duty. However, depending on the selected compact HX topology and application, various geometric parameters can be adjusted to meet the heat transfer area requirement. The possible options included in the preliminary design method used in this work are described in the following.

FIXED FRONTAL AREA

With this option, the height (Y) and width (X), which define the HX frontal area ($A_{\mathrm{fr}} = X\ Y$), are specified as inputs, while the core depth (Z) is calculated to meet the design specifications. For topologies in which the working fluid flows through flat tubes with internal microchannels, such as the one schematically represented in Figure 3.2, the core depth is calculated as

$$Z = (t_{\mathrm{mc}} + n_{\mathrm{mc}}(w_{\mathrm{mc}} + t_{\mathrm{mc}}))\,(1 + \tilde{x}_l (N_{\mathrm{z}} - 1))\,, \tag{3.10}$$

where n_{mc} is the number of microchannels of width w_{mc} within a flat tube, t_{mc} is the thickness of the material separating the microchannels, N_{z} is the number of flat tube ranks along the main flow direction of the stream outside the flat tubes, and $\tilde{x}_{\mathrm{l}}$ is the ratio of the longitudinal pitch between two ranks (x_{l}) to the flat tube width.

The second bracketed term in Equation 3.10 is typically equal to unity, as single-rank configurations are common in flat-tube microchannel heat exchangers. The required

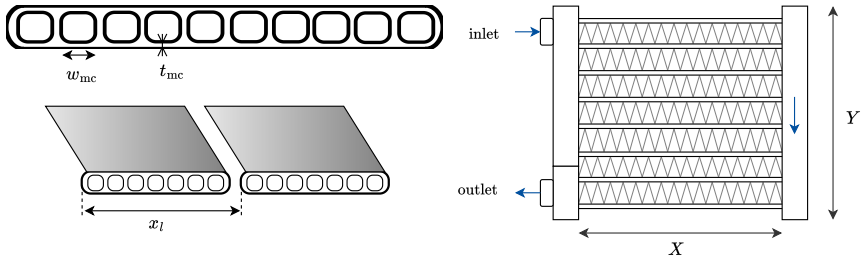

Figure 3.2: Schematic representation and geometric parameters of a flat-tube and microchannel heat exchanger core with two working fluid passes. The geometric details of the fins are omitted for clarity.

heat transfer area, taking as reference the working fluid side, can be achieved either by varying the number of microchannels within the flat tubes, calculated as

$$n_{mc} = \frac{T_p \left(\sum_{n=0}^{N_{cells}} A_{wf}^n \right)}{X \, (Y + T_p) P_{mc}} \tag{3.11}$$

where T_p is the pitch between flat tubes and P_{mc} is the perimeter of each microchannel, or by adjusting the width of the individual microchannels (w_{mc}). If the microchannels have a rectangular cross-section, w_{mc} is given by

$$w_{mc} = \frac{T_p \left(\sum_{n=0}^{N_{cells}} A_{wf}^n \right)}{2X \, (Y + T_p) \, n_{mc}} - h_{mc}, \tag{3.12}$$

with h_{mc} indicating the microchannel height.

In the case of tube-bundle HXs, the required heat transfer area in each fluid pass is achieved by adjusting the number of tube ranks (indicated with n_z in Figure 3.3) along the direction normal to the frontal area. This is done using Equation 3.11, substituting n_{mc} with n_z. The tube bundle core depth is then calculated as

$$Z = d_o + x_l \left(\sum_{n=0}^{N_p} n_z^n - 1 \right), \tag{3.13}$$

where d_o is the outer tube diameter, N_p is the number of working fluid passes, and x_l is the longitudinal pitch between tubes.

The frontal area on the air or gas stream sides is typically maximized to make full use of the available space. This is particularly well-suited for airborne applications, where spatial constraints, weight, and gas-side pressure drops are critical aspects. Opting for the maximum frontal area allows for either (i) minimizing the mean core velocity, and thus the pressure drop, for the chosen geometry, or (ii) maximizing the mass flow rate for a prescribed pressure drop. The benefit of higher mass flow rates is an increased temperature difference between the two streams, which reduces the required HX effectiveness, thereby lowering weight.

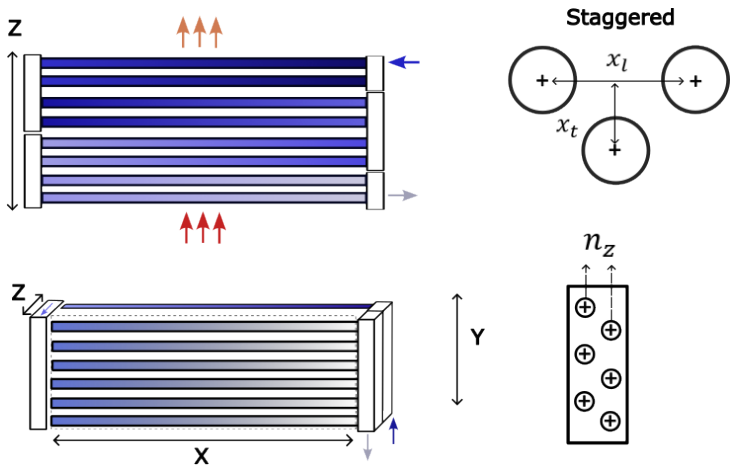

Figure 3.3: Sketch of a four-pass counter-crossflow tube bundle heater with a staggered tube arrangement.

VARIABLE FRONTAL AREA

In this case, the height Y and depth Z of the heat exchanger are prescribed. For flat tube micro-channel HXs, this corresponds to specifying the frontal area on the working fluid side. The required heat transfer area is then achieved by adjusting the core width X as

$$X = \frac{T_\mathrm{p}\left(\sum_{i=0}^{N_\mathrm{cells}} A_\mathrm{h}^n\right)(w_\mathrm{mc} + t_\mathrm{mc})}{P_\mathrm{mc}\ Y\ (Z - t_\mathrm{mc})}. \tag{3.14}$$

The same relation can be adopted for bundles of circular tubes, by replacing w_mc and t_mc with the internal diameter d_i and tube thickness t_t, respectively.

Choosing the core width as the dependent variable offers the advantage of precisely matching the required heat transfer area, avoiding the inaccuracies introduced by rounding the number of tubes. However, this choice can lead to numerical instabilities, as the convergence of the iterative calculation procedure for the heat transfer area is highly sensitive to the first guess of the frontal area. Such a sensitivity is amplified in design problems in which the overall heat transfer coefficient is primarily determined by the characteristics of the stream flowing over the tubes.

STRUCTURAL DESIGN

The structural design of the HXs is treated in a simplified manner, primarily focusing on calculating the metal thickness of the interface between the hot and cold streams to withstand internal pressure, as the main objective is to provide a realistic estimate of the weight of these components. In this regard, the total mass of an HX comprises the mass of the dry core, the working fluids, structural stability elements, and the casing. This last element consists of metal plates positioned around the core to increase structural integrity. Additional structural reinforcement elements, typically simple metal plates, may be positioned within the HX core, particularly in plain tube bundle topologies. Besides providing additional structural integrity, these elements prevent uncon-

trolled flow-induced vibrations, which can occur even at relatively low velocities and pose a serious risk of damage to HXs.

More in detail, in the case of tube bundle HXs, it is possible to distinguish between two scenarios depending on the so-called critical velocity u_{crit}. In the first scenario, vibrations induced by turbulence and vortex shedding occur at velocities lower than u_{crit}. These vibrations are normally highly irregular in space and time, and their amplitude is small [17]. As the flow speed through the tube bundle increases and reaches u_{crit}, a transition to an instability regime may occur: the aerodynamic forces that are proportional to the amplitude of the tube oscillations prevail over the mechanical stiffness of the tube, leading to destructive whirling vibrations [18]. The critical velocity can be estimated following the methodology reported in [19]:

$$u_{\text{crit}} = \frac{n_{\text{pt}}^2 {\lambda_i}^2}{2\pi X^2} \sqrt{\frac{E\, I_{\text{t}}}{m'_{\text{t}}}}\, d_{\text{o}} K \sqrt{\text{MDP}}, \tag{3.15}$$

where λ_i is the eigenvalue associated with the first vibration mode, E is the Young modulus of the tube material, and I_{t} is the tube moment of inertia considering it filled with the working fluid. Similarly, m'_{t} is the mass per unit length of a tube filled with fluid, while MDP and K are the mass damping coefficient and the fluid elastic instability constant. Guidelines for the estimation of these two coefficients are reported in Ref. [20] and [21]. A simple yet effective solution to mitigate flow-induced vibrations is to reduce the unsupported length of the tubes by positioning n_{pt} structural plates that limit the tube oscillations in the radial direction. These plates, typically 0.5 mm thick, are evenly distributed along the tube length (X). The number of plates is selected such that the critical velocity exceeds the maximum local flow velocity through the tube ranks by a factor of at least 1.5.

3.3. MODEL VALIDATION

The HX modeling approach was validated with experimental data from two test cases available in the open literature. The outcome of this comparison is summarized in Table 3.1. The choice of heat transfer coefficient and friction factor correlations used in the two HX models depends on the specific heat transfer topology. For this information, the reader is referred to Appendix A. The first test case deals with the simulation of a single-pass air-cooled plain tube bundle HX, in which water circulates within the tubes. The micro-tubes are arranged in a staggered layout. The airflow was varied in the experiment in a range corresponding to a Reynolds number from approximately 250 to 550, while the flow conditions on the water side were kept constant [22]. The measurement uncertainties associated with the pressure drop and heat duty are $\approx 2.5\%$ and $\approx 3\%$, respectively. The deviations between the experimental data and the HX model implemented in *HeXacode* are comparable to the measurement uncertainties and well within the uncertainty of the friction factor and heat transfer correlations used; therefore, the accuracy of the model is deemed satisfactory.

The second validation case involves a two-pass flat-tube condenser with louvered fins. The working fluid R134a flows through microchannels of rectangular cross-section within the flat tubes, also referred to as ports. The experimental tests detailed in Ref. [23]

characterized the HX performance by measuring the working fluid outlet temperature, mass flow rate, and pressure drop for 14 different inlet conditions on both the air and refrigerant sides. More in detail, the inlet temperature of the air stream was varied between 308 K and 323 K with relative humidity ranging from 20% to 51%. The inlet temperatures on the refrigerant side varied from 357 K to 368 K, while the inlet pressure varied from 1.3 to 2.1 MPa. The measurement accuracy of the air velocity is ±5%, while the accuracies of the refrigerant pressure and mass flow rate measurements are ±2% and ±3.4%, respectively. Considering these measurement uncertainties, which affect the values of the input variables of the HX model, the *HeXacode* model is deemed very accurate as the maximum relative error found between the numerical and the experimental data is lower than ±3.5%.

Geometry (layout)	Type & fluids	Ref.	Compared quantities & related maximum error (δ)
plain tube bundle staggered arrangement (single pass)	Cooler water-dry air	[22]	$\frac{\delta \Delta P_a}{\Delta P_{a,ref}} \leq 4\%$, $\frac{\delta \dot{Q}}{\dot{Q}_{ref}} < 5\%$
flat tube microchannel with louvered fins (multipass)	Condenser R134a - humid air	[23]	$\frac{\delta \Delta P_a}{\Delta P_{a,ref}} \leq 3.5\%$, $\frac{\delta \dot{Q}}{\dot{Q}_{ref}} \leq 2\%$, $\delta T_{wf,out} \leq 1.2°$

Table 3.1: Overview of the comparison between the reference experimental data and the predictions obtained using the heat exchanger model implemented in *HeXacode*.

3.4. HEAT EXCHANGERS FOR CC-ENGINE CONCEPTS

The HX models developed in this work were integrated into a system design optimization framework to assess the feasibility of organic Rankine cycle turbogenerators for waste heat recovery from gas turbines for propulsion and power generation aboard aircraft. As mentioned in Section 1.2.4, a system that combines a gas turbine with an ORC unit for aerospace applications is referred to as a CC-engine. Three different CC-engine concepts were analyzed. For each concept, a design problem was solved by performing the simultaneous optimization of the design variables of the ORC unit, the gas turbine, and the propulsion system, with the objective of minimizing fuel consumption over the intended aircraft mission. These three cases are briefly outlined in the following subsections, focusing on the obtained optimal system configurations and the corresponding HX designs.

3.4.1. CC-APU

This case study deals with the design of a combined-cycle auxiliary power unit (CC-APU) for providing secondary power to an Airbus A320 neo aircraft during on-ground operation [24]. The CC-APU features a supercritical organic Rankine cycle (ORC) waste heat recovery (WHR) unit that harvests thermal energy from the APU exhaust gases. The proposed CC-APU concept, illustrated in the process flow diagram in Figure 3.4, is analyzed using a multidisciplinary design optimization framework that incorporates

reduced-order models of the aircraft, gas turbine, and ORC system. The objective of the design optimization is to minimize the overall fuel needed aboard the aircraft to complete a 600 NM mission, while ensuring that the CC-APU meets secondary power demands during ground operations.

The ORC unit operates with cyclopentane as the working fluid. Its main components include a turbogenerator, a pump, a primary HX that transfers thermal energy to cyclopentane at supercritical pressure, and a condenser equipped with a fan. The fan is installed in a pusher configuration to reduce fan power consumption. Figure 3.5 shows the chosen layout and topology for both the supercritical evaporator, or primary HX, and the condenser.

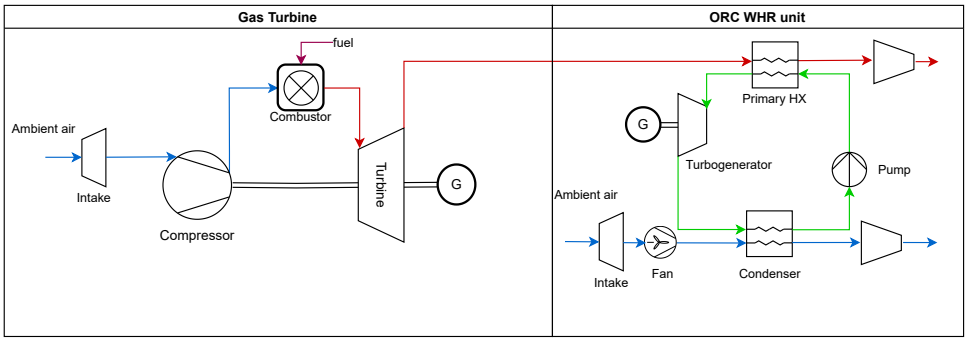

Figure 3.4: Process flow diagram of the CC-APU system concept (adapted from Ref. [24]).

The choice of a multi-pass layout and a bare-tube-bundle topology for the primary HX is motivated by (i) the better thermal match between the heat source and the working fluid [25], (ii) good fouling resistance, and (iii) low weight. The primary HX is positioned downstream of the turbine diffuser and is thus exposed to high-temperature exhaust gases. The selected material for this HX is the Nickel-base alloy *Hastelloy X*, based on thermal and mechanical considerations reported in Ref. [26, Ch.5]. The in-line tube layout is preferred over the staggered one because preliminary system design runs showed that minimizing pressure drops in the engine exhaust gases is essential for achieving high overall combined-cycle efficiencies, despite in-line tube bundle HXs tend to be heavier than their staggered counterparts for the same frontal area. The optimization variables associated with this HX topology are the dimensionless transversal ($\tilde{x}_t$) and longitudinal ($\tilde{x}_l$) pitches between tubes and the number of working fluid passes (N_p). The dimensionless tube pitches are defined as the ratio between the pitch in the considered direction and the tube outer diameter, which, in this case study, is fixed to 1.8 mm. This value of tube diameter represents a trade-off between the need for high levels of overall compactness ($\beta \geq 500$ m^{-1}) and manufacturability considerations. The pressure drop across the plain tube bundle topology is calculated based on the drag coefficient C_f per tube row [1, Part L]. The heat transfer coefficient on the hot gas side is estimated from the dimensionless pressure drop as shown by Martin [27]. For the working fluid side, the pressure drop inside the tubes is estimated using the friction factor

correlation of Brkić [28] while the Nusselt number of the supercritical fluid is calculated using correlations developed by Pioro and Mokry [29].

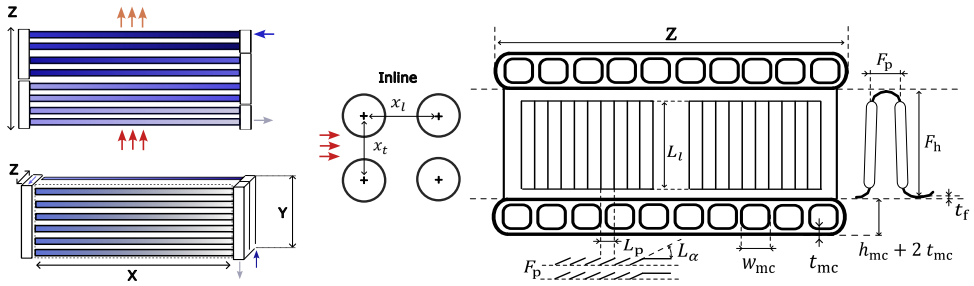

(a) Multi-pass inline bare tube bundle primary HX (b) Flat tube microchannel louvered fin condenser

Figure 3.5: Schematic representation of the adopted primary HX topology (a) and condenser topology (b).

The condenser is a flat-tube microchannel HX equipped with louvered fins. The working fluid passes through small rectangular channels embedded within the flat tubes, while air flows externally through the multi-louvered fins. The louvered-fin topology generally allows for high HX compactness and enhanced heat transfer coefficients by promoting boundary layer disruption and renewal [30]. These characteristics make such a fin topology particularly suitable for applications in the automotive and aerospace sectors, where compactness and weight reduction are critical design requirements. However, the mentioned performance benefits come at the cost of increased pressure losses relative to plain-fin designs, due to repeated flow redirection and mixing induced by the louvers [3].

Regarding the condenser design, the pitch between two microchannels (w_{mc}) is fixed to match the height of the flat-tubes h_{mc}, which measures 2 mm. The louver fin angle L_α is set to 27°, while the flat-tube length is equal to the condenser core depth Z_{cond}, which serves as an optimization variable in the preliminary design. Similarly, the louver pitch L_p is set equal to the fin pitch F_p, which is also an optimization variable. The louver length L_l is taken equal to 80% of the fin height F_h, which is another optimization variable. The thickness of the fins t_f is set to 0.11 mm, while the flat-tube wall thickness t_{mc} is 0.2 mm. These geometric parameters have been selected based on engineering judgment and considerations related to HX manufacturability. The height of the condenser Y_{cond} is fixed at 1.0 m based on the available space in the APU compartment [24]. Conversely, X is a degree of freedom in the system design. The material selected for the condenser is an aluminum alloy of the 3000 series, as recommended by an HX manufacturer [31]. In the de-superheating and subcooling zones within the microchannels, the heat transfer coefficient is estimated using the correlation for turbulent flows of Whitaker [32] with a correction factor for temperature-dependent effects [33]. The pressure drop is calculated using laminar or turbulent flow friction factors as shown in Ref. [1, Chapter L1]. For the condensing region, the local heat transfer coefficient is estimated using correlations for internal condensation in horizontal tubes for annular film flows [3, Table C.2], while the Müller-Steinhagen & Heck (MSH) model [34] is used to estimate the pressure drop per unit length. On the cold air side, the heat transfer and friction factor coeffi-

cients are estimated using the correlations by Chang and Wang [35] and Chang *et al.* [36] for multi-louver fin geometries.

The system-level optimization results indicate that the CC-APU achieves an overall efficiency of 34%, representing a 7% improvement over the baseline 250 kW GTCP36-300 APU. The ORC unit supplies 63 kW of the required 250 kW net power output, enabling a reduction in the overall fuel consumption over the mission from 78 kg to 42 kg. When accounting for the additional 31 kg mass of the CC-APU, the net mission fuel savings amount to 0.6% of the overall fuel aboard the aircraft at the beginning of the mission [24]. The core of the CC-APU is smaller but features a higher turbine inlet temperature (TIT) and overall pressure ratio (OPR) compared to the baseline 250 kW GTCP36-300 APU.

This initial case study served both to gain insight into the specific challenges associated with airborne ORC systems and to test the optimization and simulation framework later applied to study more complex combined cycle engine concepts. In contrast to stationary applications, for which the main design objective is typically to maximize thermodynamic efficiency, the design of an ORC WHR unit for aerospace applications is primarily constrained by mass and volume limitations. The analysis identifies the maximum ORC temperature as the most influential design parameter affecting system performance. The choice of maximum pressure has a lesser impact given the chosen supercritical cycle configuration for the ORC unit: the thermodynamic gains associated with higher pressures are offset by increased pump power requirements.

The amount of heat rejected by the condenser is primarily constrained by size limitations, with the result that the amount of thermal energy recuperated from the APU is lower than potentially achievable. The pressure drop in the cooling air is indirectly limited through its impact on fan power consumption, which is penalized in the optimization process. The optimization algorithm consistently selects condenser configurations that utilize the maximum available frontal area, to (i) minimize airflow velocity and, consequently, pressure drop, and (ii) reduce the core depth Z, to which the air-side pressure drop is directly proportional. Analogously, the free-flow-to-frontal-area ratio on the air side is maximized to mitigate flow acceleration and reduce maximum velocity. This is achieved by decreasing the number of flat tubes, thereby increasing fin height. In contrast, the selected fin pitch value reflects a trade-off between competing aspects, namely the maximization of heat transfer area and heat transfer coefficient versus the minimization of pressure drop in the airflow. The condenser pinch point temperature difference significantly affects both the required heat transfer area and the cold-side pressure drop. More in detail, larger temperature differences between the cold and hot streams reduce the required heat transfer area, and thus the overall condenser size. However, to increase the condenser pinch point temperature difference, higher air mass flow rates are required. This, in turn, leads to increased airflow velocities and consequently higher cold-side pressure drops. Therefore, the optimization process identifies a value of pinch point temperature difference that balances these conflicting effects.

The evaporator design is primarily governed by the sensitivity of gas turbine efficiency to back pressure, which is directly influenced by the pressure losses in the exhaust duct. Consequently, the optimal evaporator configuration is selected to minimize

the pressure drop on the exhaust gas side while satisfying the constraint on maximum core depth. For the chosen inline plain tube bundle topology, this is achieved by reducing the size and intensity of the detached flow vortices behind each tube. The extent of these recirculation zones is primarily dictated by local flow velocity, which is minimized by selecting a transverse pitch (x_t) near its upper bound. However, the consequent reduction in vortex intensity lowers the heat transfer coefficient, thereby increasing the required heat transfer area. In contrast, larger values of longitudinal pitch enhance heat transfer at the expense of a larger pressure drop due to earlier flow reattachment before impingement on the next tube [37]. Given that the improvement in heat transfer is marginal compared to the pressure drop penalty, x_l is minimized. The number of working fluid passes (N_p) is selected based on a trade-off between maximizing the heat transfer area and limiting the working fluid pressure drop. In particular, by increasing N_p, the mean temperature difference between the two streams increases and the flow arrangement tends to approach the performance of a pure counterflow configuration, thereby reducing the total number of tubes required to achieve the target heat duty. However, fewer tubes per pass quadratically increase working fluid velocity, leading to a higher pressure drop and potential numerical convergence issues.

Finally, the evaporator pinch point temperature difference is maximized to reduce the required heat transfer area, thereby minimizing both component weight and gas-side pressure drop. Despite the larger value of pinch point temperature difference in the evaporator ($\Delta T_{pp,ev} = 47$ K) compared to the condenser ($\Delta T_{pp,cond} = 32$ K), the effectiveness of this component approaches 90%. Conversely, the effectiveness of the condenser is only $\approx 33\%$. The higher effectiveness of the evaporator is facilitated by the more favorable flow configuration, as a counterflow arrangement allows for a better match between the temperature profiles of the hot and cold streams than a pure crossflow configuration. This contributes to making the condenser approximately 1.6 times heavier than the evaporator, despite the density of the nickel-based alloy used for the evaporator being approximately three times that of the aluminum alloy of the condenser.

3.4.2. CC-TS

This case study is focused on the design of a combined-cycle turboshaft (CC-TS) engine supplying electric power to the under-the-wing distributed propulsion system of the ONERA Dragon aircraft [38]. The bottoming supercritical ORC unit harvests thermal energy from the exhaust gases of a turboshaft engine and converts it into additional shaft power. The process flow diagram of the CC-TS engine is shown in Figure 3.6. In this configuration, the thermal load associated with the condensation process of the ORC working fluid, i.e., cyclopentane, is rejected into ambient air using two identical condensers positioned inside ram air ducts integrated into the nacelle of the engine. The ducts have a rectangular cross-section and are placed symmetrically above and below the engine, as shown in Figure 3.7. The condensers are tilted with respect to the flow direction to minimize the nacelle cross-sectional area. Each ram air duct is comprised of a subsonic scoop-type intake, a diffuser, a section accommodating the inclined heat exchanger, and a convergent nozzle.

As in the CC-APU test case, the CC-engine simulation framework integrates models of the turboshaft engine, ORC thermodynamic cycle, ORC turbine, and heat exchangers.

In this study, the system model also incorporates a ram air duct model to account for the aerodynamic penalty associated with ram air usage and predict the flow momentum at the outlet of the duct nozzle. Key outputs of the ram air duct model are the intake drag and pressure recovery, which are primarily governed by the intake mass flow rate ratio (MFR). This quantity is equal to the intake area A_1 divided by the free stream tube area (A_0), as defined in Figure 3.7. Subsonic scoop intakes are usually designed such that for MFR ≈ 0.7 the pressure distribution around the intake lips creates a suction force equal to the drag introduced by the redirection of the airflow [39]. In such a condition, therefore, spillage drag is negligible. Lower values of MFR increase the isentropic compression of the airflow ahead of the intake, reducing the inlet Mach number and increasing internal pressure recovery. However, spillage drag increases almost quadratically for MFR < 0.7. The optimal MFR thus depends on a trade-off between internal and external duct losses. For this reason, MFR is included among the optimization variables of the engine, along with the diffuser area ratio (A_2/A_1) and the condenser tilt angle θ_{cond}. Together, these three variables govern the total pressure losses of the duct and the static pressure rise upstream of the condenser. A detailed description of the ram air duct model used to calculate the aerothermal performance of this key sub-system is provided in Chapter 5.

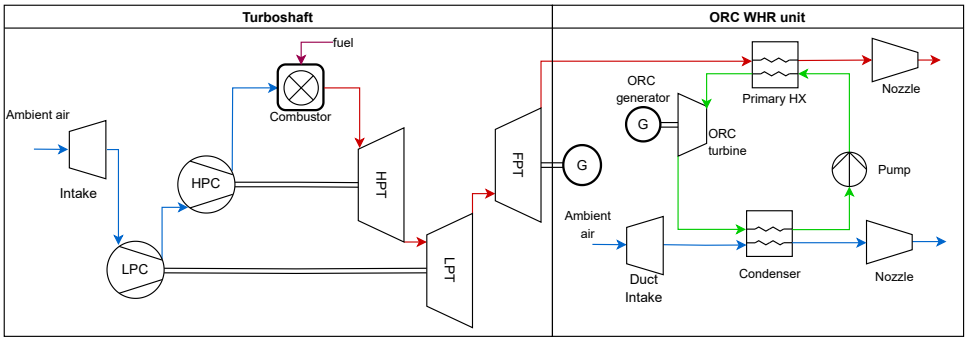

Figure 3.6: Process flow diagram of the CC-TS engine concept (adapted from Ref. [38]).

Regarding the HX models, these are analogous to those of the CC-APU test case. Moreover, the combination of design variables and fixed geometric parameters chosen for the evaporator and condenser is consistent with the choices made for the feasibility study presented in Section 3.4.1. The only exception is represented by the preliminary design methodology adopted for the condenser, which is sized by adjusting the core depth (Z) for a fixed frontal area $A_{\text{fr}} = X\ Y$ in place of the flat tube length X. This variable is included among the optimization variables, while the condenser height Y is fixed at 1.5 m, based on the estimated available space for the ram air ducts in the nacelle.

Optimization results show that replacing a conventional turboshaft engine with a CC-TS leads to a decrease in power-specific fuel consumption of 6.5 %. However, this results in a mission fuel mass reduction of 1.5% [38]. The limited fuel-saving potential of the CC-TS engine is due to the increase in the operating empty mass of the aircraft.

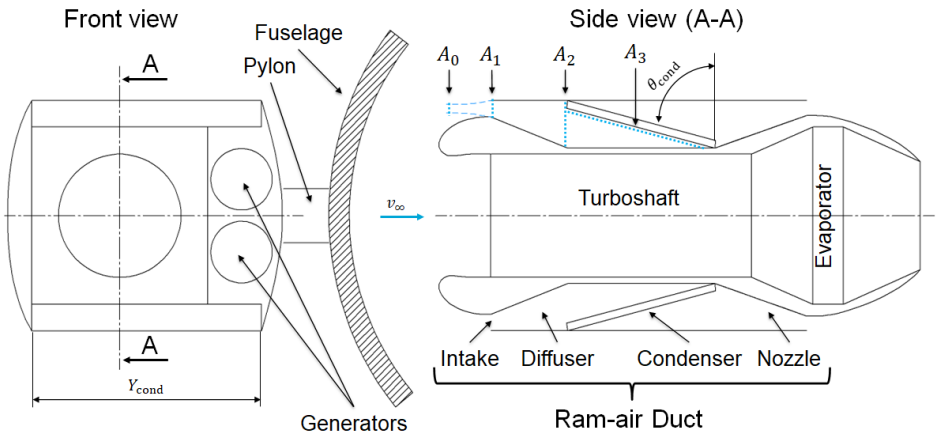

Figure 3.7: Schematic representation of the CC-TS engine concept and proposed arrangement of the main components within the engine nacelle mounted on a pylon at the aft of the aircraft. After Ref. [38].

Specifically, the CC-TS engine is heavier than the baseline turboshaft powertrain due to the additional weight of the ORC unit, which accounts for 15% of the overall CC-TS engine weight of 1710 kg. The overall aircraft takeoff mass remains nearly unchanged, as the fuel mass savings compensate for the added weight of the WHR system.

The study results also indicate that the aerodynamic drag caused by the ram-air ducts required to cool the ORC unit can be offset by the thrust resulting from the acceleration of the heated air stream in the outlet nozzle. This zero-drag condition can be achieved only for high-speed and high-altitude flight conditions, provided that both the HX geometry and ram air cooling system are optimized to minimize total pressure losses and maximize the temperature rise in the ram air stream across the condenser. Moreover, the optimal condensing temperature of the ORC working fluid corresponds to the value that best balances the trade-off between ORC unit efficiency and the increase in ram air temperature in the duct.

Heat exchangers emerge as the components that most affect the performance of the CC-TS engine. The primary HX design is optimized to minimize pressure losses in the exhaust duct, which directly penalize turboshaft thermal efficiency. In the optimal system design configuration, the primary HX introduces a pressure drop of about 2000 Pa, which corresponds to approximately 6% of the free power turbine exit pressure. The resulting penalty in gas generator performance is a decrease in thermal efficiency of approximately 1.2% of the efficiency of a gas generator without the pressure loss introduced by the primary HX. To mitigate pressure losses, flow acceleration in the HX is minimized by maximizing the transverse pitch of the tubes, while the longitudinal pitch is reduced to increase heat transfer area compactness. At the same time, the pinch point temperature difference is much higher than that of evaporators of conventional ORC systems for WHR applications. This is to reduce the required heat transfer area and thus mitigate HX weight and pressure drop, even at the cost of a decrease in the amount of thermal energy recovered from the exhaust gases. Other challenges associated with the primary HX, in

particular concerning its integration within the turboshaft exhaust path, are: (i) the limited available space to install a diffuser at the outlet of the power turbine, to sufficiently slow down exhaust flow velocity, and (ii) the non-uniformity of the velocity distribution at the primary HX inlet, which leads to decreased HX effectiveness and may cause tube vibrations, mechanical fatigue, and increased noise.

The condenser design is equally critical, as it directly impacts the internal losses within the ram-air ducts and consequently the pressure ratio across the duct nozzle. As already mentioned, the optimal geometry is that which minimizes the airflow velocity through the condenser core. This is achieved by maximizing the frontal area of the HX, as well as the fin height, which enables a reduction in the number of flat tubes. The fin pitch is instead minimized to enhance the compactness of the HX core. The benefit of such a design choice is a minimization of the condenser volume, which therefore reduces the depth of its core along the airflow direction. This reduction in the flow path length linearly reduces the pressure drop. The condenser is also inclined by 60 °with respect to the horizontal plane and is installed after a high-area ratio diffuser, which is designed to slow down the airflow and promote static pressure increase, while complying with the space limitations. At the same time, the ram air mass flow rate is minimized by adopting a large pinch point temperature difference in the condenser. This results in an increase in the minimum ORC temperature and consequently in a reduction in the efficiency of the WHR unit.

The study demonstrates that the fuel-saving potential of the CC-TS configuration is predominantly governed by the limitations associated with the performance of the HXs and their integration within the engine nacelle. Altogether, these limitations reduce the net power output of the ORC system during cruise to ≈ 6% of the total power demand. Moreover, such performance constraints are found to be largely independent of the choice of the working fluid, as demonstrated in Ref. [40]. Although some working fluids exhibit more favorable thermodynamic properties than cyclopentane, the improvement in ORC efficiencies they enable is counterbalanced by lower gas turbine performance and higher HX weight. For instance, replacing cyclopentane with toluene, which is characterized by a higher thermal stability than cyclopentane [41], enables a rise in the WHR unit cycle efficiency from 16.3% to 17.5% [40]. However, this gain comes at the cost of a 60% increase in condenser weight and a higher pressure drop in the exhaust gases, which reduces the gas turbine efficiency by 3.4 percentage points. As a result, the overall benefit of adopting toluene as the working fluid of the ORC unit translates into an increase in block fuel consumption of ≈ 0.6%. These findings underscore the strong interdependence between the overall performance of a combined-cycle engine, HX design, and their integration within the engine.

3.4.3. CC-TF

This case study is devoted to investigating the feasibility and potential fuel savings of a novel combined-cycle turbofan (CC-TF) engine concept consisting of a geared two-spool turbofan engine equipped with a bottoming ORC unit. The process flow diagram of this propulsion system concept is depicted in Fig. 3.8. The envisaged year for entry into service for the CC-TF engine is 2035, with the application being the same of the CC-TS engine: providing propulsive power to the ONERA Dragon aircraft [42].

To assess the proposed engine concept and the corresponding partial turboelectric propulsion system configuration, the ARENA multidisciplinary simulation framework is employed [13]. The overall system model integrates sub-models for the gas turbine, distributed propulsion architecture, ORC system, and aircraft, as well as the routines for the preliminary design of the heat exchangers and the turbofan bypass duct. The simulation framework is coupled with an evolutionary algorithm-based optimization routine to identify the propulsion system configuration that minimizes the fuel mass required for the aircraft mission.

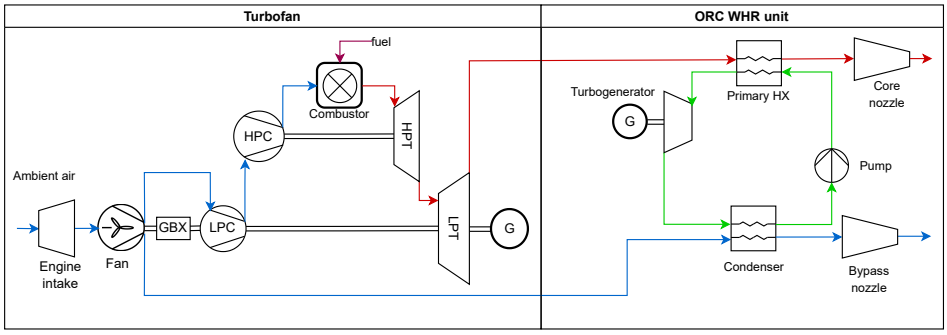

Figure 3.8: Process flow diagram of the CC-TF engine concept (adapted from Ref. [13]).

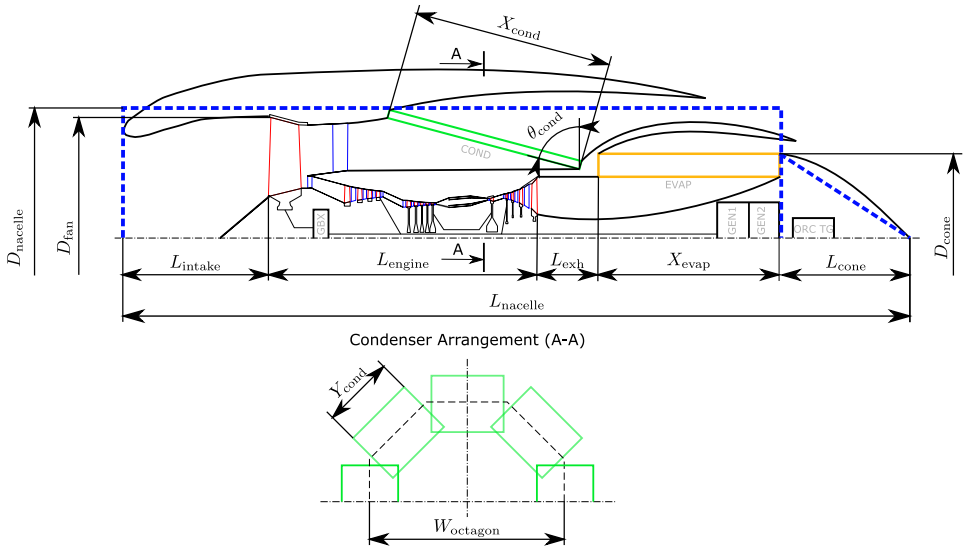

Figure 3.9: Schematic representation of the CC-TF engine concept and the condenser arrangement in the bypass duct (section view A-A). GBX: gearbox. COND: condenser of the ORC system. EVAP: evaporator of the ORC system. GEN: electrical generator. ORC TG: turbogenerator of the ORC system. The piping and feed pump of the ORC system are omitted. After Ref. [13].

Figure 3.9 illustrates the envisaged layout of the ORC system components within the

engine nacelle, which is mounted to the tail cone of the fuselage by means of a pylon. The evaporator, or primary HX, is positioned in an S-shaped annular duct downstream of the engine low-pressure turbine. The selected material and the combination of design variables and fixed geometrical parameters of the evaporator are identical to those adopted in the CC-TS study. However, the tube arrangement is adapted to fit the evaporator inside the annular duct. Specifically, the tubes are bent to conform to the radial curvature of the outlet section of the annular duct. Consequently, the evaporator can be defined as an annular-shaped multi-pass bare tube bundle HX. This configuration offers two advantages: (i) it maximizes the HX frontal area within the given nacelle diameter, and (ii) it allows for efficient integration of the electric generators inside the engine nacelle. Moreover, total pressure losses in properly designed S-ducts can be considered comparable to, or even smaller than, those in straight ducts [43]. All these aspects make annular-shaped HXs promising solutions for recuperated aero-engine configurations, as already recognized in Refs. [44], [45]. In the model, the exhaust flow at the evaporator inlet is assumed to have a uniform velocity and a direction normal to the HX frontal area. While this represents a simplification, the resulting underestimation of both the heat transfer area and gas-side pressure losses is deemed acceptable within the scope of a feasibility study.

A similar installation arrangement is used for the condensers, which are placed in the bypass duct. Instead of bending the flat tubes to match the shape of the bypass duct, eight identical condensers are arranged in parallel with respect to the working fluid flow path, occupying the duct cross-section in an octagonal pattern as illustrated in Figure 3.9. The condensers are rated for the same thermal power and are inclined at an angle θ_{cond} relative to the radial direction to augment the available HX frontal area. Each condenser core is composed of flat tubes with a wall thickness of 0.2 mm and containing square-shaped microchannels with a height of 1.6 mm. On the outside of the flat tubes, louvered fins of thickness equal to 0.20 mm are employed. A louver angle of 30 °is chosen to maximize the heat transfer rate per unit of core length, at the expense of higher friction coefficients. The fin length and the louver pitch are set to 90% of the fin height and fin pitch, respectively. All other geometric parameters, including the HX inclination angle θ_{cond}, are optimized. Finally, the condenser core is assumed to be made of an aluminum alloy of the 3000 series, as suggested by an HX manufacturer [31].

The results of the system optimization study indicate that the CC-TF configuration achieves mission fuel savings of approximately 4% compared to the benchmark turbofan engine. This is primarily attributed to:

1. *Waste heat recovery and gas turbine downsizing.* During cruise, the ORC unit generates 571 kW of net power, corresponding to 21.5% of the electric power output of a single CC engine. This additional power contribution enables a 36% reduction in the fuel mass flow rate consumed by the CC-TF gas turbine compared to the benchmark engine, allowing for a downsizing of the gas turbine. The smaller gas generator is 25% lighter than that of the benchmark engine, although it exhibits a thermal efficiency that is 8% lower. Moreover, the ORC unit contributes significantly to the engine mass, weighing 546 kg, approximately 30% of the overall CC-TF engine weight. The mass-specific power of the ORC system in this configuration is about 1 kW/kg.

2. *Improved Propulsive Efficiency.* The thermal power transferred by the ORC condenser to the bypass airflow increases the propulsive efficiency of the bypass duct by 13% and the specific thrust of the engine by 30% at cruise conditions compared to the benchmark engine. Note that the bypass propulsive efficiency is defined as the net thrust corresponding to the bypass stream divided by the fan power required to compress the air.

Heat exchangers are the main technological bottleneck to achieving higher system performance. The optimal ORC system features a net thermal efficiency of 17.7%. The primary HX recovers 71% of the thermal power available in the exhaust gases while introducing a pressure loss equivalent to 5% of the exhaust gas outlet pressure. The counter-crossflow arrangement of the primary HX enables a moderately high effectiveness of 80%, despite relatively large pinch point temperature differences ($\Delta P_{\text{pp,ev}} = 86$ K). In contrast, the condenser is characterized by a lower pinch point temperature difference ($\Delta T_{\text{pp,cnd}} = 29$ K) to maximize heat rejection, and a low effectiveness of 30% due to the unfavorable hot and cold stream temperature distribution caused by the crossflow arrangement. Due to the dominant contribution of the bypass stream to thrust generation, the condenser emerges as the most critical heat exchanger for system performance. To mitigate air-side pressure losses, the condensers are inclined at the maximum allowable tilt angle, i.e., $\theta_{\text{cond}} \approx 75°$, thus maximizing frontal area and reducing the air-side velocity through the HX core. As in previous case studies, the optimized condenser geometry reflects a trade-off between core compactness and the need to limit pressure losses in the bypass flow. In particular, the optimal design features large values of fin height and pitch to reduce the number of flat tubes and minimize the free flow to frontal area ratio of the cold stream.

Although the CC-TF engine achieves a 7% increase in overall propulsion system efficiency and a 6.3% reduction in TSFC at cruise, these performance gains are not realized at takeoff, as the ORC unit is arguably not operative during this phase of the mission. As a result, the gas generator of the CC-TF necessitates a 22% higher turbine inlet temperature (TIT) compared to a conventional turbofan engine to meet takeoff thrust requirements. This elevated TIT increases the amount of cooling air required to maintain the prescribed maximum material temperature within the high-pressure turbine. It follows that the turbine cooling system is over-sized for cruise operating conditions to a greater extent than in a conventional turbofan engine. This penalizes the CC-TF engine performance, including during cruise. Additionally, the CC-TF propulsion system is $\approx 30\%$ heavier than the benchmark engine.

3.5. DESIGN GUIDELINES

The performance of an HX is essentially determined by its core geometry. While the value of some parameters defining the core geometry can be selected based on prior knowledge or manufacturing constraints, others need to be optimized due to (i) their strong influence on the trade-off between thermal-hydraulic performance and size, including weight, and (ii) the interdependence between the optimal values of various geometric variables. The number and type of geometric variables that are critical for performance vary depending on the selected core topology, as discussed in the following.

MULTIPASS BARE TUBE BUNDLES

The performance of multipass bare tube bundles, featuring either inline or staggered circular tubes, is primarily governed by two key geometric variables: the transversal pitch and the longitudinal pitch. The number of passes (N_p) is also commonly included among optimization variables to adjust the flow velocity inside the tubes, thereby preventing excessive pressure losses or a reduction in the heat transfer coefficient on the inner side of the HX. Specifically, for a fixed heat duty, the optimal value of N_p tends to decrease as the mass flow rate inside the tubes is increased. This is because a lower number of passes allows for a larger free-flow area per pass and thus mitigates pressure drop. However, in the case of an evaporator or condenser, the influence of N_p on overall performance is typically minor compared to that of the tube pitches, due to the relatively small contribution of the working fluid side to the overall thermal resistance. The choice of tube diameter and thickness is instead straightforward in the context of aerospace applications: the optimal values for these parameters are typically those that minimize HX dimensions and weight, provided that the design complies with the limitations related to HX manufacturing and structural integrity.

To identify optimal design trends for the transverse and longitudinal tube pitches, a sensitivity analysis is conducted, in which the values of these parameters are systematically varied to assess their impact on pressure losses and weight of a multi-pass counter-crossflow tube bundle HX. The test case of this analysis concerns the preliminary design of the supercritical evaporator of the CC-APU unit described in Section 3.4.1. For simplicity, the number of passes and the frontal area are kept constant. Figure 3.10 shows the effect of the longitudinal and transversal dimensionless pitches on the thermal load per unit of HX mass and Euler number on each HX side, considering both inline and staggered tube arrangements. The Euler number is defined as the ratio of the pressure drop across an HX to the flow dynamic pressure at the inlet. The results indicate that increasing the transversal pitch leads to lower pressure drops on the hot gas side, regardless of the chosen tube arrangement. This decrease in flow resistance is attributed to the lower acceleration of the flow through the HX core, which results from the increased spacing between tubes. However, the corresponding reduction in flow velocity leads to a decrease in the heat transfer coefficient and thus the HX size and weight increase.

In contrast, the impact of the longitudinal pitch on HX performance varies depending on the tube layout. For the inline arrangement, lower dimensionless longitudinal pitch values promote lower hot side pressure drop and HX core volume, which are advantageous design features for airborne applications. At the same time, as the longitudinal pitch decreases, a larger portion of the tube area is immersed in the wake of the previous tube. This results in a slight drop in the heat transfer coefficient and an increase in core weight [37], especially for staggered tube configurations. A reduction in longitudinal pitch enables a significant enhancement of the heat transfer coefficient and increases the number of tubes per unit volume. The HX core then becomes substantially lighter and more compact. The higher heat transfer coefficient also allows for a reduction of pressure drop in the stream flowing around the tubes, as fewer tube rows are required to reach the targeted heat duty. Moreover, the Euler number of the stream inside the tubes decreases due to the higher flow velocity. It is important to note that the pressure

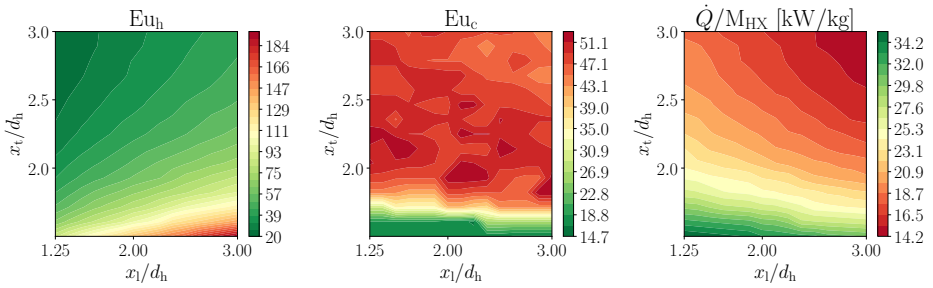

(a) Inline tube arrangement with $1.5 \leq x_t/d_h \leq 3$, and $1.25 \leq x_l/d_h \leq 3$

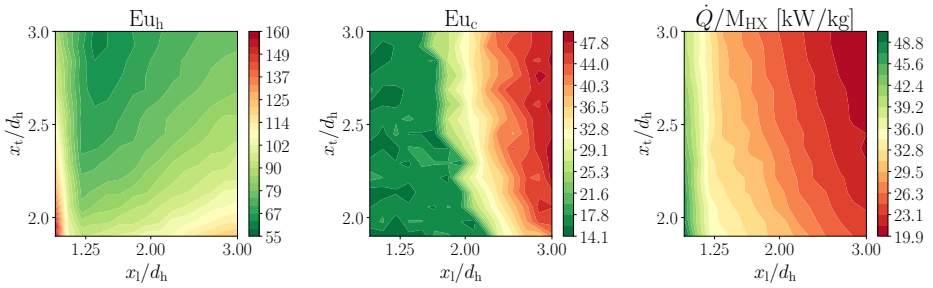

(b) Staggered tube arrangement with $1.8 \leq x_t/d_h \leq 3$, and $0.9 \leq x_l/d_h \leq 3$

Figure 3.10: Performance indicator charts for the counter-crossflow primary HX of the ORC unit described in Section 3.4.1, evaluated for a configuration with $N_p = 10$ working fluid passes. The performance indicators include the dimensionless pressure drops $\text{Eu} = \Delta P/(0.5\rho u^2)$ and mass-specific thermal power ($\dot{Q}/M_{\text{HX}}$). These quantities are presented as functions of transverse and longitudinal tube pitches (x_t/d_h, x_l/d_h).

drop on the external side of the tubes tends to reduce with lower longitudinal pitches only if this parameter remains in the range $1.25 \leq x_l/d_h \leq 3$. For values lower than 1.25, the intensity of the flow acceleration through the tube ranks increases sharply, causing a quadratic rise in pressure drop. In summary, the optimal longitudinal pitch value to minimize pressure losses on the outer side of the tubes is ≈ 1.25 outer tube diameters for both tube arrangements, while the optimal transversal pitch is approximately 3 outer tube diameters.

FINNED MICROCHANNEL HXS

The number of design variables associated with these types of HXs varies depending on the extended surface topology adopted on the gas side. For instance, the performance characteristics of offset-strip fins are governed by three key geometric parameters [46], while for louvered fins, 6 or 7 parameters are required, depending on the chosen heat transfer coefficient and friction factor correlations (see Refs. [35] and [47]). Figure 3.11 shows the main geometric parameters that define the geometry of microchannel HXs featuring either louvered or offset-strip fins.

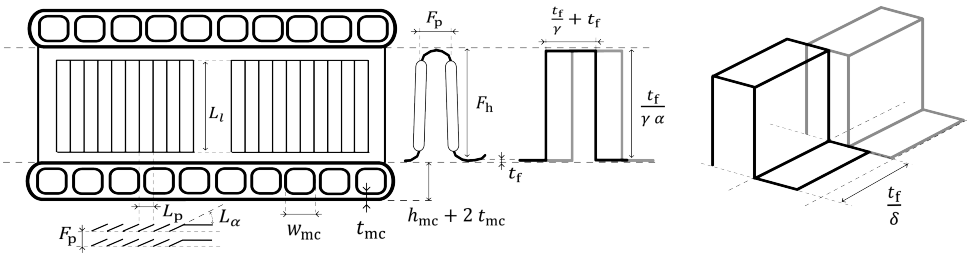

Figure 3.11: Sketch of a flat tube-and-microchannel HX core equipped with louvered or offset strip fins. The geometry of the offset-strip fins is conventionally defined by the following dimensionless parameters as shown in Ref. [46]: $\alpha = F_p/F_h$, $\delta = t_f/L_s$, $\gamma = t_f/F_p$.

Additional geometric parameters required to define the HX core geometry are those related to the microchannels within the flat tubes, namely the microchannel width (w_{mc}), microchannel thickness (t_{mc}), and flat tube height (h_{ft}). Regardless of the chosen fin topology, the number of design variables of finned microchannel HXs is much larger than that of bare tube bundles. Thus, conducting a thorough sensitivity analysis to identify optimal design trends for each geometric parameter is impractical. A more effective approach to obtain these trends is to formulate and solve a multi-objective optimization problem to identify a set of HX designs that minimize both weight and pressure drop on each fluid side, as suggested in Chapter 2. This optimization problem is formulated as shown in Equation 2.16. The selected case study concerns the design of the condenser of the CC-APU (see Section 3.4.1) for predefined operating conditions; in particular, the condenser is sized to reject 325 kW of thermal power into an airflow at 40 ° C. Three geometric constraints are imposed: the maximum width and height of the HX must not exceed 0.85 m, while the maximum core depth must satisfy $Z_{max} \leq 0.5$ m. Table 3.2 reports the lower and upper bounds of the optimization variables for the two fin topologies considered for the condenser, namely, louvered fins (lf) and offset-strip fins (osf). These bounds correspond to the range of values covered by the experimental datasets used for the development of the respective heat transfer and friction factor correlations (See Ref. [46], [35], and [36]). Both the fin thickness and the wall thickness of the flat tubes are kept constant at 0.11 and 0.2 mm, respectively.

Table 3.2: Lower and upper bounds of the optimization variables defining the geometry of the CC-APU condenser for each fin topology: louvered fin (lf) or offset-strip fins (osf).

		F_h	F_p	L_α	L_p	L_l/F_h	L_s	w_{mc}	h_{ft}
lf	x_D^L	5.0 mm	0.9 mm	10°	0.9 mm	0.7	-	1.0 mm	2.0 mm
	x_D^U	16 mm	3.6 mm	30°	3.2 mm	0.9	-	2.5 mm	2.5 mm
osf	x_D^L	3.8 mm	1.2 mm	-	-	-	2.5 mm	1.0 mm	2.0 mm
	x_D^U	10 mm	3.2 mm	-	-	-	6.0 mm	2.5 mm	2.5 mm

Figure 3.12 and 3.13 depict the Pareto surfaces resulting from the multi-objective design optimization of the condenser equipped with louvered fins and offset strip fins,

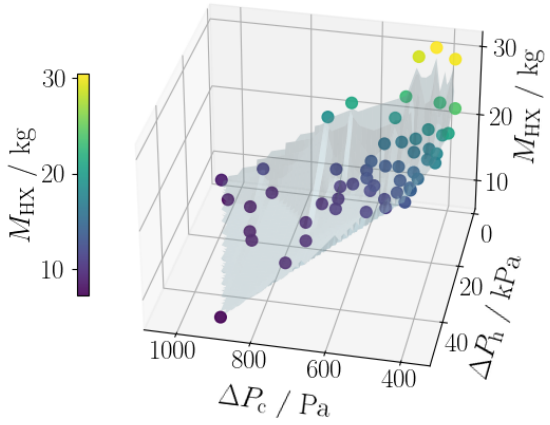

Figure 3.12: Pareto front of the design solutions obtained for the flat tube microchannel condenser with louvered fins.

respectively. In both cases, the Pareto fronts show that the minimum HX mass is significantly influenced by the cold side pressure drop targeted in the design, whereas the pressure drop on the working fluid side (ΔP_h) has a comparatively minor effect on the core weight, except for design solutions enabling low values of ΔP_c. This indicates that ΔP_c is a critical performance metric, while the hot side pressure drop can be treated as a design constraint. Imposing an upper limit on ΔP_h does not significantly affect the characteristics of the optimal geometries on the fin side, but it facilitates the identification of an optimal trade-off between cold side pressure drop and HX mass.

Each optimal solution features a value of flat tube height (h_{ft}) close to the lower bound defined for this parameter, indicating that h_{ft} can always be minimized, subject to manufacturability and mechanical strength requirements. Similarly, the optimal ratio between louver length and fin height is consistently around 0.9. In contrast, the optimal values of louver pitch (Lp) do not follow a specific trend and may be either greater or smaller than the fin pitch, regardless of the considered performance metric. Although the true optimal value of Lp can only be found via optimization, selecting $L_p \approx F_p$ typically yields HX designs with performance comparable to that of the optimized geometries. The remaining optimization variables, which are specific to each condenser topology, exhibit a strong correlation with one or two of the three objective functions. Design guidelines for these geometric parameters can be derived by calculating the Pearson correlation coefficient for each parameter-objective function pair. The computed coefficients are summarized in Table 3.3 for both condenser topologies. A performance metric is considered correlated with a geometric parameter if the absolute value of the correlation coefficient exceeds a predefined threshold, which in this case is set at 0.6.

Depending on which performance metric is prioritized (hot side pressure drop, cold

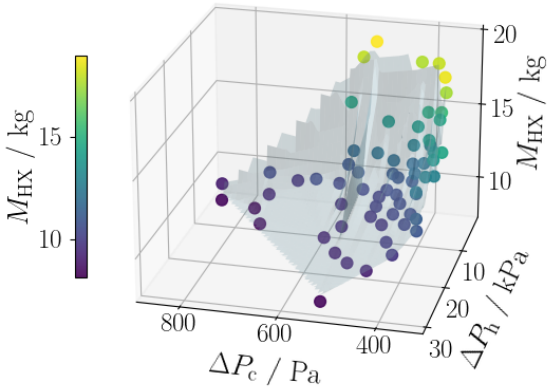

Figure 3.13: Pareto front of the design solutions obtained for the flat tube microchannel condenser with offset-strip fins.

Table 3.3: Pearson correlation coefficients for each performance metric - optimization variable pair.

	F_h (lf ; osf)	F_p (lf ; osf)	w_{mc} (lf ; osf)	L_s (osf)	L_α (lf)
ΔP_c	-0.75 ; -0.76	-0.62 ; -0.34	0.17 ; 0.39	-0.68	0.65
ΔP_h	0.12 ; 0.42	-0.63 ; -0.39	-0.77 ; -0.86	-0.28	0.37
M_{HX}	0.13 ; 0.06	0.92 ; 0.95	0.34 ; 0.14	0.60	-0.75

side pressure drop, or HX mass), the optimal geometry of the HX core can vary significantly. The following summary outlines the trends observed between the performance metrics and the optimal values of the variables defining the core geometry. These trends can serve as guidelines for optimizing the preliminary design of microchannel condensers equipped with louvered fins or offset-strip fins.

- If minimizing pressure drop on the fin side is the design priority (ΔP_c), optimal fin shapes are characterized by relatively high fin heights, which increase the spacing between the flat tubes and thus reduce the flow acceleration through the HX core. Similarly, optimal fin pitch values lie towards the upper end of the optimization range indicated in Table 3.2. Based on the results obtained for the air-cooled condenser test case, optimal louvered fin shapes feature a height (F_h) in the range between 10-13 mm, and pitch (F_p) values of about 2-3 mm. For offset-strip fins, the optimal values are $F_h \approx 7-9$ mm and $F_p \approx 3$ mm. Although the correlation coefficient between the louver angle and ΔP_c is significant, this variable essentially exhibits only two optimal values depending on the objective prioritized in the design. More specifically, the majority of optimal core geometries on the Pareto surface feature the same value of louver angle, i.e., $L_\alpha \approx 28°$, which allows for designing the lightest HX cores. However, the HX designs achieving the lowest values

of cold-side pressure drop, i.e., below 450 Pa, are characterized by a louver angle of approximately 11°. Thus, while in most cases $L_\alpha = 28°$ is the optimal choice, a value of about 11° is recommended if the main performance metric of the system depends on the cold-side pressure drop of the HX.

- Microchannel width (w_{mc}) is the variable that most influences the working fluid pressure drop within the flat tubes (ΔP_h) of optimized designs. In particular, the lowest pressure drop is obtained by selecting the microchannel width as large as possible, namely $w_{mc} = 2.5$ mm, although this choice leads to the heaviest designs. In general, ΔP_h increases as the hydraulic diameter of the microchannels is decreased. Most of the design solutions on the Pareto front, however, are obtained for narrow microchannels (i.e., with $w_{mc} \approx 1.1$ mm). These solutions exhibit the lowest combination of ΔP_c and M_{HX} values compared to designs with large w_{mc} and therefore low ΔP_h. Moreover, the pressure drop within the flat tubes (ΔP_h) is indirectly affected by the fin pitch, especially for louvered fin core topologies. More specifically, larger values of F_p directly correlate to designs featuring lower hot-side pressure drops. This is due to (i) a reduction in the heat transfer coefficient, which increases the required heat transfer area, and (ii) a reduction in core compactness. As a result, the volume of the HX core is increased, as indicated by the large value of the correlation coefficient between F_p and M_{HX}.

- If the primary target is minimizing the core mass, the fin pitch should be as low as possible to maximize the heat transfer coefficient. At the same time, the offset-strip length $L_s = t_f/\delta$ should be low such that the dimensionless strip length is close to the upper bound of the correlations $0.04 \leq \delta \leq 0.06$. For louvered fins, the louver angle should be $L_\alpha \approx 28°$. Optimal fin pitch values to minimize HX mass are $F_p \approx 1$ mm for louvered fins, and $F_p \approx 1.2$ mm for offset strip fins.

3.6. COMPARISON OF BEST DESIGNS

The design guidelines presented in Section 3.5 describe how key geometric parameters influence the performance of common compact heat exchanger topologies. However, the process of identifying which topology and configuration is best for a given set of spatial, weight, and pressure drop constraints remains unresolved. To address this problem, a multi-objective optimization is performed for the condenser of the combined-cycle turbofan (CC-TF) engine concept following the methodology introduced in Section 2.5. The design specifications adopted for this assessment are reported in Table 3.4 and correspond to those of the CC-TF configuration that minimizes mission fuel consumption [13].

The airflow at the inlet of the condenser is assumed uniform and normal to the frontal area. The maximum allowable core dimensions are limited to $X = 0.5$ m, $Y = 1.5$ m, and $Z = 0.35$ m, in accordance with the available space for each of the eight condensers installed in the engine bypass duct. Each topology is evaluated by comparing Pareto-optimal solutions in terms of air-side pressure drop and HX mass, subject to a maximum pressure drop on the hot side equal to 5% of the working fluid inlet pressure (approximately 18 kPa). This constraint is imposed because the working fluid side exerts

limited influence on both system performance and condenser mass, as discussed in Sec. 3.4.

The optimization problem is formulated as:

$$\begin{aligned} &\text{minimize} && M_{\mathrm{HX}}(x_{\mathrm{D}})\ ;\ \Delta P_{\mathrm{c}}(x_{\mathrm{D}}), \\ &\text{subject to} && \Delta P_{\mathrm{h}} \leq 0.05\ P_{\mathrm{h,in}}, \\ & && X \leq 0.5\ \mathrm{m}, \\ & && Y \leq 1.5\ \mathrm{m}, \\ & && Z \leq 0.35\ \mathrm{m}, \\ & && x_{\mathrm{D}}^{\mathrm{L}} \leq x_{\mathrm{D}} \leq x_{\mathrm{D}}^{\mathrm{U}}\ , \end{aligned} \tag{3.16}$$

where x_{D} denotes the set of geometric parameters being optimized, which vary depending on the topology. The core topologies included in the comparison, along with the corresponding bounds for x_{D}, are reported below.

1. Plain tube bundles with inline tube arrangement (ptbi):
   $x_{\mathrm{D}} = 1.25 \leq x_{\mathrm{l}}/d_{\mathrm{o}} \leq 3\ ;\ 1.6 \leq x_{\mathrm{t}}/d_{\mathrm{o}} \leq 3\ ;\ 1.8\mathrm{mm} \leq d_{\mathrm{o}} \leq 2.5\mathrm{mm}$.

2. Plain tube bundles with staggered tube arrangement (ptbs):
   $x_{\mathrm{D}} = 0.85 \leq x_{\mathrm{l}}/d_{\mathrm{o}} \leq 3\ ;\ 1.8 \leq x_{\mathrm{t}}/d_{\mathrm{o}} \leq 3\ ;\ 1.8\mathrm{mm} \leq d_{\mathrm{o}} \leq 2.5\mathrm{mm}$.

3. Flat tube microchannels with louvered fins (ftmclf): x_{D} bounds are reported in Table 3.2.

4. Flat tube microchannels with offset-strip fins (ftmcosf): x_{D} bounds are reported in Table 3.2.

5. Plain finned tube bundles with staggered tube arrangement (pftbs):
   $x_{\mathrm{D}} = 2 \leq x_{\mathrm{l}}/d_{\mathrm{o}} \leq 4\ ;\ 2 \leq x_{\mathrm{t}}/d_{\mathrm{o}} \leq 4\ ;\ 1.8\mathrm{mm} \leq d_{\mathrm{o}} \leq 2.5\mathrm{mm}\ ;\ 1.6\mathrm{mm} \leq F_{\mathrm{p}} \leq 5\mathrm{mm}$.

6. Circular finned tube bundle with inline tube arrangement (cftbi):
   $x_{\mathrm{D}} = 1.2 \leq x_{\mathrm{l}}/d_{\mathrm{o}} \leq 3\ ;\ 2 \leq x_{\mathrm{t}}/d_{\mathrm{o}} \leq 4\ ;\ 1.8\mathrm{mm} \leq d_{\mathrm{o}} \leq 2.5\mathrm{mm}\ ;\ 1.6\mathrm{mm} \leq F_{\mathrm{p}} \leq 5\mathrm{mm}\ ;$
   $2\mathrm{mm} \leq F_{\mathrm{h}} \leq 6\mathrm{mm}$.

Table 3.4: Design specifications for one of the eight identical condenser units placed in the bypass duct of the CC-TF engine.

	$\dot{m}$ / kg s^{-1}	T_{in} /K	P_{in} /kPa	fluid	$\dot{Q}$ / kW
Hot Side	0.675	435.5	337.12	cyclopentane	328
Cold Side	8.387	305.7	60.40	dry air	

The tube and fin thicknesses are fixed to 0.2 mm for all core topologies. The flat tube height is 1.8 mm. The thickness of the rigidity plates included in the plain tube bundle configurations to suppress flow-induced vibrations is set to 0.5 mm, matching the thickness of the HX core casing. The Aluminum 3105 alloy is selected as the condenser material for all investigated topologies. The corresponding density is 2700 kg/m^3, while

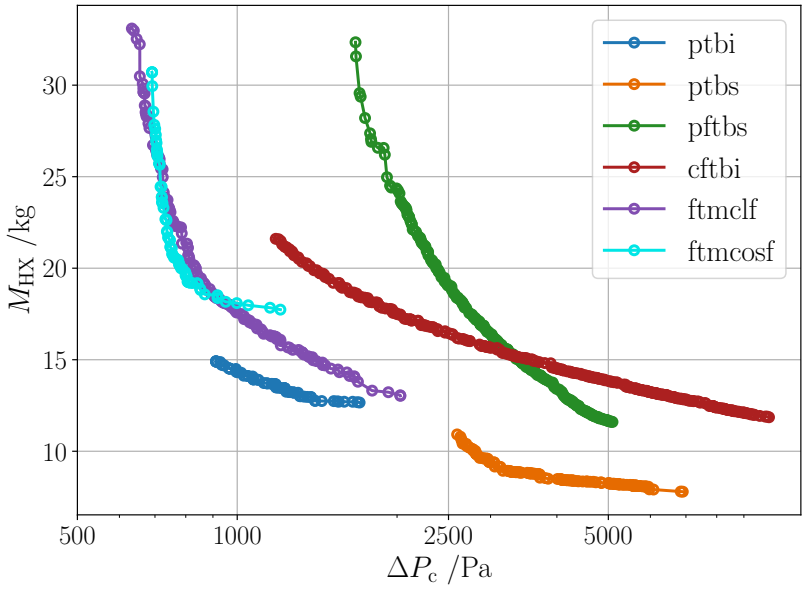

Figure 3.14: Comparison of Pareto optimal designs computed for six condenser topologies: plain tube bundles with inline (ptbi) or staggered tube arrangements (ptbs), flat tube microchannel cores with louvered (ftmclf) or offset-strip fins (ftmcosf), and finned tube bundles with plain fin and staggered tubes (pftbs) or circular fins and inline tubes (cftbi). For reference, the condensers of the CC-TF engine concept analyzed in Section 3.4.3 feature a pressure drop of ≈ 820 Pa.

the thermal conductivity is equal to 173 $W\,m^{-1}K^{-1}$.

The Pareto fronts of the design solutions obtained for the six condenser topologies are shown in Figure 3.14. All designs satisfy the imposed dimensional constraints and the limit on the working fluid-side pressure drop. Flat tube microchannel condensers exhibit the lowest air-side pressure drop among the topologies considered, but are also among the heaviest due to the presence of secondary heat transfer surfaces. The offset-strip fin variant (ftmcosf) enables considerable mass reduction with minimal penalty in ΔP_c, if pressure drops below 800 Pa are targeted in the design. Beyond this threshold, only marginal weight reductions are achieved at the cost of a large increase in pressure drop. The louvered-fin variant (ftmclf) exhibits a similar trend at low ΔP_c values, but it results in lighter designs if compared to the ftmcosf topology for $\Delta P_c > 800$ Pa. For cold-side pressure drops greater than 900 Pa, inline plain tube bundles (ptbi) emerge as a viable alternative to flat tube-and-fin topologies, offering the potential to reduce HX core weight by up to 15%. Further weight savings can be obtained with staggered plain tube bundle (ptbs) designs, although this option is only viable for pressure drops exceeding 2500 Pa.

Circular finned inline tube bundle (cftbi) cores are lighter than the plain-fin variant with a staggered tube arrangement (pftbs) at comparable cold-side pressure drop. How-

ever, this trend reverses for $\Delta P_c > 3400$. The steep increase in mass observed for plain-fin tube bundles at low air-side pressure drops is primarily attributed to a decline in overall surface efficiency. To decrease flow acceleration through the core, the optimizer adjusts the core geometry by increasing the transversal tube pitch. As a consequence, the length of the fin is increased, leading to a decrease in fin efficiency. Moreover, as the tube spacing increases, the ratio of the extended heat transfer area to the total heat transfer area also increases, further amplifying the impact of the lower fin efficiency.

3.7. CONCLUSIONS

A preliminary design methodology for HXs has been developed and integrated into a design optimization framework for system studies involving combined cycle gas turbines for airborne applications. Such systems employ an organic Rankine cycle unit to harvest thermal energy from the exhaust gases of aircraft engines or power units and convert it into additional power. The heat exchangers of the ORC unit, namely the primary HX and the condenser, have been identified as the most critical components for the feasibility of CC-engine concepts. The pressure drops on the cold air side of the condenser and on the hot exhaust gas side of the primary HX are, indeed, the major loss factors influencing the fuel saving potential of the waste heat recovery solutions analyzed in this work. Reducing pressure losses in these HXs is inherently challenging due to (i) spatial limitations that prevent increasing HX frontal area, and (ii) the weight penalties associated with mitigating pressure drops by increasing core volume. Nonetheless, the CC-TF engine concept shows potential for fuel savings because part of the rejected thermal energy from the condenser can be converted into kinetic energy within the nozzle of the bypass duct of the engine. This process enhances engine propulsive efficiency and net thrust, offsetting the aerodynamic penalty associated with installing the condensers in the bypass stream. Such a recuperation effect is often referred to as the Meredith effect [48], and its extent depends not only on the condenser core geometry but also on the design of the duct.

A sensitivity analysis was conducted to derive design guidelines for bare tube bundle cores with inline or staggered tube configurations. The results indicate that increasing the transverse pitch (x_t) between tubes reduces pressure losses on the external side of the bundle but increases core mass, regardless of the tube layout. The longitudinal pitch has a minor effect on heat transfer and pressure drop if the tube arrangement is of the inline type. More in detail, lower x_l values improve core compactness and reduce pressure losses at the expense of lower heat transfer coefficients. At higher x_l, the improvement in heat transfer performance does not compensate for the associated increase in pressure drop and volume. Conversely, for staggered tube arrangements, the heat transfer coefficient decreases with increasing x_l, leading to a much steeper increase in weight than that observed with inline tube arrangements.

Optimal design guidelines for air-cooled flat-tube microchannel condensers equipped with louvered and offset-strip fins were identified by means of a constrained multi-objective optimization. The optimization routine tunes a set of topology-specific parameters that define the geometries. The results show that fin height, which directly affects the mini-

mum flow cross-sectional area on the air side, is the parameter most strongly correlated with ΔP_c. The louver angle and offset-strip length also have a significant effect on air-side pressure drop. Specifically, larger louver angle and shorter strip length enhance flow mixing and periodic disruptions of the thermal boundary layer, thereby increasing both the heat transfer and friction coefficients. The condenser mass is proportional to the fin pitch, regardless of the fin topology: lower values of F_p result in lighter HXs. The heaviest condenser designs among the Pareto solutions are typically associated with longer offset-strip lengths and louver angles of approximately 11°, which reduce friction. The working fluid-side pressure drop (ΔP_h) is primarily determined by the width of the microchannels (w_{mc}), which defines the compactness of the hot-side heat transfer area. Larger values of w_{mc} increase the depth of the HX core, thereby reducing the working fluid mass velocity ($G = \dot{m}/A_0$). Fin characteristics, such as fin pitch and height, also indirectly influence ΔP_h, due to their impact on the heat transfer coefficient and thus on the required overall heat transfer area. However, the impact of fin characteristics on ΔP_h is secondary compared to that of w_{mc}, as the cold-side thermal resistance primarily determines the overall heat transfer coefficient.

Different HX topologies were assessed for the condenser of the CC-TF engine, as it is the most promising engine concept among those analyzed. These topologies range from tube bundle cores with or without fins to finned flat tube and microchannel geometries. The assessment involved solving a multi-objective optimization problem similar to the one used to define the design guidelines of microchannel condensers. In particular, the optimal design solutions obtained with the various HX topologies were compared based on two figures of merit: air-side pressure drop (ΔP_c) and heat exchanger mass (M_{HX}). The pressure drop on the working fluid side of the condenser was accounted for in the comparison by imposing an upper limit for such a quantity in the multi-objective optimization. This approach is justified by the fact that the hot-side pressure drop of the condenser (ΔP_h) has a limited impact on the performance of the system. Notably, if ΔP_h increases by 50%, the additional power required by the pump to maintain the same working fluid conditions at the inlet of the primary HX causes a reduction of only $\approx 6\%$ in net power output of the ORC system.

Flat tube microchannel condensers with offset-strip and louvered fins exhibit similar performance. These extended surface topologies outperform finned tube bundle topologies in terms of pressure drop, primarily due to reduced airflow acceleration and flow separation. If air-side pressure drops in the range of 800 - 900 Pa are acceptable, designs with louvered fins become the best option as they are lighter than those obtained with offset strip fins. Plain inline tube bundles outperform finned topologies in terms of weight, but they exhibit minimum values of ΔP_c which are approximately twice those of flat tube cores. The staggered plain tube bundle topology yields the lightest condenser designs, but their performance is characterized by significantly higher pressure losses, making this type of condenser a viable solution only in ducts with large cross-sectional areas. Despite their higher pressure drop, plain tube bundle HXs with very small outer diameters ($d_o < 2$ mm) appear to be promising solutions for airborne applications, owing to their compactness, low mass, mechanical robustness, and resistance to air-side

fouling [30]. Moreover, advances in additive manufacturing are enabling the fabrication of tubes with profiles obtained through CFD-based shape optimization. These methods can be exploited to reduce the air-side pressure losses in tube bundles designed for a prescribed heat duty [49], thereby supporting the development of high-performance, compact HXs for the aviation industry.

NOMENCLATURE

Roman symbols

A	Surface area [m^2]
A_0	Free flow area [m^2]
b	Extended surface channel height [m]
C^*	Heat capacity ratio [-]
c_p	Isobaric heat capacity [$kg\,m^2\,s^{-2}\,K^{-1}$]
d_h	Hydraulic diameter [m]
E	Young's modulus[GPa]
Eu	Euler number [-]
F_h	Fin height [m]
F_p	Fin pitch [m]
f	Friction factor [-]
G	Mass flux [$kg\,m^{-2}\,s^{-1}$]
g	Gravitational acceleration [m/s^2]
h	Heat transfer coefficient [$W\,m^{-2}\,K^{-1}$]
h_{mc}	Microchannel height [m]
I_t	Tube's moment of inertia [$kg\,m^{-2}$]
j	Colburn factor [-]
k	Thermal conductivity [$W\,m^{-1}\,K^{-1}$]
L_p	Louver pitch [m]
L_l	Louver length [m]
L_α	Louver angle [°]
L_s	Length of fin strip [m]
l_f	Fin length along heat conduction [m]
M	Mach number [-]
	Mass [kg]
$\dot{m}$	Mass flow rate [$kg\,s^{-1}$]
m'_t	Tube mass per unit length [$kg\,m^{-1}$]
MDP	Mass damping parameter [-]
n_{mc}	Number of microchannels/microtubes [-]
NTU	Number of Transfer Units [-]
Nu	Nusselt number [-]
n_z	Number of ranks per pass [-]
N_z	Total number of ranks [-]
N_p	Number of working fluid passes [-]
P	Pressure [Pa]
	Power [W]
Pr	Prandtl number [-]
P_{mc}	channel or tube perimeter [m]
$P_{x,f}$	cross-sectional fin perimeter [m]
$\dot{Q}$	Heat duty / thermal power [W]
R	Thermal resistance [$K\,W^{-1}$]
Re	Reynolds number [-]
T	Temperature [K]
t	Thickness [m]
T_p	Transversal tube pitch [m]
U	Overall transfer coefficient [$W\,m^{-2}\,K^{-1}$]
u	Velocity [$m\,s^{-1}$]
V	Volume [m^3]
w_{mc}	Width of the microchannel [m]
X	Width [m]
x_t	Transversal pitch [m]
x_l	Longitudinal pitch [m]
x_D	Design variables array [-]
Y	Height [m]
Z	Depth [m]

Greek symbols

α	Fin pitch over height ratio [-]
β	Heat transfer area compactness [m^{-1}]
β_s	Fluid side-specific area compactness [m^{-1}]
γ	Fin thickness over pitch ratio []
δ	Fin thickness over fin depth ratio [-]
ϵ	Effectiveness [-]
η	Efficiency [-]
θ_{cond}	Condenser tilt angle [°]
ρ	Density [$kg\,m^{-3}$]
σ	Free flow to frontal area ratio [-]

Subscripts

0	freestream
	overall heat transfer surface
1	inlet throat
2	Diffuser outlet
3	HX core inlet
air	Air stream
c	Cold side
cr	Cruise operating point
CV	Control volumes
e	Secondary(extended) heat transfer area
f	Fin
HX	Heat Exchanger
in	HX inlet conditions
lm	Logarithmic mean
m	Mechanical
mc	Microchannel/microtube
pt	Structural stability plates
ref	Reference
sc	Subcooling
sh	Superheating
st	Structure material
t	Tube
x,f	Cross-sectional area of fin
wf	Working fluid

Superscripts

L	Lower bound
n	relative to the control volume
U	Upper bound

Abbreviations

APU	Auxiliary power unit
CC	Combined cycle
COP	Coefficient Of performance
CV	Control volume
ECS	Environmental control system
FV	Finite-volume

HPC	High pressure compressor
HPC	High pressure turbine
HX	Heat exchanger
LPC	Low pressure compressor
LPC	Low pressure turbine
MB	Moving boundary
MFR	Intake mass flow rate ratio
OPR	Overall pressure ratio
ORC	Organic Rankine cycle
TF	Turbofan engine
TG	Turbogenerator
TIT	Turbine inlet temperature
TS	Turboshaft engine
WF	Working fluid
WHR	Waste heat recovery

BIBLIOGRAPHY

[1] VDI, *VDI Heat Atlas*, 2nd. Springer, 2010.

[2] R. Shah and D. Sekulic, "Heat exchangers", *Handbook of heat transfer*, vol. 3, 1998.

[3] D. Shah R. Sekulic, *Fundamentals of heat exchanger design*. John Wiley and Sons, 2003.

[4] S. Bendapudi, J. E. Braun, and E. A. Groll, "A comparison of moving-boundary and finite-volume formulations for transients in centrifugal chillers", *International Journal of Refrigeration*, vol. 31, no. 8, pp. 1437–1452, 2008, ISSN: 0140-7007. DOI: https://doi.org/10.1016/j.ijrefrig.2008.03.006. [Online]. Available: https://www.sciencedirect.com/science/article/pii/S0140700708000637.

[5] D. Kim, D. Ziviani, J. E. Braun, and E. A. Groll, "A moving boundary modeling approach for heat exchangers with binary mixtures", *Energy Procedia*, vol. 129, pp. 466–473, 2017, 4th International Seminar on ORC Power SystemsSeptember 13-15th 2017POLITECNICO DI MILANOBOVISA CAMPUSMILANO, ITALY, ISSN: 1876-6102. DOI: https://doi.org/10.1016/j.egypro.2017.09.161. [Online]. Available: https://www.sciencedirect.com/science/article/pii/S187661021734033X.

[6] H. Pangborn, A. G. Alleyne, and N. Wu, "A comparison between finite volume and switched moving boundary approaches for dynamic vapor compression system modeling", *International Journal of Refrigeration*, vol. 53, pp. 101–114, 2015, ISSN: 0140-7007. DOI: https://doi.org/10.1016/j.ijrefrig.2015.01.009.

[7] I. H. Bell, S. Quoilin, E. Georges, *et al.*, "A generalized moving-boundary algorithm to predict the heat transfer rate of counterflow heat exchangers for any phase configuration", *Applied Thermal Engineering*, vol. 79, pp. 192–201, 2015, ISSN: 1359-4311. DOI: https://doi.org/10.1016/j.applthermaleng.2014.12.028. [Online]. Available: https://www.sciencedirect.com/science/article/pii/S1359431114011570.

[8] Z. Chu and W. Zhang, "Moving-boundary and finite volume coupling algorithm for heat exchanger with fluid phase change", *International Journal of Heat and Mass Transfer*, vol. 131, pp. 313–328, 2019, ISSN: 0017-9310. DOI: https://doi.org/10.1016/j.ijheatmasstransfer.2018.11.066. [Online]. Available: https://www.sciencedirect.com/science/article/pii/S0017931018335488.

[9] H. Qiao, V. Aute, H. Lee, K. Saleh, and R. Radermacher, "A new model for plate heat exchangers with generalized flow configurations and phase change", *International Journal of Refrigeration*, vol. 36, no. 2, pp. 622–632, 2013, ISSN: 0140-7007. DOI: https://doi.org/10.1016/j.ijrefrig.2012.11.020. [Online]. Available: https://www.sciencedirect.com/science/article/pii/S0140700712003283.

[10] J. Patiño, R. Llopis, D. Sánchez, C. Sanz-Kock, R. Cabello, and E. Torrella, "A comparative analysis of a co2 evaporator model using experimental heat transfer correlations and a flow pattern map", *International Journal of Heat and Mass Transfer*, vol. 71, pp. 361–375, 2014, ISSN: 0017-9310. DOI: https://doi.org/10.1016/j.ijheatmasstransfer.2013.12.027. [Online]. Available: https://www.sciencedirect.com/science/article/pii/S0017931013010715.

[11] F. Illán-Gómez, J. García-Cascales, R. Molina-Valverde, and F. Velasco, "A discretization method for the characterization of a plate heat exchanger working as evaporator during transient conditions", *International Journal of Thermal Sciences*, vol. 184, p. 107 998, 2023, ISSN: 1290-0729. DOI: https://doi.org/10.1016/j.ijthermalsci.2022.107998. [Online]. Available: https://www.sciencedirect.com/science/article/pii/S1290072922005269.

[12] J. R. Simon and T. M. Bandhauer, "An experimentally validated evaporative phase change heat transfer model for low mass flux applications using r134a in plate heat exchangers", *International Journal of Refrigeration*, vol. 131, pp. 604–614, 2021, ISSN: 0140-7007. DOI: https://doi.org/10.1016/j.ijrefrig.2021.08.003. [Online]. Available: https://www.sciencedirect.com/science/article/pii/S0140700721003339.

[13] D. Krempus, C. M. D. Servi, R. Vos, and P. Colonna, "Organic rankine cycle waste heat recovery systems for aircraft engines", Ph.D. dissertation, Delft University of Technology, 2025.

[14] I. H. Bell, J. Wronski, S. Quoilin, and V. Lemort, "Pure and pseudo-pure fluid thermophysical property evaluation and the open-source thermophysical property library coolprop", *Industrial & Engineering Chemistry Research*, vol. 53, no. 6, pp. 2498–2508, 2014. DOI: 10.1021/ie4033999.

[15] P. Colonna and T. van der Stelt, *Fluidprop (version 3.1): A program for the estimation of thermophysical properties of fluids*, 2019. [Online]. Available: https://asimptote.com/fluidprop/.

[16] C. Ranganayakulu, K. Seetharamu, and K. Sreevatsan, "The effects of longitudinal heat conduction in compact plate-fin and tube-fin heat exchangers using a finite element method", *International Journal of Heat and Mass Transfer*, vol. 40, no. 6, pp. 1261–1277, 1997. DOI: 10.1016/S0017-9310(96)00182-2.

[17] S.-S. Chen, "Flow-induced vibration of circular cylindrical structures", Argonne National Lab. (ANL), Argonne, IL (United States), Tech. Rep., Jun. 1985. DOI: 10.2172/6331788. [Online]. Available: https://www.osti.gov/biblio/6331788.

[18] M. Pettigrew, C. Taylor, N. Fisher, M. Yetisir, and B. Smith, "Flow-induced vibration: Recent findings and open questions", *Nuclear Engineering and Design*, vol. 185, no. 2, pp. 249–276, 1998, ISSN: 0029-5493. DOI: https://doi.org/10.1016/S0029-5493(98)00238-6.

[19] H. Gelbe, M. Jahr, and K. Schröder, "Flow-induced vibrations in heat exchanger tube bundles", *Chemical Engineering and Processing: Process Intensification*, vol. 34, no. 3, pp. 289–298, 1995, ISSN: 0255-2701. DOI: https://doi.org/10.1016/0255-2701(94)04016-8.

[20] M. Pettigrew and C. Taylor, "Fluid elastic instability of heat exchanger tube bundles: Review and design recommendations", *Journal of Pressure Vessel Technology*, vol. 113, no. 2, pp. 242–256, 1991. DOI: https://doi.org/10.1115/1.2928752.

[21] K. Schroder and H. Gelbe, "New design recommendations for fluidelastic instability in heat exchanger tube bundles", *Journal of Fluids and Structures*, vol. 13, no. 3, pp. 361–379, 1999, ISSN: 0889-9746. DOI: https://doi.org/10.1006/jfls.1999.0208.

[22] H. Lim, U. Han, and H. Lee, "Design optimization of bare tube heat exchanger for the application to mobile air conditioning systems", *Applied Thermal Engineering*, vol. 165, p. 114 609, 2020, ISSN: 1359-4311. DOI: https://doi.org/10.1016/j.applthermaleng.2019.114609.

[23] Z. Tian, B. Gu, L. Yang, and F. Liu, "Performance prediction for a parallel flow condenser based on artificial neural network", *Applied Thermal Engineering*, vol. 63, no. 1, pp. 459–467, 2014, ISSN: 1359-4311. DOI: https://doi.org/10.1016/j.applthermaleng.2013.10.060.

[24] D. Krempus, F. Beltrame, M. Majer, *et al.*, "Organic Rankine cycle waste heat recovery systems for aircraft auxiliary power units", *Journal of the Global Power and Propulsion Society*, vol. 9, 2025. DOI: 10.33737/jgpps/204721.

[25] A. S. Sabau, A. H. Nejad, J. W. Klett, A. Bejan, and K. Ekici, "Novel evaporator architecture with entrance-length crossflow-paths for supercritical organic rankine cycles", *International Journal of Heat and Mass Transfer*, 2018.

[26] H. Grieb, *Projektierung von Turboflugtriebwerken*. Birkhäuser Basel, 2004. DOI: 10.1007/978-3-0348-7938-5.

[27] H. Martin, "The generalized lévêque equation and its practical use for the prediction of heat and mass transfer rates from pressure drop", *Chemical Engineering Science, Volume 57, Issue 16*, 2002.

[28] P. Brkić D.and Praks, "Unified friction formulation from laminar to fully rough turbulent flow.", *Applied sciences*, 2018.

[29] I. Pioro and S. Mokry, "Heat transfer to supercritical fluids", *Heat Transfer - Theoretical Analysis, Experimental Investigations and Industrial Systems*, 2011.

[30] J. Hesselgreaves, R. Law, and D. Reay, *Compact Heat Exchangers: : Selection, Design, and Operation*. Elsevier Science, 2016, Second edition, ISBN: 978-0-08-100305-3.

[31] Kaltra GmbH, "Microchannel condensers: Heat exchangers for condenser applications", Tech. Rep., 2020, accessed on 17 January 2025. [Online]. Available: %5Curl%7Bhttps://www.kaltra.com/wp-content/uploads/2020/04/TM_Microchannel-Condensers_Ver.3.0_EN.pdf%7D.

[32] S. Whitaker, "Forced convection heat transfer correlations for flow in pipes, past flat plates, single cylinders, single spheres, and for flow in packed beds and tube bundles", *AIChE Journal*, vol. 18, no. 2, pp. 361–371, 1972. DOI: https://doi.org/10.1002/aic.690180219.

[33] E. N. Sieder and G. E. Tate, "Heat transfer and pressure drop of liquids in tubes", *Industrial & Engineering Chemistry*, vol. 28, no. 12, pp. 1429–1435, 1936. DOI: 10.1021/ie50324a027. [Online]. Available: https://doi.org/10.1021/ie50324a027.

[34] H. Muller-Steinhagen and K. Heck, "A simple friction pressure drop correlation for two-phase flow in pipes", *Chem. Eng. Process Intensification*, vol. 20, no. 6, pp. 297–308, 1986.

[35] Y. Chang and C. Wang, "A generalized heat transfer correlation for louver fin geometry", *International Journal of Heat and Mass Transfer*, 1997.

[36] Y. Chang, K. Hsu, Y. Lin, and C. Wang, "A generalized friction correlation for louver fin geometry", *International Journal of Heat and Mass Transfer*, 2000.

[37] A. M. F. El-Shaboury and S. J. Ormiston, "Analysis of laminar forced convection of air crossflow in in-line tube banks with nonsquare arrangements", *Numerical Heat Transfer, Part A: Applications*, vol. 48, no. 2, pp. 99–126, 2005.

[38] D. Krempus, F. Beltrame, M. Majer, C. M. De Servi, and R. Vos, "Orc waste heat recovery system for the turboshaft engines of turboelectric aircraft: Correction", in *TU Delft Flight Performance and Propulsion*, vol. 10^{th} EUCASS, 2023. [Online]. Available: https://resolver.tudelft.nl/uuid:3eca4e81-1449-4cce-8e6c-cf8d2929d6ea.

[39] ESDU, *ESDU86002: Drag and Pressure Recovery Characteristics of Auxiliary Air Inlets at Subsonic Speeds*, 2004.

[40] F. Sinopoli, R. Carandente, Y. Schulz, *et al.*, "Impact of the working fluid in orc-based waste heat recovery usystems for turboshaft engines", in *Proceedings of Global Power and Propulsion Society*, vol. GPPS Chania 2024, 2024. [Online]. Available: https://gpps.global/wp-content/uploads/2024/09/GPPS-TC-2024_paper_075.pdf.

[41] C. M. Invernizzi, P. Iora, G. Manzolini, and S. Lasala, "Thermal stability of n-pentane, cyclo-pentane and toluene as working fluids in organic rankine engines", *Applied Thermal Engineering*, vol. 121, pp. 172–179, 2017, ISSN: 1359-4311. DOI: https://doi.org/10.1016/j.applthermaleng.2017.04.038.

[42] P. Schmollgruber, D. Donjat, M. Ridel, *et al.*, "Multidisciplinary design and performance of the ONERA hybrid electric distributed propulsion concept (Dragon)", in *AIAA SciTech Forum*, doi: 10.2514/6.2020-0501, 2020.

[43] M. Badger, A. Julien, A. D. LeBlanc, S. H. Moustapha, A. Prabhu, and A. A. Smailys, "The PT6 engine: 30 years of gas turbine technology evolution", in *Proceedings of the ASME Turbo Expo*, doi: 10.1115/93-GT-006, 1993.

[44] R. W. Heldenbrand and W. S. Miller, "Regenerative engine analysis program (REAP)", USAAVRADCOM, Tech. Rep., 1981.

[45] S. Kaiser, O. Schmitz, P. Ziegler, and H. Klingels, "The water-enhanced turbofan as enabler for climate-neutral aviation", *Applied Sciences*, vol. 12, no. 23, 2022, doi: 10.3390/app122312431.

[46] R. Manglik and A. Bergles, "Heat transfer and pressure drop correlations for the rectangular offset strip fin compact heat exchanger", *Experimental thermal and fluid science*, 1995.

[47] Y.-G. Park and A. M. Jacobi, "Air-side heat transfer and friction correlations for flat-tube louver-fin heat exchangers", *Journal of Heat Transfer*, vol. 131, no. 2, p. 021 801, Dec. 2008, ISSN: 0022-1481. DOI: 10.1115/1.3000609. [Online]. Available: https://doi.org/10.1115/1.3000609.

[48] F. W. Meredith, "Cooling of aircraft engines with special reference to ethylene glycol radiators enclosed in ducts", Aeronautical Research Committee Reports and Memoranda, Tech. Rep. No 1683, Aug. 1935. [Online]. Available: https://naca.central.cranfield.ac.uk/handle/1826.2/1425?show=full.

[49] P. Pai Raikar, N. Anand, M. Pini, and C. De Servi, "Concurrent optimization of multiple heat transfer surfaces using adjoint-based optimization with a cad-based parametrization", *International Journal of Heat and Mass Transfer*, vol. 236, p. 126 230, 2025, ISSN: 0017-9310. DOI: https://doi.org/10.1016/j.ijheatmasstransfer.2024.126230. [Online]. Available: https://www.sciencedirect.com/science/article/pii/S0017931024010603.

4

Optimal Design of Aircraft Thermal Systems and Their Heat Exchangers Leveraging a Data-Driven Surrogate Model

Problems can never be solved
by the way of thinking that first created them.

Albert Einstein

Parts of this chapter have been published in:

F. Beltrame, P. Colonna, C.M. De Servi, "Optimal Design of Aircraft Thermal Systems and Their Heat Exchangers Leveraging a Data-Driven Surrogate Model", *International journal of heat and mass transfer*, 2025, issn 0017-9310, DOI: https://doi.org/10.1016/j.ijheatmasstransfer.2025.127502

Abstract

Heat exchangers are arguably the most critical components in next-generation propulsion systems featuring thermal energy recovery. This is due to the complex interdependence between thermal performance and constraints on weight and volume. This chapter details the development of a systematic methodology for optimizing airborne thermal systems, with a focus on addressing the computational challenges of integrated design. Three design strategies are compared: (i) optimization of the sole cycle parameters while performing heat exchanger sizing for values of the geometrical characteristics defined a priori based on a preliminary investigation of the design space of these components, (ii) concurrent optimization of both the thermodynamic cycle and of the most critical heat exchanger, e.g., the condenser, and, (iii) use of a data-driven surrogate model of the condenser to predict the optimal heat exchanger geometry as a function of any feasible thermodynamic conditions to reduce the number of optimization variables of the integrated design problem.

The three design strategies are applied to two case studies featuring supercritical ORC systems utilizing cyclopentane as the working fluid: a combined cycle auxiliary power unit (CC-APU) and a combined cycle turboshaft (CC-TS) engine. Findings indicate that integrated optimization yields performance gains that vary depending on the heat exchanger topology, application, and thermodynamic cycle. For instance, CC-APU designs obtained with the integrated design optimization method are up to 15% lighter than designs obtained with the optimization of the thermodynamic cycle parameters alone, for the same net power output. Microchannel condenser designs with offset strip fins allow for obtaining a better performance than louvered fin-based designs if a low-pressure drop is targeted, whereas louvered fins are advantageous if a higher pressure drop is allowed. The design strategy employing the surrogate model considerably reduces the computational cost, without significantly affecting accuracy: the relative deviation between the Pareto front obtained with the surrogate model and that obtained with the integrated optimization strategy ranges between 1% and 2.9%. These values are comparable to the uncertainty of the predictions of the heat exchanger model. The reduction in computational time required to generate the Pareto fronts associated with the two case studies is up to 200%.

4.1. INTRODUCTION

Weight and size are critical metrics in the design of heat exchangers for propulsive applications such as automotive, marine, and aircraft engines. The selection of an appropriate topology and its optimal geometry is a process that is closely linked to the design of the thermodynamic cycle and imposed space constraints. For instance, in organic Rankine cycle (ORC) waste heat recovery (WHR) units, system performance and feasibility depend not only on conversion efficiency – directly tied to HX effectiveness and thermo-hydraulic performance – but also on overall system weight and spatial constraints. Despite the relevance of these inter-dependencies, only a limited number of studies document the integrated design of heat exchangers in conjunction with the thermodynamic optimization of WHR systems. For instance, Ref. [1] details a method for coupling the thermodynamic model of an ORC system serving as a bottoming unit of a stationary gas turbine with a thermo-hydraulic design methodology for plate heat exchangers. The integrated optimization of the system and HX specifications (inlet temperatures, mass flow rates, etc.) allows for the quantification of the trade-off between net power output and investment cost. The off-design performance of a medium power capacity ORC unit recovering thermal energy from stationary internal combustion engines is documented in [2]. The subcritical non-recuperated ORC system was optimized to maximize the net power output of the combined power plant for both nominal and off-design operations; however, the geometrical characteristics of the HXs and the expander were fixed. The study details the comparison of system performance using two predefined HX and expander configurations. The design procedures reported in Refs. [1] and [2] rely on predefined values of the HX geometric parameters, while weight and size are not constrained. However, the optimization of the HX geometry is crucial for the effective design of aerospace thermal systems. For instance, as documented in Ref. [3], the optimization of the precooler geometry of an unconventional air-breathing engine operating at high Mach number is essential not only for enhancing performance but also for ensuring the operational feasibility of the engine.

More recently, in Ref. [4], the authors showcase a design methodology for vapor compression cycle (VCC) systems in aerospace applications, based on the integrated optimization of the thermodynamic cycle and the preliminary sizing of the main system components. Results show that more efficient systems are only possible at the expense of heavier components and that constraints on condenser size negatively impact system efficiency. The results of this study also show that the optimal HX size depends on the selected thermodynamic conditions, working fluid, and objective function of the optimization. The integrated design framework has been subsequently extended to perform a multipoint and multi-objective design optimization of a bleed-less air cycle machine (ACM) and an electrically driven VCC system for a single-aisle, short-haul aircraft [5].

In this context, the work reported here is related to the development of a computationally efficient methodology to predict the performance of optimal HXs in the early design phase of aerospace thermal systems. The performance benefit of the simultaneous optimization of the thermodynamic cycle and the most critical HX (the condenser) is assessed. Moreover, the procedure is improved from a computational point of view by replacing the conventional preliminary sizing procedure of the condenser with a data-driven surrogate model. The target is a reduction in the degrees of freedom associated

with the integrated optimization procedure, with the consequent decrease in computational time and complexity of the design problem.

The use of data-driven surrogate models to predict the performance of thermodynamic systems or their components is documented in the literature. Artificial neural networks (ANN) have been used for estimating the thermal performance of HXs. Common ANN architectures employed for this purpose include multilayer feed-forward networks [6], generalized regression neural networks, and adaptive neuro-fuzzy interface systems [7]. The application of these models ranges from predicting the overall HX thermal performance to simulating the flow phase change. In particular, Ref. [6] details the development of a neural network model to predict the performance of fin-and-tube condensers used in air-cooled systems. A multi-layer perceptron (MLP) with one hidden layer, also known as a three-layer perceptron, was trained on a dataset obtained with a first-principle rating model to predict the refrigerant- and air-side pressure drops, given the HX inlet conditions. Though the data-driven model predictions show a good level of accuracy if compared to experimental results, the range of applicability is very limited, as the HX geometry was fixed in the definition of the training dataset. The authors in [8] developed data-driven models of a turbocharger and air intake for the dynamic simulation of the gas exchange process of an internal combustion engine. Two MLPs with one hidden layer are used to replace the models of the two components and predict over time the charge flow and the intake manifold pressure under varying engine operating conditions. Ref. [9] documents a methodology to implement a data-driven model of single-stage centrifugal compressors to facilitate the design optimization of an electrically driven vapor compression cycle system for aircraft. The surrogate model of the compressor is based on a MLP trained on a large synthetic dataset of centrifugal compressor designs. Specifically, two distinct regression models have been trained to predict the performance of a compressor design for given geometrical and thermodynamic specifications. The results demonstrated the computational benefit of replacing the mean line design procedure of the centrifugal compressor with a data-driven model, both in terms of the number of objective function evaluations needed to converge to an optimal solution and in terms of improved robustness of the system model. However, the literature currently lacks the documentation of studies about the use of ANN-based surrogate models to predict the performance of optimal HXs with size constraints. The development of such models can yield a significant reduction of the computational cost associated with the integrated design optimization of a thermodynamic system and its components.

The main objectives of this study are (i) to quantify the performance improvements that can be obtained if the HX with the largest influence on the system performance is optimized together with the thermodynamic cycle and, (ii) to assess the computational cost reduction associated with using a data-driven surrogate model of optimized HXs to obtain the same optimal performance that is achieved through an integrated system-and-HX optimization. This Chapter is structured as follows. First, Section 4.2 introduces two case studies in which a supercritical ORC system is used as a bottoming cycle to harvest thermal energy from aerospace-grade gas turbines. Subsequently, the thermodynamic modeling of the ORC WHR unit is briefly described in Section 4.3.

The methodology Section also reports the HX design procedure and highlights the differences between the three system design approaches investigated in this study. Section 4.3 also details how the HX design method was employed to generate a dataset of optimized HX geometries for the ORC condenser. This dataset is then used to train an ANN-based regression model that predicts sets of Pareto optimal solutions of different condenser topologies over varying thermodynamic design specifications. The results of the system optimization employing the surrogate model in place of the detailed condenser model are reported and discussed in Section 4.4. Finally, the main outcomes of the study are summarized in Section 4.5 together with an outlook on future developments.

4.2. CASE STUDIES

The feasibility and advantages of the proposed method over the conventional approach to system preliminary design are demonstrated by solving the optimal design problem of an ORC system recovering thermal energy from aircraft power and propulsion systems. The two case studies analyzed in this Chapter are briefly introduced in the following subsections.

CC-APU

The first case study focuses on the combined-cycle auxiliary power unit introduced in Sec. 3.4.1. The gas turbine of the CC-APU is a single-spool turboshaft engine and is coupled with a bottoming supercritical ORC unit. The system, whose process flow diagram is reported in Fig. 3.4, is active only when the aircraft is on the ground. The ambient conditions assumed for system design correspond to atmospheric pressure and an ambient air temperature of 40 °C. The temperature and mass flow rate of the hot exhaust gases flowing through the primary HX are fixed at 847 K and 0.84 kg/s, based on the nominal operating conditions of the APU gas turbine as reported by [10]. The exhaust gases are discharged to the ambient after passing through the primary HX of the ORC unit, thus heating the working fluid, which is in a supercritical state. The ORC turbine's gross power is converted into electrical power via a dedicated generator. The output of the system model, which is described in Section 4.3.1, includes the net power output of the ORC unit ($\dot{W}_{\text{net,ORC}}$) and its mass (M_{ORC}). The optimization variables associated with this thermodynamic system correspond to the degrees of freedom associated with the cycle configuration, which are the maximum temperature (T_{max}) and minimum temperature (T_{min}) of the working fluid, the maximum cycle pressure (P_{max}), as well as the evaporator and condenser pinch point temperature differences ($\Delta T_{\text{pp,ev}}$ and $T_{\text{pp,cnd}}$).

CC-TS

The second case study is about the design of the combined cycle turboshaft (CC-TS) engine introduced in Sec. 3.4.2. The CC-TS engine concept, whose process flow diagram is reported in Fig. 3.6, features a non-recuperated two-spool turboshaft engine and a bottoming supercritical ORC unit that harvests thermal energy from the gas turbine exhaust. The engines are placed in dedicated pods positioned aft of the turboelectric ONERA Dragon aircraft concept [11] and provide electrical power to the under-the-wing

distributed propulsion system consisting of electrically driven ducted fans. Each CC-TS engine has two ram air ducts symmetrically positioned above and below the midplane housing the condensers of the ORC WHR unit as shown in Fig. 3.7. The primary HX is positioned aft of the gas turbine and transfers thermal energy from the exhaust gases to the working fluid in a supercritical state. The design point of the combined-cycle engine corresponds to the cruise condition, which is defined by a cruise speed of $M_0 = 0.78$ and an altitude of 10 km. The net power that the combined cycle engines must generate ($\dot{W}_{\text{net}}$) is determined by solving the following thrust-drag balance

$$\frac{\eta_{\text{p}}\eta_{\text{tr}}\dot{W}_{\text{net}}}{u_0} = D - (T_{\text{duct}} + T_{\text{jet}}), \tag{4.1}$$

where η_{p} and η_{tr} are the ducted fan propulsive and transmission efficiencies, D is the aircraft drag, T_{duct} is the thrust associated with the ram air duct, T_{jet} is thrust resulting from the discharge of the gas turbine exhaust gases and u_0 is the cruise speed. In Equation 4.1, ($\dot{W}_{\text{net}}$) is given by the sum of the net power generated by the turboshaft ($\dot{W}_{\text{net,TS}}$) and by the ORC unit ($\dot{W}_{\text{net,ORC}}$). A Newton–Raphson gradient-based solver is employed to solve the equations resulting from coupling the gas turbine, ORC system, and ram air duct models. The optimization variables of this system are the five degrees of freedom associated with the thermodynamic cycle, plus the number of passes of the primary HX (N_p), the condenser tilt angle (θ), and the ram air duct intake mass flow rate ratio (MFR). These three additional design variables have been included to optimize the main dimensions of the ram air duct and allow for a wider range of primary HX designs.

4.3. METHODOLOGY: MODELS AND DESIGN

4.3.1. WASTE HEAT RECOVERY UNIT

The two heat exchangers of the ORC system under consideration are the primary HX, or supercritical evaporator, which recovers part of the thermal energy of the exhaust of the gas turbine, and the condenser, which rejects to the ambient the thermal energy required to condense the working fluid.

The ORC unit is modeled using an in-house tool for on-design thermodynamic cycle calculations. The Helmoltz-energy explicit equation of state (HEOS) model implemented in an open source program [12] is used for thermodynamic property modeling of the ORC working fluid, while the ideal gas model [13] is adopted for the gas turbine exhaust, whose mass-specific composition is fixed and assumed to be 74% N2, 15.9% O2, 6.4% CO2, 2.5% H2O, 1.2% Ar for both test cases. The ORC turbine power output is calculated assuming a constant isentropic efficiency of 0.94 [10], a mechanical efficiency of 0.99, and a generator efficiency of 0.97 for both test cases. The working fluid is pressurized by a centrifugal pump, whose isentropic efficiency and electromechanical conversion efficiency are assumed constant and equal to 0.65 and 0.98, respectively [14]. The electromechanical conversion efficiency is the product of the mechanical and electrical motor efficiencies.

For the CC-TS case study, the ram air flows through the condenser duct thanks to the dynamic pressure resulting from the aircraft motion. The model used to estimate the ram air duct net drag is documented in [15]. Conversely, for the case of the CC-APU,

the required condenser air mass flow rate ($\dot{m}_{\text{air}}$) is provided by a dedicated fan, driven by electrical power generated by the ORC turbo-generator. The isentropic efficiency of the electrically driven fan is assumed to be 0.6, while the electromechanical conversion efficiency is set equal to 0.98. As a result, the net power output of the WHR unit ($\dot{W}_{\text{net,ORC}}$) is obtained by subtracting the pump and, if present, the fan power consumption from the turbo-generator power output.
The ORC system mass (M_{ORC}) is estimated as the sum of the mass of the main ORC system components. The HX mass is an outcome of the preliminary design method detailed in Chapter 3. Assuming that the primary HX is fully flooded at start-up, the working fluid mass is estimated as the product of the fluid density at standard ambient conditions times the volume of the primary HX cold side, augmented by 20% to account for system piping. The turbo-generator mass is estimated assuming a specific power of around 5.5 kW/kg, based on the results reported in [16]. The same approach is adopted for the centrifugal pump, whose specific power is assumed to be 4 kW/kg as documented in [14]. The balance-of-plant weight is assumed to be 5% of the overall system mass. This factor is increased to 10% if the fan and its electric motor are present.

4.3.2. HEAT EXCHANGERS

The preliminary design of heat exchangers is a procedure that consists of finding the heat transfer area that satisfies the heat duty requirement given the inlet temperature, pressure, and mass flow rate of both the hot and cold streams. For this task, the FV-based methodology detailed in Sec. 3.2 is employed. The preliminary design tools for the condenser and evaporator are part of the in-house software *HeXacode*, and have been verified against the results of a widely adopted commercial software [17] and experimental data available in the literature (See Sec. 3.3). For both the heat exchangers of the ORC unit, the gas-side height Y and width X, which determine the frontal area, are input to the design routine. The heat exchanger depth Z is instead calculated to meet the design specifications. The heat transfer and pressure drop correlation used for the HXs are reported in Appendix A.

CONDENSER

Two main topologies are considered for the ORC condenser: (1) flat-tube microchannel compact heat exchangers with louvered fins, and (2) flat-tube configurations with offset-strip fins (See Fig. 3.11). In both cases, the working fluid flows in small rectangular channels within the flat tubes, while the air flows through the fins. These fin topologies promote small and light HX designs [18], and are often used in the automotive and aerospace sectors. The fin and flat tube thicknesses are both set to 0.2 mm, while the height of the microchannels (h_{mc}) is set to 1.6 mm. The louver fin length (L_l) is fixed to 90% of the fin height. These fixed geometry-specific parameters are chosen based on engineering judgment and manufacturability considerations. All the other geometric parameters (see Table 5.4) are degrees of freedom of the integrated design strategy. The condenser core material is a manganese-based aluminum alloy of the 3000 series, characterized by high levels of strength, good formability, and corrosion resistance [19].

PRIMARY HX

The chosen topology for the primary HX consists of a multi-pass bare-tube bundle where the working fluid circulates inside the tubes, in a counter-crossflow arrangement with respect to the exhaust gases (See Fig. 4.1). Advantages of bare tube bundles with small tube diameters (< 2mm) include lighter designs if the working fluid inside the tubes is at medium to high pressure, easier moisture removal, and lower susceptibility to fouling than finned topologies. A nickel-based alloy named HastelloyX is chosen as the material of the primary HX core due to its high oxidation resistance up to 1200°C and good mechanical properties up to temperatures greater than the maximum exhaust temperature of aero engine gas turbines [20].

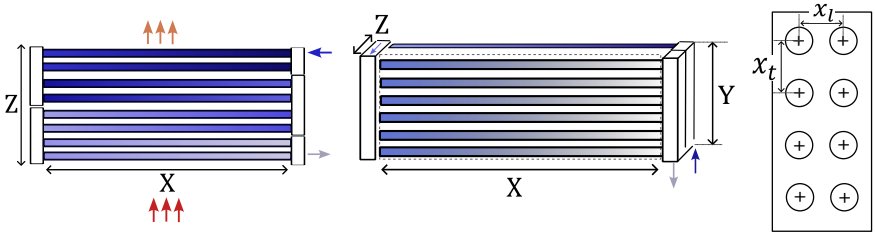

Figure 4.1: Sketch of the multipass bare tube bundle primary heat exchanger, with an inline tube arrangement.

The tube outer diameter (d_o) is fixed to 1.8 mm, while the tube thickness is calculated given the pressure difference between the working fluid and the exhaust gases, assuming 0.2 mm as the minimum value. The optimal values of transverse (x_t) and longitudinal (x_l) pitches between the tubes were determined through a sensitivity study, in which the preliminary design of the primary HX was repeated while varying the values of these variables along with the design specifications of the component. Figure 4.2 shows the results of the sensitivity study in terms of pressure drop on the exhaust gas side, normalized by the dynamic pressure in this stream at the HX inlet, and the ratio between the overall core weight and the heat duty. The trends in the design map indicate that the optimal transverse and longitudinal pitches between the tubes are 3 and 1.25 outer diameters, respectively. These values minimize the hot-side pressure drop while ensuring a lightweight HX design.

4.3.3. DESIGN STRATEGIES

The thermodynamic specifications and size constraints strongly affect the maximum mass-specific performance and optimal configuration of aerospace-grade HXs. Three design strategies are employed to optimize two different ORC WHR units that harvest thermal energy from the exhaust of gas turbines.

- In the *baseline* design strategy, the combined cycle system design is optimized assuming a fixed condenser geometry for both topologies. The fixed geometric parameters were selected based on a preliminary investigation of the design space of the condenser and choosing a combination of parameters enabling a trade-off between air-pressure drop and HX weight.

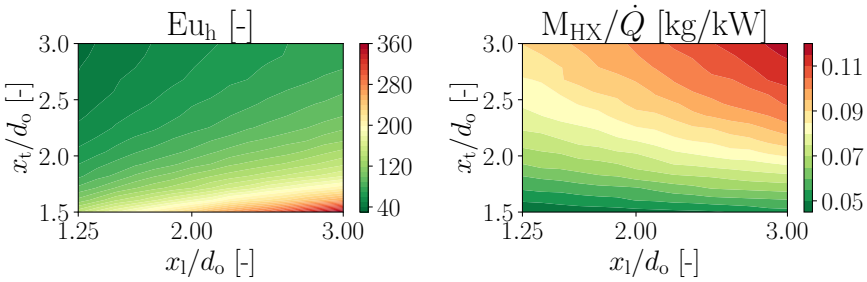

Figure 4.2: Effect of the dimensionless circular tube pitches on the hot-side Euler number (Eu_h and HX weight over the heat duty $M_{HX}/\dot{Q}$ for an inline bare tube bundle HX.

- Conversely, in the *integrated* design strategy, the condenser geometry is simultaneously optimized together with the CC-APU or CC-TS system design variables. The decision to solely optimize the design of the condenser, together with the system, stems from its critical effect on overall system performance. The design variables associated with each condenser topology vary depending on the selected topology and can range from 3 to 6 or more. As a consequence, the total number of design variables increases significantly for each HX whose geometry is optimized, thus increasing the computational cost associated with solving the integrated design problem.

- The *surrogate-model* (SM) strategy is aimed at demonstrating the benefits of employing a data-driven surrogate model to predict the optimal performance of the condenser within the integrated system design optimization framework. In this approach, the conventional condenser sizing model is replaced by a data-driven surrogate model that estimates the performance of an optimized condenser for given thermodynamic design specifications. The surrogate model consists of neural networks trained on datasets of optimized condenser geometries obtained using the heat exchanger sizing tool described in 3.2. The advantage of this design strategy is a drastic reduction in the computational cost. The number of design variables associated with a heat exchanger being replaced by the surrogate model is reduced from any number to always one, as explained in 4.3.4, regardless of the topology.

While for all three design strategies the primary HX core geometry is fixed to an inline tube bundle characterized by tube pitches that minimize the gas-side pressure drop, the condenser geometry and model differ depending on the adopted strategy.

The NSGA2 multi-objective optimization algorithm [21] is employed to obtain a set of Pareto-optimal solutions. The design space is constrained in all the optimizations to ensure that this is consistent with the validity range of the surrogate model. The objective functions are tailored to the specific case study under consideration. For the CC-APU design optimization, the primary goals are the minimization of the ORC system mass (M_{ORC}) and the maximization of the net power output ($\dot{W}_{net,ORC}$). Conversely,

the CC-TS design optimization objective is to identify a set of Pareto-optimal solutions that minimize the thrust-specific fuel consumption TSFC = $\dot{m}_f / T_{tot}$ while simultaneously maximizing the mass-specific power generated by the waste heat recovery unit $e_{ORC} = \dot{W}_{ORC} / M_{ORC}$. The resulting Pareto front is independent of the aircraft model and mission constraints, providing a clear representation of the trade-offs between the fuel mass flow rate and the corresponding mass-specific power of the ORC WHR unit.

4.3.4. SURROGATE MODEL

Figure 4.3 shows the flow chart of the proposed methodology to derive a data-driven surrogate model of an optimally designed heat exchanger. Each action of the flow chart is described in the following. The first action consists of generating a database of optimized HX geometries for a range of process conditions and for each considered HX topology (Sec. 4.3.4). The database contains n_s number of samples, each identified by a specific set of thermodynamic specifications, and a set of Pareto solutions featuring minimum mass (M_{HX}) and air-side pressure drop (ΔP_c). After non-dimensionalizing the Pareto fronts in a so-called fitting space, the data are post-processed by removing outliers and Pareto fronts whose fit accuracy is too low (i.e., the R2 score is lower than 0.95) until a dataset suitable for regression analysis is generated (Sec. 4.3.4). This dataset is then used to train the surrogate model in predicting the Pareto front of a heat exchanger topology for a given set of dimensionless thermodynamic inputs (Sec. 4.3.4).

DATASET OF OPTIMAL HEAT EXCHANGER DESIGNS

First, to generate the dataset of optimal HX designs, the values of geometric parameters that are not optimized, such as the flat tube height and thickness of the fins and microchannels, need to be specified. Similarly, the lower x_D^L and upper x_D^U bounds of the optimization variables must also be defined, see Table 5.4. These values are chosen based on structural and manufacturability considerations as well as the applicability range of the adopted heat transfer coefficient and friction factor correlations. The width-over-height ratio (AR) of the HX is also allowed to vary between 0.5 and 2 to increase the design space of the HX. The multi-objective optimization of the HX design is subjected to two constraints. First, the working fluid pressure drop (ΔP_{wf}) cannot exceed the threshold $\lambda_P = 5\%$ of the working fluid side inlet pressure ($P_{wf,in}$), such that its effect on the performance of the system is negligible. Second, the value of the depth of the HX core, i.e., the flat tube width, must be larger than a set threshold $\lambda_Z = 0.025$ m, due to manufacturability considerations. Thus, being x_D the array of geometry-related optimization variables, the HX design problem can be formulated as the following constrained multi-objective optimization problem

$$\begin{aligned} \text{minimize} \quad & M_{HX}(x_D)\,;\, \Delta P_c(x_D), \\ \text{subject to} \quad & \Delta P_{wf} \leq \lambda_P\, P_{wf,in}, \\ & Z \geq \lambda_Z, \\ & x_D^L \leq x_D \leq x_D^U\,. \end{aligned} \tag{4.2}$$

Next, the thermodynamic specifications obtained from the cycle calculation and required to solve the HX design problem are nondimensionalized to be independent of the

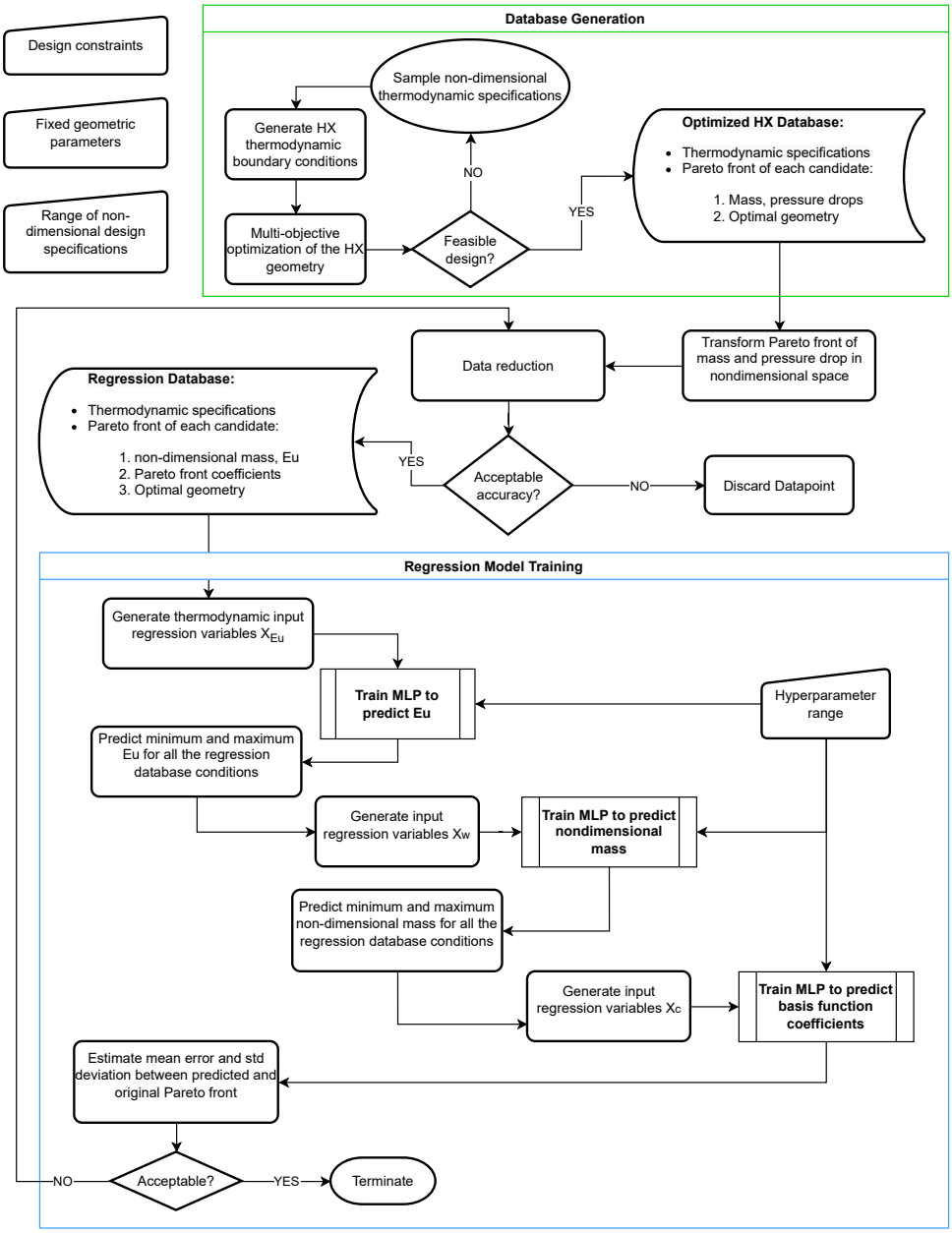

Figure 4.3: Flowchart of the methodology used to train the HX surrogate model.

Table 4.1: Overview of the chosen HX geometry-specific parameters and their bounds.

	variable	bounds	parameter	imposed value
HX	w_{mc} [mm]	1 - 2.5	h_{ft} [mm]	1.8
	AR [−]	0.5 - 2	t_{mc} [mm]	0.2
			A_{fr} [m^2]	1
Louvered fins	F_h [mm]	6 - 16	t_f [mm]	0.2
	F_p [mm]	1.2 - 4	L_l [mm]	0.9 F_h
	L_α [°]	10 - 30	-	
	L_p [mm]	1.2 - 3.6	-	
Offset-strip fins	α [−]	0.1 - 1	t_f [mm]	0.2
	δ [−]	0.012 - 0.037	-	
	γ [−]	0.038 - 0.122	-	

HX size, working fluid, and ambient conditions. These are

$$\mathrm{TD}_{in} = \left[P_{g,in}, P_{wf,in}, T_{g,in}, T_{wf,in}, \dot{m}_g, \dot{m}_{wf}, \dot{Q}\right]. \tag{4.3}$$

Assuming that the working fluid at the outlet of the condenser is saturated liquid conditions, and that the working fluid side pressure drop must satisfy Equation 4.2, the number of required inputs decreases from 7 to 6, because the specified heat duty can be defined as

$$\dot{Q} = \dot{m}_{wf}\left(H_{wf}(T_{wf,in}, P_{wf,in}) - (H_{wf}(0.95P_{wf,in}, v_q = 0)\right). \tag{4.4}$$

In most cases, the working fluid pressure losses over desuperheating are negligible; therefore, the input vector of Equation 4.3 can be replaced with a set of dimensionless inputs that reads

$$\tilde{\mathrm{TD}}_{in} = \begin{cases} Re_{g,in} = \frac{\dot{m}_g d_{ref}}{\mu(T_{g,in}) A_{fr}} \\ R = \dot{m}_{wf}/\dot{m}_g \\ \tilde{P}_g = P_{g,in}/P_{g,ref} \\ \tilde{T}_g = T_{g,in}/T_{g,ref} \\ \tilde{T}_{cnd} = T_{cnd}/T_{boil} \\ \delta_{dsh} = \frac{T_{wf,in} - T_{cnd}}{T_{cnd}} \end{cases} \tag{4.5}$$

where A_{fr} is the HX frontal area, d_{ref} is the reference dimension for the Reynolds number, which for the considered condenser topology is assumed to be equal to the flat tube height, T_{cnd} is the condensation temperature, and T_{boil} is the boiling temperature of the working fluid. Moreover, the gas side reference temperature ($T_{g,ref}$) and pressure ($P_{g,ref}$) are chosen to be 273 K and 1 bar, respectively. The chosen dimensionless groups are not only valid for different HX topologies, sizes, and temperatures but also for different working fluids. Table 4.2 reports the chosen range for the dimensionless input quantities in Equation 4.5. The upper and lower limits are defined based on knowledge about the design space of ORC systems for airborne applications (see Refs. [10] and [22]).

Note that not all the combinations of the parameters listed in Table 4.2 generate a valid set of design specifications. The outlet cold stream temperature must be less than

Table 4.2: Bounds of the dimensionless variables of the input vector $\tilde{\mathrm{TD}}_{\mathrm{in}}$, Eq. (4.5).

	$Re_{\mathrm{g,in}}$	R	$\tilde{P}_{\mathrm{g}}$	$\tilde{T}_{\mathrm{g}}$	$\tilde{T}_{\mathrm{cnd}}$	δ_{dsh}
min	600	0.075	0.4	1	1.13	0
max	1200	0.16	1.01	1.148	1.21	0.2

the working fluid outlet condensation temperature. Thus, it can be demonstrated that the input specifications are constrained by

$$\tilde{T}_g\, T_{\mathrm{ref}} + R\frac{\Delta H_{\mathrm{wf}}(\tilde{T}_{\mathrm{cnd}}, \delta_{\mathrm{dsh}})}{c_{\bar{p}_g}} - \tilde{T}_{\mathrm{cnd}}\, T_{\mathrm{boil}} <= 0\,, \tag{4.6}$$

in which

$$c_{\bar{p}_g} = c_p\left(\tilde{T}_g\, T_{\mathrm{ref}} + R\frac{\Delta H_{\mathrm{wf}}(\tilde{T}_{\mathrm{cnd}}, \delta_{\mathrm{dsh}})}{2c_{p_g}(\tilde{T}_g, \tilde{P}_g)}, \tilde{P}_g P_{\mathrm{ref}}\right)$$

is an estimate of the isobaric specific heat capacity of the gas stream, i.e., of the cold air in the case of the condenser. The working fluid enthalpy drop ΔH_{wf} is estimated from Equation 4.4. The dataset for each HX topology is constructed using Latin hypercube sampling to generate approximately 3000 samples of $\mathrm{TD}_{\mathrm{in}}$. The HX design is optimized only if the constraint of Equation 4.6 is satisfied.

DATA REDUCTION

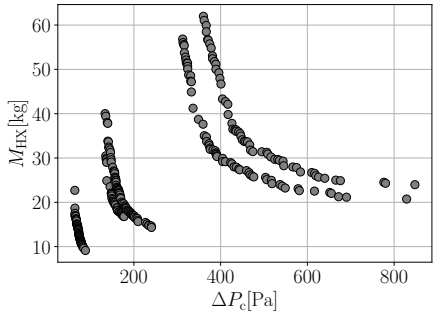

Figure 4.4: Pareto front in the original dimensional space.

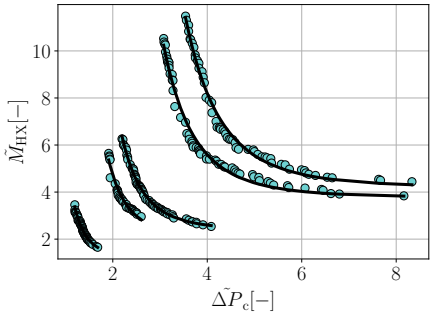

Figure 4.5: Pareto fronts in the dimensionless space.

Figure 4.4 shows five exemplary sets of Pareto-optimal solutions in terms of mass and air side pressure drop for flat tube microchannel condensers with louvered fins. Each Pareto front is associated with a different set of thermodynamic design specifications, while each point of a Pareto curve is characterized by a different core geometry. Data reduction is necessary to (i) facilitate the regression analysis, (ii) make the optimal designs dimensionally independent of the HX size, and (iii) identify and remove outliers. More in detail, the reduction of the number of regression model outputs is achieved by

fitting the Pareto fronts with common basis functions and coefficients that are unique for each curve. In mathematical form, an arbitrary set of Pareto optimal solutions $\{PF\}$ is approximated in a dimensionless plane $(\tilde{x}, \tilde{y}) \in \mathrm{R}^2$ as

$$\tilde{y} = \phi(\tilde{x}, c^*) \ , \text{with} \ \ \tilde{x}_{\min} \leq \tilde{x} \leq \tilde{x}_{\max} \ , \tag{4.7}$$

where ϕ is a fitting basis function, and c^* are curve-specific coefficients. The optimal basis function is obtained by testing all the functions of a predefined set and identifying the one that fits the largest number of Pareto curves with a coefficient of determination exceeding a specified threshold. By normalizing the heat exchanger mass and the pressure drop over the cold air side of each optimal solution as

$$\begin{cases} \tilde{M}_{\mathrm{HX}} = \dfrac{M_{\mathrm{HX}}}{\rho_{\mathrm{mat}} \ A_{\mathrm{fr}} \ d_{\mathrm{ref}}} \\ \\ \tilde{\Delta P}_{\mathrm{c}} = \dfrac{\rho_{c,\mathrm{in}} \Delta P_{\mathrm{c}} \ A_{\mathrm{fr}}^2}{\dot{m}_{\mathrm{c}}^2} \ , \end{cases} \tag{4.8}$$

the basis function form

$$\phi(\tilde{x}) = \left(\frac{\tilde{x}}{c_0^2} \right)^{-c_1^2} + c_2^{5/3} \tag{4.9}$$

is capable of fitting over 90% of the Pareto fronts with R^2 scores above 95%. The optimal basis function selection depends on both the heat exchanger topology and the considered thermodynamic design space. Figure 4.5 shows the sets of Pareto-optimal solutions of Figure 4.4 in the dimensionless plane; the solid black lines are the fits of the dimensionless Pareto curves obtained with Equation 4.9. Because the accuracy of the basis function depends on the number of data points used to fit its coefficients, the Pareto fronts featuring fewer than 6 design points are discarded.
The range of validity of each fitted basis function is determined by identifying the minimum and maximum Euler number of each curve, i.e., the minimum and maximum value of the horizontal coordinate of each Pareto Front. The dataset used to fit the surrogate model is indicated in the flow chart of Figure 4.3 as the regression database. This is constructed by associating the coefficients c^* and the two Euler numbers that define the validity range of the fitted basis function to each set of design specifications used to generate a Pareto front.

REGRESSION METHODOLOGY

The objective of the surrogate model is to predict the set of Pareto-optimal solutions given a feasible set of design specifications. It is constructed by chaining three multilayer perceptrons (MLP). The first MLP predicts the maximum and minimum dimensionless gas-side pressure drop, the second MLP predicts the corresponding dimensionless mass, and the third MLP predicts the coefficients of the basis function ϕ that best fit the Pareto curves. The benefit of using cascading perceptrons is the possibility of training simpler yet more specialized models, which, despite the limited size of the training dataset, can achieve higher accuracy over multiple dependency structures compared to

one single, more complex regression model. Each MLP comprises multiple layers of interconnected nodes, including an input layer, one or more hidden layers, and an output layer. Each connection between nodes is associated with a weight, and each node within the hidden layers incorporates activation functions that introduce non-linearity into the model. This characteristic makes MLP particularly suitable for strongly nonlinear regression problems. The MLP operates in a feed-forward manner: the information flows from the input layer through the hidden layers to the output layer. The training of the network is conducted using the Adam algorithm [23], a gradient-based optimizer with adaptive learning rate and momentum term, which leverages gradients computed via backpropagation [24] to efficiently adjust the network weights and biases. The accuracy of the regression models depends on their hyperparameters, which need to be tuned in the validation procedure. The hyperparameters are defined as parameters external to the model and whose value cannot be estimated from the data [25].

Table 4.3: Hyperparameter range and optimal set for the MLPs that predict the cold-side Euler number (Eu), the dimensionless core weight (w), and basis function coefficients (c).

Hyperparameter	Range	MLP (Eu)	MLP (w)	MLP (c)
Layers	3 - 4	3	3	3
Hidden nodes	64 - 320	256	256	256
Regularization strength	10^{-5} - 10^{-2}	10^{-5}	10^{-4}	10^{-4}

Due to the relatively small size of the MLPs, a grid search algorithm was employed to determine the optimal settings for each network. This required constructing a multilayer perceptron for each combination of the parameters in Table 4.3, using the open-source Scikit-learn library [26]. The optimal set of parameters for each MLP is selected as the one that minimizes the mean squared error (MSE) loss function

$$\mathrm{MSE}(\theta) = \frac{1}{n_\mathrm{s}} \sum_{i=1}^{n_\mathrm{s}} (\hat{y}_i - y_i)^2 \,, \tag{4.10}$$

in which θ is the set of hyperparameters, n_s is the number of samples, and $\hat{y}_i$ is the value estimated with the model.

The choice of input features for each neural network strongly affects the accuracy of the model. To identify which variables are most suited for the regression problem, the input vector for each MLP is obtained by performing a variance-based sensitivity analysis using the first and second-order Sobol indices [27]. The outcome of this analysis is summarized here. The input vector of the MLP that predicts the minimum and maximum Euler number of the Pareto front reads

$$\mathrm{X_{Eu}} = \left[Re_\mathrm{g,in} \,,\, R \,,\, \frac{\Delta T_\mathrm{lm,1} \dot{Q}_\mathrm{dsh}}{\dot{Q}\, T_\mathrm{g,in}} \,,\, \frac{\Delta T_\mathrm{lm,2}}{T_\mathrm{g,in}} \left(1 - \frac{\dot{Q}_\mathrm{dsh}}{\dot{Q}}\right) \,,\, \delta_\mathrm{dsh} \,,\, \frac{\rho_\mathrm{g,out}}{\rho_\mathrm{g,in}} \right]. \tag{4.11}$$

In addition to the dimensionless design variables $Re_\mathrm{g,in}$, R, and δ_dsh used to generate the optimal datasets of HX designs, the input vector of the first perceptron ($\mathrm{X_{Eu}}$) includes the gas-side density ratio across the condenser core ($\rho_\mathrm{g,out}/\rho_\mathrm{g,in}$) and two terms that are

proportional to the mean logarithmic temperature difference associated with the two main sections of the condenser, namely that of the desuperheating section $\Delta T_{\text{lm},1}$ and that of condensation section $\Delta T_{\text{lm},2}$. These temperature differences are estimated as

$$\Delta T_{\text{lm},1} = \frac{T_{\text{wf,in}} - T_{\text{cnd}} - \dfrac{\dot{Q}_{\text{dsh}}}{\dot{m}_{\text{c}} c_p}}{\ln\left[\dfrac{T_{\text{wf,in}} - T_{\text{c,in}} - \dot{Q}/(\dot{m}_{\text{c}} c_p)}{T_{\text{cnd}} - T_{\text{c,in}} - (\dot{Q} - \dot{Q}_{\text{dsh}})/(\dot{m}_{\text{c}} c_p)}\right]} \tag{4.12}$$

$$\Delta T_{\text{lm},2} = \frac{\dfrac{\dot{Q}_{\text{dsh}} - \dot{Q}}{\dot{m}_{\text{c}} c_p}}{\ln\left[\dfrac{T_{\text{cnd}} - T_{\text{c,in}} - (\dot{Q}_{\text{dsh}} - \dot{Q})/(\dot{m}_{\text{c}} c_p)}{T_{\text{cnd}} - T_{\text{g,in}}}\right]}. \tag{4.13}$$

These equations imply the assumptions that the specific heat capacity of the cooling air ($c_{p_{\text{c}}}$) is constant and that the pressure drop has a negligible effect on the enthalpy decrease of the condensing fluid. These two temperature differences are used as input features to the first MLP by rescaling them with the corresponding fraction of thermal power exchanged in their corresponding section, i.e., desuperheating or condensing. These are nondimensionalized with the gas-side inlet temperature ($T_{\text{g,in}}$).

The predicted Euler numbers are then added to X_{Eu} together with a dimensional scaling parameter, namely the heat duty per frontal area of the HX, to form the input vector of the second MLP

$$\text{X}_{\text{w}} = \left[X_{\text{Eu}}\,,\ \frac{\dot{Q}}{A_{\text{fr}}}\,,\ Eu_{\text{min}}\,,\ Eu_{\text{max}} - Eu_{\text{min}}\right], \tag{4.14}$$

which predicts the minimum w_{min} and maximum w_{max} dimensionless weight of the Pareto curves.

Similarly, the predicted dimensionless weights are included in the input vector of the third MLP, which reads

$$\text{X}_{\text{c}} = \left[Re_{\text{c,in}}\,,\ R\,,\ \frac{\Delta T_{\text{lm},1}}{\Delta T_{\text{lm},2}}\,,\ \delta_{\text{dsh}}\,,\ \frac{\dot{Q}}{A_{\text{fr}}}\,,\ Eu_{\text{min}}\,,\ w_{\text{max}} - w_{\text{min}}\right]. \tag{4.15}$$

The final outputs are the coefficients c^* of the basis function ϕ which approximates the shape of the Pareto front in the dimensionless space for a given HX topology and a given set of design specifications. The predicted dimensionless Pareto front can then be projected into the physical space according to Equation 4.8 by knowing the HX frontal area, material density, gas-side inlet conditions, and reference diameter.

If the surrogate model is used to explore the design space of a HX, the degrees of freedom associated with a given design reduce to one, namely the dimensionless air side pressure drop ($\Delta\tilde{P}_{\text{c}}{}^*$), which, in the case of the condenser, is the metric that influences the overall system performance the most. However, the use of this parameter is impractical, as there is no way to know in advance if the value of a selected dimensionless pressure drop is within the range of values of the predicted Pareto front. To overcome this

problem, an optimal HX design on the predicted Pareto front is selected by specifying the normalized optimal Euler number ratio

$$Eu^* = \frac{\Delta\tilde{P}_c^* - Eu_{\min}}{Eu_{\max} - Eu_{\min}}, \tag{4.16}$$

whose values range between 0 and 1. The lower value indicates a design that minimizes the pressure drop associated with both sides of the HX regardless of the weight, while the upper value represents a geometry that minimizes the HX weight at the cost of high-pressure drops.

MODEL ACCURACY

Each MLP model is trained on 85% of the post-processed dataset, of which 10% is used as a validation set. The remaining 15% is used as a test set to assess the accuracy of the models. Figure 4.6 allows for comparing the prediction of each MLP corresponding to the surrogate model of the flat tube and louvered fin condenser with the values of the whole dataset: over 95% of the points are contained in a ±15% relative uncertainty interval. Table 4.4 reports the accuracy of the three neural networks that constitute the surrogate model, in terms of mean percentage error (MPE) and mean absolute percentage error (MAPE).

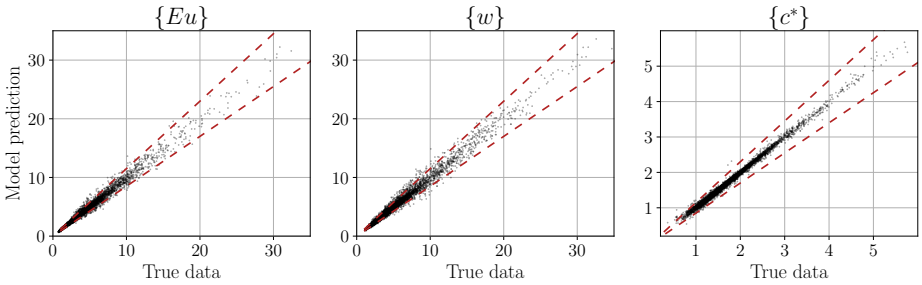

Figure 4.6: Surrogate model predictions plotted against the values of the dataset for flat tube louvered fins condensers. The dashed lines indicate the ±15% uncertainty band.

Table 4.4: Accuracy of the three MLP models

Condenser core topology	Output	R2 score	MPE %	MAPE %
flat tubes & louvered fins (lf)	Eu	0.985	0.25	5.31
	w	0.977	-0.77	5.97
	c	0.991	-0.30	2.49
flat tubes & offset-strip fins (osf)	Eu	0.969	-0.24	6.85
	w	0.934	0.29	8.39
	c	0.984	0.81	4.16

Although the neural network associated with the surrogate model of the optimal louvered-fins condenser is affected by lower error compared to that of condensers with offset-

strip fins, the accuracy of both surrogate models is deemed satisfactory. For given design specifications of the condenser, the pressure drop and mass reduction that can be achieved through design optimization of the geometry are usually much larger than the uncertainty associated with the predictions of the surrogate model. Moreover, the uncertainty related to the adopted friction factor and heat transfer coefficient correlations is of the order of 10-15%, thus also larger than the uncertainty related to the surrogate models.

4.4. RESULTS

This simulation and design optimization method has been applied to two case studies, namely that of a combined cycle APU and that of a combined cycle turboshaft aero engine providing power to an electrically driven distributed propulsion system. The objectives of this study are (i) to investigate the performance improvements achievable by simultaneously optimizing the HX geometry and thermodynamic cycle for an airborne ORC WHR unit, (ii) to compare two condenser topologies in terms of minimum weight and air-side pressure drop for the considered applications, and (iii) to demonstrate the effectiveness of the proposed surrogate modeling technique for the preliminary design optimization of aerospace-grade thermal systems.

4.4.1. CC-APU

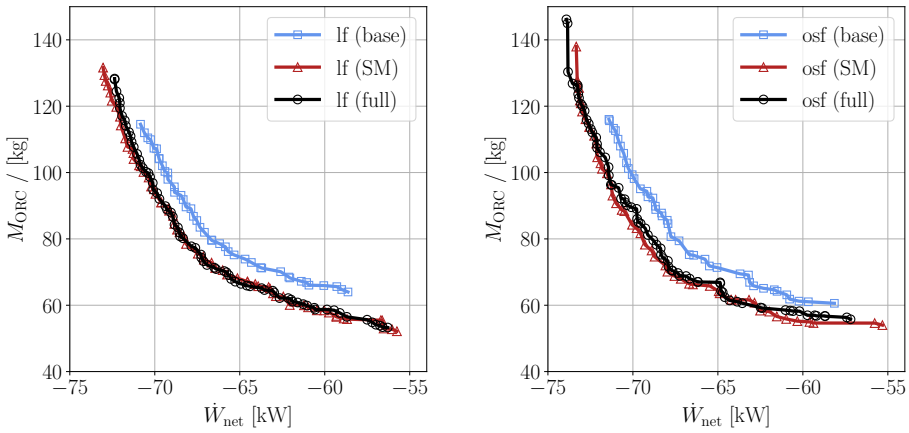

(a) Results for the flat tube microchannel and louvered fins condenser

(b) Results for the flat tube microchannel and offset-strip fins condenser

Figure 4.7: Pareto optimal designs of the CC-APU ORC WHR unit obtained by (i) optimizing the cycle with a fixed condenser geometry (base), (ii) performing an integrated condenser geometry-and-cycle optimization (full), and (iii) using the optimal condenser surrogate model (SM).

The results of the optimizations of the design of the CC-APU WHR system according to the design strategies highlighted in Section 4.3.3 are reported in Figure 4.7 for two condenser topologies, namely a flat tube microchannel condenser equipped with louvered

fins (lf) or with offset strip fins (osf). The condenser geometry used in the design strategy # 1 (baseline) is reported in Table 4.5. These values were selected based on previous results to enable a feasible design of the condenser across a wide range of thermodynamic specifications [10]. Table 4.6 reports the upper bounds (UB) and lower bounds (LB) of the thermodynamic cycle design variables considered in all three design strategies.

Table 4.5: Values of baseline condenser geometric parameters.

Parameter	Value	Units	Parameter	Value	Units
w_{mc}	1.1	mm	L_p	2.6	mm
AR	1	-	α	0.32	-
F_h	9	mm	δ	0.03	-
F_p	2.6	mm	γ	0.077	-
L_α	26	°			

Table 4.6: CC-APU cycle design variables and their corresponding bounds.

Variables	Description (Units)	LB	UB
T_{min}	Minimum ORC temperature (K)	367	379
T_{max}	Maximum ORC temperature (K)	517	549
P_{max}/P_{crit}	Maximum over critical ORC pressure ratio (-)	1.04	1.48
$\Delta T_{pp,ev}$	Evaporator pinch point ΔT (K)	10	50
$\Delta T_{pp,cnd}$	Condenser pinch point ΔT (K)	15	50

Figure 4.7 displays the Pareto fronts associated with the design of the ORC system and highlights the relationship between the system net power $\dot{W}_{net}$ output and mass M_{ORC}. The net power output is displayed with negative values for visualization purposes: system designs featuring condensers optimized for low pressure drops are on the leftmost side of the Pareto front in analogy with the trend of the Pareto fronts in Figure 4.4. Several conclusions can be drawn by comparing the light blue and black lines of Figure 4.7a and 4.7b.

1. For the same net power output, the value of the weight of the WHR unit designed with a fixed condenser geometry is, on average, 10-15% larger than that of a system designed with the integrated HX design optimization strategy, and this is valid for both condenser topologies.

2. Offset strip fin condensers enable the design of systems that feature a higher maximum net power output for similar weight if compared to systems featuring a condenser with louvered fins. However, condensers with louvered fins allow for the design of lighter systems at the cost of larger pressure drops and thus lower net power output. It follows that, depending on the chosen trade-off between weight and net power output of the ORC system, the optimal HX topology changes.

3. The set of Pareto optimal solutions obtained with the condenser equipped with the offset strip fins covers a wider net power output and weight range compared to the solutions obtained with the louvered fins.

These results demonstrate that the optimization of the HX geometry together with the thermodynamic cycle, although computationally more expensive, allows for obtaining preliminary system designs whose performance is significantly improved with respect to designs obtained via conventional methods. Moreover, this integrated system design method allows for exploring a wider design space compared to a design strategy for which the HX geometry is fixed a priori.

Regarding the accuracy of the surrogate models, it can be observed that the mean relative deviation between the Pareto front associated with the use of the condenser surrogate model and that associated with the use of the detailed model is 1.1% and 2.3% for the louvered fins and offset strip fin condenser topologies, respectively. This metric is calculated as

$$\bar{\epsilon_r} = \frac{1}{N_{\text{CP}}} \sum_{i=0}^{N_{\text{CP}}} \frac{|L_{\text{SM}}(x_i) - L_{\text{full}}(x_i)|}{L_{\text{full}}(x_i)} \tag{4.17}$$

in which N_{CP} is the number of comparison points between the two curves, L_{full} is the linear interpolation of the Pareto front associated with the integrated system optimization based on detailed models, and L_{SM} is the Pareto front associated the integrated system optimization based on surrogate models. The difference between the black and red curves in Figures 4.7a and 4.7b can be considered negligible from an engineering point of view. This proves that, as far as this study is concerned, the surrogate model-based design strategy (SM) can be used to generate system Pareto fronts that are analogous to the ones obtained with the integrated optimization strategy employing detailed models, but at a much lower computational cost, as highlighted in Table 4.7.

Two factors contribute to the computational time reduction: 1) the dimensionality of the optimization problem is reduced, namely the number of optimization variables (N_{opt}) decreases, together with the population size and number of generations required for the genetic algorithm to reach convergence; 2) since the surrogate model function evaluation is two orders of magnitude faster than the evaluation of the condenser sizing model, the evaluation time of the average objective function decreases by about 20%.

Table 4.7: Computational time of the three design optimization strategies applied to the CC-APU test case. The optimization computations are performed with an 8-core personal computer whose processor is an AMD Ryzen 4000.

Design strategy	N_{opt}	Population	Generations	Time /min
Baseline	5	48	48	16
Detailed (lf)	11	80	80	42
Detailed (osf)	10	88	80	45
SM	6	48	48	13

4.4.2. CC-TS

The results of this design optimization case are reported in terms of Pareto optimal solutions for minimum TSFC and maximum mass-specific power of the system. Again, each curve in Figure 4.8 corresponds to the solutions of the multi-objective optimization problem defined by the design strategies discussed in Section 4.3.3. The mass-specific power e_{ORC} is displayed as negative values to visualize a Pareto type IV distribution in

analogy with the condenser Pareto curve. The optimization calculations have been performed for systems in which the condenser is a flat tube microchannel heat exchanger with louvered fins, in analogy to what is documented in the study of [22]. The geometric parameters of the condenser used for design strategy #1 (baseline) are selected based on the system optimization results performed by [22] and are reported in Table 4.8.

Table 4.8: Values of the geometric parameters of the condenser used in the baseline design strategy for the CC-TS case study. The fins are of the louvered type.

Parameter	Value	Units	Parameter	Value	Units
w_{mc}	1.28	mm	F_p	1.4	mm
AR	0.66	-	L_α	29	°
F_h	10	mm	L_p	1.4	mm

Table 4.9: CC-TS system design variables, excluding those related to the condenser geometry, and their corresponding bounds.

Variables	Description (Units)	LB	UB
T_{min}	Minimum ORC temperature (K)	353	413
T_{max}	Maximum ORC temperature (K)	520	570
P_{max}/P_{crit}	Maximum over critical ORC pressure ratio (-)	1.15	1.45
$\Delta T_{pp,ev}$	Evaporator pinch point ΔT (K)	60	110
$\Delta T_{pp,cnd}$	Condenser pinch point ΔT (K)	30	90
N_p	Primary HX number of working fluid passes (-)	7	10
MFR	Ram air duct intake mass flow rate ratio (-)	0.45	0.7
θ	Condenser inclination angle (°)	50	70

The range of the optimization variables associated with the thermodynamic cycle of the WHR unit is reported in Table 4.9. Figure 4.8 shows the results of the three optimizations in terms of Pareto fronts. The results show that solutions maximizing the mass-specific power are characterized by larger specific fuel consumptions. These optimal design points feature lightweight condensers, which, however, are characterized by a significant pressure drop over the ram air path and thus additional drag. As a result, the combined cycle engine power requirement increases, and with it, the fuel consumption. Moreover, the thermodynamic cycles associated with designs whose outcome is lighter systems feature lower cycle efficiency. This effectively reduces the benefit of harvesting thermal energy from the exhaust gases to improve the combined cycle efficiency. As a result, for a fixed total thrust requirement, the fuel consumption decreases as the ORC WHR units are (i) more effective with respect to thermal energy recovery and (ii) feature ram air duct designs that cause low additional drag.

Similarly to the CC-APU case study, the application of the integrated system-HX design optimization method allows for obtaining significant performance improvement and enables the exploration of a larger design space. By fixing the ORC condenser geometry, the minimum TSFC that can be obtained is 12.91 with an ORC unit weighing 0.87 kg for every kW of net power output. However, if the HX geometry is allowed to change for every combination of system variables, the minimum TSFC is 12.85 with a

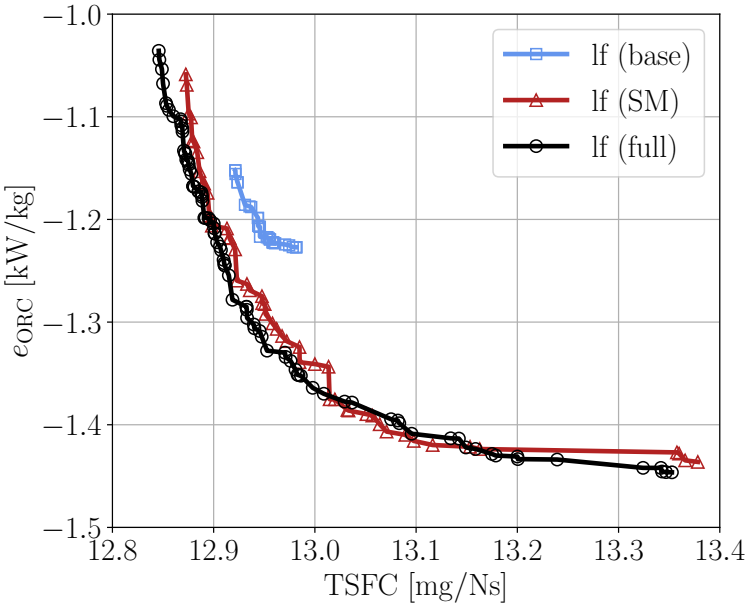

Figure 4.8: Pareto optimal designs of the CC-TS obtained by (i) optimizing the cycle with a fixed condenser geometry (base), (ii) performing an integrated condenser geometry-and-cycle optimization with detailed models, and (iii) using the optimal condenser surrogate model (SM).

specific power of the ORC unit of 1.04 kW/kg. Furthermore, the results of this case study prove that the Pareto optimal solutions in terms of system performance obtained with a standard integrated system optimization are similar to those obtained with the surrogate model at a much lower computational cost. More in detail, taking the solution of the detailed system model as a reference, the mean relative deviation between the two Pareto fronts is 2.9%. Table 4.10 reports the size of the population and the number of generations required to reach convergence for each design strategy. The average objective function evaluation time is reduced by about 22%, which is very similar to the improvement in computational efficiency determined for the CC-APU test case. The overall computational time associated with the design strategy with the surrogate model is slightly more than half of the time required with that employing the condenser sizing model. In the other case study, the total computational time benefit is more significant due to the larger impact of reducing the number of optimization variables on the total function evaluations needed to reach convergence.

4.5. CONCLUSIONS

This work contributes to the definition of a surrogate modeling methodology for optimal HX designs that can be used in conceptual design studies about advanced power and propulsion systems. This methodology is particularly suitable for airborne thermal

Table 4.10: Computational performance parameters associated with the three design optimization strategies applied to the CC-TS test case. The optimization calculations were performed with an 8-core personal computer featuring an AMD Ryzen 4000 processor.

Design strategy	N_{opt}	Population	Generations	Time /min
Baseline	8	64	48	354
Detailed (lf)	13	112	64	724
SM	9	98	48	399

systems whose performance is strongly dependent on the preliminary design of HXs, as is the case for the applications analyzed in Section 4.4. The optimal design of HXs for airborne thermal systems is inherently conditional on the design of the thermodynamic cycle. It follows that the maximum performance can be estimated only by means of an integrated system design optimization method. The computational effort of such a method is inherently large due to the large number of design parameters that need to be treated as system optimization variables. For the specific case documented here, a data-driven surrogate model of a condenser was constructed using three chained multilayer perceptrons. The neural networks are trained to predict the optimal design solutions in terms of minimum mass and pressure drop. Two suitable HX topologies were considered. The dataset used for the training and validation of the surrogate model was generated by using an in-house tool for the preliminary design and rating of heat exchangers. The design strategy relying on the surrogate model was applied to perform the preliminary design optimization of a bottoming ORC unit that harvests thermal energy from the exhaust gases of a gas turbine aero engine. The first case study considers a combined cycle power plant as an auxiliary power unit of a passenger aircraft, while the second test case is about a combined cycle turboshaft engine providing electrical power to the distributed propulsion system of a passenger aircraft.

The following conclusions are therefore drawn:

- Performance gains associated with the integrated optimization method vary depending on HX topology, application, and thermodynamic cycle. For instance, the integrated optimization of the combined-cycle auxiliary power unit (CC-APU) results in designs of systems that are $10-15\%$ lighter than the benchmark design for the same net power output. Moreover, the microchannel condenser equipped with offset strip fins features lower weight than its louvered fins counterpart for high net power outputs of the ORC unit, while the adoption of louvered fins allows for obtaining lighter system designs if higher pressure drops in the cooling air stream are acceptable. This demonstrates that the optimal HX topology depends on the system design specifications. Finally, the results of the combined-cycle turboshaft (CC-TS) case study highlight how the integrated optimization allows for obtaining a much wider range of feasible system designs compared to an optimization method for which the condenser geometry is fixed a priori.

- The proposed methodology to develop a surrogate model for the prediction of the optimal design space of a HX has proven to be effective. The use of the surrogate model enables a reduction of the computational cost of the solution of an optimal

system design problem without compromising model accuracy. The average deviations between the Pareto fronts associated with system designs obtained with the condenser surrogate model and the ones obtained with the detailed HX model range from 1% to 2.9%, depending on the case study and condenser topology. The match between the results of the integrated and surrogate model-based optimizations is deemed satisfactory as these deviations are within the uncertainty range of the models. Furthermore, the results indicate that the accuracy of the surrogate model is comparable to that of the preliminary design tool, regardless of the HX topology, although its predictive capabilities are affected by the limited dataset size.

- The benefit derived from the integrated system optimization approach is larger than the uncertainty of the surrogate model, and the computational time reduction is significant. More in detail, in addition to a decrease of $\approx 20\%$ of the time to evaluate the objective function due to the surrogate model (its evaluation time is two orders of magnitude shorter than that of the detailed model), the total number of function evaluations required to reach convergence decreases significantly. This occurs because replacing the HX sizing model with the surrogate model reduces the number of optimization variables associated with the HX geometry, thus included in the system design vector, to just one, regardless of the HX topology. For the analyzed test cases, this variable is the normalized optimal dimensionless pressure drop over the cooling air side. The replacement of more HX sizing models with data-driven surrogate models is expected to further increase the advantage in terms of computational time at the cost of increasing the uncertainty of the results. It is thus recommended to use the surrogate model in place of the sizing model for preliminary design assessments in case (i) the geometries of heat exchangers are complex, thus the number of geometric parameters to optimize is large, and (ii) the HX design has a significant effect on system performance.

The predictive capabilities of the developed surrogate model are limited by the size of the training dataset and the range of design specifications considered for its generation. To increase the validity range and accuracy of the model, future work should thus focus on the generation of a larger dataset for the training of the surrogate model, including different working fluids. Furthermore, the surrogate model could be extended to deal simultaneously with multiple HX topologies. This would eliminate the need to repeat the integrated system and component design optimization for each HX topology.

NOMENCLATURE

Roman symbols

A	Surface area [m^2]
A_0	Free flow area [m^2]
AR	HX width over height ratio [-]
c^*	Curve coefficients [-]
c_p	Specific heat capacity at constant pressure [$kg\,m^2\,s^{-2}\,K^{-1}$]
d_h	Hydraulic diameter [m]
d_o	Outer tube diameter [m]
d_i	Inner tube diameter [m]
e	Mass-specific power [$kW\,kg^{-1}$]
Eu	Euler number [-]
F_h	Fin height [m]
F_p	Fin pitch [m]
f	Friction factor [-]
g	Gravitational acceleration [$m\,s^{-2}$]
h	Heat transfer coefficient [$W\,m^{-2}\,K^{-1}$]
H	Enthalpy [$J\,kg^{-1}$]
h_{mc}	Microchannel height [m]
I_t	Tube's moment of inertia [$kg\,m^{-2}$]
j	Colburn factor [-]
k	Thermal conductivity [$W\,m^{-1}\,K^{-1}$]
L_p	Louver pitch [m]
L_l	Louver length [m]
L_α	Louver angle [°]
L_s	Length of fin strip [m]
M	Mach number [-]
	Mass [kg]
$\dot{m}$	Mass flow rate [$kg\,s^{-1}$]
n_{mc}	Number of microchannels/microtubes [-]
N_{opt}	Number of optimization variables [-]
N_p	Number of passes [-]
NTU	Number of Transfer Units [-]
Nu	Nusselt number [-]
n_z	Number of ranks per pass [-]
N_z	Total number of ranks [-]
P	Pressure [$kg\,m^{-1}s^{-2}$]
Pr	Prandtl number [-]
P_{mc}	channel or tube perimeter [m]
$\dot{Q}$	Heat duty / thermal power [W]
R	Thermal resistance [$K\,W^{-1}$]
	fluids mass flow rate ratio [-]
Re	Reynolds number [-]
T	Temperature [K]
$\tilde{T}$	Dimensionless temperature [-]
TSFC	Thrust-specific fuel cons. [mg/Ns]
t	Thickness [m]
u	Velocity [$m\,s^{-1}$]
v_q	Vapor quality [-]
w	Dimensionless weight [-]
w_{mc}	Width of the microchannel [m]
$\dot{W}$	Power [W]
X	Width [m]
	Input vector [-]
x_t	Transversal pitch [m]
x_l	Longitudinal pitch [m]
x_D	Design variables array [-]
Y	Height [m]
Z	Depth [m]

Greek symbols

α	Fin pitch over height ratio [-]
β	Heat transfer area compactness [m^{-1}]
β_s	Fluid side-specific surface area density [m^{-1}]
γ	Fin thickness over pitch ratio [-]
Δ	Difference between two values [-]
δ	Fin thickness over fin depth ratio [-]
δ_{dsh}	De-superheating degree [-]
ϵ	Effectiveness [-]
η	Efficiency [-]
θ	Inclination angle [°]
λ_P	Constraint on max. pressure loss [-]
λ_Z	Constraint on max. core depth [m]
ρ	Density [$kg\,m^{-3}$]
σ	Free flow to frontal area ratio [-]
ϕ	Basis function [-]

Subscripts

0	freestream
	overall heat transfer surface
air	Air stream
boil	boiling conditions at 1 atm
c	Cold side
cnd	Condensation
cr	Cruise operating point
crit	Critical point
CV	Control volumes
e	Secondary(extended) heat transfer area
ev	Evaporator
dsh	De-superheating
f	Fin
fr	Frontal
g	Exhaust gas
HX	Heat exchanger
in	HX inlet conditions
lm	Logarithmic mean
m	Mechanical
mat	Core material
mc	Microchannel/microtube
ORC	ORC system
p	Propulsive/propeller
pp	Pinch point
ref	Reference
sc	Subcooling
sh	Superheating
st	Structure material
t	Tube
tr	Transmission

wf	Working fluid

Superscripts

L	Lower bound
n	relative to the control volume
U	Upper bound

Abbreviations

ACM	Air cycle machine
ANN	Artificial neural network
APU	Auxiliary power unit
CC	Combined cycle
FV	Finite volume
HPC	High pressure compressor
HPT	High pressure turbine
HX	Heat exchanger
LPC	Low pressure compressor
LPT	Low pressure turbine
MAPE	Mean absolute percentage error
MB	Moving boundary
MFR	Intake mass flow rate ratio
MLP	Multi-layer perceptron
MPE	Mean percentage error
ORC	Organic Rankine cycle
SM	Surrogate model
TF	Turbofan engine
TG	Turbogenerator
TS	Turboshaft engine
VCC	Vapor compression cycle
WF	Working Fluid
WHR	Waste heat recovery

BIBLIOGRAPHY

[1] S. Lecompte, M. Van den Broek, and M. De Paepe, "Optimal selection and sizing of heat exchangers for organic Rankine cycles (ORC) based on thermo-economics", in *Proceedings of the* 15^{th} *International Heat Transfer Conference*, 2014, pp. 7381–7394. DOI: 10.1615/IHTC15.rne.008989.

[2] M. Chatzopoulou, S. Lecompte, M. De Paepe, and C. N. Markides, "Off-design optimisation of organic Rankine cycle (ORC) engines with different heat exchangers and volumetric expanders in waste heat recovery applications", *Applied Energy*, vol. 53, p. 113 442, 2019. DOI: https://doi.org/10.1016/j.apenergy.2019.113442.

[3] S. Yu, S. Jones, H. Ogawa, and N. Karwa, "Multi-objective design optimization of precoolers for hypersonic airbreathing propulsion", *Journal of Thermophysics and Heat Transfer*, vol. 31, pp. 421–433, 2016. DOI: 10.2514/1.T4921.

[4] F. Ascione, P. Colonna, and C. De Servi, "Integrated design optimization method for novel vapour-compression-cycle-based environmental control systems", *Applied Thermal Engineering*, vol. 236, p. 121 261, 2024, ISSN: 1359-4311. DOI: https://doi.org/10.1016/j.applthermaleng.2023.121261.

[5] A. Giuffre', F. Ascione, P. Colonna, and C. De Servi, "Integrated design optimization of environmental control systems for next-generation aircraft", *Journal of Aircraft*, pp. 1–18, 2025. DOI: 10.2514/1.C038093.

[6] L. Yang, Z.-Y. Li, L.-L. Shao, and C.-L. Zhang, "Model-based dimensionless neural networks for fin-and-tube condenser performance evaluation", *International Journal of Refrigeration*, vol. 48, pp. 1–9, 2014, ISSN: 0140-7007. DOI: https://doi.org/10.1016/j.ijrefrig.2014.01.006.

[7] M. Mohanraj, S. Jayaraj, and C. Muraleedharan, "Applications of artificial neural networks for thermal analysis of heat exchangers – a review", *International Journal of Thermal Sciences*, vol. 90, pp. 150–172, 2015, ISSN: 1290-0729. DOI: https://doi.org/10.1016/j.ijthermalsci.2014.11.030.

[8] J. P. González, K. Ankobea-Ansah, Q. Peng, and C. M. Hall, "On the integration of physics-based and data-driven models for the prediction of gas exchange processes on a modern diesel engine", *Proceedings of the Institution of Mechanical Engineers, Part D: Journal of Automobile Engineering*, vol. 236, no. 5, pp. 857–871, 2022. DOI: 10.1177/09544070211031401.

[9] A. Giuffre', F. Ascione, C. D. Servi, and M. Pini, "Data-driven modeling of high-speed centrifugal compressors for aircraft environmental control systems", *International Journal of Refrigeration*, vol. 151, pp. 354–369, 2023, ISSN: 0140-7007. DOI: https://doi.org/10.1016/j.ijrefrig.2023.03.019.

[10] D. Krempus, F. Beltrame, M. Majer, *et al.*, "Organic Rankine cycle waste heat recovery systems for aircraft auxiliary power units", *Journal of the Global Power and Propulsion Society*, vol. 9, 2025. DOI: 10.33737/jgpps/204721.

[11] P. Schmollgruber, O. Atinault, I. Cafarelli, *et al.*, "Multidisciplinary exploration of DRAGON: An ONERA hybrid electric distributed propulsion concept", in *AIAA Scitech 2019 Forum*, American Institute of Aeronautics and Astronautics Inc., 2019, pp. 1–27. DOI: 10.2514/6.2019-1585.

[12] I. H. Bell, J. Wronski, S. Quoilin, and V. Lemort, "Pure and pseudo-pure fluid thermophysical property evaluation and the open-source thermophysical property library coolprop", *Industrial & Engineering Chemistry Research*, vol. 53, no. 6, pp. 2498–2508, 2014. DOI: 10.1021/ie4033999.

[13] P. Colonna and T. van der Stelt, *Fluidprop (version 3.1): A program for the estimation of thermophysical properties of fluids*, 2019. [Online]. Available: https://asimptote.com/fluidprop/.

[14] H. D. Kwak, S. Kwon, and C. H. Choi, "Performance assessment of electrically driven pump-fed LOX/kerosene cycle rocket engine: Comparison with gas generator cycle", *Aerospace Science and Technology*, vol. 77, pp. 67–82, Jun. 2018, ISSN: 1270-9638. DOI: 10.1016/J.AST.2018.02.033.

[15] F. Beltrame, L. Van Dongen, C. M. De Servi, and P. Colonna, "Optimal design of a ram air cooling duct housing the condenser of an airborne orc whr unit", in *Proceedings of Global Power and Propulsion Society*, vol. GPPS Chania 2024, 2024. DOI: 10.33737/gpps24-tc-107.

[16] M. Van Der Geest, H. Polinder, J. A. Ferreira, and M. Christmann, "Power Density Limits and Design Trends of High-speed Permanent Magnet Synchronous Machines", *IEEE Transactions on Transportation Electrification*, vol. 1, pp. 266–276, 3 2015, ISSN: 23327782. DOI: 10.1109/TTE.2015.2475751.

[17] GREThh, *Echtherm*, https://greth.fr/en/echtherm/, 2024.

[18] K. Guo, N. Zhang, and R. Smith, "Design optimization of multi-stream plate-fin heat exchangers with multiple fin types", *Applied Thermal Engineering*, vol. 131, pp. 30–40, 2018. DOI: 10.1016/j.applthermaleng.2017.11.099.

[19] Kaltra GmbH, "Microchannel condensers: Heat exchangers for condenser applications", Tech. Rep., 2020, accessed on 17 January 2025. [Online]. Available: %5Curl%7Bhttps://www.kaltra.com/wp-content/uploads/2020/04/TM_Microchannel-Condensers_Ver.3.0_EN.pdf%7D.

[20] W.-G. Kim, S.-N. Yin, W.-S. Ryu, J.-H. Chang, and S.-J. Kim, "Tension and creep design stresses of the "hastelloy-X" alloy for high-temperature gas-cooled reactors", *Materials Science and Engineering: A*, vol. 483-484, pp. 495–497, 2008, 14th International Conference on the Strength of Materials, ISSN: 0921-5093. DOI: https://doi.org/10.1016/j.msea.2006.12.184.

[21] K. Deb, A. Pratap, S. Agarwal, and T. Meyarivan, "A fast and elitist multiobjective genetic algorithm: NSGA-II", *IEEE Transactions on Evolutionary Computation*, vol. 6, no. 2, pp. 182–197, 2002. DOI: 10.1109/4235.996017.

[22] D. Krempus, F. Beltrame, M. Majer, C. M. De Servi, and R. Vos, "Orc waste heat recovery system for the turboshaft engines of turboelectric aircraft: Correction", in *TU Delft Flight Performance and Propulsion*, vol. 10^{th} EUCASS, 2023. [Online]. Available: https://resolver.tudelft.nl/uuid:3eca4e81-1449-4cce-8e6c-cf8d2929d6ea.

[23] D. Kingma and J. Ba, "Adam: A method for stochastic optimization", in *International Conference on Learning Representations (ICLR)*, San Diego, CA, USA, 2015.

[24] S. Haykin, *Neural Networks: A Comprehensive Foundation*. Prentice Hall, 1999.

[25] M. Kuhn and K. Johnson, *Applied predictive modeling*. Springer, 2023. DOI: http://dx.doi.org/10.1007/978-1-4614-6849-3.

[26] F. Pedregosa, G. Varoquaux, A. Gramfort, *et al.*, "Scikit-learn: Machine learning in Python", *Journal of Machine Learning Research*, vol. 12, pp. 2825–2830, 2011.

[27] I. Sobol, "Global sensitivity indices for nonlinear mathematical models and their Monte Carlo estimates", *Mathematics and Computers in Simulation*, vol. 55, no. 1, pp. 271–280, 2001, The Second IMACS Seminar on Monte Carlo Methods, ISSN: 0378-4754. DOI: https://doi.org/10.1016/S0378-4754(00)00270-6.

5

OPTIMAL DESIGN OF RAM AIR COOLING DUCTS HOUSING COMPACT HEAT EXCHANGERS FOR AIRBORNE THERMAL SYSTEMS

Science is a way of thinking
much more than it is a body of knowledge

Carl Sagan

Parts of this chapter have been published in:

F. Beltrame, L.J. Van Dongen, C.M. De Servi and P. Colonna, "Optimal design of a ram air cooling duct housing the condenser of an airborne ORC WHR unit", *Proceedings of Global Power and Propulsion Society*, 2024, issn 2504-4400, DOI: https://doi.org/10.33737/gpps24-tc-107

Abstract

A key challenge in the implementation of ORC systems for airborne applications is the design of compact, aerodynamically efficient ram air ducts for condenser cooling. Although the use of ram air is a lightweight and simple cooling solution, it introduces additional aerodynamic drag, which diminishes the overall fuel savings obtained through the use of the ORC unit. Similar thermal management challenges are encountered in other emerging propulsion concepts, such as those featuring multi-megawatt electric power converters and motors, as well as fuel cells. This study presents the development of a lumped parameter model for ram air ducts and proposes guidelines for the design of this component. The ram air duct housing the condenser of a bottoming ORC unit recovering exhaust heat from a turboshaft engine is analyzed as a representative case study. A duct lumped parameter model (LPM) is developed based on first-principle relations and empirical correlations to predict key performance metrics. The model accuracy is assessed against the results of 2D RANS simulations, in which the heat exchanger is modeled as an anisotropic porous medium. Discrepancies between the initial lumped parameter model and CFD results prompted the development of improved sub-models of the duct components to better capture diffuser performance, heat exchanger integration effects, and the impact of flow maldistribution at the inlet of the heat exchanger. The predictions of the improved lumped parameter model show strong agreement with the CFD results, with average deviations in the estimated net drag of -0.16% and total pressure losses within 2.1%. A sensitivity analysis is conducted to quantify the influence of design variables, such as mass flow rate ratio, diffuser area ratio, and tilt angle of the heat exchanger, on net drag. The outcomes of the sensitivity analysis are confirmed by the results of an optimization study in which the optimal design of the duct and the heat exchanger is addressed simultaneously for various maximum duct lengths. Key findings include: (i) maximum thrust production is achieved when the available duct space is fully utilized, with optimal designs characterized by high mass flow rate ratios, large diffuser area ratios, and tilt angles approaching 70°; (ii) optimal heat exchangers feature high porosity, in excess of 80%, as their design is primarily driven by the need to minimize pressure losses in the ram air; and (iii) the optimization of the preliminary heat exchanger and duct designs can be decoupled. These results, together with the results of the optimization study, inform practical guidelines for the design of low-drag ram air ducts for the thermal management systems on board next-generation aircraft.

5.1. INTRODUCTION

As discussed in Chapter 1, one of the major challenges associated with airborne organic Rankine cycle waste heat recovery units is the design and integration of compact heat exchangers into the propulsion system and airframe. An extensive review of the various technical options for the cooling of airborne thermal systems is provided by [1]. Among the possible solutions, ram air cooling stands out as the most suitable method for cooling the ORC unit condenser, primarily due to its relative simplicity and ease of implementation. However, the use of ram air can lead to an increase in the overall drag of the aircraft, which can offset the fuel savings achievable through the ORC system. At the same time, the increase in ram air temperature across the condenser can be exploited to reduce drag or even generate net thrust [2], provided that the pressure losses in the ram air duct are minimized. This phenomenon is also known as the Meredith effect.

Ram air duct design is critical not only for airborne ORC units, but also for novel propulsion systems, such as those featuring multi-megawatt electric power converters and motors, as well as fuel cell-based propulsion systems [1], [3], [4]. For instance, the preliminary design of the thermal management system (TMS) for a vertical takeoff and landing (VTOL) electric aircraft is detailed in [5]. The drag associated with the TMS system is calculated by subtracting the thrust generated by the nozzle from the theoretical ram air momentum at the duct inlet. The intake is modeled as a concentrated pressure drop source corresponding to 1% of the freestream total pressure. The HX size and its design specifications were optimized to minimize TMS weight and ram air drag under different flight conditions.

The authors in [4] implemented a lumped parameter system model of the ram air cooling duct of the thermal management system (TMS) of a 1 MW proton exchange membrane fuel cell (PEMFC) powered propulsion system. The radiator is a tube bundle with louvered fins and is placed aft of a dedicated fan, with a 0° angle with respect to the mean airflow direction. The duct model is based on first-principle energy and momentum balance, with nozzle and diffuser performance characterized by fixed adiabatic efficiencies and the radiator modeled using a specified drag coefficient. The duct model was used to conduct a parametric study to establish the impact of the primary TMS design parameters on the ram air duct thrust. Their results show that duct losses primarily influence the duct net drag. However, the authors demonstrate that it is feasible to reduce and even cancel the drag of the TMS by increasing the radiator exit temperature. However, the authors did not assess the accuracy of their ram air duct model or the effect of key duct geometry design variables on system performance.

The research work reported in Ref. [6] deals with the conceptual design of the TMS of a nacelle-integrated fuel cell stack powering an electric regional aircraft. The results of this study show that the HXs are the bulkiest components and the most critical for system efficiency, given their impact on system drag. Different TMS design options were explored by varying the size, number, and location of HXs and air intakes, and the power capacity of the compressors. After selecting the HX geometry, 2D CFD numerical simulations of the cooling duct were performed for each of the proposed system configurations. The HX in the duct was modeled as just an array of flat tubes [7]. The use of guide vanes to redirect the flow at the inlet of the heat exchanger can result in lower total pressure

losses and improved performance if the HXs feature large frontal areas and are installed with a high inclination angle. Moreover, results indicate that longer ducts allow for a more uniform flow at the HX inlet, and that HX designs with low pressure drops are key to mitigating the drag of the TMS.

The use of CFD models to assess the performance of ram air cooling ducts is hampered by the high computational cost of the simulations, primarily due to the fine meshes required to resolve the flow within the HXs accurately. To mitigate this problem, several methods have been proposed in the literature that allow for simulating the flow through a heat exchanger without the need to resolve the flow within the complex core geometries of these devices in detail.

For instance, a body force modeling approach can be used for simulating the presence of a compact HX in a fuselage-mounted ram air cooling duct [8]. The HX geometry is not included in the simulation domain, and the pressure drop and heat transfer occurring in the device are modeled by means of specialized additional terms in the Navier-Stokes equations. Similarly, Porous media models (PMM) are another promising approach that has been gaining momentum to perform CFD simulations of ducts housing HXs. The fundamental element of a PMM is the unit cell, namely the smallest element characterized by a uniform porosity inside the computational domain. Within each unit cell, the flow and the HX core material are treated as a single entity. Similarly to the body force modeling approach, specific source terms are included in the Navier-Stokes equations to model the pressure drop and enthalpy change in the fluid flow [9]. Several formulations of these source terms, with varying levels of complexity, have been proposed in the literature. For instance, the authors in Ref. [10] used a 2D PMM approach to simulate an airflow through finned tube bundle condensers. A constant heat source was imposed in each unit cell to model the heat transfer process. The results show that the drag coefficient of the bundle is a function of the core porosity. At the same time, the study reports that different HX core geometries can have a comparable performance, as long as they have similar porosity. Musto et al. [11] used a similar PMM method to simulate the presence of an oil cooler in a ram air duct of a turboprop-powered small aircraft. The coefficients of the momentum loss term in the momentum equation and the volumetric source term in the energy equation were calibrated based on experimental data provided by the HX manufacturer. The results indicate that the presence of the cooler in the ram air duct homogenizes the airflow velocity, pressure, and temperature distributions. A more detailed and generalized porous medium model for the simulation of heat exchangers of aero engines is documented in [12]. The model features a 2D anisotropic formulation of the Darcy–Forchheimer pressure drop source term, allowing for a precise representation of the pressure drop across the HX core in the various flow directions. To predict the heat transfer rate, a heat transfer model that estimates the flow Nusselt number in each cell of the PM is used in place of a constant volumetric heat transfer rate source term. This model requires as input the wall temperature of the HX to estimate the local temperature difference and subsequently determine the heat transfer rate. Thus, contrary to models with constant heat source terms, the method reported in Ref. [12] allows for capturing local changes in the heat transfer coefficient within the HX core as a function of the flow conditions even during off-design operation. The same PMM was

subsequently used to optimize an elliptical tube bundle HX harvesting thermal energy from the exhaust gases of an aero engine [13].

The authors in [14] formulated the porous media governing equations in cylindrical coordinates to calculate the pressure drop associated with the flow through a bundle of serrated fin tubes. The developed PMM allows for the accurate capture of the flow resistance of a single finned tube. Results show that the PMM predicts pressure losses that are less than 10% lower than the experimental data, and 5% larger than the predictions of 3D RANS simulations over a wide range of Reynolds numbers. The deviation between the PMM and the 3D RANS model is reduced to less than 1% if the tube bundle features six or more finned tubes. At the same time, the mesh size used for the PM model was 15 times smaller than that used for the 3D RANS simulations.

In summary, the literature shows that the use of a PM can be very effective for modeling the thermohydraulic performance of HXs, as well as for predicting the flow field before and after the HX core if (i) sufficient accurate data is available to calibrate the source terms of the porous media models, and (ii) the unit cell size is significantly smaller than the overall HX size [15]. Despite the studies reported above, the literature currently does not provide consolidated guidelines for the optimal design of ram air ducts for the cooling of airborne thermal systems. Moreover, the validity range and degree of accuracy of the lumped parameter models used for the conceptual design of such systems remain uncertain. In this context, the goals of the present work are to (i) identify how different geometrical parameters of the duct affect the drag, (ii) assess the degree of accuracy of a lumped parameter model of the duct by comparing its predictions against the results of 2D CFD simulations, and (iii) provide optimal design guidelines for cooling ducts of airborne WHR units.

This Chapter is structured as follows. First, the case study, namely the modeling of a ram air duct housing the condenser of an ORC WHR unit of a combined cycle turboshaft engine, is presented. Next, the methodology section outlines the lumped parameter model of the duct and the corresponding 2D RANS model, in which the HX is treated as a porous zone. Finally, the results section presents the comparison between the predictions of the lumped parameter model and those of the CFD simulations, and the modifications suggested for the improvement of the former. Furthermore, the improved lumped parameter model is used to perform a sensitivity study to assess the influence of the main design variables of the duct on net drag, and to investigate the variation of the duct optimal design depending on the assumed maximum duct length.

5.2. TEST CASE

The present investigation focuses on the simulation and preliminary design of a ram air duct that houses the condenser of an ORC WHR unit harvesting thermal energy from the exhaust gases of the turboshaft engines powering the ONERA Dragon aircraft [16]. As detailed in Ref. [17], the proposed propulsion system configuration employs two combined-cycle turboshaft (CC-TS) engines housed in pods aft of the aircraft. The power units supply electrical power to distributed, electrically driven ducted fans installed under the wing of the plane. According to the findings of the feasibility, whose outcome is discussed in Sec. 3.4.2, the performance of the combined-cycle engine is strongly af-

fected by the drag caused by the ram air cooling duct.

Figure 5.1 illustrates how the ram air duct is integrated within the nacelle of the turboshaft engines. Each engine is equipped with two ram air ducts symmetrically positioned above and below the midplane of the nacelle. Moreover, each duct has a constant width W_D of 1.5 m, ingests about 7 kg/s of ram air, and houses a condenser that rejects 740 kW of thermal energy into the ram air stream. The operating conditions chosen as the design point of the ORC WHR unit and the ram air duct correspond to aircraft cruise ($M_0 = 0.78$) at an altitude of 10 km for an ambient temperature equal to ISA +15.

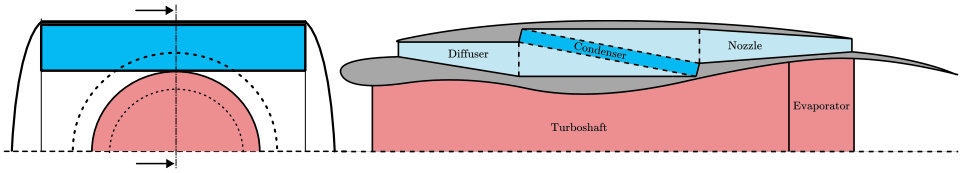

Figure 5.1: Sketch illustrating the integration of the WHR unit ram air duct within the nacelle of the combined-cycle turboshaft engine.

5.3. METHODOLOGY

5.3.1. RAM AIR DUCT LUMPED PARAMETER MODEL

The main components of the ram air duct of the ORC bottoming unit are the intake, the diffuser, the condenser, and the convergent nozzle. Figure 5.2 provides a schematic representation of the ram air duct model, highlighting its main sections and geometric parameters. The model inputs are the air mass flow rate, the free stream conditions, the thermodynamic state of the working fluid at the inlet and outlet of the condenser, and the duct design variables, namely the mass flow rate ratio MFR= $\dot{m}/\dot{m}_0$, the diffuser area ratio AR, and the HX inclination angle θ. The geometric parameters indicated in orange within the figure are estimated based on the input values, assuming that the tilt and tilt-back lengths, namely L_3 and L_5, are equal. Moreover, the intake captured area corresponds to the diffuser inlet area, thus $H_1 = H_2$. For this reason, the length of the intake channel L_1 is taken equal to zero. Conversely, the length of the diffuser L_2, the heat exchanger depth L_4, and the nozzle length L_6 are outputs of the model.

The first component of the duct is a subsonic scoop intake that captures the ram air mass flow rate $\dot{m}$. This airflow then enters the diffuser in station 2. The intake height H_1 is determined based on the required mass flow rate. Once the intake geometry is known, the flow quantities in station 2 are calculated along with the total gross drag of the duct, D_g, based on the assumption of complete deceleration of the ram air. The drag caused by the intake can be split up into multiple contributions, namely the ram, spillage, datum, skin friction, and diverter drag components. Each contribution is modeled according to the methodology outlined in [18]. The performance of the intake is significantly influenced by the design mass flow rate ratio (MFR), which represents the fraction of mass flow ingested by the intake relative to the mass flow that would pass through the inlet forward projected area. The intake MFR is typically a design variable and is set to a value

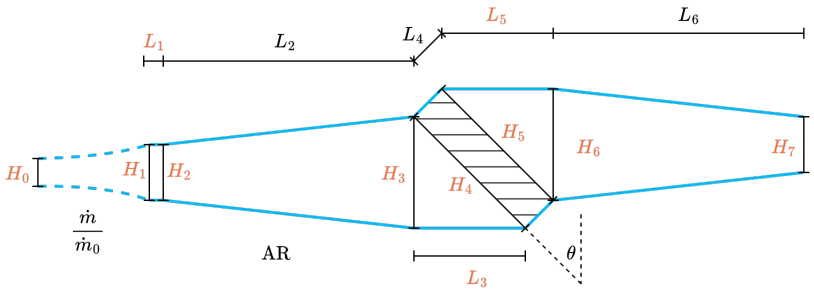

Figure 5.2: Conceptual representation of the ram air duct geometry highlighting the main geometrical variables of the model.

less than one. It follows that the incoming air stream undergoes a compression process ahead of the intake, with a consequent reduction in the airflow velocity. This process is assumed to be isentropic. Thus, the intake inlet Mach number M_1 is calculated from the following equation

$$\frac{M_1}{\text{MFR}}\left(1+\frac{\gamma-1}{2}M_1^2\right)^{\frac{-\gamma-1}{2(\gamma-1)}} - M_0\left(1+\frac{\gamma-1}{2}M_0^2\right)^{\frac{-\gamma-1}{2(\gamma-1)}} = 0\,. \tag{5.1}$$

The advantage of choosing an MFR value lower than one is a decrease in the total pressure losses inside the ram air duct due to the lower flow velocity. However, the drawback is that a portion of the airflow mass flow rate at station 0, equal to 1− MFR, does not enter the duct, and thus is forced to deviate and flow around the intake, resulting in the so-called spillage drag. Therefore, the optimal choice of MFR depends on a trade-off between internal and external losses; consequently, its optimal value is case-dependent.

The intake is followed by a planar diffuser that slows down the flow (section 2 to 3 in Figure 5.2). The corresponding static pressure increase is estimated as

$$P_3 - P_2 = \bar{q}_2\bar{\epsilon}_0\left(1-\frac{1}{\text{AR}^2}\right) \tag{5.2}$$

where $\bar{\epsilon}_0$ is the diffuser effectiveness and $\bar{q}_2$ is the mass-averaged dynamic pressure at the diffuser inlet. The effectiveness $\bar{\epsilon}_0$ represents the fraction of static pressure recovery achieved in the diffuser compared to an ideal component with no flow separation or losses and is defined as

$$\bar{\epsilon}_0 = \frac{1}{E_2^2}\left[\frac{1-\left(\frac{E_2}{E_3\text{AR}}\right)^2}{1-\text{AR}^{-2}}\right]\,. \tag{5.3}$$

E_2 and E_3 in Eq. 5.3 are the effective area fractions at stations 1 and 2, respectively. These are defined as

$$E = A\int^A \frac{u}{\max(u)}\,\mathrm{d}A = \frac{\bar{u}}{U_{\max}}\,, \tag{5.4}$$

and represent the portion of the cross-sectional area that would be required if the flow had a uniform velocity equal to the maximum one $U_{\max}$ at the given station along the

duct. Thus, E is the ratio of the average velocity and maximum velocity and is a measure of the flow non-uniformity at a given cross-section. The effective area fraction at the diffuser inlet can be computed by knowing the boundary layer thickness δ_2^* as

$$E_2 = 1 - \frac{2\delta_2^*}{H_2}. \tag{5.5}$$

Since the diffuser is essentially exposed to undisturbed freestream flow, the boundary layer thickness at its inlet is extremely small. Assuming sharp inlet lips of 1 cm in length and laminar flow, the boundary layer thickness at the diffuser inlet can be estimated according to Blasius solution, which yields $2\delta_2^*/H_2 = B_2 \approx 0.3\%$. E_3 is, instead, calculated according to the correlation derived by Sovran and Klomp [19] for subsonic diffusers, based on the area ratio and the value of E_2, and assuming to design this component for the highest pressure recovery in the prescribed dimensionless length. Regarding the geometry of the diffuser, this is determined based on the specified area ratio (AR) and the performance charts for planar diffusers originally developed by [20] and used as the foundation for the work in Ref. [19]. Notably, the authors in [20] report the optimal half-angle of the diffuser as a function of the non-dimensional length. This information is sufficient to calculate the diffuser length L_2, as the optimal geometry is independent of the boundary layer thickness. As far as the heat exchanger is concerned, the height H_4 is calculated as

$$H_4 = \frac{H_2\,\mathrm{AR}}{\cos(\theta)} \tag{5.6}$$

where the tilt angle θ is defined as the angle between the heat exchanger frontal area plane and the vertical direction (see Fig. 5.2). Larger tilt angles enable the design of HXs with larger frontal areas for a fixed maximum duct cross-sectional height. This results in lower air-side inlet velocities and, in theory, lower air-side pressure drops. However, larger θ angles imply a higher flow deflection in front of the HX core and, consequently, an additional pressure loss in the duct. An experimental investigation on the pressure drop associated with this flow turning is reported in Ref. [21] for a tilted intercooler. For simplicity, the HX inlet conditions on the air side are estimated in the lumped parameter model assuming that the pressure loss due to the flow turning in front of the condenser is lumped at the inlet of this component and that an isentropic process occurs between station 3 to station 4. The total pressure loss is evaluated, to a first approximation, by multiplying the pressure drop in the HX core by an empirical factor obtained by fitting the experimental results reported in [21] as a function of the inlet air velocity. The depth of the HX L_4, as well as the associated temperature increase and pressure drop in the airflow, are estimated using the condenser sizing model discussed in the next section. Downstream of the condenser, the flow accelerates in the tilt-back region between sections 5 to 6 in 5.2. This process is assumed to be isentropic, in analogy to the simplification adopted for the diffusion process occurring in front of the HX. The pressure losses due to the flow turning in the tilt-back region are negligible if compared to those occurring in the other sections of the duct. Finally, the airflow momentum F_n at the duct outlet is computed by solving the expansion process in the nozzle. The total pressure loss associated with this process is mainly due to viscous effects [22]. Assuming a one-dimensional flow, the variation of total pressure along the nozzle can be expressed in a

differential form as

$$\frac{\mathrm{d}P^0}{P^0} = -\frac{\gamma}{2} M^2 f_t \frac{P_w}{A_s} \mathrm{d}x \tag{5.7}$$

where f_t is the turbulent friction coefficient estimated according to the methodology reported in Ref. [23] and P_w / A_s is the ratio between the perimeter and the cross-sectional area of the duct. The total pressure ratio of the nozzle thus reads

$$\eta_{p7} = 1 + \int_6^7 -\frac{\gamma}{2} M^2 f_t \frac{2}{W_D} \left(\frac{W_D}{H(x)} + 1 \right) \mathrm{d}x. \tag{5.8}$$

The effect of flow misalignment with respect to the drag direction is considered negligible for symmetric nozzles [22]. The net drag of the duct D_n can be calculated by subtracting the nozzle uninstalled thrust from the gross drag of the duct as

$$D_\mathrm{n} = D_\mathrm{g} - \dot{m} \sqrt{\frac{2\gamma}{\gamma - 1} R \, {T_5}^0 \left(1 - \left(\frac{P_7}{\eta_{p7} {P_5}^0} \right)^{\frac{\gamma-1}{\gamma}} \right)}, \tag{5.9}$$

where $\dot{m}$ is the airflow mass flow rate that passes through the duct. Finally, the length of the nozzle L_6 is estimated assuming a fixed half-angle of 15°.

CONDENSER MODEL

The rating and sizing of the condenser of the ORC unit are performed using the software *HeXacode* introduced in Chapter 3. The accuracy of this tool has been verified by comparing its prediction with those of a commercial code for HX preliminary design [24] and against experimental data as reported in Section 3.3. The thermohydraulic correlations used for the sizing and rating of the condenser are listed in Ref. [25]. The sizing routine takes the frontal area of an HX as input, while the depth of the HX core L_4 is calculated to meet the design specifications. For the condenser topologies considered in the present work, this entails determining the number of microchannels of width w_mc within the flat tubes according to Eq. 3.11. The output of this procedure includes the heat exchanger size, mass, and pressure drops on both fluid sides. The HX sizing model is part of the procedure implemented for the preliminary design of the duct. *HeXacode* is also used to solve HX rating problems: the heat duty $\dot{Q}$ and pressure drops are determined given the specified geometry, size, and inlet flow conditions on both fluid sides. The rating model is used to generate the calibration curves required to tune the heat and momentum source terms of the porous zone of the CFD model of the duct.

Two condenser topologies featuring flat tube and microchannels have been investigated in this work. These topologies differ in the type of fins employed on the outer surface of the flat tubes, namely louvered (ft-lf) or offset-strip fins (ft-osf). Figure 3.11 shows a sketch of these topologies, highlighting their main geometrical parameters. These fin types allow for high levels of heat transfer area compactness, exceeding 1100 $\mathrm{m}^2/\mathrm{m}^3$, at the expense of larger pressure drop per unit length compared to plain fins [26]. The working fluid flows through rectangular-shaped microchannels inside the flat tubes in a cross-flow arrangement with respect to the airflow direction.

5.3.2. CFD MODEL OF THE DUCT

The CFD model of the ram air duct has been implemented by resorting to a 2D steady-state RANS solver of a well-known commercial fluid dynamics simulation software [27]. The presence of the heat exchanger in the duct is simulated by means of a porous media model. The boundary conditions of the numerical simulations are the total pressure and temperature at the duct inlet and the outlet static pressure. The mass flow rate, inlet static pressure, and outlet total pressure are thus outputs of the CFD simulations. The following sections describe the porous media model of the condenser and its calibration methodology, followed by the details of the overall numerical simulation setup.

POROUS MEDIA MODEL OF THE HX

The ORC condenser is modeled as a 2D anisotropic porous zone having the same dimensions as the heat exchanger of the lumped parameter model. The porous zone is characterized by a constant porosity α, representing the portion of the condenser volume occupied by the airflow. The flow entering the porous zone is forced to accelerate such that the velocity increases by a factor of $1/\alpha$, as a consequence of the cross-section reduction caused by the HX. The value of α depends on the HX core geometry.

The momentum and energy conservation equations in the porous zone account for additional source terms that, respectively, model the pressure drop ($\mathbf{S}_m$) and heat transfer ($\mathbf{S}_e$) occurring on the air side of the heat exchanger [9]. The general form of the governing equations [28] in the porous zone reads

$$\frac{\partial \rho}{\partial t} + \nabla \cdot \left(\rho \vec{v}\right) = 0 \tag{5.10}$$

$$\frac{\partial (\rho \vec{v})}{\partial t} + \nabla \cdot \left(\rho \vec{v}\, \vec{v}\right) = -\nabla P + \nabla \cdot \bar{\bar{\tau}} + \vec{\mathbf{S}}_{\mathrm{m}} \tag{5.11}$$

$$\frac{\partial}{\partial t}\left(\alpha \rho E + (1-\alpha)\rho_{\mathrm{s}} E_{\mathrm{s}}\right) + \nabla \cdot (\vec{v}(\rho E + P)) = \nabla \cdot (\bar{\bar{\tau}} \cdot \vec{v}) + \nabla \cdot (k \nabla T) + \mathbf{S}_{\mathrm{e}}\,. \tag{5.12}$$

The momentum source term is defined based on the Darcy-Forchheimer quadratic drag law as described by [12], i.e.,

$$\vec{\mathbf{S}}_m = -\left(\frac{\mu}{\bar{\bar{K}}}\vec{v} + \frac{\rho}{2}\bar{\bar{F}}|\vec{v}|\vec{v}\right), \tag{5.13}$$

where $\bar{\bar{K}}$ is the matrix of specific permeability in each flow direction and $\bar{\bar{F}}$ is the Forchheimer drag matrix of the porous media model. The flow through the chosen HX topologies can be considered one-dimensional, as the flat tubes act as a flow straightener. To enforce this flow characteristic in the porous zone, the specific permeability in any direction other than the one normal to the HX frontal area is set to values close to zero. The corresponding flow resistance in the transversal direction is three orders of magnitude higher than that through the HX core.

As a result, the flow through the porous zone is essentially one-dimensional and aligned with the major axis of the flat tubes. Thus, only two coefficients in Eq. 5.13, namely K_{xx} and F_{xx}, require calibration. The energy source term models the heat transfer rate in the condenser as proportional to the difference between the local fluid temperature T_{b} and the wall temperature T_{w}, the heat transfer area density β, and the local

heat transfer coefficient, which can be expressed in the form of a Nusselt-Reynolds number correlation [12]. The energy source term for each cell reads

$$\mathbf{S}_e = a\, Re^n\, k(T_\mathrm{b}) Pr^{1/3} (T_\mathrm{w} - T_\mathrm{b}) \beta\, d_\mathrm{ref}^{-1}\,, \tag{5.14}$$

where the fluid thermal conductivity k is a function of the local cell bulk temperature and d_ref is the air-side hydraulic diameter, which depends on the HX core geometry. Note that the core temperature T_w is fixed to a constant value corresponding to the average temperature of the metal walls predicted by the rating model of the HX being simulated. The same model is used to calibrate the coefficients a and n in 5.14 as well as the coefficients K_{xx} and F_{xx} in 5.13. More in detail, for each test case, the rating model of the condenser is used to estimate the overall pressure gradient across the HX $\Delta P/Z$ and the mean air-side heat transfer coefficient for a range of air inlet conditions. The working fluid side inlet conditions are instead kept constant and set to the values obtained from the system optimization performed by [17]. The coefficients of the source terms of the porous media model are estimated through a non-linear least squares fit of the functions defined by Equation 5.13 and 5.14 to the predictions of the rating model. In this calibration process, the local air temperature T_b and density are replaced with the mean values of these quantities between the inlet and outlet of the condenser. Note that the pressure drop calculated by the rating model of the condenser also includes the pressure recovery at the HX core outlet [29]. This contribution has to be excluded when calculating the pressure gradient across the HX for the calibration of the porous media model, to avoid underestimating the overall pressure drop in the airflow in the CFD simulations. To verify the calibration of the porous zone, the results of 2D inviscid simulations for a simple straight duct housing the condenser are compared to the data points obtained using the condenser rating model for a range of air inlet conditions. Figures 5.3 and 5.4 illustrate this comparison for the total pressure drop per unit core length and total temperature increase in the airflow, respectively. The match is deemed satisfactory because the mean relative deviations in pressure drop and temperature increase are smaller than the inherent uncertainty of the rating model of the condenser.

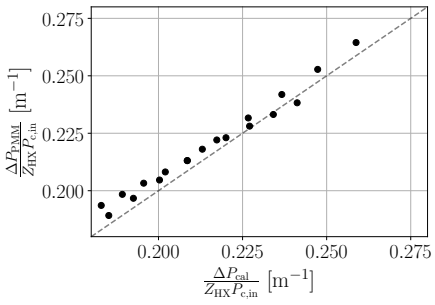

Figure 5.3: Comparison of the pressure gradient calculated by the PMM with the calibration data.

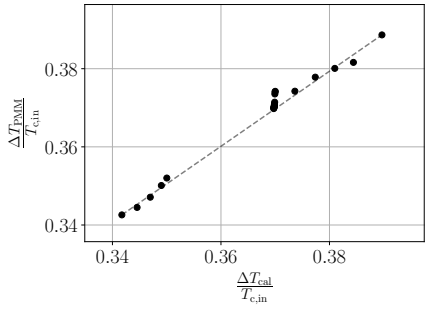

Figure 5.4: Comparison of the temperature increase calculated by the PMM with the calibration data.

NUMERICAL SIMULATION FRAMEWORK

The CFD model is solved by means of multiblock grids generated using the *Ansys* Meshing tool. The mesh is structured within all duct zones except for the tilt L_3 and tilt-back L_5 regions, in which an unstructured mesh with triangular elements is used. A no-slip condition is imposed on all the duct walls except those of the porous zone. On the walls of this zone, a slip condition is used, since the resistance to the flow is governed by the momentum source term 5.13. The shear stress transport (SST) turbulence model is adopted in the duct flow domain [30]. This model has been preferred as it is generally considered to provide better predictions of flow separation in adverse pressure gradient conditions compared to other models that rely on wall functions such as the k-ϵ model [31]. This choice of the turbulence model for the CFD simulation of a duct housing an HX modeled as a porous zone is further supported by the validation study performed by [32], which showed good agreement between the numerical results and the experimental data for an aero engines intercooler. Regarding the solution method, the RANS simulations are performed utilizing a pseudo-time step method with automatic time step control and setting the residual convergence threshold equal to 10^{-5}. The fluid is modeled as an ideal compressible gas featuring temperature-dependent properties. These are estimated using polynomial curves calibrated by fitting data generated utilizing the thermodynamic property library *CoolProp* [33].

To assess the suitability of the adopted mesh, a grid independence study is carried out. The test case considered for this purpose is that of a duct with an intake area ratio of 0.7, a diffuser area ratio of 3.6, and an offset-strip fin heat exchanger inclined at 70 degrees. The monitored model outputs are the total pressure drop, the temperature increase within the duct, and the effective area fraction at the diffuser exit E_3. The reason for this choice is that the primary objective of the model is to predict the net drag of the ram air duct. Such quantity is closely related to the total pressure losses across the various duct components, as well as to the temperature increase in the airflow across the condenser, which can be exploited to accelerate the flow through the nozzle. The effective area fraction E_3 is representative of the flow non-uniformity at the diffuser exit, a factor that significantly affects the heat exchanger performance. Figure 5.5 reports the relative difference $\delta_{\mathrm{f,c}}$ in total pressure drop, total temperature increase, and effective area fraction obtained with meshes of different sizes compared to the finest mesh. The various grids were generated by applying refinement ratios ranging from 1.3 to 1.6. The results indicate that the grid size has a weak influence on the estimate of total temperature at the duct outlet and the effective area ratio, while its impact on the total pressure drop prediction is significant. The mesh featuring 1.1M cells is deemed the best compromise between computational cost and accuracy, as the deviation in the estimate of the total pressure loss with respect to the result obtained with the finest mesh is less than 2%, while the simulation time is appreciably lower. Thus, the mesh with 1.1 M cells has been selected for the simulations performed in this study.

The CFD model mesh features a uniform inflation layer which is characterized by a thickness of five times the internal mesh element size, a growth rate of 1.2, and 34 layers. This ensures a smooth transition to the internal mesh. The y^+ values are lower than one in the whole flow domain for solving the viscous sublayer with adequate resolution. Regarding the porous media model, the characteristic element is the so-called representative ele-

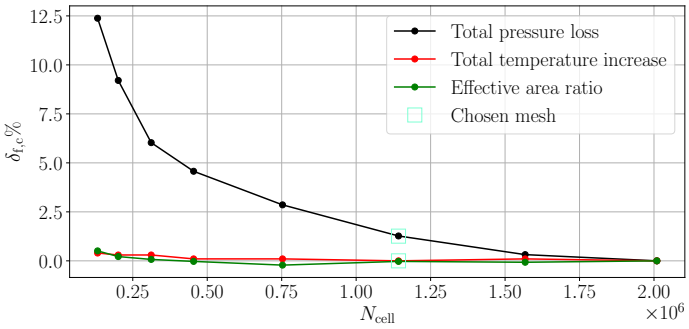

Figure 5.5: Mesh sensitivity study displaying the relative difference in key flow properties $\delta_{f,c}$ compared to the results obtained with the finest mesh.

mentary volume (REV), which must be sufficiently large for the averaged flow properties within it to be independent of its size, yet significantly smaller than the overall dimensions of the porous media domain [9]. The cell size of the porous zone representing the heat exchanger has to be smaller than or, at most, equal to the smallest characteristic length of the REV [34]. However, if the cell size approaches this characteristic dimension, numerical instabilities occur, and the solutions deviate more from experimental data or the results of high-fidelity CFD simulations [34]. For the two-dimensional simulations performed in this work, the smallest characteristic length of the REV is the flat tube pitch. An optimal balance between computational time and numerical stability was found using porous zone cells with a size equal to one-tenth of this characteristic REV dimension.

5.3.3. VERIFICATION OF THE LUMPED PARAMETER MODEL AGAINST CFD SIMULATIONS

The accuracy of the lumped parameter model is assessed by comparing its results with the predictions of CFD simulations conducted for several duct designs. Figure 5.6 illustrates the procedure adopted to generate a database of solutions for the comparison of the two modeling approaches. To ensure a fair comparison, the geometry, boundary conditions, and air mass flow rate must be consistent between the two models. This is achieved for each combination of design inputs being analyzed by first running the lumped parameter model in sizing mode, thereby defining the full duct geometry used to generate the CFD model mesh. However, when the corresponding CFD simulation is run, the solution converges to an inlet static pressure and mass flow rate that differ, though to a limited extent, from the values specified as input to the lumped parameter model. To resolve the discrepancy, the lumped parameter model is rerun in rating mode, as this calculation mode allows for imposing the inlet conditions of interest. Since the inlet pressure is not a direct input of the lumped parameter model in this case either, its value is matched to that determined in the CFD simulation by adjusting the intake mass flow rate ratio.

The design vector $X_D = \{\dot{m}/\dot{m}_0, \theta, AR\}$ is uniformly sampled within the bounds defined by the lower bound vector LB = {0.5, 50, 2} and the upper bound vector LB = {0.7, 70, 4}. These limits reflect the validity range of the various correlations adopted in the duct lumped parameter model as well as the expected design space of the duct for the considered application, namely the combined-cycle turboshaft engine studied by Krempus et al. [17]. The design space exploration is performed by taking 5 samples for each design variable of the duct, resulting in a total of 125 unique design combinations. However, not all of these combinations are feasible or of practical relevance. For instance, designs involving high MFR values and relatively low inclination angles of the condenser lead to excessive airflow velocities at the heat exchanger inlet that may exceed the validity range of the correlations adopted in the *HeXacode* condenser model. As a result, only approximately half of the initial 125 combinations have generated valid solutions. Given that the choice of the HX geometry has a negligible impact on the accuracy of the duct LPM, the HX core geometry is held constant across all simulations run to generate the solution database. Specifically, the condenser consists of a flat tube micro-channel HX with offset-strip fins featuring a thickness of 0.18 mm, a height of 12 mm, a pitch of 2 mm, and a depth of 4 mm.

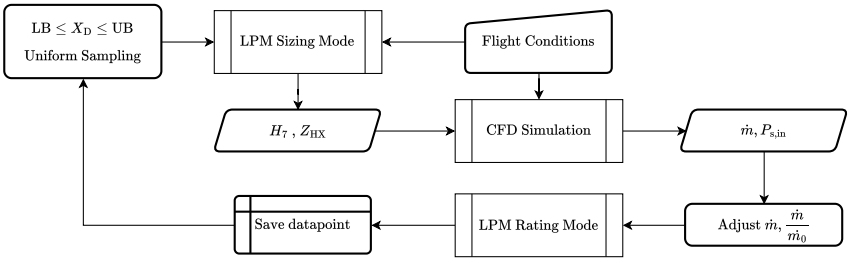

Figure 5.6: Flow chart of the procedure for generating the database used to compare the predictions of the lumped parameter model with the results of CFD simulations.

5.4. RESULTS & DISCUSSION

5.4.1. ACCURACY OF THE DUCT LUMP PARAMETER MODEL

The figure of merit considered to evaluate the performance of the various ram air duct design solutions is the thrust ratio TR = $F_n/D_g - 1$. This metric reflects the aerodynamic efficiency of a design: a TR value of zero implies a neutral impact of the ram air duct on the aircraft aerodynamics, while positive and negative values indicate net thrust or drag, respectively. Figure 5.7 reports the thrust ratio predicted by the CFD model for a range of duct configurations differing in terms of intake mass flow rate ratio MFR, diffuser area ratio AR, and HX inclination angle θ. The results indicate that (i) the TR increases with both AR and θ, but tends to plateau at higher values of these design variables if MFR exceeds 0.55, (ii) the impact of the inclination angle θ on TR is more pronounced at lower AR values, and (iii) increasing MFR positively affects the TR at high inclination angles, whereas the opposite trend is observed at low θ.

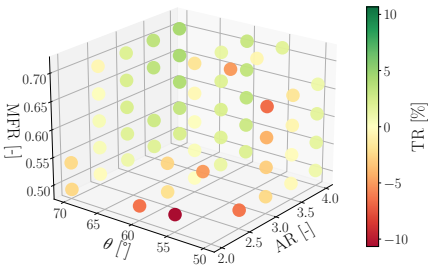

Figure 5.7: Thrust ratio resulting from the CFD simulations for different duct designs.

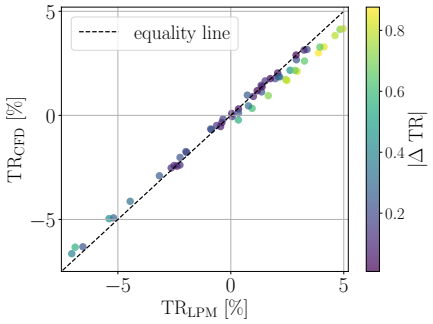

Figure 5.8: Comparison of the thrust ratio calculated using the CFD model vs the lumped parameter model (LPM).

5

The accuracy of the lumped parameter model in predicting the overall thrust or drag of the ram air duct is assessed by comparing the TR values predicted by this model to those estimated by the CFD simulations across a range of different duct designs. As shown in Figure 5.8, the predictions of the two models are closely aligned over the entire design space, with an average deviation of only 0.24% and a standard deviation of 0.38%. More specifically, the LPM tends to slightly underpredict TR for designs that generate net drag, whereas the opposite trend is observed for the best-performing solutions that enable net positive thrust. This overestimation becomes appreciable for TR≥ 2%, averaging 0.42% of the total gross drag, with a standard deviation of 0.26%. By estimating the maximum deviation as the average plus three times the standard deviation, results indicate that the LPM may overestimate the thrust produced by each ram air duct by up to 1.2% of the gross drag, equivalent to approximately 100 N for the two CC-TS engines of the considered test case. This error is deemed acceptable in the context of propulsion system preliminary design.

The small deviations in the estimate of the duct thrust compared to the CFD simulations do not necessarily imply that the LPM correctly predicts the flow conditions within the ram air duct. To assess more in detail the predictive capabilities of the LPM, the following quantities estimated by means of the two modeling approaches at the duct stations highlighted in Figure 5.2 are compared: mass-weighted average velocity, Mach number, total and static pressures, and temperatures. The comparison is performed for the duct design solution that yields the highest net thrust among those subjected to a maximum length constraint of 3 m. The chosen duct configuration features a condenser installed with an inclination angle of 70 degrees. The fin topology is that of offset strip fins with a height, pitch, and depth of 13 mm, 1.96 mm, and 4 mm, respectively. The condenser is located downstream of a diffuser with an area ratio of 3.8. The CFD model domain only encompasses the internal geometry of the duct, specifically from the diffuser inlet (station 2) to the nozzle exit (station 7).

As shown in Figure 5.9, the LPM predicts a more uniform diffusion of the flow be-

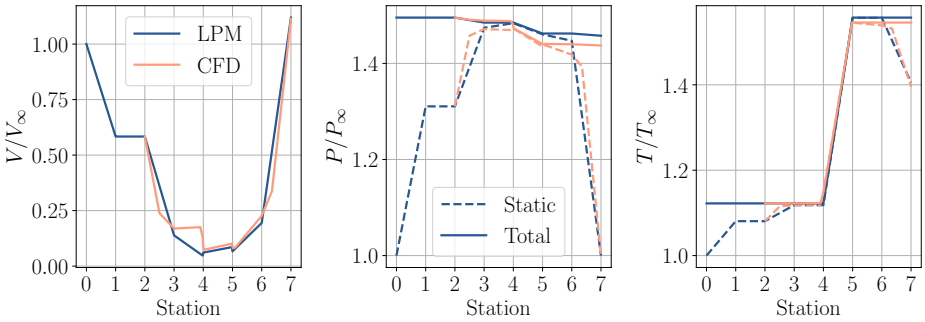

Figure 5.9: Per-station comparison between the results of the LPM (blue) and CFD simulations (red) in terms of velocity, total & static pressures, and total & static temperatures.

5

tween section 2 to 4, whereas the CFD simulation indicates a more abrupt flow deceleration in the diffuser, followed by a region where the average velocity remains nearly constant (station 3 to 4). This discrepancy is due to the flow separation in the diffuser predicted by the CFD model as a consequence of the severe adverse pressure gradient. The flow separation is evident in the velocity contour plot from the CFD simulation reported in Figure 5.10. As the velocity magnitude decreases to below 50% of the inlet value, the extent of the separation becomes so large that further increases in cross-sectional area within the diffuser or tilt region have little to no effect on the flow. Subsequently, as the flow is redirected through the HX core, the velocity decreases further and exhibits improved uniformity. This reduction in velocity is accompanied by a total pressure loss at the HX inlet, primarily resulting from the partial dissipation of the velocity component transverse to the orientation of the flat tubes. A comparable localized total pressure loss was reported by Patrao et al. [35] and is evident near station 4 in the total pressure distribution shown in Figure 5.9. Across the HX, both models predict similar results, although the total pressure loss estimated in the CFD simulations is systematically higher than that predicted by the LPM. This discrepancy is attributed to the slightly elevated air velocity at the HX inlet predicted by the CFD model. Similarly, as shown in Figure 5.9, both models provide comparable temperature distributions throughout the duct. However, the LPM tends to overestimate the total temperature increase in the condenser by approximately 2%. Such a discrepancy can be attributed to the inability of the LPM to capture flow non-uniformity at the HX core inlet. Finally, both models predict small and comparable total pressure losses as the flow accelerates downstream of the condenser, from station 5 to 7.

To assess whether the discrepancies between the two modeling approaches identified in the station-by-station comparison are consistent and independent of the specific test case analyzed, Figure 5.11 reports the total pressure losses calculated across the different duct sections as predicted by the LPM (on the x-axis) and the CFD model (on the y-axis) for the whole database of duct designs. The comparison reveals that the LPM does not accurately predict the losses in the diffuser (section 2 to 3) and the tilt region in front

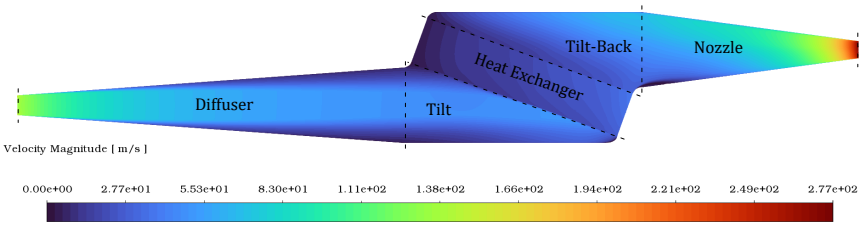

Figure 5.10: Velocity contour plot predicted by the CFD model.

of the HX (section 3 to 4). Specifically, the LPM consistently overestimates total pressure losses in the diffuser, while it significantly underestimates losses in the tilt region. The average and standard deviation of these discrepancies are reported in the first and third columns of Table 5.1, in which positive values imply that the LPM underestimates pressure losses compared to the CFD simulation, while negative values indicate the opposite. The second and fourth columns of the same table report the differences in static pressure change across the diffuser and the tilt region, respectively. Results show that deviations between the LPM and CFD simulations in estimating total pressure losses in the diffuser are larger than those associated with the estimation of the static pressure rise. This occurs because the excessive total pressure losses estimated by the LPM compensate for inaccuracies in the estimation of the static pressure increase across the diffuser. In contrast, the simple relations used in the LPM to predict total pressure in the tilt region upstream of the condenser result in a substantial overestimation of the conversion of dynamic pressure into static pressure.

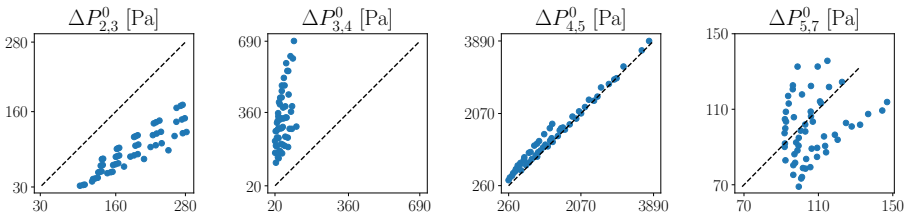

Figure 5.11: Total pressure losses between the main ram air duct stations based on the adopted modeling approach. The results of the CFD model are on the y-axis, while the results of the LPM are on the x-axis.

The heat exchanger is the primary source of total pressure loss within the duct, with values ranging from approximately 350 Pa to nearly 3900 Pa, as shown in Figure 5.11. The LPM predicts total pressure losses across the HX that are, on average, 140 ± 125 Pa lower than those resulting from the CFD simulations. This deviation is larger for higher inclination angles. Although the differences in the predicted total pressure loss in the duct upstream of the condenser are smaller in magnitude than those relative to the HX core, their impact on the estimated duct performance can be more significant. The reason

Table 5.1: Average deviations in key flow quantities across the stations highlighted in Figure 5.2 computed by subtracting the values predicted by the LPM from those resulting from the CFD simulations.

	Average	std. dev.		Average	std. dev.
$\delta\Delta P^0_{2,3}$	-99 [Pa]	26 [Pa]	$\delta\Delta P_{2,3}$	-21 [Pa]	25 [Pa]
$\delta\Delta P^0_{3,4}$	275 [Pa]	120 [Pa]	$\delta\Delta P_{3,4}$	-238 [Pa]	128 [Pa]
$\delta\Delta P^0_{4,5}$	141 [Pa]	125 [Pa]	$\delta\Delta P_{4,5}$	173 [Pa]	123 [Pa]
$\delta\Delta P^0_{5,7}$	-23 [Pa]	18 [Pa]	$\delta\Delta P_{5,7}$	-428 [Pa]	237 [Pa]
$\delta\Delta P^0_{2,7}$	289 [Pa]	220 [Pa]	$\delta\Delta P^0_{2,7}/\Delta P^0_{2,7\ \mathrm{CFD}}$	-16.9%	13.3%
δu_7	-0.40 [m/s]	1.03 [m/s]	$\delta\Delta P_{5,7}/\Delta P_{5,7\ \mathrm{CFD}}$	-4%	2.2%

thereof is that the airflow velocity and density at the HX inlet, which essentially dictate the heat transfer and pressure losses occurring in this component, are directly influenced by the flow conditions predicted at the diffuser and tilt region outlet. Notably, for ducts with a thrust ratio (TR)≥ 3%, the LPM overestimates, on average, the temperature increase across the HX by almost 2%. Conversely, the total pressure losses in the nozzle have a lower impact on the flow established in the duct as they are low in magnitude and only affect the thermodynamic states downstream of the condenser.

In summary, the errors in the individual sub-models of the LPM tend to offset one another. The difference in total pressure loss across the entire duct predicted with the two modeling approaches amounts, on average, to 17% of the total pressure loss calculated from the CFD simulation results. For the chosen test case, this corresponds to just 1.2% of the ambient pressure at cruise altitude. Although these differences are not large enough to compromise the model accuracy in estimating flow momentum at the ram air duct outlet during cruise conditions, and thus the power requirement of the CC-TS, they may become critical when the LPM is used as a tool for ram air duct preliminary design in system optimization studies. In such a context, inaccuracies in predicting the HX inlet conditions, particularly velocity and pressure, might lead to an overestimation of the thermohydraulic performance of this component. The error may propagate through the system model, for example, causing a misestimate of the working fluid condensation temperature, thereby amplifying the overall uncertainty in the predicted system performance.

The comparisons presented so far do not reveal how the individual duct design variables affect the accuracy of the LPM. Figures 5.12a and 5.12b show the differences in total pressure and temperature at the duct exit, as predicted by means of the two modeling approaches, as a function of the main design variables. Several conclusions can be drawn from the analysis of these figures. First, the LPM tends to underestimate total pressure losses and overestimate the total temperature increase. These discrepancies become more pronounced for high values of the inclination angle of the condenser. The reason is that large values of θ lead to increasingly non-uniform flow conditions at the HX inlet, whose negative impact on performance cannot be captured by the LPM. Second, the relative deviations in total temperature increase are consistently smaller than those associated with total pressure loss. This trend can be explained by the following considerations. The total temperature at the HX exit is influenced by the local heat trans-

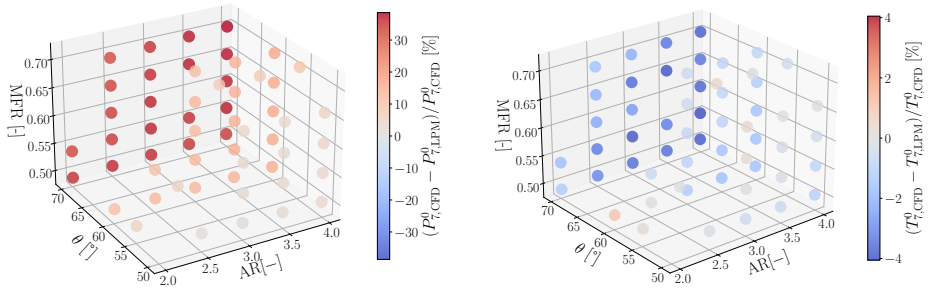

(a) Relative total pressure deviations.

(b) Relative total temperature deviations

Figure 5.12: Difference in total pressure and temperature at the exit of the duct relative to the values predicted via the CFD simulations.

fer coefficient, which scales with the flow velocity raised to an exponent less than one. In contrast, the pressure drop is approximately proportional to the square of the flow velocity. As a result, velocity non-uniformities have a more pronounced negative impact on total pressure losses than on the heat transfer process. Third, the LPM often fails to converge for low values of the diffuser area ratio AR and θ as the flow velocity entering the HX corresponds to Re values exceeding the validity range of the heat transfer coefficient and friction factor correlations. Consequently, fewer data points are available for comparison in such a region of the design space. This limitation, however, does not compromise the applicability of the LPM for ram air duct preliminary design, as these combinations of duct design variables typically correspond to solutions with high net drag and are thus of limited practical relevance for aerospace applications. In contrast, the choice of high condenser inclination angles and diffuser area ratios enables duct designs characterized by high values of thrust ratio. However, in these cases, the accuracy of the LPM is reduced due to the increased flow non-uniformity at the condenser inlet.

LUMPED PARAMETER MODEL OF IMPROVED ACCURACY

As discussed in the previous section, the largest deviations between the LPM and CFD simulation results occur in cases where there is significant flow non-uniformity at the HX inlet. The main reasons are:

- The diffuser in the LPM is treated as an isolated component. Thus, the calculated effective area fraction E_3 is independent of the flow conditions established in the tilt region in front of the HX or at the duct inlet. In contrast, the CFD simulations highlight that E_3 reduces with high values of the HX inclination angle and mass flow rate ratio (MFR). This decrease is proportional to θ and is amplified by both the diffuser area ratio and the blocked flow area fraction at the duct inlet.

- The airflow total pressure loss and static pressure increase at the HX inlet (station 4 in Figure 5.2) depend not only on the HX inclination angle but also on the dynamic pressure at the exit of the diffuser and the area ratio between the diffuser outlet

and the HX inlet H_4/H_0. Moreover, Table 5.1 shows that the original tilt model overestimates the static pressure at the HX inlet.

- The performance of the HX tends to deteriorate as the flow non-uniformity at the inlet is larger, an effect that is neglected in the current implementation of the LPM.

These limitations of the LPM are addressed by proposing a new formulation for the effective area fraction E_3 in the diffuser model, by adopting a new total pressure loss correlation for the tilt region, and by introducing two thermo-hydraulic performance deterioration factors in the HX model. The objective is to better approximate the results of the CFD simulations over the explored duct design space. Concerning the diffuser model, the effective area fraction at the diffuser exit E_3 is calculated as

$$E_3 = E_{3,\mathrm{SK}} - \frac{\tau(\frac{\theta}{45})^{\psi \mathrm{MFR}}}{\mathrm{e}^{-(\chi AR(100B_2)^{0.25}-1)^2}}\,, \tag{5.15}$$

where $E_{3,\mathrm{SK}}$ is the effective area fraction estimated using the methodology detailed in [19], while the coefficients $\tau = 0.0123$, $\psi = 0.780$, and $\chi = 0.662$ are estimated through non-linear least squares fitting of the E_3 values calculated from the CFD results. This updated value of E_3 is then used to calculate the static pressure recovery of the diffuser using equations 5.2 and 5.3. Figure 5.13a compares the values of the effective area fraction $E_{3,\mathrm{SK}}$ estimated using the correlation proposed by Sovran and Klomp [19] with those calculated based on the CFD simulation results and equation 5.15. Notably, since $E_3 \leq E_{3,\mathrm{SK}}$, the average velocity at the diffuser exit will be higher than that predicted by the original LPM. The validity range of the proposed correlation for E_3 is the same as the correlation in Ref. [19] for fully turbulent 2D ducts. However, equation 5.15 has only been assessed for $45 \leq \theta \leq 70$ and $0.4 \leq \mathrm{MFR} \leq 0.7$.

The correlation for the estimate of the total pressure loss in the tilt region ΔP_θ^0 was developed by fitting the results from the CFD simulations and reads

$$\frac{\bar{q}_3}{\Delta P_\theta^0} = a\left(\frac{\sin(\theta)}{\tilde{Y}}\right)^b + c\left(\frac{\Delta P_{\mathrm{HX}}}{\bar{q}_3}\right)^d, \tag{5.16}$$

where ΔP_{HX} is the pressure drop across the HX core, and

$$\tilde{Y} = \frac{H_4}{H_0} = \frac{AR}{\cos\theta}\left(\frac{\dot{m}_0}{\dot{m}}\right) \tag{5.17}$$

represents the dimensionless heat exchanger height. This dimensionless parameter is defined by the three independent duct design variables and expresses the area ratio between the flow cross-sections at station 4 (at the HX core inlet) and station 0 (intake) of the duct. The coefficients a, b, c, and d of Equation 5.16 that best fit the results of the CFD simulations are 1.569, 0.312, 0.128, and 1.141, respectively. Given the set of duct designs explored in this study, the range of validity of the proposed correlation is $45 \leq \theta \leq 70$ and $6 \leq \tilde{Y} \leq 24$. Figure 5.13b compares the ratio between $\bar{q}_3$ and the total pressure loss in the tilt region as estimated with the original LPM (in orange), the CFD simulations

(blue), and the new correlation (green) as a function of two parameters: the sine of the inclination angle θ over the dimensionless height, and the pressure drop across the HX core over the dynamic pressure at the diffuser outlet. The total pressure drop across the tilt region estimated with Eq. 5.16 is significantly higher than that predicted with the old LPM, and its trend with θ is now consistent with the CFD simulations. Note that the calculation of the static pressure and temperature at station 4 now requires an iterative procedure, since the modified diffuser and tilt models need information about the performance of their downstream component. Convergence is typically achieved in less than three iterations, as the value of static pressure at station 4 is often very close to that at station 3.

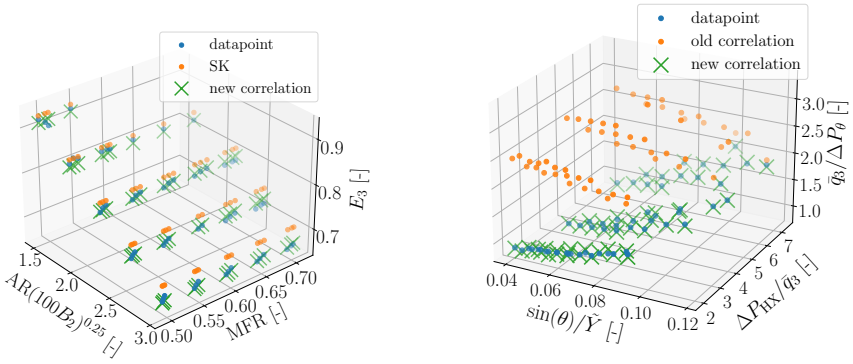

(a) Diffuser (stations 2 to 3)

(b) Tilt region upstream of the HX (stations 3 to 4)

Figure 5.13: Effective area fraction E_3 (a) and total pressure drop in the tilt region upstream of the HX (b) as predicted by the original LPM (orange), CFD simulations (blue), and the modified LPM (green).

The HX lumped parameter model is modified to account for the effect of flow non-uniformity at the inlet by defining two performance deterioration factors, namely $\Gamma_P = \Delta P_{4,5}/\Delta P_{HX}$ and $\Gamma_T = \Delta T_{4,5}/\Delta T_{HX}$. Γ_P is the ratio between the actual pressure drop in the HX and that which would occur in the same HX if the upstream flow is uniform. Similarly, Γ_T is the ratio of the actual temperature increase in the airflow over that which would be achieved in case of flow uniformity at the HX inlet. The values of these factors vary depending on both the extent of flow separation at the diffuser exit, represented by E_3, and the heat exchanger tilt angle θ, as shown in Figure 5.14. However, it is possible to correlate the variation of Γ_P and Γ_T using a single regression parameter, namely the effective area fraction projected onto the HX frontal area

$$E_\theta = E_3 \cos(\theta). \tag{5.18}$$

The values of these empirical factors are estimated in the LPM by means of the following

analytical expressions

$$\Gamma_P = p_0^2 \frac{\sqrt{E_\theta}}{e^{p_1 E_\theta}} + p_2 \text{ , and } \quad \Gamma_T = t_0 (E_\theta - t_1)^{0.2} + t_2 \tag{5.19}$$

The coefficients that best fit the numerical data are $p = [4.86, 12.75, 0.95]$ and $t = [0.17, 0.15, 0.865]$ for $0.22 \leq E_\theta \leq 0.58$. Figure 5.15 shows the trend of the performance deterioration factors with E_θ and the predictions of the fitted polynomials.

Though the values of the coefficients of the correlation in Equation 5.19 are, in principle, independent of the specific HX type, they may require a recalibration when simulating HXs with characteristics significantly different from those considered in this study. However, the correlation remains accurate for different HX topologies provided that (i) the HX has a high porosity, i.e., $\alpha \geq 0.7$, and (ii) the airflow through the HX is essentially one-dimensional, and (iii) the air pressure drop range is similar to that of the condensers analyzed in this study.

The accuracy of the modified LPM is assessed by comparing its predictions with the results of the CFD simulations. To this purpose, the LPM is run in rating mode to reproduce all the test cases analyzed with the CFD model. The improved model no longer overestimates the thrust of the best-performing ducts. The average deviation in the predicted TR decreases from $0.42\% \pm 0.26\%$ to $-0.16\% \pm 0.13\%$. More importantly, the LPM provides an accurate estimate of the flow conditions within the ram air duct, as demonstrated in Table 5.2, which reports the average discrepancy and the corresponding standard deviation between the two models in the estimate of the total pressure loss and static pressure variation across the main stations of the duct, and the airflow velocity at the duct outlet. Compared to the results shown in Table 5.1, the average differences between the two models and the related standard deviations decreased significantly, except for the velocity at the duct outlet. Furthermore, the total temperature increase across the HX is now predicted with deviations consistently below 0.1% regardless of the duct geometry.

Table 5.2: Average difference and corresponding standard deviation computed by subtracting the values predicted by the improved LPM from those estimated based on the CFD simulation results. The compared flow quantities are the total pressure loss ΔP^0, the static pressure change ΔP across the main stations of the duct as indicated in Figure 5.2, and the airflow velocity at the duct outlet u_7.

	Average	std. dev.		Average	std. dev.
$\delta\Delta P^0_{2,3}$	-24 [Pa]	12 [Pa]	$\delta\Delta P_{2,3}$	-6 [Pa]	19 [Pa]
$\delta\Delta P^0_{3,4}$	-26 [Pa]	24 [Pa]	$\delta\Delta P_{3,4}$	-48 [Pa]	75 [Pa]
$\delta\Delta P^0_{4,5}$	46 [Pa]	49 [Pa]	$\delta\Delta P_{4,5}$	70 [Pa]	66 [Pa]
$\delta\Delta P^0_{5,7}$	-22 [Pa]	18 [Pa]	$\delta\Delta P_{5,7}$	-110 [Pa]	71 [Pa]
$\delta\Delta P^0_{2,7}$	-26 [Pa]	39 [Pa]	$\delta\Delta P^0_{2,7}/\Delta P^0_{2,7\ \mathrm{CFD}}$	-2.1%	2.7%
δu_7	0.57 [m/s]	0.32 [m/s]	$\delta\Delta P_{5,7}/\Delta P_{5,7\ \mathrm{CFD}}$	-1.1%	0.8%

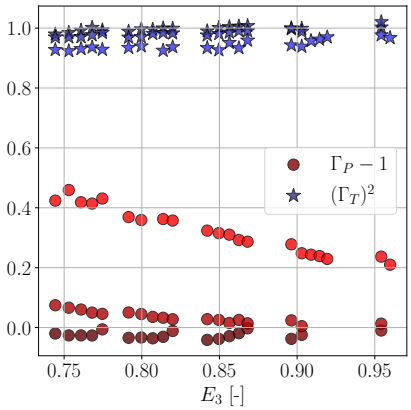

Figure 5.14: Effect of the diffuser outlet effective area ratio on Γ_P and Γ_T. Lighter colors correspond to larger inclination angles.

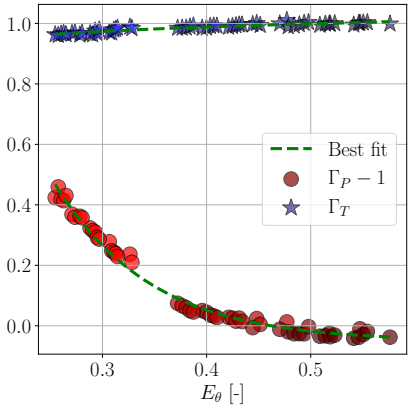

Figure 5.15: Γ_P and Γ_T variation as a function of the effective area fraction projected onto the HX frontal area. Lighter colors correspond to larger inclination angles

5

5.4.2. SENSITIVITY ANALYSIS OF RAM AIR DUCT PERFORMANCE TO DESIGN INPUTS

The improved LPM is used to perform a sensitivity analysis to explore the influence of the main design variables on ram air duct performance. More in detail, the value of three duct design parameters, i.e., intake MFR,θ, and diffuser AR, were varied independently within the bounds reported in Table 5.3 to assess a wide range of possible design configurations. Furthermore, the sensitivity study was repeated for the two condenser topologies considered for the ORC system. The lower and upper bounds for MFR are selected based on the optimal range for this variable recommended for scoop-type intakes [18]. The bounds of the inclination angle and the diffuser area ratio are determined, instead, by the validity range of the correlations adopted in the modified LPM. A lower limit of 50° for θ is chosen due to the negligible performance improvements observed below this value and the reduced numerical robustness of the LPM solution procedure for high airflow velocities at the HX inlet.

Table 5.3: Range and reference values of the duct design parameters considered in the sensitivity analysis.

Parameter	Lower bound	Upper bound	Reference value
MFR	0.40	0.70	0.64
θ	50 °	70 °	66 °
AR	2.0	4.0	2.8

Figure 5.16 summarizes the results of the sensitivity study for the flat tube condenser equipped with offset strip fins and louvered fins. The contour plots highlight the relationship between the thrust ratio and the three duct design parameters listed in Table 5.3. The dark gray lines in the contour plots indicate sets of solutions characterized

by the same total duct length, with the corresponding length value, in meters, reported along these lines. The shaded regions denote the areas of the design space in which the LPM failed to converge, typically due to excessive airflow velocities at the HX inlet. The absence of valid solutions in these regions does not compromise the significance of the sensitivity analysis, as the associated designs generally yield low thrust ratios and are thus of limited practical interest. Figure 5.16a and 5.16d show that, for a given MFR, designs with higher diffuser area ratios and inclination angles lead to improved system performance, albeit at the expense of increased duct lengths.
The improvement in performance stems from a substantial reduction in the HX core inlet velocity. Additionally, the slope of the dark gray lines indicating the duct length implies that the diffuser area ratio affects the total duct length more than the other two design variables. Figures 5.16b and 5.16e show that, for a fixed HX inclination angle, the constraint on the maximum allowable duct length limits the achievable thrust ratio and influences the optimal choice of MFR. At the same time, the optimal AR of the diffuser tends to be the highest value that still satisfies the maximum length constraint. Finally, Figure 5.16c and 5.16f highlight the benefit of higher inclination angles: larger angles correspond to design solutions that enable higher TR, with only a modest increase in total duct length. In contrast, the optimal MFR value is more sensitive to the imposed maximum length constraint.

Overall, the trends observed in the sensitivity study are consistent for both of the considered HX topologies. However, the adoption of offset strip fins seems to enable higher thrust ratio values compared to the louvered fin topology. This means that, while the HX configuration influences the absolute values of the thrust-drag balance, the optimal values of the duct design variables remain largely unaffected by the specific HX topology. Thus, the optimization of the duct design can be decoupled from the HX design process, as also confirmed by the results in the next section.

5.4.3. DUCT AND HX DESIGN CONSTRAINED OPTIMIZATION

Once the accuracy of the refined lumped parameter model is established, the integrated optimization of the ram air duct and HX geometries is tackled next. The objectives are to: (i) determine the maximum ram air duct thrust achievable for the considered test case as a function of the available installation space, (ii) quantify the performance gains attainable by the simultaneous optimization of the condenser and duct designs, and (iii) establish optimal design guidelines for ram air ducts.

The sensitivity study has demonstrated that both duct performance and the associated optimal design parameters are influenced by the constraint on the maximum allowable duct length L_{max}. In light of this, the optimal duct design problem is solved for different values of L_{max}. Moreover, to quantify the benefits of integrated design, two optimization strategies are applied for each HX topology. In the first approach, a set of HX geometrical parameters, denoted by $\{G\}$, is included among the optimization variables X_D, thus enabling the simultaneous optimization of the duct and HX geometries. In the second approach, the values of the HX geometrical parameters are fixed based on the results of a prior optimization of the HX design aimed at minimizing the pressure drop in the airflow given the typical operating conditions of the system. The optimization

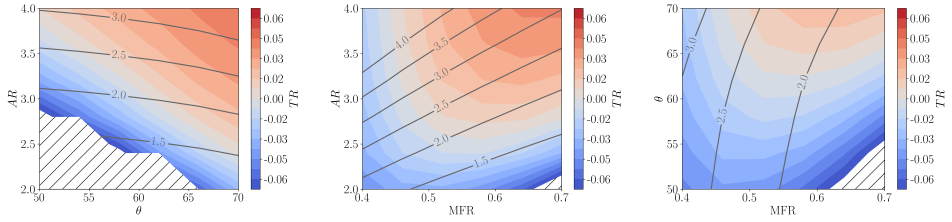

(a) MFR = 0.64 (b) $\theta = 66°$ (c) AR = 2.8

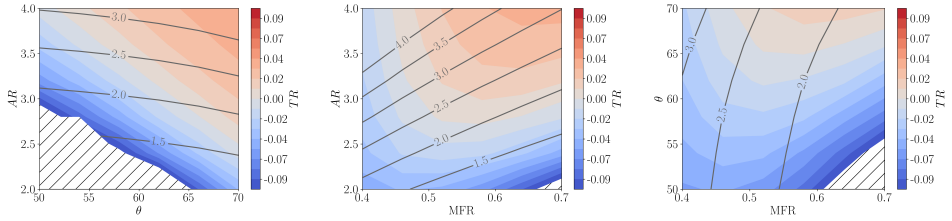

(d) MFR = 0.64 (e) $\theta = 66°$ (f) AR = 2.8

Figure 5.16: Results of the sensitivity analysis for both the condenser topologies considered in the study. The top charts (5.16a, 5.16b,5.16c) refer to the case of a condenser with offset-strip fins, while those at the bottom (5.16d, 5.16e, 5.16f) pertain to the case of a condenser with louvered fins. The dark gray lines indicate the total duct length in meters.

problem is thus formulated as

$$\begin{aligned} \text{minimize:} \quad & D_g - F_n, \\ \text{with:} \quad & x_\text{D} = [\text{MFR}, \theta, \text{AR}, \{G\}] \text{, and } [\text{MFR}, \theta, \text{AR}] \\ \text{subject to:} \quad & 0 < L \leq L_\text{max}, \\ & x_\text{D}^\text{L} \leq x_\text{D} \leq x_\text{D}^\text{U} \text{ .} \end{aligned} \tag{5.20}$$

The upper and lower bounds of the design variables of the duct considered in the optimization are consistent with those used in the sensitivity study (see Table 5.3), whereas the bounds of the HX design variables for both topologies are provided in Table 5.4. The fin and micro-channel wall thicknesses are held constant at 0.18 mm and 0.2 mm, respectively. The optimization problem is solved by coupling a Genetic Algorithm (GA) with a sequential least squares programming algorithm (SLSQP) [36]. The GA is used to generate a population of candidate solutions, each represented by a genome vector of length equal to the number of design variables. The algorithm improves the fitness of each generation of individuals through the repetitive application of sampling, crossover, mutation, and evaluation of the objective function. The GA is terminated when the difference between the average and best fitness of the individuals of a given generation is

Table 5.4: Design variables included in the optimization study of the HX and their bounds for both the offset-strip fins (osf) and the louvered fins (lf) condenser topologies. The last column reports the optimal value of the design variables in case the HX geometry is optimized to minimize the pressure drop in the airflow given the typical operating conditions of the system.

HX design variables	Lower - upper bound		Optimal value	
$\{G\}$	osf	lf	osf	lf
w_{mc}	1.0 - 2.0 mm	1.0 - 2.0 mm	1 mm	1 mm
h_{ft}	1.8 - 2.2 mm	1.8 - 2.2 mm	1.8 mm	1.8 mm
F_h	6 - 13 mm	8 - 15 mm	12.0 mm	13.0 mm
F_p	2 - 5 mm	1.4 - 3.6 mm	3.8 mm	3.2 mm
F_d	5 - 15 mm	NA	10.0 mm	NA
L_f/L_l	NA	0.6 -0.9	NA	0.9
L_α	NA	15 - 30 °	NA	17 °
L_p	NA	1.4 - 3 mm	NA	2.8 mm

5

less than the specified tolerance of 0.2%. Then, the best individual from the final GA generation is used to initialize the gradient-based solver, which refines the solution by only adjusting the values of the duct design variables. This hybrid strategy ensures the identification of the optimal solution while limiting computational cost.

Figure 5.17 shows the thrust ratio of the optimal duct design as a function of the maximum allowable duct length. The TR increases with the available length until L_{max} reaches a value of about 3.5 m. Beyond that value, the optimal design becomes insensitive to further increases in L_{max}. The reason for this trend is the upper limit imposed on the diffuser area ratio, which cannot exceed a value of 4, per the validity range of the correlation adopted in the LPM to estimate E_3. For both HX topologies, the highest thrust ratios are obtained for diffuser area ratios and HX tilt angles close to their upper bounds, mass flow rate ratios (MFR) around 0.7, and a total duct length of approximately 3.2 m. Although the absolute value of the thrust ratio is influenced by the thermal-hydraulic performance and heat duty of the condenser, the optimal values of the duct design variables (MFR, AR, and θ) are found to be independent of the HX topology, as also observed in the sensitivity analysis.

Furthermore, the marginal difference between the results of the two optimization strategies, namely the simultaneous optimization of the duct and HX geometry (solid lines in Figure 5.17) and the optimization of the duct design variables alone (dashed lines), confirms that, for the current test case, the optimal HX design is primarily driven by the objective of minimizing pressure losses in the airflow. This finding supports the conclusion that the HX and duct design processes can be effectively decoupled. Concerning the HX topology, offset-strip fin condensers exhibit reduced air-side pressure drops than their louvered fin counterparts at comparable inlet Reynolds numbers, thus enabling higher thrust ratios.

Moreover, the optimal condenser designs are always characterized by a high porosity to mitigate airflow acceleration through the HX core. The optimal porosity is nearly constant and ranges from 0.8 to 0.82. At the same time, high porosity entails lower heat

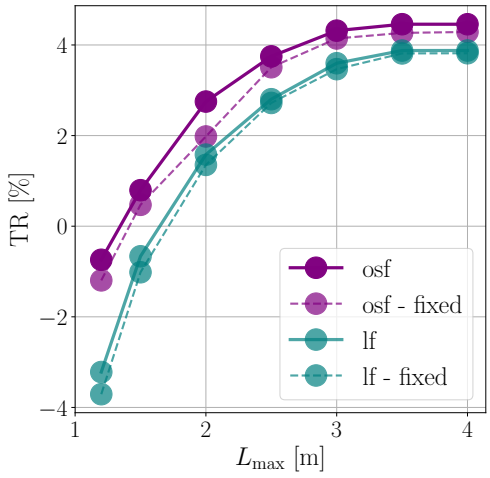

Figure 5.17: Thrust ratio corresponding to the optimal duct design as a function of the maximum allowable duct length. The dashed lines correspond to the results of optimizations performed with a condenser geometry defined according to the values of the geometrical parameters indicated as optimal in Table 5.4 .

transfer coefficients and reduced area compactness. As a consequence, the HX core depth (L_4) in the optimal designs may be larger than that typically found in automotive radiators or condensers. The reason for this design choice is that the pressure drop in the HX core scales nearly quadratically with the airflow velocity, and thus the reciprocal of porosity, while only linearly with the flow path length L_4.

DESIGN GUIDELINES AND PRELIMINARY ESTIMATES

The trends identified in the sensitivity and optimization studies enable the definition of guidelines for estimating the optimal duct geometry in a preliminary design stage. As shown in Figure 5.18, the optimal values of MFR and AR can be mapped as a function of the dimensionless optimal total length of the duct, which is defined as

$$\hat{L}_{\text{tot}} = \frac{L_{\text{tot}}}{H_0} = \frac{L_2}{H_0} + \frac{L_4 \cos(\theta)}{H_0} + \frac{AR \tan(\theta)}{\text{MFR}} + \frac{AR}{\text{MFR}} \frac{(1 - AR_N)}{\tan(\alpha_N)} \tag{5.21}$$

where AR_N and α_N are the area ratio and half-angle of the nozzle, respectively. During the conceptual design phase, designers can estimate, to a first approximation, $\hat{L}_{\text{tot}}$ based on the maximum available duct length, the freestream conditions, and the design specifications of the heat exchanger as

$$\hat{L}_{\text{tot}} = \frac{\rho_0 u_0 L_{\text{max}} W_\text{D}}{\dot{m}} = \frac{c_p \rho_0 M_0 \sqrt{\gamma R T_0} \Delta T_{\text{HX}} L_{\text{max}} W_\text{D}}{\dot{Q}}, \tag{5.22}$$

where W_D is the width of the duct, $\dot{Q}$ is the heat duty of the HX, ΔT_{HX} is the total temperature increase of the ram air across the HX, ρ_0, T_0, and M_0 are the density, static temperature, and Mach number of the freestream air. It should be noted that, based on

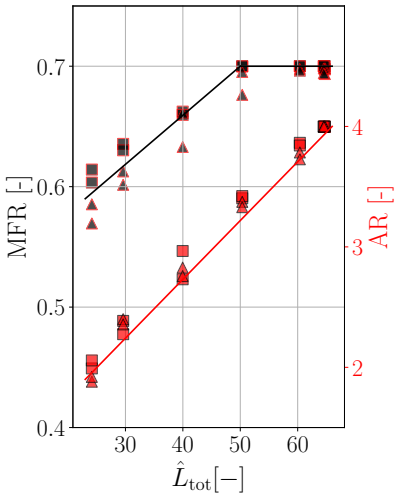

Figure 5.18: Optimal values of MFR and AR as a function of the dimensionless total duct length $\hat{L}_{\text{tot}}$. Condensers featuring offset strip fins are marked as □ , while louvered fin ones are marked as △ .

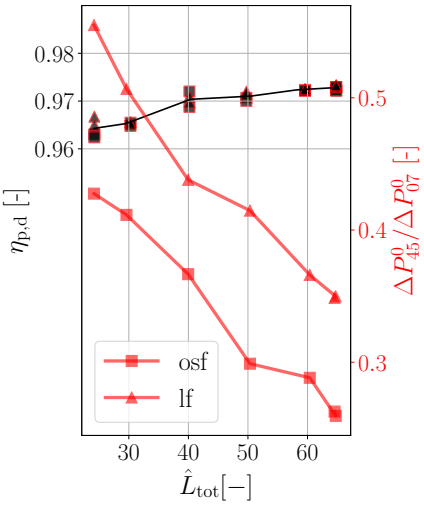

Figure 5.19: Total pressure ratio in the duct minus the contribution of the HX pressure losses ($\eta_{p,d}$), and the ratio of the HX pressure drop (ΔP^0_{45}) over the duct total pressure loss (ΔP^0_{07}) vs $\hat{L}_{\text{tot}}$.

the design space explored in the optimization study, which is constrained by the validity range of the correlations implemented in the LPM, $\hat{L}_{\text{tot}}$ cannot exceed a value of 65. This upper bound is also evident from Figure 5.18.

Regarding the HX inclination angle θ, its optimal value consistently converges to 70°. Finally, designers must ensure that the resulting maximum height of the duct $Y_{\text{d,max}}$ is compatible with the available installation space, given the chosen combination of design variables. Notably, $Y_{\text{d,max}}$ can be estimated as

$$Y_{\text{d,max}} = H_0 \tilde{Y} \cos(\theta) = \frac{\dot{Q}}{c_p \Delta T_{\text{HX}} \rho_0 u_0 W_{\text{D}}} \frac{\text{AR}}{\text{MFR}}, \tag{5.23}$$

where $\tilde{Y}$ is the dimensionless heat exchanger height. Note that the contribution of the HX depth to the duct height is not accounted for in Equation 5.23, as it is negligible compared to that of other geometrical variables, in particular AR and θ.

For a preliminary estimate of the performance, the expected TR of the ram air duct can be calculated as

$$\text{TR} = \frac{\dot{m}\sqrt{\dfrac{2\gamma}{\gamma-1} R\, T_{\text{t,5}} \left(1 - \left(\dfrac{P_0}{\eta_{p,07} P_{\text{t,0}}}\right)^{\frac{\gamma-1}{\gamma}}\right)}}{D_g} - 1, \tag{5.24}$$

where $\eta_{p,07} = P_{\text{t,7}}/P_{\text{t,0}}$ is the total pressure ratio across the duct. Accounting only for

ram, datum, and spillage drag contributions to D_g, TR can be determined, to a first approximation, as

$$\mathrm{TR} \approx \frac{\sqrt{\frac{2\gamma}{\gamma-1}R\left(1-\frac{1}{\left(1+\frac{(\gamma-1)}{2}M_0^2\right)\eta_{p,07}^{(\gamma-1)/\gamma}}\right)\left(T_0\left(1+\frac{\gamma-1}{2}M_0^2\right)+\Delta T_{\mathrm{HX}}\right)}}{M_0\sqrt{\gamma R T_0}\left(1+\frac{C_{\mathrm{D,d}}+C_{\mathrm{D,sp}}}{2}\right)} - 1\,, \tag{5.25}$$

where $C_{\mathrm{D,d}}$ is the datum drag coefficient, typically set to 0.1 for high aspect ratio scoop intakes [18], while the spillage drag coefficient can be approximated as $C_{\mathrm{D,sp}} \approx (0.7 - \mathrm{MFR})(1.2(0.7-\mathrm{MFR})+0.2)$ for $0.2 \leq \mathrm{MFR} \leq 0.7$ based on the data reported in [18]. It follows that TR can be calculated given the total pressure ratio across the duct $\eta_{p,07}$, which can be divided into a duct-only total pressure loss contribution and that related to the presence of the HX. As shown in Figure 5.19, the total pressure ratio of the duct excluding the contribution of the HX pressure losses ($\eta_{p,d}$) is approximately constant over a wide range of $\hat{L}_{\mathrm{tot}}$, provided the duct is optimally designed. Conversely, the pressure drop across the HX (also plotted in Figure 5.19, see left y-axis) is case-specific, and varies significantly depending on the HX core geometry, duct configuration, and design specifications.

In a preliminary design phase, an estimate of $\eta_{p,07}$, and then of TR, can be derived from the trendline of $\eta_{\mathrm{p,d}}$ in Figure 5.19, combined with an estimate of the HX pressure drop. The latter cannot be estimated from a chart and must instead be obtained using an HX sizing tool as a function of expected operating conditions. Therefore, the proposed approach to evaluating TR does not require knowledge of the design variables of the duct, but only of the flight conditions and the HX design specifications. As an alternative, Equation 5.25 can be used to determine the maximum total pressure losses to achieve a specified net drag under the given operating conditions, since the net drag of the duct can be expressed in terms of TR as

$$D_{\mathrm{net}} = -\mathrm{TR}\ \dot{m}\ u_0\left(\frac{1+C_{\mathrm{D,sp}}+C_{\mathrm{D,d}}}{2}\right)\,. \tag{5.26}$$

Note that, for scoop intakes with $0.6 < \mathrm{MFR} \leq 0.7$, the net drag of the duct is approximately equal to the product of TR and the ram drag ($\dot{m}\ u_0$), assuming that the datum drag coefficient contribution is negligible.

In summary, Equation 5.22, 5.23 and 5.25, and the trendlines in Figure 5.18 and 5.19, in combination with a HX preliminary design tool, can aid designers during the conceptual design phase to (i) estimate the optimal duct geometry given the available space constraints, and (ii) predict the relationship between the temperature increase in the ram air across the HX and the duct drag or thrust.

5.5. CONCLUSIONS

This study contributes to the definition of optimal design guidelines for ram air ducts housing compact heat exchangers for thermal management systems aboard aircraft. The

considered test case concerns the design of a ram duct for the condenser of a bottoming organic Rankine cycle unit, which recovers thermal energy from the exhaust gases of a turboshaft engine.

A lumped parameter model (LPM) of the ram air duct was developed based on first principle relations and empirical correlations in the literature. Its accuracy is assessed against the results of 2D RANS simulations, in which the HX is modeled as an anisotropic porous medium. The CFD simulations revealed limitations of the original LPM and prompted the development of improved sub-models of the duct components. In particular, the new submodels allow for more accurate capture of diffuser performance, HX integration effects, and the impact of flow maldistribution at the HX inlet. These modifications improve the accuracy of the LPM predictions of the airflow conditions along the whole duct regardless of the considered condenser topology, i.e., flat-tube microchannel HXs with either offset-strip fins or louvered fins. A sensitivity analysis was conducted to evaluate the influence of the design variables on the aerodynamic performance of the ram air duct. The trends observed in this analysis were confirmed by the results of an optimization study addressing simultaneously the optimal design of the duct and the condenser for different values of the maximum allowable duct length. The key findings of this study can be summarized as follows:

- The improved LPM accurately predicts the overall net drag of the ram air duct, with an average deviation of -0.16% compared to CFD simulations. The model also effectively estimates the flow velocity variation within the duct and the associated overall total pressure loss with deviations averaging 2.1% relative to the CFD results. Furthermore, the improved LPM reliably captures the sensitivity of system performance to the main design parameters, such as diffuser area ratio, mass flow rate ratio, and HX tilt angle. The LPM is thus well-suited for use in preliminary design and optimization studies.

- Concerning the optimal design of the duct, the sensitivity analysis showed that higher inclination angles are generally beneficial for performance, while the optimal values of the mass flow rate ratio (MFR) and diffuser area ratio (AR) depend on the maximum allowable duct length. In a preliminary design phase, the optimal value of these variables can be estimated from the dimensionless duct length, regardless of the considered HX topology.

- The optimization study revealed that the preliminary design of the HX can be addressed independently of the optimal duct configuration. The HX design is primarily driven by the objective of minimizing total pressure loss in the airflow. The optimized condenser geometries are all characterized by high porosity, in excess of 0.8, to mitigate airflow acceleration through the HX core. Although increased porosity is associated with lower heat transfer coefficients and reduced area density, the resulting larger HX core yields a lower pressure drop due to the reduction in mean airflow velocity. For this reason, offset-strip fin condensers consistently outperform their louvered fin counterparts due to their lower average friction factors at comparable Reynolds numbers.

- Maximum performance is achieved when the full available duct length is utilized

in the design. Optimal duct configurations are characterized by high mass flow rate ratios, maximum diffuser area ratios, and HX tilt angles close to 70 °, independently of the HX topology. As the allowable duct length is decreased, the first design variable to be reduced is the diffuser area ratio, followed by the mass flow rate ratio. The HX tilt angle is only reduced in very short ducts, although to a minor extent. These findings provide practical guidelines for the conceptual design of ram air ducts of airborne thermal management systems.

Future work will focus on extending the CFD model to simulate the external aerodynamics of the duct to validate the lumped parameter model for the estimation of the spillage and datum drag contributions.

The preliminary design optimization of the CC-TF engine concept, summarized in Sec. 3.4.3, revealed that the total pressure increase generated by the fan upstream of the HX may substantially enhance the thrust resulting from the acceleration of the heated airflow. Moreover, an annular duct geometry instead of a planar configuration may be more suitable for the integration of a ram air duct within an aero engine. Therefore, the CFD simulation framework discussed in this Chapter has been extended to investigate the aerodynamic effects associated with the installation of a condenser in the bypass duct of a turbofan engine. The CFD simulation framework has been extended to model the flow around and inside the bypass duct of the CC-TF engine using axis-symmetric instead of planar simulations. Moreover, the actuator disk (AD) method is used to model the fan and outlet guide vanes as permeable disks that exert forces on the airflow inside the bypass duct [37]. The internal geometry of the bypass duct is parametrized using cubic splines defined by a set of control points and is optimized to maximize thrust generation. Preliminary results indicate that activation of the ORC condenser increases the thrust of the combined-cycle turbofan (CC-TF) by approximately 4.5% relative to a reference configuration in which no thermal energy is transferred to the bypass flow. Further optimisation of the internal duct geometry yields an additional thrust increase of approximately 3.2%. Details of the extended CFD simulation framework and preliminary aerothermal performance results for the CC-TF configuration are provided in Appendix B.

Future modeling efforts should also be devoted to including the impact of the system weight on the overall net drag associated with the ram air duct.

NOMENCLATURE

Roman symbols

A	Section area [m^2]
AR	Area ratio [-]
AR_N	Nozzle area ratio [-]
$C_{D,d}$	Datum drag coefficient [-]
$C_{D,sp}$	Spillage drag coefficient [-]
c_p	Specific heat capacity at constant pressure [$kg\,m^2\,s^{-2}\,K^{-1}$]
D_g	Gross drag [$kg\,m\,s^{-2}$]
D_{net}	Net drag [$kg\,m\,s^{-2}$]
d_h	Hydraulic diameter [m]
Eu	Euler number [-]
F_h	Fin height [m]
F_p	Fin pitch [m]
f	Friction factor [-]
g	Gravitational acceleration [$m\,s^{-2}$]
$\{G\}$	Set of geometry-specific parameters
h	Heat transfer coefficient [$W\,m^{-2}\,K^{-1}$]
H	Section height [m]
h_{mc}	Microchannel height [m]
j	Colburn factor [-]
k	Thermal conductivity [$W\,m^{-1}\,K^{-1}$]
L	Length [m]
L_p	Louver pitch [m]
L_l	Louver length [m]
L_α	Louver angle [°]
L_s	Length of fin strip [m]
$\tilde{L}_{tot}$	Dimensionless total duct length [–]
M	Mach number [-]
$\dot{m}$	Mass flow rate [$kg\,s^{-1}$]
n_{mc}	Number of microchannels/microtubes [-]
N_{opt}	Number of optimization variables [-]
Nu	Nusselt number [-]
P	Pressure [Pa]
Pr	Prandtl number [-]
$\dot{Q}$	Heat duty / thermal power [W]
R	Gas constant [$J\,kg^{-1}K^{-1}$]
Re	Reynolds number [-]
$\tilde{\mathbf{S}}_e$	Energy source term [$J\,m^{-3}$]
$\tilde{\mathbf{S}}_m$	Momentum source term [$kg\,m^{-2}s^{-2}$]
T	Temperature [K]
TR	Thrust ratio [-]
u	Velocity [$m\,s^{-1}$]
$\vec{v}$	Velocity vector[$m\,s^{-1}$]
w_{mc}	Width of the microchannel [m]
W_D	Duct width [m]
X	HX width [m]
x_D	Design variables array [-]
Y	HX height [m]
Y_d	Duct height [m]
Z	HX depth [m]

Greek symbols

α	Fin pitch over height ratio [-]
	Porosity [-]
β	Heat transfer area compactness [m^{-1}]
β_s	Fluid side-specific surface area density [m^{-1}]
γ	Fin thickness over pitch ratio [-]
	Ratio of specific heats [-]
δ	Fin thickness over fin depth ratio [-]
ϵ	Effectiveness [-]
η_p	Total pressure ratio [-]
θ	Inclination angle [°]
μ	Dynamic viscosity [$kg\,m^{-1}s^{-1}$]
ρ	Density [$kg\,m^{-3}$]
σ	Free flow to frontal area ratio [-]

Subscripts

0	Freestream
2,3	Diffuser
3,4	Tilt
4,5	Heat exchanger
5,6	Tilt-back
6,7	Nozzle
air	Air stream
cr	Cruise operating point
crit	Critical point
d	Duct-only (no HX)
f	Fin
fr	Frontal
HX	Heat exchanger
in	HX inlet conditions
lm	Logarithmic mean
max	Maximum / constraint
mc	Microchannel/microtube
ORC	ORC system
pp	Pinch point
ref	Reference
s	Solid material
sc	Subcooling
sh	Superheating
t	Total (stagnation) quantity
wf	Working fluid

Superscripts

L	Lower bound
U	Upper bound

Abbreviations

AD	Actuator disk
CC	Combined cycle
CFD	Computational fluid dynamics
HX	Heat exchanger
LPM	Lumped parameter model
MAE	Mean absolute error
MAPE	Mean absolute percentage error
MB	Moving boundary
MFR	Intake mass flow rate ratio

MPE	Mean percentage error
OGV	Outlet guide vane
ORC	Organic Rankine cycle
std. dev.	Standard deviation of the mean
TF	Turbofan engine
TS	Turboshaft engine
WF	Working fluid
WHR	Waste heat recovery

BIBLIOGRAPHY

[1] M. Coutinho, D. Bento, A. Souza, *et al.*, "A review on the recent developments in thermal management systems for hybrid-electric aircraft", *Applied Thermal Engineering*, vol. 227, p. 120 427, 2023, ISSN: 1359-4311. DOI: https://doi.org/10.1016/j.applthermaleng.2023.120427.

[2] L. Piancastelli, L. Frizziero, and G. Donnici, "The Meredith ramjet: An efficient way to recover the heat wasted in piston engine cooling", *ARPN Journal of Engineering and Applied Sciences*, vol. 10, pp. 5327–5333, Jan. 2015.

[3] H. Kellermann, M. Lüdemann, M. Pohl, and M. Hornung, "Design and optimization of ram air–based thermal management systems for hybrid-electric aircraft", *Aerospace*, vol. 8, no. 1, 2021, ISSN: 2226-4310. DOI: 10.3390/aerospace8010003.

[4] A. C. Frey, J. Stonham, D. Bosak, C. M. Sangan, and O. J. Pountney, "Radiators in fuel cell powered aircraft: The effect of heat rejection on drag", *Applied Thermal Engineering*, vol. 274, p. 126 697, 2025, ISSN: 1359-4311. DOI: https://doi.org/10.1016/j.applthermaleng.2025.126697.

[5] J. W. Chapman, S. L. Schnulo, and M. P. Nitzsche, "Development of a thermal management system for electrified aircraft", in *AIAA Scitech 2020 Forum*. ARC, 2020. DOI: 10.2514/6.2020-0545.

[6] C. K. Sain, J. Hänsel, and S. Kazula, "Conceptual design of air and thermal management in a nacelle-integrated fuel cell system for an electric regional aircraft", in *AIAA AVIATION 2023 Forum*, 2023. DOI: 10.2514/6.2023-3875.

[7] C. K. Sain, J. Hänsel, and S. Kazula, "Preliminary design of air and thermal management of a nacelle-integrated fuel cell system for an electric regional aircraft", in *2023 IEEE Transportation Electrification Conference & Expo (ITEC)*, 2023, pp. 1–8. DOI: 10.1109/ITEC55900.2023.10187105.

[8] A. Huebner and J. Kirz, "Numerical prediction of heat exchanger performances for a hybrid electric propulsion aircraft concept", in *AIAA AVIATION 2023 Forum*, 2023. DOI: 10.2514/6.2023-3385.

[9] D. Nield and A. Bejan, *Convection in Porous Media, Fourth Edition*. Springer New York, 2013, ISBN: 978-1-4614-5540-0. DOI: 10.1007/978-1-4614-5541-7.

[10] K. Hooman and H. Gurgenci, "Porous medium modeling of air-cooled condensers", *Transport in Porous Media*, vol. 84, pp. 257–273, 2010. DOI: https://doi.org/10.1007/s11242-009-9497-8.

[11] M. Musto, N. Bianco, G. Rotondo, F. Toscano, and G. Pezzella, "A simplified methodology to simulate a heat exchanger in an aircraft's oil cooler by means of a porous media model", *Applied Thermal Engineering*, vol. 94, pp. 836–845, 2016, ISSN: 1359-4311. DOI: https://doi.org/10.1016/j.applthermaleng.2015.10.147.

[12] D. Missirlis, S. Donnerhack, O. Seite, *et al.*, "Numerical development of a heat transfer and pressure drop porosity model for a heat exchanger for aero engine applications", *Applied Thermal Engineering*, vol. 30, no. 11, pp. 1341–1350, 2010, ISSN: 1359-4311. DOI: https://doi.org/10.1016/j.applthermaleng.2010.02.021.

[13] D. Missirlis, Z. Vlahostergios, M. Flouros, *et al.*, "Optimization of heat exchangers for intercooled recuperated aero engines", *Aerospace*, vol. 4, no. 1, 2017, ISSN: 2226-4310. DOI: 10.3390/aerospace4010014.

[14] Z.-Z. Li, Y.-D. Ding, Q. Liao, M. Cheng, and X. Zhu, "An approach based on the porous media model for numerical simulation of 3d finned-tubes heat exchanger", *International Journal of Heat and Mass Transfer*, vol. 173, p. 121 226, 2021, ISSN: 0017-9310. DOI: https://doi.org/10.1016/j.ijheatmasstransfer.2021.121226.

[15] Q. Zhu, M. Pishahang, M. Caccia, *et al.*, "Validation of the Porous Medium Approximation for Hydrodynamics Analysis in Compact Heat Exchangers", *Journal of Fluids Engineering*, vol. 144, no. 8, p. 081 403, 2022, ISSN: 0098-2202. DOI: 10.1115/1.4053898.

[16] P. Schmollgruber, O. Atinault, I. Cafarelli, *et al.*, "Multidisciplinary exploration of DRAGON: An ONERA hybrid electric distributed propulsion concept", in *AIAA Scitech 2019 Forum*, American Institute of Aeronautics and Astronautics Inc., 2019, pp. 1–27. DOI: 10.2514/6.2019-1585.

[17] D. Krempus, F. Beltrame, M. Majer, C. M. De Servi, and R. Vos, "Orc waste heat recovery system for the turboshaft engines of turboelectric aircraft: Correction", in *TU Delft Flight Performance and Propulsion*, vol. 10^{th} EUCASS, 2023. [Online]. Available: https://resolver.tudelft.nl/uuid:3eca4e81-1449-4cce-8e6c-cf8d2929d6ea.

[18] ESDU, *ESDU86002: Drag and Pressure Recovery Characteristics of Auxiliary Air Inlets at Subsonic Speeds*, 2004.

[19] G. Sovran and E. D.Klomp, "Experimentally determined optimum geometries for rectilinear diffusers with rectangular, conical or annular cross-section", General Motors Research Laboratories, Tech. Rep., 1968.

[20] L. R. Reneau, J. P. Johnston, and S. J. Kline, "Performance and design of straight, two-dimensional diffusers", *Journal of Basic Engineering*, vol. 89, no. 1, pp. 141–150, Mar. 1967, ISSN: 0021-9223. DOI: 10.1115/1.3609544.

[21] M. R. Nichols, "Investigation of flow through an intercooler set at various angles to the supply duct", NASA Langley Research Center, Tech. Rep., 1942, Technical Report.

[22] J. D. Mattingly, W. H. Heiser, and D. T. Pratt, *Aircraft Engine Design*, 2nd. AIAA, 2002.

[23] O. C. Jones Jr., "An improvement in the calculation of turbulent friction in rectangular ducts", *Journal of Fluids Engineering*, vol. 98, no. 2, pp. 173–180, Jun. 1976, ISSN: 0098-2202. DOI: 10.1115/1.3448250.

[24] GREThh, *Echtherm*, https://greth.fr/en/echtherm/, 2024.

[25] F. Beltrame, D. Krempus, P. Colonna, and C. M. D. Servi, "Reduced order modelling of optimized heat exchangers for maximum mass-specific performance of airborne orc waste heat recovery units", in *Proceedings of the* 7^{th} *International Seminar on ORC Power Systems*. Seville, Spain: University of Seville, 2023. DOI: 10.12795/9788447227457_93.

[26] J. Hesselgreaves, R. Law, and D. Reay, *Compact Heat Exchangers: : Selection, Design, and Operation*. Elsevier Science, 2016, Second edition, ISBN: 978-0-08-100305-3.

[27] Ansys, *Fluent*, 2024. [Online]. Available: https://www.ansys.com/products/fluids/ansys-fluent.

[28] G. K. Batchelor, *An Introduction to Fluid Dynamics* (Cambridge Mathematical Library). Cambridge University Press, 2000. DOI: 10.1017/CBO9780511800955.

[29] R. K. Shah and D. P. Sekulić, "Heat exchanger pressure drop analysis", in *Fundamentals of Heat Exchanger Design*. John Wiley & Sons, Ltd, 2003, ch. 6, pp. 378–424, ISBN: 9780470172605. DOI: https://doi.org/10.1002/9780470172605.ch6.

[30] F. Menter, "Zonal two equation k-w turbulence models for aerodynamic flows", in *23rd Fluid Dynamics, Plasmadynamics, and Lasers Conference*. 1993. DOI: 10.2514/6.1993-2906.

[31] T. Dal Bello, V. Dippold, and N. J. Georgiadis, "Computational study of separating flow in a planar subsonic diffuser", NASA Glenn Research Center, Tech. Rep., 2005. [Online]. Available: https://ntrs.nasa.gov/citations/20050237896.

[32] X. Zhao, M. Tokarev, E. Adi Hartono, V. Chernoray, and T. Grönstedt, "Experimental validation of the aerodynamic characteristics of an aero-engine intercooler", *Journal of Engineering for Gas Turbines and Power*, vol. 139, no. 5, p. 051 201, 2016, ISSN: 0742-4795. DOI: 10.1115/1.4034964.

[33] I. H. Bell, J. Wronski, S. Quoilin, and V. Lemort, "Pure and pseudo-pure fluid thermophysical property evaluation and the open-source thermophysical property library coolprop", *Industrial & Engineering Chemistry Research*, vol. 53, no. 6, pp. 2498–2508, 2014. DOI: 10.1021/ie4033999.

[34] S. Ahlinder, "On modelling of compact tube bundle heat exchangers as porous media for recuperated gas turbine engine applications", Ph.D. dissertation, Brandenburgische Technische Universität Cottbus-Senftenberg, Brandenburg, Germany, 2006.

5

[35] A. C. Patrao, I. Jonsson, C. Xisto, A. Lundbladh, and T. Gronstedt, "Compact heat exchangers for hydrogen-fueled aero engine intercooling and recuperation", *Applied Thermal Engineering*, vol. 243, p. 122 538, 2024, ISSN: 1359-4311. DOI: https://doi.org/10.1016/j.applthermaleng.2024.122538.

[36] E. Jones, T. Oliphant, P. Peterson, *et al.*, *SciPy: Open source scientific tools for Python*, [Online], 2001. [Online]. Available: http://www.scipy.org/.

[37] G. Stich, L. Fernandes, J. Duensing, J. Housman, G. Kenway, and C. Kiris, "Validation of actuator disk, actuator line and sliding mesh methods within the LAVA solver", in *The 11th International Conference on Computational Fluid Dynamics*, 2022.

6

Conclusions and Recommendations

Thermal energy recovery is arguably a viable technical solution to improve the efficiency of future aero engines and reduce specific emissions. Among available technologies, the organic Rankine cycle (ORC) system, due to its configurational flexibility, is a suitable candidate for the development of combined cycle (CC) propulsion systems. The implementation of waste heat recovery in aero engines is associated with additional complexity compared to stationary power plants due to the interdependence between efficiency improvements and the penalty related to added mass and aerodynamic drag, which affect the overall aircraft performance. Moreover, strict spatial constraints significantly limit the design space, further complicating the system-level design procedure. As a consequence, methodologies developed for stationary power plants are not directly applicable to airborne systems. The optimal design of CC engines requires a multidisciplinary, multi-objective optimization framework involving the concurrent design of the airframe, propulsion system, gas turbine, and ORC unit. Moreover, and importantly, there is no consolidated design practice and operational experience, as aero engine concepts involving thermal energy recovery are new. In this context, aerospace-grade heat exchangers are key enabling components, and specific design methods and guidelines are not available. Their optimal configuration results from complex application-specific trade-offs between thermohydraulic performance and system-level constraints on mass and volume.

This dissertation documents research work on the modeling and optimal methodology for the design of compact heat exchangers and ram air cooling ducts applied to the case of airborne waste heat recovery systems. This effort is part of the ARENA project, a research program carried out by the Propulsion and Power group of Delft University of Technology involving both academic and industrial partners, aiming to assess the potential of combined-cycle engine systems featuring a bottoming ORC unit to harvest thermal energy from the gas turbine exhaust. The main objective of the research pro-

gram is to develop the necessary models and guidelines for optimal system design by coupling compact HX models with multidisciplinary optimization frameworks tailored to the unique constraints of aircraft applications.

The main research areas identified and addressed in this dissertation are:

- The development of accurate, computationally efficient tools for compact HX design and rating to advance the state-of-the-art regarding optimal compact HX design guidelines and optimal HX selection for airborne systems;
- The assessment of the drag recovery potential associated with placing the condenser in the ram air duct (the so-called Meredith effect) of combined cycle engines and the identification of optimal design guidelines.

Based on the results of this work, the main conclusions are summarized as follows.

Compact HX design for airborne systems

1. Traditional HX performance evaluation criteria (PECs) are insufficient if applied to the identification of optimal HX geometries for airborne systems. This is due to the impact of space constraints on the HX design and the dependence of the overall performance on the HX core mass. The selection of the HX core geometry should instead follow guidelines resulting from a space-constrained multi-objective geometry optimization, while the flow arrangement and topology are selected based on considerations about integration feasibility and pinch point analysis. Once the flow configuration, topology, and primary core geometry parameters are selected, the optimal HX design depends on application-specific objectives.

2. Accurate and computationally efficient compact HX sizing and rating tools can be obtained via the integration of a finite-volume method with a moving boundary-like cell discretization method based on local heat duties. This methodology allows for the correct modeling of complex fluid property variations, e.g., those of supercritical fluid flows, with reduced computational cost and increased robustness. It is therefore suited for the design and off-design analysis of compact heat exchangers within complex multidisciplinary optimization frameworks.

3. Design guidelines for compact heat exchangers have been devised based on the results of multiple constrained multi-objective optimizations applied to the case of an air-cooled condenser of an ORC WHR unit. Primary surface microtube-bundle geometries yield the lowest estimated weight, at the expense of a larger pressure drop and lower compactness. The use of extended surfaces, such as fins in tube-bundle configurations, results in designs with increased estimated structural mass, comparatively larger flow friction factor, and lower porosity, which collectively reduce mass-specific performance in systems subject to high flow velocity through the core and strict weight and volume constraints. In such conditions,

typical of aerospace-grade HXs, maximizing the free-flow to frontal area ratio becomes essential. This can be achieved through the adoption of flat tube-and-fin geometries with large fin height and minimal tube thickness.

4. The integrated system and component design optimization of ORC bottoming units allows for (i) a wider range of possible Pareto-optimal designs, and (ii) higher system performance for equal weight if compared to a system optimization in which the HX geometry is fixed. More specifically, for the exemplary cases of ORC WHR systems for auxiliary power units or turboshaft engines, the optimal HX are estimated to achieve 10-15% mass reduction at comparable net power output if the condenser core design parameters are added as degrees of freedom of the system optimization procedure. These improvements are observed for the two analyzed condenser topologies, i.e., flat-tube and microchannel core with louvered or offset strip fins. However, the computational cost associated with the system optimization increases significantly if the design of the condenser is optimized and not assumed a priori. This increase in computational time is proportional to the number of geometry-specific optimization variables associated with the HX design.

5. A novel surrogate model-based optimization method has been proposed to estimate the integrated system design optimization performance without the need for HX sizing or geometry optimization. The result is an enhancement of both the robustness and computational efficiency of the integrated design method without compromising the accuracy of the results. Deviations between the Pareto fronts obtained using the surrogate model optimization strategy and the integrated optimization strategy are within the uncertainty of the preliminary design model. The computational benefit of replacing the detailed condenser model with the surrogate model arises primarily from the reduction in the number of objective function evaluations required to achieve convergence of the system-level optimization. In contrast, the speed-up of individual objective function evaluations has a comparatively minor impact on the total computational time. The development of the surrogate model necessitates the generation of a training dataset, which is computationally demanding and requires prior definition of the HX thermodynamic operating range. However, this dataset must be generated only once for each working fluid and condenser configuration.

Drag recovery of ram air cooling ducts

1. A CFD framework combining the Reynolds-Averaged Navier–Stokes (RANS) model with a porous media model (PMM) to simulate the presence of the HX within the ram air duct has been developed. The localized thermohydraulic performance of the HX is approximated by means of energy and momentum source terms added to the RANS equations specialized for the porous zone. This methodology has been proven to be sufficiently accurate if compared to simulations in which the flow within the HX is fully resolved, and can be used to reduce the computational cost of CFD simulations of ducted heat exchangers.

2. A state-of-the-art lumped parameter model for ram-air cooling ducts has been developed, improved, and verified against the results of the porous-media-model-based CFD simulation framework for the representative case of a bypass duct of a combined-cycle turboshaft engine concept incorporating an inclined condenser. The original model overestimates the net thrust potential of the best-performing duct designs by up to 1.2% of the total gross drag and fails to capture the total pressure losses in the diffuser and tilt regions. As a result, the model is unable to provide reliable estimates of the sensitivity of overall system performance to key geometric parameters. To address these limitations, improved sub-models for the diffuser and HX tilt section have been developed and implemented. These enhancements reduce discrepancies in total pressure loss and flow velocity predictions between the lumped-parameter model and CFD simulations across multiple flow stations and for a wide range of geometrical configurations. The improved model provides results that are in good agreement with CFD results in terms of pressure distribution, flow velocity, and net aerodynamic drag over a wide design space defined by variations in diffuser area ratio, ram mass flow rate, and heat exchanger inclination angle. This demonstrates the suitability of the improved lumped-parameter model for preliminary design and system-level optimizations involving ram-air-cooled heat exchanger configurations.

3. The net drag of the ram air duct depends on the aerothermal performance of the HX, the duct design, the flight speed, and the altitude. The thrust generated by the acceleration of the heated airflow through a nozzle can compensate and even exceed the drag penalty introduced by the presence of the ORC condenser located inside the ram air duct. More in detail, for the case study of a CC-TS engine concept operating at cruise conditions (M_0 = 0.78, altitude of 10 km), a temperature increase of approximately 100 K across the air side of the condenser enables the optimized ram air duct to generate thrust exceeding the duct gross aerodynamic drag by up to 4%. Additional thrust gains can be achieved by incorporating a fan within the duct, which increases the inlet pressure and enhances the effectiveness of thermal energy discharge.

4. Design guidelines for the conceptual design of ram-air cooling ducts have been derived through parametric analyses and spatially constrained optimization studies employing an improved lumped-parameter model. The available duct length is found to be the dominant design constraint, with peak thrust achieved when the maximum length is fully utilized. While larger heat exchanger inclination angles enhance performance, the optimal values of the mass flow rate ratio (MFR) and diffuser area ratio (AR) depend primarily on the imposed geometric constraints, irrespective of the heat exchanger topology. In addition, the optimization of the heat exchanger is predominantly governed by the minimization of pressure losses, which permits its design to be treated independently from that of the duct. Accordingly, the heat exchanger geometry should be selected to maximize porosity and minimize frictional losses while remaining compliant with the imposed spatial limitations.

6.1. LIMITATIONS AND RECOMMENDATIONS

The main limitations of the research work documented in this dissertation are outlined in the following, along with recommendations on how to address them in future research.

- The performance evaluation methodology treated in Chapter 2 is based on a multi-objective optimization routine that enables the comparison of optimized HX geometries under prescribed spatial constraints. The application of this methodology requires the availability of rating or sizing tools that are appropriate for the case study under investigation. For instance, in Chapter 2, a simple effectiveness–NTU sizing method validated against literature data [1, Ch. 9] is sufficient to analyze the performance of different fin topologies for the test case of an air-to-air plate-fin HX. However, for applications involving significant fluid property variations, such as condensers or supercritical heaters, the use of the simplified model may lead to non-negligible inaccuracies. In such cases, it is recommended to substitute the simple sizing routine with a more detailed HX model, such as the one documented in Chapter 3, to ensure reliable performance predictions.

- The accuracy of the hybrid finite-volume heat exchanger model documented in Chapter 3 is primarily limited by the uncertainty associated with empirical correlations for heat transfer and pressure drop. While widely used compact HX configurations are well characterized, other geometries, such as elliptical or finned tube bundles arranged in non-standard layouts, are supported by limited experimental data. In these cases, the applicability and uncertainty of existing correlations remain unclear. Therefore, future studies should verify their validity through high-fidelity CFD simulations or experimental investigations prior to applying them to the optimization of unconventional core geometries.

- The dataset used to train the surrogate model of optimal HXs detailed in Chapter 4 has been generated for one working fluid, i.e., cyclopentane. Although the methodology is independent of the working fluid, to reduce potential bias and expand the range of applicability, future work should extend the dataset by incorporating optimal heat exchanger designs obtained for multiple working fluids. Additionally, increasing the total number of optimized geometries for each heat exchanger topology is recommended to enhance the model accuracy across a broader design space. Furthermore, the current surrogate modeling framework is restricted to one heat exchanger topology for each model instance. A more versatile approach would enable the simultaneous analysis, comparison, and selection of multiple heat exchanger topologies within a unified surrogate model, thereby facilitating their integration into system-level optimization routines.

- The surrogate modeling approach detailed in Chapter 4 is based on the assumption that only the pressure loss on a single fluid side–specifically, the air side in the case of the condenser–significantly affects system performance. As a result, pressure losses on the working fluid side are not considered, despite their potential relevance in certain applications. To address this limitation, future work should

extend the surrogate model to generate three-dimensional Pareto fronts that incorporate pressure drops on both fluid sides in addition to heat exchanger mass. The model could also be refined by including supplementary output parameters, such as core porosity and compactness, to more accurately characterize the geometric and thermohydraulic features of Pareto-optimal designs.

- The improved lumped parameter model (LPM) used for the ram air duct analysis in Chapter 5 has been verified against two-dimensional RANS simulations. However, the accuracy of RANS simulations for diffusing flows is dependent on the choice of turbulence model and the test case [2], [3]. In the case of highly separated flows, RANS simulations may fail to capture the velocity field and wall pressure distribution, even if the total pressure at the end of the duct may be in good agreement with experimental data [4]. Therefore, future work should focus on characterizing the accuracy of the RANS simulation framework by comparison with experimental data.

- The CFD simulations used to calibrate the lumped parameter model only resolve the internal flow within the duct. As a result, the accuracy of the intake submodel, which is used within the LPM to estimate the aerodynamic performance of the external portion of the duct, remains uncertain. To address this limitation, future work should extend the CFD simulation framework to include the modeling of the flow field external to the ram air duct and explore multiple operating conditions beyond cruise. This would allow for a comprehensive accuracy evaluation of the intake model and increase confidence in the predictive capabilities of the LPM. Moreover, the developed simulation framework cannot account for three-dimensional effects introduced by the integration of the duct with surrounding structures such as the fuselage, pylon, and wing. However, these effects are installation-specific and should therefore be incorporated in high-fidelity, detailed studies to improve the accuracy of the aerodynamic performance assessment of the duct.

- The porous media model (PMM) used in the CFD simulations documented in Chapter 5 does not explicitly resolve the flow within the core geometry of the heat exchanger and may therefore fail to capture localized flow phenomena, particularly near the HX outlet, such as flow separation, turbulence, and recirculation. Additionally, the model employs a single anisotropic porous zone characterized by a uniform wall temperature. While this approximation is appropriate for heat exchangers operating under quasi-isothermal conditions, such as condensers and evaporators, it becomes less accurate if significant wall temperature gradients develop along the flow direction. In such cases, although the model may still yield reasonable predictions of bulk performance quantities such as total pressure drop and heat duty, it may not accurately reproduce the velocity and temperature fields downstream of the core. To address this limitation, a more refined modeling strategy based on a multi-zone porous representation is recommended, wherein the wall temperature is imposed locally within each zone. This approach enables a more accurate prediction of the heat exchanger influence on the thermal and fluid dynamic characteristics of the surrounding flow field. Furthermore, future work

should focus on calibrating the porous media resistance coefficients using experimental measurements and comparing the results against those obtained via the off-design HX model implemented in *HeXacode*, to assess the consistency and reliability of both calibration approaches.

- The framework for the optimal design of ram air ducts developed in this work does not account for the induced drag associated with an increase in aircraft weight due to changes in the duct or heat exchanger geometry. Specifically, any additional mass δM leads to an increment in the required cruise lift coefficient δC_L, which results in an increased induced drag coefficient according to the relation $\delta C_{D,i} = \delta C_L / (\pi\, e\, \mathrm{AR})$, where e is the Oswald factor and AR is the wing aspect ratio, calculated as the square of the span divided by the wing area. However, for modern aircraft such as the Airbus A320neo, the induced drag penalty associated with additional mass is relatively small, typically on the order of 4.5% of the added weight [5] [6] [7]. Consequently, the optimal design trends presented in this work neglect the contribution of induced drag on the overall net thrust. Additionally, skin friction drag is assumed to remain constant under the assumption that the duct is fully embedded within a nacelle of fixed external geometry, and hence, independent of duct length. However, future studies addressing the detailed design of propulsion systems employing ram-air cooling should include the effects of changes in weight and duct geometry on induced and skin friction drag to improve the fidelity of performance predictions.

6.2. OUTLOOK ON FUTURE RESEARCH DIRECTIONS

The research work documented in this dissertation has advanced knowledge about the optimal design and the integration of compact heat exchangers within airborne power and propulsion systems. The *HeXacode* software, developed as part of this work, is a modular, robust, and computationally efficient framework that enables the preliminary design, rating, and optimization of compact heat exchangers and their integration into ram air cooling ducts. Its structure allows for direct and seamless coupling with system-level optimization environments such as the ARENA framework [8], and supports a range of flow arrangements, heat exchanger topologies, and working fluid conditions. These features render *HeXacode* particularly suitable for conceptual studies on energy recovery systems and thermal management in aerospace applications. Future developments of the software should focus on expanding its predictive capabilities by:

- **Expanding the geometry library** to include additional primary and extended surface topologies. Examples of extended surface topologies to be included in the geometry class of the software are pin fins, corrugated triangular fins, and perforated or serrated fins. Examples of primary surface topologies to be included in the software are airfoil-shaped tubes, elliptical, and twisted tube bundles. Note that each new topology requires heat transfer and pressure drop correlations that are specific to the HX topology, as opposed to the common practice of relying on generalized correlations.

- **Including sub-models for local pressure losses** associated with manifolds, bends,

and uneven flow distribution between multiple passes on the working fluid side.

- **Integrating high-fidelity thermo-mechanical stress models** to assess structural integrity and fatigue of the HX core under high-speed and high-temperature flows such as gas turbine exhaust conditions.
- **Implementing multi-point optimization capabilities** leveraging the HX rating model to evaluate optimal designs across a set of specified operating conditions.

The models developed within this research are steady-state and suitable for preliminary design studies. While off-design simulations can be used to conduct multi-point analyses, transient operations such as startup, shutdown, and dynamic changes are not captured. Modeling these unsteady effects is essential for a detailed assessment of the feasibility of thermal systems such as ORC WHR units for airborne and, more generally, mobile applications [9]. Consequently, the development of low-order, time-resolved models suitable for dynamic simulations of both heat exchangers and ram air cooling ducts constitutes a natural and necessary extension of the present work.

Developments in GPU-accelerated CFD software have substantially reduced simulation times by harnessing the parallel processing capabilities of modern graphics hardware [10] [11]. However, the computational cost of detailed CFD simulations remains prohibitive for integrating such models within system-level design optimization studies involving large design space exploration. Nonetheless, these advancements can facilitate high-fidelity simulations of flows through complex heat exchanger geometries, supporting the derivation of thermohydraulic correlations for unconventional core designs produced through shape or topology optimization [12]–[14]. These unconventional core topologies can therefore be incorporated into *HeXacode* to support advanced system-level optimization studies.

The surrogate modeling strategy presented in Chapter 4 is a promising approach to reduce computational cost and enhance the robustness of optimal system design exploration studies. This approach, which involves replacing the detailed heat exchanger model with a data-driven surrogate that predicts the performance of optimal designs, can be extended to additional system components such as the ORC turbogenerator [15]. This would broaden the applicability of the methodology in early-stage design studies.

The detailed aerodynamic and thermodynamic characterization of ram-air-cooled systems is essential to support the transition from preliminary to detailed design and to ensure their successful integration into next-generation propulsion and thermal management systems [16]. The lumped parameter model developed for the design of ram air ducts has demonstrated satisfactory predictive capabilities for preliminary design studies, providing estimates of internal flow velocities, net aerodynamic drag, and local pressure losses with good agreement against two-dimensional RANS simulations. However, novel propulsion systems featuring waste heat recovery, electrification, or fuel cell power generation increasingly impose stringent thermal management requirements [17]. In such configurations, the influence of ram air cooling systems on overall aircraft aerodynamic and propulsive performance must be carefully assessed. To this end, future

research should focus on extending the lumped parameter model to model fan-assisted configurations, unconventional heat exchanger placements, and three-dimensional effects, particularly in the intake region, to improve the accuracy of installed performance predictions and spillage loss estimates.

High-fidelity CFD simulations remain essential for validating and refining the underlying assumptions of the lumped parameter model. More in detail, three-dimensional simulations incorporating detailed modeling of the flow through the heat exchanger core, nacelle integration, engine bypass flow interaction, and realistic aircraft boundary conditions are required to correctly model flow distortion, separation phenomena, and spillage drag effects. Of particular interest is the interaction between the duct inlet, engine nacelle geometry, and adjacent airframe surfaces, which may significantly influence the local flow field and system performance. The findings documented in this dissertation also indicate that the porosity of the heat exchanger strongly affects flow acceleration and the associated pressure loss. Future research should thus investigate alternative heat rejection configurations that minimize the requirement for the entire airflow to pass through a porous core. Promising configurations include skin-mounted heat exchangers, which are currently being studied for high-heat-load thermal management systems, particularly in the context of fuel-cell-powered aircraft [18], [19].

Ultimately, the predictive capabilities of the developed models must be validated against experimental data. Future research should therefore support the design of experiments and testing of subscale or full-scale demonstrators operated under representative thermodynamic and aerodynamic conditions. Particular emphasis should be placed on the experimental characterization of the aerothermal performance of the condenser integrated within the ram air duct, as this component plays a critical role in the propulsion system efficiency and aerodynamic drag.

BIBLIOGRAPHY

[1] D. Shah R. Sekulic, *Fundamentals of heat exchanger design*. John Wiley and Sons, 2003.

[2] T. Dal Bello, V. Dippold, and N. J. Georgiadis, "Computational study of separating flow in a planar subsonic diffuser", NASA Glenn Research Center, Tech. Rep., 2005. [Online]. Available: https://ntrs.nasa.gov/citations/20050237896.

[3] X. Ren, Y. Li, and C. Gu, "Influence of turbulence models on the numerical prediction of flow in an industrial gas turbine intake system", in *Proceedings of Global Power and Propulsion Society*, vol. GPPS Chania 2024, 2024. DOI: 10.33737/gpps24-tc-172.

[4] M. C. Hein, M. Reissmann, J. A. Scheibel, M. Stößel, R. Sandberg, and D. Kožulović, "Numerical simulation of a highly bent intake duct using machine learning algorithms to close the rans equations", in *Proceedings of Global Power and Propulsion Society*, vol. GPPS Chania 2024, 2024. DOI: 10.33737/gpps24-tc-083.

[5] E. Karadotcheva, S. N. Nguyen, E. S. Greenhalgh, M. S. P. Shaffer, A. R. J. Kucernak, and P. Linde, "Structural power performance targets for future electric aircraft", *Energies*, vol. 14, no. 19, 2021, ISSN: 1996-1073. DOI: 10.3390/en14196006.

[6] AIRBUS, *A318-A319-A320-A321 flight crew operating manual*, 2017. [Online]. Available: https://repo.poltekbangsby.ac.id/id/eprint/571/.

[7] J. Sun, J. Hoekstra, and J. Ellerbroek, "Aircraft drag polar estimation based on a stochastic hierarchical model", in *Eighth SESAR Innovation Days*, Dec. 2018. [Online]. Available: https://resolver.tudelft.nl/uuid:9977a616-4506-4acb-9d27-b9e27f9ddb8d.

[8] D. Krempus, C. M. D. Servi, R. Vos, and P. Colonna, "Organic rankine cycle waste heat recovery systems for aircraft engines", Ph.D. dissertation, Delft University of Technology, 2025.

[9] F. Fatigati, A. Coletta, M. Di Bartolomeo, and R. Cipollone, "The dynamic behaviour of orc-based power units fed by exhaust gases of internal combustion engines in mobile applications", *Applied Thermal Engineering*, vol. 240, p. 122 215, 2024, ISSN: 1359-4311. DOI: https://doi.org/10.1016/j.applthermaleng.2023.122215.

[10] Y. Zhang, W. Ren, H. Yu, and H. Li, "Development of gpu-based parallel cfd solver for unstructured meshes", in *2023 7th International Conference on Electrical, Mechanical and Computer Engineering (ICEMCE)*, 2023, pp. 469–473. DOI: 10.1109/ICEMCE60359.2023.10490481.

[11] X. Zhang, X. Guo, Y. Weng, X. Zhang, Y. Lu, and Z. Zhao, "Hybrid mpi and cuda parallel finite volume unstructured cfd simulations on a multi-gpu system", *Future Generation Computer Systems*, vol. 139, pp. 1–16, 2023, ISSN: 0167-739X. DOI: https://doi.org/10.1016/j.future.2022.09.005.

[12] S. S. Yogesh, A. S. Selvaraj, D. K. Ravi, and T. K. R. Rajagopal, "Heat transfer and pressure drop characteristics of inclined elliptical fin tube heat exchanger of varying ellipticity ratio using cfd code", *International Journal of Heat and Mass Transfer*, vol. 119, pp. 26–39, 2018, ISSN: 0017-9310. DOI: https://doi.org/10.1016/j.ijheatmasstransfer.2017.11.094.

[13] R. Deeb, "Correlations and numerical analysis of thermal-hydraulic performance of staggered mixed tube bundle composed of circular and drop-shaped tubes", *International Journal of Heat and Mass Transfer*, vol. 199, p. 123 487, 2022, ISSN: 0017-9310. DOI: https://doi.org/10.1016/j.ijheatmasstransfer.2022.123487.

[14] R. Deeb, "New correlations for predicting convective heat transfer of single and multi-row heat exchangers employing staggered drop-shaped tubes", *International Journal of Heat and Mass Transfer*, vol. 202, p. 123 689, 2023, ISSN: 0017-9310. DOI: https://doi.org/10.1016/j.ijheatmasstransfer.2022.123689.

[15] M. Majer and M. Pini, "Design guidelines for high-pressure ratio supersonic radial-inflow turbines of organic rankine cycle systems", *Journal of the Global Power and Propulsion Society*, vol. 9, pp. 19–46, 2025. DOI: 10.33737/jgpps/195437.

[16] A. C. Frey, J. Stonham, D. Bosak, C. M. Sangan, and O. J. Pountney, "Radiators in fuel cell powered aircraft: The effect of heat rejection on drag", *Applied Thermal Engineering*, vol. 274, p. 126 697, 2025, ISSN: 1359-4311. DOI: https://doi.org/10.1016/j.applthermaleng.2025.126697.

[17] M. Coutinho, D. Bento, A. Souza, *et al.*, "A review on the recent developments in thermal management systems for hybrid-electric aircraft", *Applied Thermal Engineering*, vol. 227, p. 120 427, 2023, ISSN: 1359-4311. DOI: https://doi.org/10.1016/j.applthermaleng.2023.120427.

[18] S. Schaefer, F. Quaium, N. Muhsal, A. Speerforck, F. Thielecke, and C. Becker, "Integration of a cooling system architecture with a skin heat exchanger for high thermal loads in fuel cell powered aircraft", in *International Refrigeration and Air Conditioning Conference*. 2022. [Online]. Available: https://docs.lib.purdue.edu/iracc/2347.

[19] A. Felgueroso, I. González-Nieves, M. Díaz-Barja, and J. García-Rodríguez, "Numerical modeling of a two-phase skin heat exchanger for hybrid-electric regional aircraft", in *AIAA AVIATION FORUM AND ASCEND*. 2024. DOI: 10.2514/6.2024-3579. [Online]. Available: https://arc.aiaa.org/doi/abs/10.2514/6.2024-3579.

A

THERMOHYDRAULIC CORRELATIONS FOR HEAT EXCHANGERS

This appendix reports the correlations implemented in *HeXacode* that have been used to estimate the thermohydraulic performance of the compact HX cores investigated in the research documented in this dissertation.

A

GASEOUS FLOW THROUGH HX CORE GEOMETRIES

For the tube bundle-type heat exchangers, the fluid side with the higher thermal resistance flows in a cross-flow arrangement with respect to the tubes, where the working fluid flows. The correlations for tube bundles reported in Table A.1 and A.2 are valid for tubes of circular cross-section. Alternative tube shapes documented in the open literature include elliptical, airfoil, or drop-shaped cross sections. However, limited experimental data and correlations are available for these unconventional tube shapes and will thus not be reported in this document. For the extended surface core topologies, the employed correlations are independent of the arrangements of the fluid on the other side or the geometry of the core. Therefore, these correlations can be applied to flat-tube or plate-fin topologies.
The heat transfer correlations are expressed in the form of

- Nusselt number

$$Nu = \frac{h\, d_\mathrm{h}}{k} \tag{A.1}$$

- or Colburn factor

$$j = \frac{h\, d_\mathrm{h}}{k\, Re\, Pr^{1/3}}\,. \tag{A.2}$$

The flow properties (Re, k) used in the correlations are the average between the inlet and outlet.

Heat transfer correlations			
Geometry	**Property**	**Ref.**	**Notes**
plain tube bundle (inline / staggered)	Nu	[1]	$Re > 200$, $Pr \geq 0.6$, $N_r \geq 2$
plain fin tube bundle (staggered arrangement)	j	[2]	$Re \geq 150$, $1.4 < \tilde{x}_\mathrm{t} < 5$, $1 < \tilde{x}_\mathrm{l} < 4.3$
circular fin tube bundle (inline arrangement)	Nu	[3]	$5000 \leq Re \leq 7 \times 10^4$, $N_r > 3$
louvered fins (lf)	j	[4]	$100 \leq Re\frac{L_\mathrm{p}}{d_\mathrm{h}} \leq 3000$, $0.5 \leq Pr \leq 15$
offset-strip fins (osf)	j	[5]	$120 \leq Re \leq 10^4$, $0.5 \leq Pr \leq 15$
wavy fins (twf)	j	[6], [7]	$600 < Re \leq 6500$

Table A.1: List of empirical correlations selected for the heat transfer coefficient estimation on the air/gas side.

The pressure drop correlations are expressed in the form of

- the average pressure drop coefficient of the tube bundle

$$C_\mathrm{f} = \frac{2\Delta P}{\rho u_\mathrm{m}^2 N_r}\,, \tag{A.3}$$

- average Euler number

$$Eu = \frac{\Delta P}{\frac{1}{2}\rho u_{\mathrm{m}}^2} = C_{\mathrm{f}} N_r \,, \tag{A.4}$$

- or the average Fanning friction factor in the core

$$f = \frac{\rho_m}{\rho_1}\frac{A_0}{A}\left(\frac{2\rho_1 \Delta P_{\mathrm{core}}}{G_0^2} - 2\left(\frac{\rho_1}{\rho_2} - 1\right)\right) , \tag{A.5}$$

where ΔP_{core} is the pressure drop across the HX without entrance and exit effects [8], the subscripts $_1$ and $_2$ refer to the inlet and outlet, respectively.

Pressure drop correlations			
Geometry	**Property**	**Ref.**	**Notes**
plain tube bundle (inline / staggered)	C_{f}	[9]	$Re > 200$, $Pr \geq 0.6$, $N_r \geq 2$
plain fin tube bundle (staggered arrangement)	C_{f}	[2]	$Re \geq 150$, $1.4 < \tilde{x}_{\mathrm{t}} < 5$, $1 < \tilde{x}_{\mathrm{l}} < 4.3$
circular fin tube bundle (inline arrangement)	$Eu = \frac{C_{\mathrm{f}}}{N_r}$	[3]	$5000 \leq Re \leq 7 \times 10^4$, $N_r > 3$
louvered fins (lf)	f	[10]	$100 \leq Re\frac{L_{\mathrm{p}}}{d_{\mathrm{h}}} \leq 3000$, $0.5 \leq Pr \leq 15$
offset-strip fins (osf)	f	[5]	$120 \leq Re \leq 10^4$, $0.5 \leq Pr \leq 15$
wavy fins (twf)	f	[6], [7]	$600 < Re \leq 6500$

Table A.2: List of empirical correlations selected for the pressure drop estimation on the air/gas side.

A

FLOW INSIDE TUBES AND CHANNELS

The thermohydraulic performance correlations reported in Table A.3 and A.4 apply to flows within tubes and channels. In the turbulent regime, the correlations are independent of the tube or channel shape. In the laminar regime, however, the Nusselt number and friction factor correlations depend on the shape of the flow passage. The correlations implemented in *HeXacode* allow for tubes and channels of circular, elliptical, rectangular, or triangular cross section.

Heat transfer correlations			
WF state	**Property**	**Ref.**	**Notes**
single-phase	Nu_{lam}	[11]	$Re < 2300$
	Nu_{trans}	[11]	$2300 \leq Re \leq 4000$
	Nu_{turb}	[12]	$Re > 4000$
	Nu_{turb}	[13]	$Re > 4000$ & supercritical
two-phase (evaporation)	h	[14]	$Re_{\text{LO}} > 100$
two-phase (condensation)	h	[15]	$P_{\text{sat}}/P_{\text{cr}} \leq 0.946$, $1.1 \leq G_0 \leq 1400$

Table A.3: List of empirical correlations selected for the heat exchanger heat transfer coefficient estimation on the working fluid side.

Pressure drop correlations			
WF state	**Property , range**	**Ref.**	**Notes**
single-phase	f_{lam}	[11, Ch. 7]	$Re < 2100$
	f_{trans}	Bhatti–Shah [11, Ch. 7]	$2100 \leq Re \leq 4000$
	f_{turb}	Colebrook-White [12]	$4000 < Re \leq 10^7$
two-phase (evap./cond.)	$\frac{\mathrm{d}P}{\mathrm{d}Z}$	[16]	$0.07 \leq P_{\text{sat}}/P_{\text{cr}} \leq 0.6$, $\frac{R_a}{d_{\text{h}}} \leq 0.007$

Table A.4: List of empirical correlations selected for the heat exchanger pressure drop estimation on the working fluid side flowing inside channels or tubes.

BIBLIOGRAPHY

[1] H. Martin, "The generalized lévêque equation and its practical use for the prediction of heat and mass transfer rates from pressure drop", *Chemical Engineering Science, Volume 57, Issue 16*, 2002.

[2] C.-C. Wang, K.-Y. Chi, and C.-J. Chang, "Heat transfer and friction characteristics of plain fin-and-tube heat exchangers, part ii: Correlation", *International Journal of Heat and Mass Transfer*, vol. 43, no. 15, pp. 2693–2700, 2000, ISSN: 0017-9310. DOI: https://doi.org/10.1016/S0017-9310(99)00333-6. [Online]. Available: https://www.sciencedirect.com/science/article/pii/S0017931099003336.

[3] M. Mi Sandar, "Numerical investigation of air-side heat transfer and pressure drop in circular finned-tube heat exchangers", Ph.D. dissertation, TU Bergakademie Freiberg, 2003. [Online]. Available: https://nbn-resolving.org/urn:nbn:de:swb:105-26331.

[4] Y. Chang and C. Wang, "A generalized heat transfer correlation for louver fin geometry", *International Journal of Heat and Mass Transfer*, 1997.

[5] R. Manglik and A. Bergles, "Heat transfer and pressure drop correlations for the rectangular offset strip fin compact heat exchanger", *Experimental thermal and fluid science*, 1995.

[6] D. Junqi, C. Jiangping, C. Zhijiu, Z. Yimin, and Z. Wenfeng, "Heat transfer and pressure drop correlations for the wavy fin and flat tube heat exchangers", *Applied Thermal Engineering*, vol. 27, no. 11, pp. 2066–2073, 2007, ISSN: 1359-4311. DOI: https://doi.org/10.1016/j.applthermaleng.2006.11.012. [Online]. Available: https://www.sciencedirect.com/science/article/pii/S1359431106004121.

[7] J. Dong, L. Su, Q. Chen, and W. Xu, "Experimental study on thermal–hydraulic performance of a wavy fin-and-flat tube aluminum heat exchanger", *Applied Thermal Engineering*, vol. 51, no. 1, pp. 32–39, 2013, ISSN: 1359-4311. DOI: https://doi.org/10.1016/j.applthermaleng.2012.09.018.

[8] A. Kays W.M. London, *Compact heat exchangers*. Scientific International, 2018.

[9] VDI, *VDI Heat Atlas*, 2nd. Springer, 2010.

[10] Y. Chang, K. Hsu, Y. Lin, and C. Wang, "A generalized friction correlation for louver fin geometry", *International Journal of Heat and Mass Transfer*, 2000.

[11] D. Shah R. Sekulic, *Fundamentals of heat exchanger design*. John Wiley and Sons, 2003.

[12] W. Kast, (by Hermann Nirschl), E. S. Gaddis, K.-E. Wirth, and J. Stichlmair, "L1 pressure drop in single phase flow", in *VDI Heat Atlas*. Springer Berlin Heidelberg, 2010, pp. 1053–1116. DOI: 10.1007/978-3-540-77877-6_70.

[13] I. Pioro and S. Mokry, "Heat transfer to supercritical fluids", *Heat Transfer - Theoretical Analysis, Experimental Investigations and Industrial Systems*, 2011.

[14] S. G. Kandlikar and P. Balasubramanian, "An extension of the flow boiling correlation to transition, laminar, and deep laminar flows in minichannels and microchannels", *Heat Transfer Engineering*, vol. 25, no. 3, pp. 86–93, 2004. DOI: 10.1080/01457630490280425.

[15] M. M. Shah, "Improved correlation for heat transfer during condensation in conventional and mini/micro channels", *International Journal of Refrigeration*, vol. 98, pp. 222–237, 2019, ISSN: 0140-7007. DOI: https://doi.org/10.1016/j.ijrefrig.2018.07.037.

[16] D. Del Col, A. Bisetto, M. Bortolato, D. Torresin, and L. Rosetto, "Experiments and updated model for two-phase frictional pressure drop inside minichannels", *International Journal of Heat and Mass Transfer*, vol. 67, pp. 326–337, 2013. DOI: https://doi.org/10.1016/j.ijheatmasstransfer.2013.07.093.

B

Shape Optimization of a Turbofan Bypass Duct Housing a Condenser

Parts of the methods and content reported in this appendix have been published in [1]. The Author is thankful for the contributions of K. Wessendorp.

Introduction

The thrust that can be obtained via accelerating the heated ram air through a nozzle can be increased if the airflow is heated at a higher static pressure [2]. The combined cycle turbofan discussed in Sec. 3.4.3 therefore features the ORC condenser positioned downstream of a fan, outlet guide vane, and diffuser. This HX integration and engine configuration increases the cooling mass flow rate and air density compared to a non-compressed duct, thereby improving the propulsive efficiency of the bypass duct. An increase in propulsive efficiency would correlate with a reduction in fuel consumption provided that thermal efficiency and weight remain constant.

However, modeling the integration of the condenser within the bypass duct of the aero engine is a complicated task. The accuracy of the simplified lumped parameter model used in Sec. 3.4.3 is not yet known. The CFD framework detailed in Chapter 5 cannot yet be used to perform numerical simulations on the CC-TF bypass duct. This is because the model does not include the presence of a fan inside the duct and does not resolve the flow upstream and around the aero engine nacelle. Spillage effects are

thus not considered. Therefore, the CFD simulation framework requires modifications to solve the flow field upstream and around the engine to correctly estimate the overall engine net thrust and to account for the presence of the fan and outlet guide vanes in the bypass duct.

The objective of the study reported in this appendix is therefore the development of a computationally efficient CFD simulation framework that enables the analysis and shape optimization of air cooling or bypass ducts housing fans and heat exchangers. The bypass duct of the CC-TF engine concept is used as a case study [3]. The fan and outlet guide vanes are modeled using actuator disk models, the duct shape is parametrized using cubic splines and control points, and the heat exchanger is simulated using a porous media model [4].

METHODOLOGY

The condenser core geometry consists of a flat-tube microchannel HX with louvered fins, mounted in an annular configuration to allow for a simple and axisymmetric integration within the bypass duct. The heat exchanger is modeled using the porous media model (PMM) detailed in Chapter 5. The flow outside of the porous zone is solved using RANS simulations with the $k-\omega$ SST turbulence model [5]. The effect of the airflow required by the CC-TF engine core on the bypass flow is simulated via a mass flow rate sink. An actuator disk (AD) method is used to model the fan and outlet guide vanes as permeable disks that exert forces on the air passing through without needing to resolve the exact geometry of the blades or vanes. The total pressure ratio obtained using the AD model has been partially validated through comparison with experimental data [6]. The total pressure distribution after the fan and the swirl angle obtained using the AD models have been verified against high-fidelity unsteady RANS simulations [7].

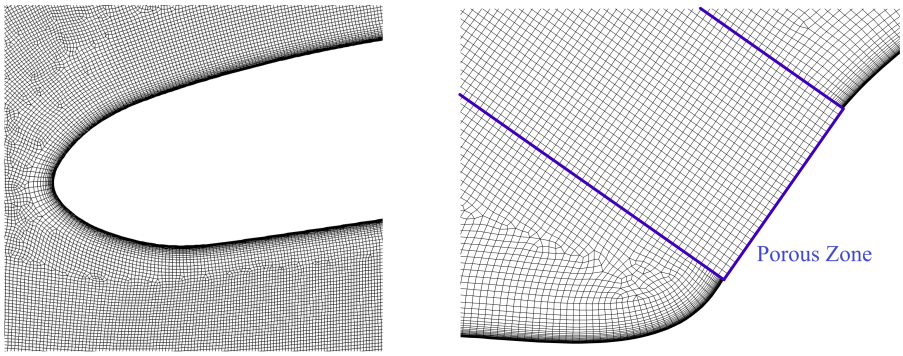

Figure B.1: Detail of the mesh near the inlet lip of the turbofan engine (left) and across the porous zone near the bottom wall of the bypass duct (right).

The resolved flow domain spans ahead of the engine inlet by 5.2 nacelle diameters, and around the engine by 6.5 nacelle diameters. A hybrid and adaptive mesh featuring large uniform cells in the far airflow field and smaller unstructured mesh elements near the engine and HX inlet is used to balance accuracy and computational efficiency. The ge-

ometry of the CC-TF engine is based on the LEAP-1A engine, representative of a modern high-bypass ratio (BPR) turbofan configuration.

The developed CFD simulation framework is employed to analyze the thrust generated by the bypass flow of a turbofan engine for 4 cases:

- Case #1: The bypass duct has no heat exchanger (reference case).
- Case #2: The condenser is placed in the bypass duct; however, the ORC unit is switched off. Therefore, the condenser is not discharging thermal energy to the ram air.
- Case #3: The ORC unit is active: the condenser is transferring thermal energy to the bypass flow.
- Case #4: The ORC unit is active, and the bypass duct shape is optimized.

The shape of the bypass duct is parametrized by means of a set of control points that define the internal bypass duct wall cubic spline profiles. The y-coordinate of each control point is constrained within individually defined upper and lower bounds based on estimated clearances and the spatial positioning of the surrounding components in the turbofan engine. This allows the current turbofan dimensions to remain the same as those of the reference engine. However, this constraint limits the maximum net thrust increase that the optimizer can achieve. The adaptive-single objective (ASO) optimization routine implemented in ANSYS Fluent is used to maximize the net thrust of the engine by optimizing the bypass duct shape. A computational mesh consisting of 500,000 cells was selected for detailed CFD simulations based on the outcome of a grid-convergence study. To reduce the computational cost of the optimization routine, a coarser mesh with 350,000 cells was employed. The maximum deviation observed between the two mesh resolutions concerns the temperature rise across the heat exchanger, with a difference of approximately 0.5%. This level of discrepancy is considered negligible, enabling a substantial reduction in simulation time without compromising the accuracy of the results.

Results

As shown in Fig. B.2, he presence of a heat exchanger that is not transferring thermal energy results in a 13.7% reduction in net thrust relative to the reference configuration. If the ORC unit is active and thermal energy is discharged into the ram air flow, the thrust penalty is reduced to 9.3%, indicating partial conversion of the added thermal energy into kinetic energy.

The presence of the condenser inside the bypass duct causes an inward shift of the stagnation point on the engine inlet, resulting in a higher pre-diffusion effect upstream of the turbofan intake and larger spillage drag. The increased spillage causes a greater airflow acceleration around the intake of the turbofan, leading to the formation of a weak shock on the outer wall of the engine nacelle as shown in Fig. B.3. The normalized static pressure $\frac{p}{p_\infty}$ at the inlet of the fan increases from 1.3 to approximately 1.42 in case #3.

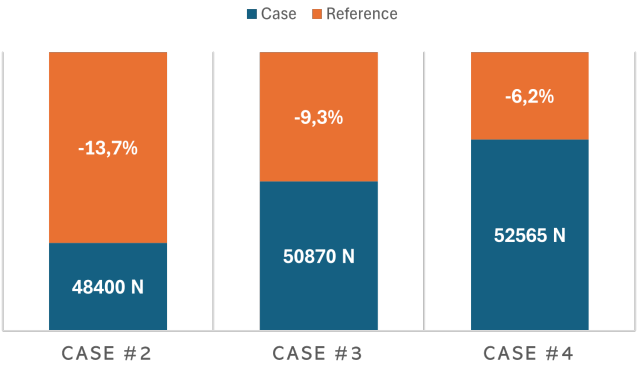

Figure B.2: Comparison of the net thrust generated by the CC-TF engine that integrates the condenser inside the bypass duct with the reference turbofan engine, which is 56.08 kN. Note that the thrust contribution of the hot exhaust gases of the engine core is neglected in all four cases.

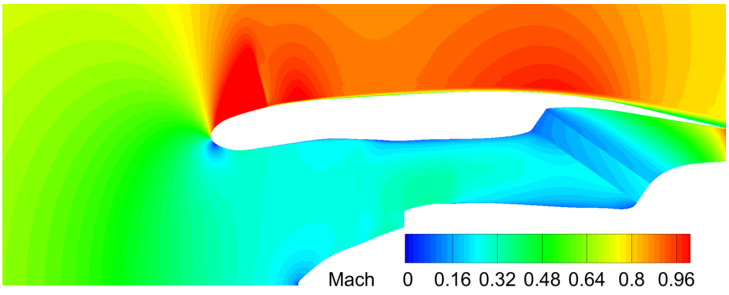

Figure B.3: Contour plot of the air stream Mach number around the CC-TF engine and inside the bypass duct. A weak shock is observed on the outer wall of the engine nacelle.

The bypass stream of the CC-TF is therefore characterized by larger pressures upstream of the porous zone caused by the additional blockage introduced by the condenser [1].

The HX introduces a non-uniform pressure loss as shown in Fig. B.4. More specifically, the pressure losses are greater in the lower duct region, where the flow velocity is much higher. A small pressure recovery is observed immediately downstream of the porous zone due to the sudden increase in flow area, followed by a gradual pressure decrease as the flow expands through the nozzle. As graphically displayed in Figure B.5, the lower flow velocity near the upper wall of the bypass duct causes a non-uniform temperature distribution downstream of the condenser. A sharp increase in temperature, indicated by closely spaced contour lines, is observed at the inlet of the HX due to the large temperature difference between the airflow and the condenser wall. As the flow progresses through the HX, the spacing between contour lines increases due to the decreasing temperature difference between the HX wall and the airflow, resulting in a reduced heat transfer rate. As the flow expands through the nozzle, the static temperature decreases by $\approx 40°$ and becomes more uniform. This temperature drop is associated with the conversion of thermal energy into kinetic energy as the flow expands in the noz-

zle, which results in a 2473 N increase in net thrust if compared to Case #2.

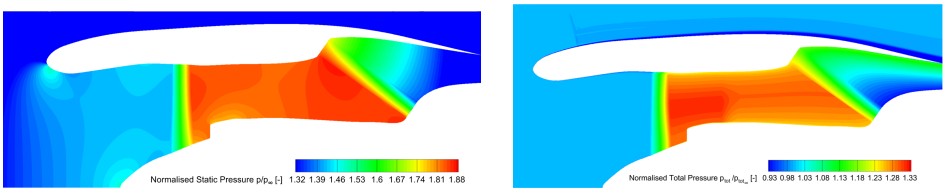

Figure B.4: Static pressure (left) and total pressure (right) contour plots resulting from the CFD simulations of the airflow around and inside the CC-TF engine bypass duct. The values are normalized with the ambient static or total pressure, respectively.

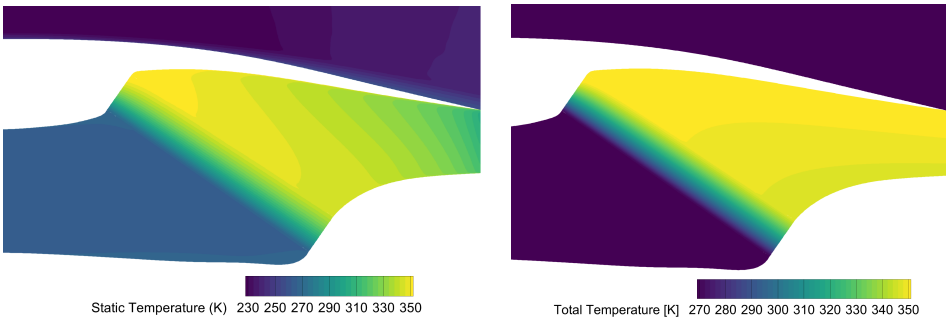

Figure B.5: Static temperature (left) and total temperature (right) contour plots of the flow near the condenser inside the CC-TF engine bypass duct.

The thrust generated by the CC-TF can be increased further by optimizing the internal shape of the bypass duct. The optimization routine reached convergence in 220 iterations. As shown in Fig. B.6, the optimized duct features a narrower nozzle and a more aggressive diffuser, which results in a slightly higher flow uniformity and lower flow velocity at the HX inlet, and a higher nozzle outlet velocity. The thrust produced by the CC-TF with the optimized bypass duct is approximately 3.4% larger than that of case #3. Note that this performance improvement is obtained without changing the nacelle size of the engine. However, the heat duty of the condenser for the test case #4 is reduced by about 2% due to the slight reduction in mass flow rate going through the bypass duct. This reduction, although small, should be taken into account in future work to ensure that the working fluid is fully condensed at the HX outlet. Moreover, larger improvements can arguably be achieved by extending the design space of the duct, allowing changes to the overall size of the nacelle and component configuration to target higher net thrust.

Although the results in Figure B.2 may indicate that the CC-TF is a less efficient propulsion system if compared to the reference turbofan engine, the assessment cannot be taken as conclusive. The study reported in this appendix only focuses on the thrust produced by the bypass stream and therefore does not consider the thermody-

namic benefit of the ORC waste heat recovery unit, which, as shown in Sec. 3.4.3 increases the overall engine thermal efficiency and contributes to approximately 27% of the total net engine power, which allows for a downsizing of the gas turbine compared to the simple-cycle turbofan engine benchmark. Whether or not the CC-TF can outperform the standard turbofan engine will ultimately depend on the aircraft, mission, propulsion system configuration, safety regulations, and overall weight.

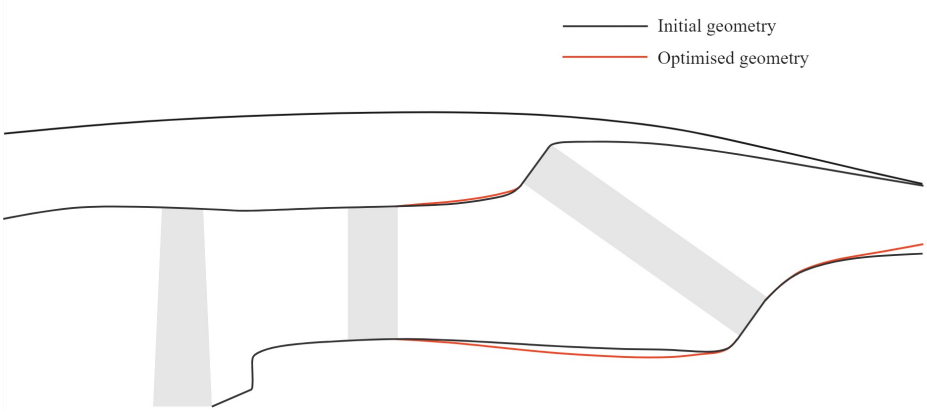

Figure B.6: Comparison of the initial CC-TF bypass duct geometry with the final optimized solution displayed in red.

BIBLIOGRAPHY

[1] K. Wessendorp, "Aerodynamic optimisation of a turbofan bypass duct with a heat exchanger modelled as a porous zone", M.S. thesis, Delft University of Technology, 2025. [Online]. Available: https://resolver.tudelft.nl/uuid:1550ddd3-c99f-4224-b552-7d74b183a024.

[2] E. M. Greitzer, C. S. Tan, and M. B. Graf, *Internal Flow: Concepts and Applications* (Cambridge Engine Technology Series). Cambridge University Press, 2004.

[3] D. Krempus, C. M. D. Servi, R. Vos, and P. Colonna, "Organic rankine cycle waste heat recovery systems for aircraft engines", Ph.D. dissertation, Delft University of Technology, 2025.

[4] F. Beltrame, L. Van Dongen, C. M. De Servi, and P. Colonna, "Optimal design of a ram air cooling duct housing the condenser of an airborne orc whr unit", in *Proceedings of Global Power and Propulsion Society*, vol. GPPS Chania 2024, 2024. DOI: 10.33737/gpps24-tc-107.

[5] F. Menter, "Zonal two equation k-w turbulence models for aerodynamic flows", in *23rd Fluid Dynamics, Plasmadynamics, and Lasers Conference*. 1993. DOI: 10.2514/6.1993-2906.

[6] C. Hughes, "Aerodynamic performance of scale-model turbofan outlet guide vanes designed for low noise", in *40th AIAA Aerospace Sciences Meeting & Exhibit*. 2014. DOI: 10.2514/6.2002-374.

[7] S. Spinner, D. Keller, R. Schnell, and M. Trost, "A blade element theory based actuator disk methodology for modeling of fan engines in rans simulations", in *AIAA AVIATION 2020 FORUM*. 2020. DOI: 10.2514/6.2020-2749.

C

Logarithmic Mean Temperature Difference Expression for Effectiveness Approaching Zero

By definition, the expression for the logarithmic mean temperature difference reads

$$\Delta T_{\mathrm{ml}} = \frac{(T_{\mathrm{h,in}} - T_{\mathrm{c,out}}) - (T_{\mathrm{h,out}} - T_{\mathrm{c,in}})}{\ln(T_{\mathrm{h,in}} - T_{\mathrm{c,out}}) - \ln(T_{\mathrm{h,out}} - T_{\mathrm{c,in}})} \,. \tag{C.1}$$

This expression can be rewritten as

$$\Delta T_{\mathrm{ml}} = \frac{\Delta T_{\mathrm{h}} - \Delta T_{\mathrm{c}}}{\ln(\Delta T_{\mathrm{max}} - \Delta T_{\mathrm{c}}) - \ln(\Delta T_{\mathrm{max}} - \Delta T_{\mathrm{h}})} \,, \tag{C.2}$$

where $\Delta T_{\mathrm{h}} = T_{\mathrm{h,in}} - T_{\mathrm{h,out}}$ and $\Delta T_{\mathrm{c}} = T_{\mathrm{c,out}} - T_{\mathrm{c,in}}$ are the hot and cold stream temperature differences, and $\Delta T_{\mathrm{max}} = T_{\mathrm{h,in}} - T_{\mathrm{c,in}}$ is the maximum temperature difference, i.e., the one between the inlets of the two streams.

Let us assume a discretization of the HX into n control volumes (CV) in which the outlet temperatures on the hot and cold stream can be expressed as

$$\begin{cases} T_{\mathrm{h}}^{\,i+1} = T_{\mathrm{h}}^{\,i} + \delta T_{\mathrm{h}}^{\,n} \\ T_{\mathrm{c}}^{\,j+1} = T_{\mathrm{c}}^{\,j} + \delta T_{\mathrm{c}}^{\,n} \,. \end{cases} \tag{C.3}$$

As the number of control volumes n increases, the effectiveness of the CV decreases due to the reduction in the temperature difference $\delta T^{\,n}$ between the inlet nodes $(i,\ j)$

and outlet nodes $(i+1,\ j+1)$ on each fluid side. The local mean logarithmic temperature difference associated with the n-th control volume reads

$$\Delta T_{\mathrm{ml}}^{n} = \frac{\delta T_{\mathrm{h}}{}^{n} - \delta T_{\mathrm{c}}{}^{n}}{\ln(T_{\mathrm{h}}^{i} - T_{\mathrm{c}}^{j} - \delta T_{\mathrm{c}}{}^{n}) - \ln(T_{\mathrm{h}}^{i} - T_{\mathrm{c}}^{j} - \delta T_{\mathrm{h}}{}^{n})}\,, \tag{C.4}$$

where $T_{\mathrm{h}}^{i} - T_{\mathrm{c}}^{j} = \Delta T_{\mathrm{max}}{}^{n}$ is the maximum temperature difference of the control volume.

Assuming a fine discretization of the HX such that

$$\epsilon^{n} \approx \frac{\delta T_{\mathrm{h}}}{\Delta T_{\mathrm{max}}} \approx \frac{\delta T_{\mathrm{c}}}{\Delta T_{\mathrm{max}}} \to 0\,, \tag{C.5}$$

$\Delta T_{\mathrm{lm}}{}^{n}$ can be approximated using a Taylor expansion for the logarithm functions in the denominator

$$\ln(\Delta T_{\mathrm{max}} + x)_{x\to 0} \approx \frac{x}{\Delta T_{\mathrm{max}}} - \frac{x^2}{2\,\Delta T_{\mathrm{max}}^{2}} + \mathrm{O}(x^2) \tag{C.6}$$

as

$$\Delta T_{\mathrm{ml}}{}^{n} = \frac{\delta T_{\mathrm{h}}{}^{n} - \delta T_{\mathrm{c}}{}^{n}}{\dfrac{\ln(\Delta T_{\mathrm{max}}{}^{n} - \delta T_{\mathrm{c}}{}^{n})}{\ln(\Delta T_{\mathrm{max}}{}^{n} - \delta T_{\mathrm{h}}{}^{n})}} \approx \frac{\delta T_{\mathrm{h}}{}^{n} - \delta T_{\mathrm{c}}{}^{n}}{-\dfrac{\delta T_{\mathrm{c}}{}^{n}}{\Delta T_{\mathrm{max}}{}^{n}} + \dfrac{\delta T_{\mathrm{c}}{}^{n2}}{2\,\Delta T_{\mathrm{max}}{}^{n\,2}} + \dfrac{\delta T_{\mathrm{h}}{}^{n}}{\Delta T_{\mathrm{max}}{}^{n}} - \dfrac{\delta T_{\mathrm{h}}{}^{n2}}{2\,\Delta T_{\mathrm{max}}{}^{n\,2}}}\,. \tag{C.7}$$

As per Eq. C.5, Equation C.7 reads

$$(\Delta T_{\mathrm{ml}}{}^{n})_{\epsilon^{n}\to 0} \approx T_{\mathrm{h}}^{i} - T_{\mathrm{c}}^{j}\,. \tag{C.8}$$

Therefore, by decreasing the effectiveness of each control volume, the differences between the logarithmic mean temperature difference, true mean temperature difference, and maximum driving temperature difference between the two fluids approach zero. As a result, the correction factor F^{n} tends to one.

About The Author

Fabio Beltrame

Born in Italy on March 18th 1995, Fabio decided to pursue the path of a researcher in aerospace engineering during his senior year in high school in the United States. He later obtained his Bachelor's and his Master's degree cum laude in Aerospace engineering at Politecnico di Torino. During his studies, he joined the Polito Sailing Team in the efforts of designing, constructing, and testing sustainable high-performance sailing yachts to participate in international competitions. His interest in sailing and engineering led him to undertake the role of project manager and coordinator of the research areas of the team. Fabio also founded and led the dynamics and performance research department, which aimed at modeling the sailing yacht to optimize performance. His work contributed to the team's first two podium placements in consecutive years.
Passionate about fluid dynamics and energy conversion systems, he joined the Propulsion & Power group of Delft University of Technology in 2019 as a post-graduate researcher in the efforts of commissioning a new experimental setup for non-ideal fluid dynamics fundamental studies and performing the first experimental campaigns. The project led to two publications. His interest in the world of scientific research and development grew and motivated him to pursue a PhD in Aerospace Engineering at Delft University of Technology under the supervision of Prof. Colonna and Dr. De Servi. During his doctorate, Fabio performed scientific research on thermal systems and heat exchangers for novel aircraft power and propulsion systems in collaboration with industrial partners within the ARENA project. Moreover, he supervised five M.Sc. students and a team of 12 undergraduate students undertaking their final project, provided support during lectures and exams of the M.Sc. course on power systems modeling. His passion for contributing to hands-on, ambitious projects and his knowledge of thermal management systems and fluid dynamics sparked a tight collaboration with the AeroDelft team and industry experts for the design and realization of a 2-seater hydrogen aircraft powered by fuel cells.

In his free time, Fabio enjoys traveling, riding motorcycles, exercising, and sports - in particular the ones that keep him in contact with nature, such as skiing, surfing, sailing, scuba diving, and mountain climbing. He is also passionate about music and loves to learn, rehearse, jam, and perform with friends.

WORK EXPERIENCE

2025- *Post doctoral researcher* on thermal systems
Delft University of Technology, The Netherlands

2020-2025 *PhD.* in Thermal Systems for Propulsion & Power applications
Delft University of Technology, The Netherlands

2017-2020 *Dynamics & performance engineer*, Polito Sailing Team
Politecnico di Torino, Italy

EDUCATION

2017-2020 M.Sc. in Aerospace engineering, *Fluid Dynamics & Propulsion systems*
Politecnico di Torino, Italy
Thesis: "Accuracy assessment of the SU2 flow solver for non-ideal organic vapor supersonic expansions using experimental data."

2014-2017 B.Sc. in Aerospace Engineering
Politecnico di Torino, Italy

AWARDS

2020 Pegasus Award
- for academic research & development projects conducted abroad.

2019 Scholarship "Thesis abroad program" from Politecnico di Torino.

2013 National BETA club membership, Atlanta, GA, USA.

LIST OF PUBLICATIONS

10. **F. Beltrame**, C.M. De Servi, *Optimal design of ram air cooling ducts housing compact heat exchangers for airborne thermal systems*, Submitted to the Journal of Aerospace Science and Technology (2026).

9. D. Krempus, **F. Beltrame**, M. Majer, C.M. De Servi, M. Pini, R. Vos, P. Colonna, *Organic Rankine cycle waste heat recovery systems for aircraft auxiliary power units*, Journal of the Global Power and Propulsion Society, vol.9 (2025).

8. **F. Beltrame**, P. Colonna, C.M. De Servi, *Optimal design of aircraft thermal systems and their heat exchangers leveraging a data-driven surrogate model*, Int. Journal of Heat and Mass Transfer, vol. 253 (2025).

7. **F. Beltrame**, L.J. Van Dongen, P. Colonna, C.M. De Servi, *Optimal design of a ram air cooling duct housing the condenser of an airborne ORC WHR unit*, Proceedings of Global Power and Propulsion Society (2024).

6. F. Sinopoli, R. Caradente, Y. Schulz, D. Krempus, **F. Beltrame**, C.M. De Servi, P. Nachtigal, D. Mimic, P. Colonna, M. Pini, *Impact of the working fluid in ORC-based waste heat recovery usystems for turboshaft engines*, Proceedings of Global Power and Propulsion Society (2024).

5. D. Krempus, **F. Beltrame**, M. Majer, P. Colonna, C.M. De Servi, R. Vos, *ORC waste heat recovery system for the turboshaft engines of turboelectric aircraft*, Proceedings of the Aerospace Europe Conference, 10^{th} EUCASS-9^{th} CEAS (2023).

4. **F. Beltrame**, D. Krempus, P. Colonna, C.M. De Servi, *Reduced order modelling of optimized heat exchangers for maximum mass-specific performance of airborne ORC waste heat recovery units*, Proceedings of the 7^{th} International Seminar on ORC Power Systems (2023).

3. A.J. Head, T. Michelis, **F. Beltrame**, B. Fuentes-Monjas, E. Casati, C.M. De Servi, P. Colonna, *Mach number estimation and pressure Pprofile measurements of expanding dense organic vapors*, Proceedings of the 4^{th} International Seminar on Non-Ideal Compressible Fluid Dynamics for Propulsion and Power (2023).

2. **F. Beltrame**, A.J. Head, C.M. De Servi, M. Pini, F. Schrijer, P. Colonna, *First experiments and commissioning of the ORCHID nozzle test section*, Proceedings of the 3^{th} International Seminar on Non-Ideal Compressible Fluid Dynamics for Propulsion and Power (2021).

1. **F. Beltrame**, L. Liboà, A. Ruggeri, G. Bracco, G. Mattiazzo, *Development of a velocity prediction program for a high-performance eco sustainable SKIFF sailing yacht*, Global Oceans 2020: Singapore – U.S. Gulf Coast (2020).